Contribution to digital microrobotics : modeling, design and fabrication of curved beams, U-shaped actuators and multistable microrobots

Hussein Hussein

SPIM

Thèse de Doctorat

école doctorale **sciences pour l'ingénieur et microtechniques**

UFC UNIVERSITÉ DE FRANCHE-COMTÉ

Contribution to Digital Microrobotics: Modeling, Design and Fabrication of Curved Beams, U-shaped Actuators and Multistable Microrobots

HUSSEIN HUSSEIN

SPIM

Thèse de Doctorat

UFC

école doctorale **sciences pour l'ingénieur et microtechniques**

UNIVERSITÉ DE FRANCHE-COMTÉ

THÈSE présentée par

HUSSEIN HUSSEIN

pour obtenir le

Grade de Docteur de
l'Université de Franche-Comté

Spécialité : **Sciences pour l'ingénieur**

Contribution to Digital Microrobotics: Modeling, Design and Fabrication of Curved Beams, U-shaped Actuators and Multistable Microrobots

Unité de Recherche :
FEMTO-ST, UMR CNRS 6174

Soutenue publiquement le 11 Dècembre 2015 devant le Jury composé de :

ORPHÉE CUGAT	Président du jury	Directeur de Recherche, CNRS, G2ELAB, Grenoble
JOËL POUGET	Rapporteur	Directeur de Recherche, CNRS, ∂'Alembert, Paris
CHRISTINE PRELLE	Rapporteur	Professeur, UTC, Compiègne
RAFIC YOUNES	Examinateur	Professeur, UL, Beyrouth Liban
PHILIPPE LUTZ	Directeur de thèse	Professeur, UFC, Besançon
YASSINE HADDAB	Encadrant de thèse	Professeur,UM, Montpellier
PATRICE LE MOAL	Encadrant de thèse	Chargé de recherche , CNRS, FEMTO-ST, Besançon
GILLES BOURBON	Encadrant de thèse	Ingénieur de recherche, CNRS, FEMTO-ST, Besançon

Acknowledgment

My thesis was realized in the AS2M department of Femto-st institute. I would like to express my sincere gratitude to all the members of the department, starting from the director Michaël Gauthier and the colleagues for their support and the bright and stimulating environment of the department.

I would like to express the deepest appreciation and thanks to my advisors Prof. Philippe Lutz, Prof. Yassine Haddab, Dr. Patrice Le Moal and Dr. Gilles Bourbon, who supported me greatly during the thesis and did every possible effort to help me in order to achieve the best results. I am more than thankful for them for their kindness, patience, and endless encouragement. I could not have imagined having a better advisor and mentor for my Ph.D study. Thanks to you.

I would like to thank the rest of my thesis committee: Dr. Orphée Cugat, Dr. Joël Pouget, Prof. Christine Prelle, and Prof. Rafic Younes, for serving as my committee members and for letting my defense to be an enjoyable moment. Your insightful comments incented me to widen my research from various perspectives. Thanks to you.

A special thanks to my family, you are everything for me. Words cannot express how grateful I am to my mother and father for all of the sacrifices that you have made on my behalf. I would also like to thank my brother and sisters for always being there beside me through thick and thin.

I specially extend appreciation to my beloved wife, Fatima, who was always my support. The day you stepped into my life, you changed it into something so beautiful and meaningful. You are just so amazing to have around. I love you so much.

Finally, a new ray of sunshine will enter our lives in the next days; we are waiting the arrival of our little princess Zahraa. Thank you my babe for the pleasure and happiness you have added before your arrival. We are waiting impatiently ....

Hussein Hussein

Contents

List of Figures

List of Tables

General introduction

Since the mid-20th century, the relationship between humans and machines are experiencing a tremendous development. Electronic products and smart devices have become an extremely important part of our daily life. The actual and coming tech boom makes and will make our life so mush easier. Personal computers, smart phones, cameras, televisions and thousands of other intelligent devices, all are operated by the silicon chips and integrated circuits inside. All the developments nowadays in every single domain of our life including the economy, all kinds of industries, energy production, transport, communication, medicine and many others have been made possible mostly with the help of these powerful silicon chips. They allowed us to access the nearby planets and explore the most distant galaxies in the large scale, and to discover the smaller organisms ever and dive in the particles and atoms world in the downscale.

As we go down in size, there are a number of interesting opportunities coming up, plenty of room, applications and possibilities at the bottom are not yet discovered, while the technology of small devices is expanding fast. Micro-Electro-Mechanical Systems, or MEMS, is the technology of miniaturized systems. It consists of micro-electro-mechanical elements that are made using the techniques of microfabrication. An extremely large number of MEMS devices are available in the market and many of them have demonstrated performances exceeding those of their macroscale counterparts.

The accelerated research and development in the field of miniature systems and integrated circuits introduced innovative products in our society and revealed the necessity to develop micromanipulators to handle microobjects, fabricate structures, assemble products, interact with a patient, etc.. Two main elements are generally implemented in the design of a micromanipulator:

- A **tool** to make the final function. The tool can be a probe or a microgripper used for handling an object, grasping, performing pick and place, pushing, pulling, positioning, orienting, etc..
- A **micropositioning system** to position the tool or another substrate. This system must be able to deliver displacement strokes with sub micrometer level accuracy, high precision and repeatability.

Each of these elements has its own characteristics and constraints. As for the tool, scale effect appears due to the miniaturization which is represented by the predominance of surface

forces (adhesion forces ...) on the volume forces (gravity, weight ...) for small objects. Thus, handling an object is more complicated due to the predominance of some forces (such as electrostatic, Van der Waals, and capillary forces) which are negligible in traditional manipulation.

As for the micropositioning systems, several issues can be noted such as the limitation in the fabrication process that constraints several aspects in the design (monolithic structure, multi DoF, out of plane displacement, assembly, etc.), the need to make high precision and repeatable systems, the need of sensors for precise positioning, the miniaturization, extending the range of motion in the workspace, the integration in complicated environments, etc.. There are still few work on the design of robotic carriers which are dedicated to the microworld.

Digital microrobotics is an emergent branch in micropositioning systems which avoids the necessity of a feedback to control the position by placing the moving part in several stable positions defined in the design. This avoids the use of bulky sensors which increases the size of the whole device, allows going further in miniaturization, simplifying the control and integrating the device in more complicated environments. Digital microrobots consist generally of multistable mechanisms with switching and holding functions.

For many years, the AS2M department of FEMTO-ST institute focuses in its research on the design of robotic systems suitable for micromanipulation and micro-assembly. In this context, digital microrobotics was recently a matter of concern in the laboratory and it was the topic of two PhD theses made in prior years. Mr. Qiao Chen in his thesis (2010) has proposed a bistable module that is based on the use of a buckled beam structure and U-shaped actuators. Mr. Vincent Chalvet in a subsequent thesis (2013) has proposed a multistable microfabricated digital microrobot DiMiBot, where a number of the bistable modules (those developed in the thesis of Mr. Qiao Chen) are connected with an elastic structure to one end effector. The structure of the DiMiBot allows its end effector to reach a number of discrete positions in a square workspace distribution. The positions are non redundant with respect to the states of the modules, and adding more positions in the workspace is made by adding extra bistable modules.

The works made in the actual thesis is a continuation of the previous works made in the department on digital microrobotics. Based on past achievements, the thesis objectives focus on improving the functioning of the DiMiBot, optimizing its design and improving its fabrication process, in order to make it more accurate, more controllable and smaller. To achieve these goals, analytical studies were run for the main components in the DiMiBot (Buckled beam structure and U-shaped actuator) in order to explore their limits in terms of the miniaturization whilst delivering the required performance. In addition, new structure of the DiMiBot was proposed with multistable mechanisms that allow more positions in the workspace without adding more elementary modules and increasing the size. This allows also to realize complex trajectories in the workspace in an open loop control. These two limitations were the main drawbacks of the previous DiMiBot. In addition, some changes were made in the fabrication process in order to reduce the possibility of defects and getting proper structures. A new mechanism was proposed and used in the new DiMiBot in order to compensate the fabrication tolerances and to improve the accuracy of the discrete positions.

Challenges for a new generation of the DiMiBot are presented in Chapter 1. The different solutions found in literature to realize a digital system in terms of the switching, holding and multistable mechanisms are then presented. The thesis objectives and working axes are presented and the next chapters are introduced. Two working axes were followed in the the-

sis: the first one concerns the analytical modeling and design of preshaped curved beam and U-shaped actuator, which are the main components in the DiMiBot, the second axis concerns the development and fabrication of a new generation of the DiMiBot with multistable modules.

Chapter 2 concerns the modeling and design of a preshaped curved beam. Analytical modeling of the snapping forces and internal stresses are firstly investigated. The influence of the material and dimensions on the behavior of the curved beam and its design and optimization are investigated subsequently.

Chapter 3 concerns the modeling and design of the actuator. The problem is treated by a sequence of two analytical models: electro-thermal and thermo-mechanical models. The influence of the different dimensions and electro-thermo-mechanical properties on the behavior of the actuator and its design are investigated in a second stage.

The principle and design of a new generation of the DiMiBot is investigated in Chapter 4. Only two multistable modules are used in the new DiMiBot instead of all the bistable modules in the old generation. The design of the different components, each internal system in the multistable module and the global structure of the module and the DiMiBot are presented.

Finally, the fabrication and experiments are presented in Chapter 5. All the difficulties encountered and solutions provided in the fabrication and the experiments are detailed. Operational prototypes of the multistable module are fabricated and showed a proper functioning in the experiments.

Chapter 1

Digital Microrobotics

Digital microrobotics and the digital microrobot "DiMIBot" are presented in this chapter including challenges for a new generation of the DiMiBot. A classification of the solutions found in literature that allow realizing digital systems and imporoving the DiMiBot is then presented. Finally, the thesis objectives and working axes are presented and the next chapters are introduced.

Chapter contents

1.1 Introduction

Numerous are the technological devices in the market where the miniaturization is an objective. This applies in many application areas, from the general public to the highly specialized products. The miniaturization of many products becomes more and more a pressing need and the development in this regard is on the rise. The development in microsystems is based mainly on adding extra functionalities in smaller space and on the development of microfabrication techniques.

Having already proven their utility at the macroscale, robots also show their usefulness when we approach the infinitely small. The way to the microworld is not that simple, designing microrobots is not an easy task. MEMS devices and processes are non-standard, they are generally multidisciplinary and multiphysics. The materials and fabrication process are intricately involved. Every product requires a different design, fabrication process, expertise and specific knowledge in various domains simultaneously. Actually, it is not sufficient to miniaturize each part of an existing robot, then assemble them to get a robot that is less than one or few millimeters in size. For example, engines of the macroscale are not suited to this scale, therefore other MEMS-compatible actuation technologies are employed.

Taking the example of a microspectrometer which is an instrument to measure the wavelength of light [28]. Such an instrument is generally bulky, expensive and cannot be easily ported outside of lab environments, while MEMS technology offers an excellent opportunity for miniaturizing the spectrometer. An automated assembly of the microspectrometer components is presented in [28] and shown in Figure 1.1.

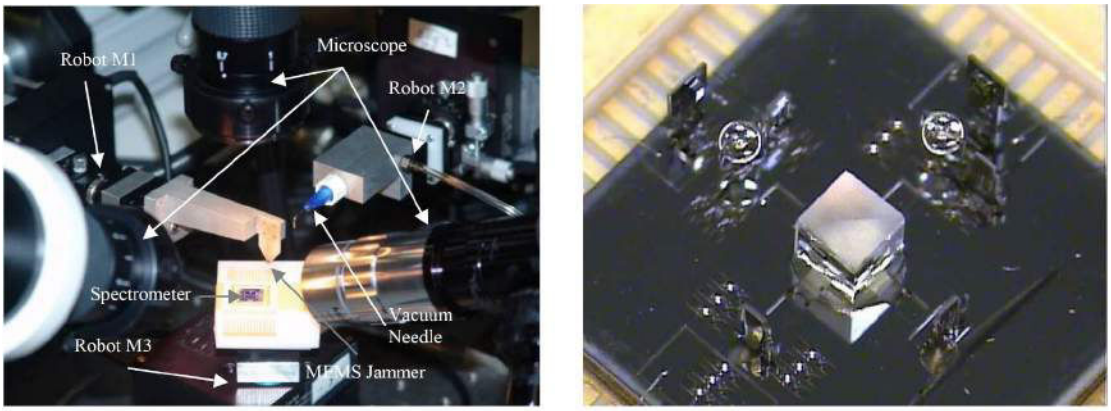

FIGURE *1.1: Assembly platform for a microspectrometer (a), the assembled microspectrometer (b) [28].*

Several miniaturized components (glass lenses, optical fibers, laser sources, and detectors onto silicon fixtures and microactuators) are integrated in a single precision bench to form the microspectrometer. Three micropositioning robots are used to move precisely the spectrometer, a MEMS Jammer and a vacuum needle respectively. Three microscopes are used for controlling the assembly process.

The race for miniaturization has revealed the need to handle precisely some micrometer-sized objects. To address this need, considerable advances in the microrobotic field are made for generating displacement and manipulating objects at the microscale. Micromanipulators were developed and used in many fields of microrobotics in order to handle an object, fabricate a structure, assemble a product, operate with a patient, etc.. However the necessity of vision and measurement systems to manipulate or assemble micro components remains a challenge to overcome.

Mechanical positioning systems are back-bone systems behind every object manipulation task. Numerous systems for the positioning with high precision at micrometric scale have been developed and are available in the market.

The micropositioning systems work generally in closed loop control and consist of single or multiple actuators, feedback sensors, mechanical platform, control unit and a power source [65]. Figure 1.2 shows a general schematic diagram of the functioning of a positioning system with feedback.

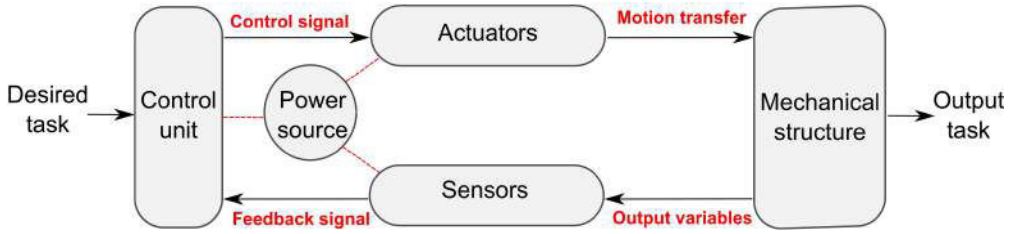

FIGURE *1.2: Schematic diagram for the functioning of a positioning system with feedback.*

The different components of the continuous positioning system perform their respective functions to achieve positioning tasks in a well defined workspace. Actuators are the components used to change the state of the system. The input energy is converted through the actuator into motion, force or combination of both. In general, the actuators are able theoretically to reach any position continuously in the workspace. However, continuous energy must be applied to maintain any position.

The main technologies used in MEMS for the actuation are based mainly on thermal, electrostatic, magnetic and smart material (piezoelectric material, shape memory alloy (SMA), electroactive polymers (EAP), etc.) principles.

Sensors are the components that measure a physical quantity (output variable of the system) and convert it into a feedback signal to be treated by the control unit. A large number of microsensors have been proposed by MEMS developers for almost every possible sensing modality including temperature, displacement, pressure, inertial forces, chemical species, magnetic fields, radiation, etc..

Micropositioning systems require measurement and vision systems, often bulky and expensive, in order to perform accurate measurement of the position and orientation of the micro-objects. However, most of these sensors provide limited information feedback (for example interferometers measure the displacement only in one direction), forcing to use in a large number. Therefore, the need of one or several sensors is not compatible with the miniaturization of the positionners and their integration in confined spaces. Besides, various problems are associ-

ated with the use of sensors, such as nonlinearity, complex control law, continuous feeding and servoing, complex connectivity, low signal to noise ratio, etc.. These problems vary with respect to the type, technology, material and other properties of the sensor.

In addition to the high precision requirement, the integration of micromanipulation platforms in reduced environments (such as scanning and transmission electron microscope) is a recurring problem due to the complexity of the micropositioning systems.

It is often difficult to integrate the various components (sensors, power source, actuators, etc.) into the micromanipulation platform, especially in confined spaces where the integration of these components can be quite challenging. In the efforts to address this challenge, digital concept in micropositioning is introduced couple of years ago [13, 21, 103, 104, 136].

1.2 Digital microrobot

In the previous theses of Vincent Chalvet [12] and Qiao Chen [20], the works have led to the development of a digital microrobot called "DiMiBot". Prototypes of the DiMiBot were fabricated, characterized and showed a good functioning in the experiments. However, this thesis deals with and provides solutions for some challenging issues of concern for the DiMiBot. The principle of digital microbotics and the DiMiBot are presented in this section. The challenges and requirements for a new generation of the DiMiBot are then presented.

1.2.1 Digital microrobotics

Digital microrobotics is an emergent branch in micropositioning systems which consists in placing accurately the moving-part/end-effector of the system discretely without feedback. The digital concept avoids the use of sensors and measurement systems by adding a holding function of the mobile part at several positions. Digital microrobots have a defined number of repeatable states called "discrete positions", while the positions in between are considered as unstable positions. Based on this definition, the positions of a mobile part can be classified with respect to their level of stability as illustrated in Figure 1.3.

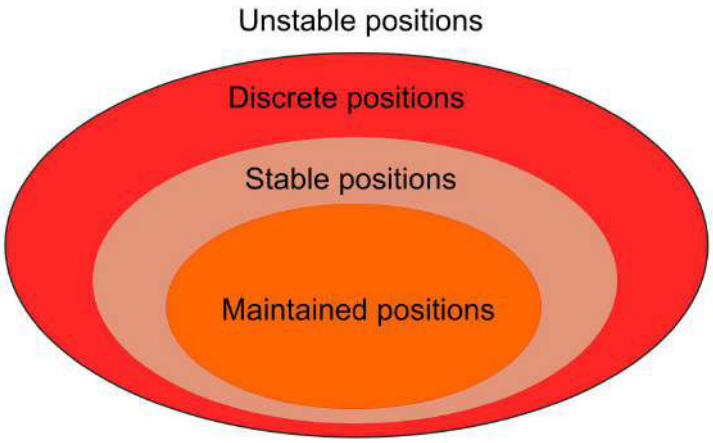

FIGURE *1.3: Unstable, discrete, stable and maintained positions.*

The discrete position is a position in a state of equilibrium that does not change with time. The stable position is a discrete position which tends to return to its initial state after a small variation. These positions have a local minimum energy. The maintained position is a stable position that retains its state in front of external disturbance, a force barrier (holding force) must be exceeded before changing the state of the system. In contrast, the unstable position is a position out of static equilibrium or tends to change its state after a very small variation (local maximum energy). The different positions with respect to their stability level are presented in Figure 1.4 using the example of the ball on a surface, only subject to gravity.

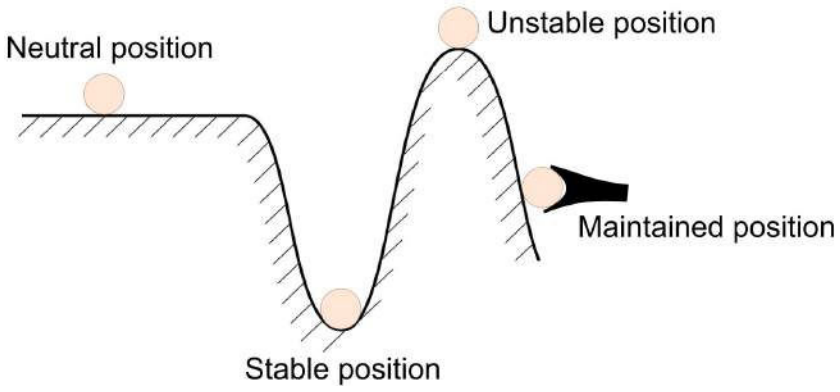

FIGURE *1.4: Example of the ball on a surface in different positions.*

The different positions of the ball represent the possible states of a position. Relatively to the potential energy, the stable position is in a local minimum, while the unstable position in the figure is in a local maximum. The maintained position is maintained using an external tool. The neutral position is a discrete but not stable position. It keeps its new state after displacement.

Under these definitions, the mobile part of digital systems/microrobots passes through unstable positions during transition between a discrete position and the other. The mechanical structure in these systems is generally a multistable mechanism. The transition between the different stable states of the mechanism is satisfied by two main functions: switching and holding. Generally, the switching function is satisfied using continuous actuators that generate the required force and displacement in the digital system.

The holding function allows maintaining the discrete positions in front of external loads and disturbances. The holding can be ensured either by active or passive maintain. In active maintain, the mechanism needs some external energy to keep its place, while it's not the case in passive maintain where the mechanism is inherently stable at each position without consuming energy.

Figure 1.5 shows a general schematic diagram for the functioning of digital microrobots. The input on the actuator serves for switching the mobile part of the multistable mechanism between a discrete position and the other. Once the mobile part is placed in the desired position, different holding methods are used in digital systems for the holding.

The digital concept has many advantages, it allows robust and repeatable positions without measurement systems, simplifying the structure, the connectivity and the control, integrating the microrobot in complicated environments, going further in miniaturization and avoiding the

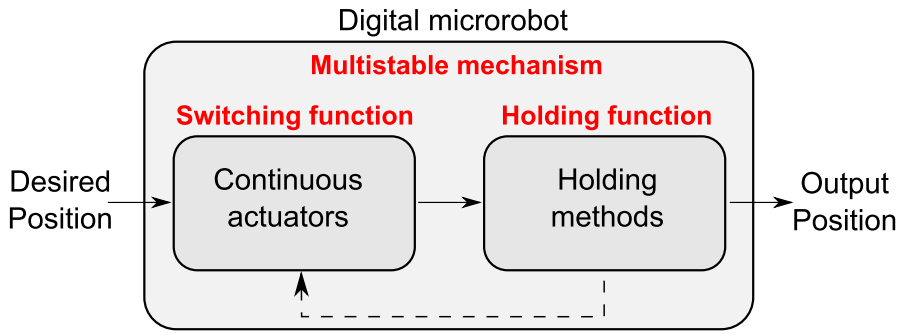

FIGURE *1.5: Schematic diagram for the functioning of a digital microrobot.*

general problems of sensors in microstructures (size, connectivity, noise accuracy, control laws, etc.). The different solutions used in literature to realize the switching function, the holding function and the multistable mechanisms are presented later in this chapter.

Numerous applications are based on the digital concept, such as switches [109, 29], valves [38], relays [39], positioners [17, 11, 102], braille displays [93], digital microrobots [13, 104, 103], etc.. The design purpose in many of these applications is not necessarily to realize digital robots, but they operate on the digital principle and can be classified as digital systems.

1.2.2 The DiMiBot

Vincent Chalvet [12] developed in his thesis the DiMiBot which consists of several bistable modules in a symmetrical spatial distribution. The monolithic structure of the DiMiBot is an essential characteristic in order to be compatible with the microfabrication technology. The bistable modules used in the DiMiBot are the same developed in the thesis of Qiao Chen [20]. Each module switches its shuttle (moving part) between two maintained positions. The shuttles of all the bistable modules are connected by beams and compliant hinges to the end effector. Thereby, the end effector of the DiMiBot can be placed directly in the desired position by switching the different modules to the corresponding states. The concept, design, advantages and disadvantages of the DiMiBot are presented in the following.

Architecture of the DiMiBot The general architecture of the DiMiBot is presented in Figure 1.6. The structure of the DiMiBot consists of connecting beams, hinges and bistable modules. The beams are designated by the rectilinear lines, the hinges are designated by the small circles, and the bistable modules are designated by the rectangular blocks. The nomenclature inside the blocks (bl0, bl1..., br0, br1...) refers to the side and position of the module. The letters 'bl' and 'br' stand for left and right bistable modules respectively, while the number stands for the position, it starts by 0 at the bottom and rises with the level of the module.

The hinges are used as connection between two components (beam-beam, beam-module and beam-substrate) and enable a free rotation relatively between them. The structure in each side is a series of horizontal and vertical curved beams in the form of a staircase structure. The two staircase structures are symmetrically distributed between the left and the right of the DiMiBot.

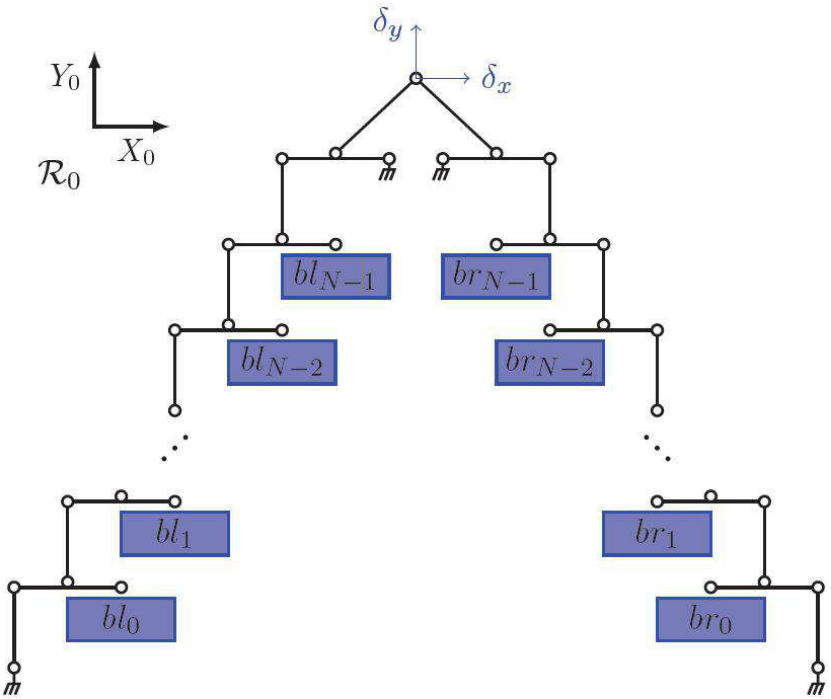

FIGURE *1.6: Schematic of the general structural architecture of the DiMiBot. [12].*

A top head mechanism is placed at the top of the two staircase structures and consists of two slanted beams. The top of the DiMiBot contains the end effector.

N bistable modules are placed symmetrically in each side of the DiMiBot. The shuttles of these modules are connected to the free ends of the horizontal beams in each staircase structure. All the modules have the same dimensions and generate the same displacement in a vertical direction between two maintained positions. This parallel structure simplify the electrical connectivity of all the bistable modules and relates all the moving parts separately from the modules which is not possible in serial structures.

In the condition of small displacement hypothesis, the stroke of each bistable module is divided by 2 at each level of the staircase structure, starting counting from the corresponding staircase level. In this way, the smaller step of displacement at the top of the staircase structure is the one caused by the switching of the first bistable module. The step caused by the switching of the second bistable module is two times bigger, and so on, the variation due to the switching of the module (M) is two times bigger than the variation due to the switching of the previous module (M-1).

In this way, we obtain 2^N discrete positions at the top of each staircase structure due to the contribution of the N bistable modules. The discrete positions of the two structures are combined through the top head mechanism to form a workspace with $2^N \times 2^N$ discrete positions at the end effector. In small displacement conditions, the displacement at the end effector of the top head mechanism are in the same direction of the slanted beams of the mechanism. Thereby,

if the two angles of the slanted beams are equivalent to 45°, the discrete positions form a square workspace which is rotated 45°with respect to X_0 Y_0 axes.

Design of the DiMiBot In terms of the mechanical structure, Figure 1.7 shows a CAD drawing of the DiMiBot with four bistable modules. This drawing is for an operational prototype of the DiMiBot which is fabricated and tested in the previous thesis. The overall size of the prototype is $36mm \times 24.5mm$.

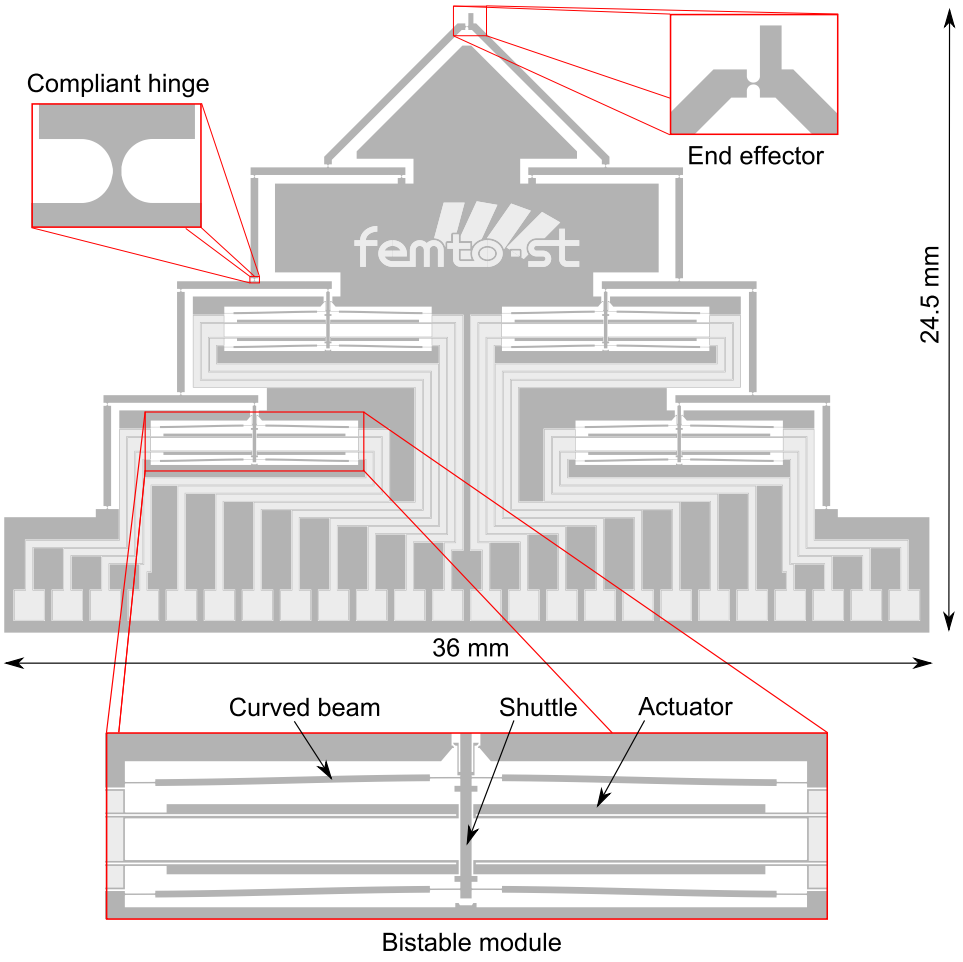

FIGURE *1.7: Drawing of the DiMiBot with four bistable modules with zooms on a bistable module, a compliant hinge and the end effector.*.

The DiMiBot is fabricated on SOI wafers which consist of silicon device and handle layers separated by a thin layer of buried oxide (SIO_2). The active parts of the DiMiBot (bistable modules, beams and hinges) are fabricated in the device layer, while the substrate contains the three layers.

The bistable module consists of a bistable mechanism and actuators. The mechanism consists of a pair of preshaped curved beams connected to the shuttle in the middle which makes

a structural guidance of motion. The switching is made using four U-shaped electrothermal actuators. Each pair of actuators is used to switch the bistable mechanism in a direction. The shuttle can move between two stop blocks which are used to define the stroke and add holding forces on the positions. The principle of the stop block is clarified later in the holding methods section.

The hinge used in the structure is a compliant flexible hinge with a circular shape. In contrast to other shapes of compliant hinges (rectangular, oval), in this shape, the rotation occurs around a reduced area which is the closest solution which ensures similar behavior of an ideal hinge. However, the stress is concentrated and more important in the reduced area compared to other solutions where the stress is not concentrated and less important.

The connecting beams have a rectangular shape. The length of these beams is chosen to be long enough to be able to consider a small displacement at the borders with respect to the length. The width is wide enough, so that the beam is rigid and does not suffer from elastic deformation during functioning.

A metal layer (aluminum) is deposited on the top of the device layer to supply the actuators in the bistable modules. 24 metal lines are used to supply the bistable modules, 6 for each one. Each actuator need to be supplied from two lines. In order to reduce the total number of metal lines, one line is used in common between two nearby actuators in the two sides of the bistable module. The metal lines are separated electrically from each other by etching the silicon layer around until the buried oxide which is an electrical insulator. All the metal lines are related to square pads at the bottom of the DiMiBot, which in turn, are connected to an external circuit using wire bonding.

At the end effector, a rectangular shape is extruded as a probe to handle with micro-objects. It is worth noting here that, in the previous and the actual theses on digital microrobotics, the focus is on the realization of a digital micropositioning system, the final function of the end effector is outside of the objectives. However, in future prospects, a specific design can be developed for specific applications that require a digital positioning and a defined final function.

1.2.3 Advantages and challenges

1.2.3.1 Advantages

The DiMiBot has obvious and numerous advantages either in the concept or in the design. It combines the advantages of the digital concept, passive maintain, compliant mechanism, monolithic structure, and unlimited multistable mechanisms with elementary modules.

Each one of these features has its own advantages. The digital concept allows positioning in robust and repeatable stable positions without need of measurement systems. This simplify the structure, the connectivity and the control, avoids the general problems of sensors in microstructures (bulky size, accuracy, complicated control laws, etc.), makes the system insensitive to noise and disturbances, and enables going further in miniaturization.

The stability of the discrete positions in the workspace of the DiMiBot returns to the stability of the positions in each bistable module. These positions are passively maintained at rest with the buckled beam structure of the bistable mechanism. This is an important feature since no external energy is needed to keep the state of the system.

The compliant structure of the DiMiBot exhibits many advantages such as increased precision and reliability, no friction, no backlash, reduced wear, and low manufacturing costs. The use of silicon in the device layer exhibits also many advantages. The silicon has an almost perfect elastic behavior with highly repeatable motion and without hysteresis and energy dissipation, it has also a long lifetime with little fatigue. This material is widely exploited in MEMS applications, its physical properties are well defined and the fabrication processes with silicon are well developed.

In addition, The DiMiBot is a monolithic structure. On one hand, this feature simplify the fabrication process and allows the fabrication in a large scale, on the other hand, it allows the integration in complicated and compact environments.

The last feature is the unlimited principle of the used mechanism. The principle itself is an advantage where additional positions can be added as required by simply adding more elementary modules. However, the obtained positions in the workspace are non redundant positions where each position is equivalent to one set of states of the bistable modules. In this way, one can switch to a desired position directly by switching the bistable modules to the corresponding states.

1.2.3.2 Challenges for a new generation of the DiMiBot

In the other side, several limitations can be cited for the DiMiBot in the concept, design, fabrication and functioning. Limitations of the DiMiBot are presented hereinafter, followed by the challenges for a new generation.

The first limitation is that the DiMiBot is not able to reach all the positions in between in the workspace. This is the feature that we lose when we turn to digital systems. The distance between two adjacent positions is the resolution of the system. The resolution can be adjusted with respect to the application.

Secondly, the transition between the discrete positions in the workspace is not always possible between the neighbor positions. This is due to the non redundant architecture of the DiMiBot, where the switching of a bistable module produces 2^i steps (binary jump) in the workspace in a direction, no other module is able to produce 2^i steps in the same direction (i is a positive integer). Thereby, the transition to the adjacent positions is not possible in all the cases in one step, and long trajectories are mandatory sometimes to reach a near position, the realization of specific trajectories becomes also complicated.

Another limitation is that the number of stable positions in the workspace is related to the number of bistable modules. For higher number of stable positions, higher number of bistable modules are needed. The use of more bistable modules increases the size of the DiMiBot, increases the failure possibilities in the fabrication, adds 6 electrical input for each module, and the structure of the DiMiBot becomes weaker.

Further, another limitation is that the realization of the digital systems and the DiMiBot requires a high fabrication quality in order to ensure the accuracy. This is required to avoid the important fabrication tolerances and step/stroke differences. Several runs of microfabrication in the previous thesis were necessary to get functional robots. One prototype with four bistable modules was fabricated successfully and showed a proper functioning during characterization. The measured workspace of the fabricated prototype is shown in Figure 1.8.

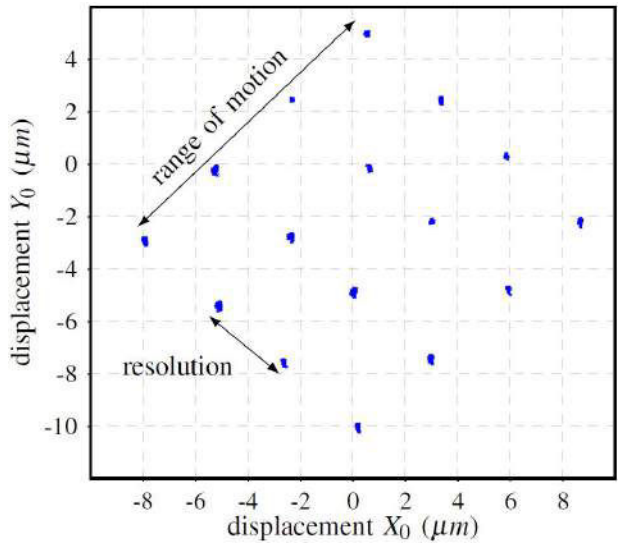

FIGURE *1.8: Workspace of the fabricated prototype of the DiMiBot.*

However, the fabrication tolerances were important in the prototype. The bistable modules were designed to have a bistable distance of $25\mu m$ between the two stop blocks, while the measured displacement variates between 33.6 and $36.5\mu m$ in the different modules. This indicates a large excess of etching at the sidewalls of the device layer and a variation in the etching conditions on the large surface of the DiMiBot.

At the workspace, there was also some differences in the displacement induced by each module between the theoretical calculation and the measurements. These differences may return to the simplifications taken in the calculation (small displacement hypothesis, rigid connecting beams) and the fabrication tolerances.

The non holding of the end effector in front of external loads is another limitation of the DiMiBot. In contrast to the positions of the bistable modules, the discrete positions in the workspace are stable but not maintained. This is due to the elastic structure of the external mechanisms formed by the connecting beams and the hinges.

The last limitation to be cited is in the design of the DiMiBot, where at the beginning of the thesis, we were not able to define the miniaturization limits of the DiMiBot. The miniaturization of the total structure is related to the minimal size of components that ensure the switching and holding in each module. The main components are the curved beams and the actuators. It lacks models, analytical or numerical, that describe the behavior of each component and shows the influence of each dimension on their behaviors, which allows choosing the dimensions that ensure the required performance and defining their limits of miniaturization.

In result, four main challenges can be cited for a new generation of the DiMiBot:

- Proposing new structures/mechanisms that allows generating complicated trajectories and reducing the size of the DiMiBot.
- Proposing some structural solutions to reduce or compensate the fabrication tolerances which influence the accuracy of the positions and steps.

- Improving the fabrication process in order to avoid the difficulties encountered in the previous thesis.
- Developing models for the curved beam and U-shaped actuator which are then used for the dimensioning and defining miniaturization limits.

The works in the thesis have risen to and overcome these challenges and important results were reached with respect to each challenge.

1.3 Solutions for digital systems

After presenting the digital microrobot, the purpose of this section is to present the solutions found in literature to realize digital systems. Several classifications for the digital systems were presented previously in [13, 21, 103, 104, 136] based on the number of discrete or stable positions, technology of the actuators, holding principles and applications.

However, a digital system is simply a multistable mechanism with switching and holding functions. The main element in the switching is the actuator, different actuating technologies which are compatible with MEMS and were used in digital systems are presented in the following. The different holding methods are presented afterwards. Finally, different approaches to realize multistable mechanisms are introduced. Examples of digital systems which use the different solutions for the switching, holding and mechanisms are cited in each paragraph.

1.3.1 Switching function

The first elementary function in digital systems is the switching of the mobile part between discrete positions. To realize the switching function, a driving force is generated and exerted on the mobile part using continuous actuators. In digital MEMS, electromagnetic, electrostatic, electrothermal and smart materials principles are the most common physical principles used to generate the switching. The different actuating technologies were extensively addressed in literature, a brief presentation of those used in digital systems is given hereinafter, while examples of digital systems are only cited for each principle.

1.3.1.1 Electromagnetic principle

The electromagnetic actuation principle is characterized by the interaction between the magnetic and the electrical phenomena, where the Lorentz force appears after charging electrically a particle in the presence of a magnetic flux. The actuators realized with electromagnetic principle generate the electromagnetic forces via three forms:

- **Reluctance force** [6, 66, 82, 83, 112, 138]: where the mobile part tend to align with the fixed part in order to minimize the magnetic circuit reluctance.
- **Laplace force** [31, 102, 104, 129, 133]: which is a manifestation of the Lorentz force acting on a current-carrying wire in a magnetic field.

- **Induction force** [114]: which results from an interaction between induced currents (Faraday's law) in a plane and a magnetic field.

The main advantages of these actuators, in general, include fast response, large force and displacement, contactless actuation, simple design, low cost and suitability in harsh environment. However, these actuators have a bulky size which is not compatible with the miniaturization.

1.3.1.2 Electrostatic principle

Electrostatic actuators [8, 15, 49, 70, 72, 95, 110, 125] operate on the principle of Coulomb attraction due to the application of a bias voltage between two plates (moving and fixed). Opposed charges appear at the opposed surfaces of the two plates and generate attractive force. The electrostatic principle is used with several geometric configurations (simple parallel plate, comb drive, curved electrode, etc.).

Electrostatic actuators provide contactless actuation, high positioning resolution and fast response. They are characterized by the straightforward MEMS-compatible fabrication, and low power consumption. The main drawback of these actuators is that the output force is inversely nonlinearly related to the gap between the plates which limits the stroke.

1.3.1.3 Electrothermal principle

Electrothermal actuators [12, 20, 23, 79, 84, 107, 113] operate on the principle of Joule heating and thermal expansion. The structure of the electrothermal actuator amplifies the thermal expansion of its internal arms which is limited relatively. The most common designs of these actuators include the bimorph, U-shaped and V-shaped actuators. The bimorph and U-shaped actuators work on the principle of amplifying thermal expansion difference between a cold side and hot side. The bimorph design consists of two or more dissimilar materials bonded together and having various expansion coefficient, while the U-shaped actuator is a monolithic structure made of various width-length-resistivity arms. In contrast, in the V-shaped actuator, a symmetric expansion of two opposed arms is amplified in the orthogonal direction.

Due to their straightforward integration with standard MEMS based fabrication processes, relatively smaller footprint, design simplicity, high force output, large range of displacement and tolerance to working conditions (dust, moisture...), electrothermal actuators are suitable and extensively used for MEMS applications. However, their main drawbacks include the temperature dependency, high working temperature, slow actuation and control difficulties.

1.3.1.4 Smart materials

Smart materials are characterized by the ability to change one or more properties (including mechanical, thermal, optical, or electromagnetic properties) in a predictable or controllable manner in response to their environment. This change is reversible and can be repeated many times. Among the available smart materials, piezoelectric materials and shape memory alloys have been largely used for MEMS applications and for digital systems as well.

- **Piezoelectric actuators** [10, 43, 88]: where some materials have the ability to deform in the presence of an electric field. These actuators provide several advantages, such as

instant response, important output force, high energy conversion efficiency, while they suffer from a nonlinear behavior (hysteresis, creep) and low displacement range.

- **Shape Memory Alloy (SMA)** [1, 5, 48, 67, 74, 81, 127, 136]:which is an alloy that remembers its original shape due to an internal phase transformation and returns to its initial state when heated after deformation. SMA actuators have many remarkable features, such as high power to weight ratio, sensing ability, low driving voltage, silent actuation, lightweight, large force and displacement. In contrast, these actuators suffer from some weak points, such as low energy efficiency, low response time, and non-linear behavior.

1.3.1.5 Synthesis

Common physical principles in literature used for the switching function including electromagnetic, electrostatic, electrothermal, piezoelectric and SMA have been presented. For the electromagnetic principle, the main advantages include high speed, simple design and low cost. The piezoelectric switching principle provides the advantages of instant response and high energy conversion, while their main drawback is the small displacement capacity. The SMA actuators are lightweight and provide large force and displacement. These technologies have been ignored for the DiMiBot due to the complexity of their integration in a monolithic structure.

In the other side, the main advantage of electrostatic and electrothermal principles relatively is their straightforward integration and compatibility with the standard MEMS based fabrication processes. The electrostatic switching principle provides contactless actuation but its main drawbacks is the limited stroke and the need of a large footprint relatively to produce the desired force. The electrothermal switching principle has the advantage to exhibit strong forces and large displacement simultaneously with smaller footprint. Therefore, electrothermal actuators were chosen in the old and the new DiMiBot. Otherwise, if faster microrobots are concerned in the future, other technologies can be selected.

1.3.2 Holding function

The holding function is the second important function that characterizes digital systems. Thanks to the holding method, the digital system holds the mobile part in discrete or stable positions. Different holding principles can be found in literature, these principles are either active or passive. A classification for the most common principles, used in literature to realize the holding function, is presented in Table 1.1.

TABLE *1.1: Classification of holding principles.*

Holding principles	
Active holding	Passive holding
• Continuous switching function • Active locking actuator	• Passive locking actuator • Permanent magnet • Buckled beam structure (constrained or uncontrained)

Noting that a holding principle is a characteristic of the position and not of the digital system. Thereby, it is possible that we find a digital system with a holding principle for a position and another holding principle for another position. The active holding is outside of our interest for the DiMiBot, therefore, their principles are described briefly in the following. Afterwards, the passive holding principles are detailed with examples.

1.3.2.1 Active holding

Holding via continuous switching function The simplest way to realize the holding function is to use the switching actuators for generating the holding force continuously during the holding time [23, 29, 37, 44, 53]. The use of this holding principle reduces the number of needed actuators in the system and is efficient for applications with temporary holding time or high switching frequency.

Holding via active locking actuator The other principle in active holding is the active locking actuator [32, 84, 117]. This holding principle is similar with the continuous switching function principle while the main difference is that the holding force is provided from another actuator. Generally, the reasons behind the use of another actuator for the holding in these systems are generally for reducing the energy consumption of the switching actuator or improving the holding force.

1.3.2.2 Passive holding

Holding via passive locking actuator Another category of the holding principles used in digital systems is the use of an external locking actuator [26, 95]. In this category, the holding function is ensured by employing a separate locking actuator that locks or unlocks the mobile part at the discrete positions. This method requires energy while locking and unlocking the mobile part, which is provided by an additional actuating mechanism, but no energy is consumed once the mobile part is locked. This holding principle is illustrated with the example of the ball on a surface as shown in Figure 1.9(a). The ball is latched in the positions B & C using an external latch-lock mechanism.

Cochran et al. [26] have developed an optical switch based on electrothermal actuators for the switching and the holding functions (Figure 1.9(b)). In the upper position of the slider, the input fiber is aligned with the output fiber (close state), while no light passes through the output fiber in the down position (open state). During the switching, the locking actuator is pulled back, the slider is switched upward or downward between two discrete positions, after that, the locking actuator is inserted in the groove to hold the slider position.

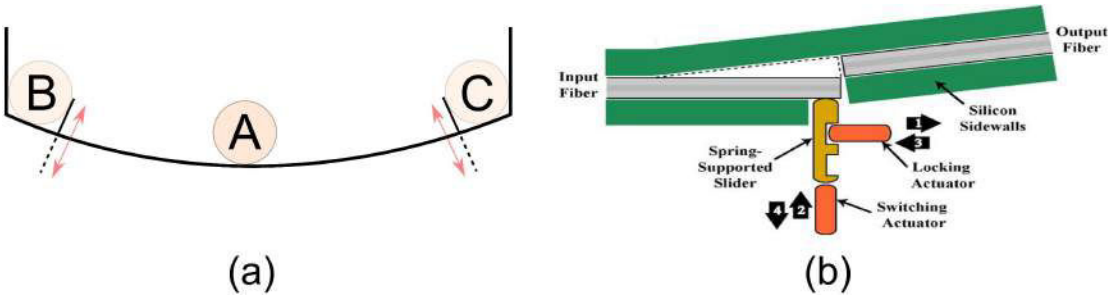

FIGURE *1.9: Holding principle via passive locking actuator(a), optical switch using passive locking actuator [26] (b).*

Holding via permanent magnet Holding via permanent magnet is another passive holding principle which is widely used in digital systems [5, 6, 7, 31, 41, 48, 83, 87, 104, 112, 117, 133, 138]. The magnetic holding principle is based on the generation of a magnetic interaction force between magnetic materials (mostly interaction between a permanent magnet and ferromagnetic parts). The use of a permanent magnet ensures a passive holding of the mobile part in the discrete positions where no external energy is needed. The main advantages of this holding principle are the simple concept of the magnetic attraction and the easy of use in microsystems.

Figure 1.10 shows the principle of magnetic holding based on the example of the ball on a surface. The material of the ball must be able to interact with the magnetic field of the permanent magnet at the borders. The ball is positioned immediately in the discrete position (A or B) when it is placed in the attraction zone of the permanent magnet. To switch the ball, the switching force must be high enough to overcome the magnetic force offered by the permanent magnet, and then, it should be capable to move the ball to the attraction zone of the second permanent magnet.

FIGURE *1.10: Holding principle via permanent magnet.*

Petit et al. [104] have presented a quadristable electromagnetic actuator based the Laplace force (Figure 1.11). A square moving permanent magnet (MPM) is placed in a square framework, four fixed permanent magnet (FPM) with different polarization are placed around the square framework for maintaining the MPM in one of the four corners. Two fixed electrical coils are placed below for the switching function. Once a coil is energized, Laplace force appears and switch the MPM to another stable position.

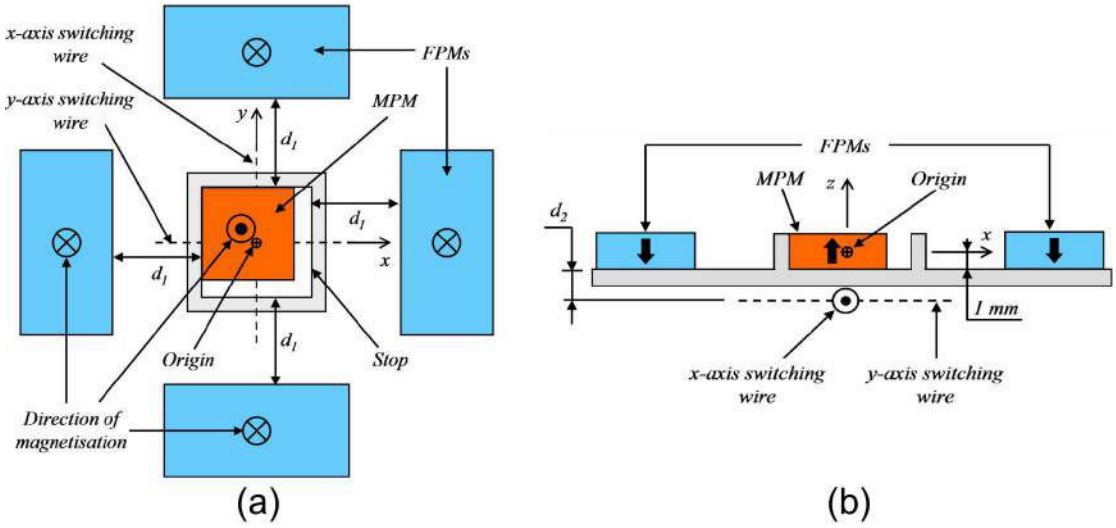

FIGURE *1.11: Top (a) and front view (b) of a quadristable system [104].*

Holding via buckled beam structure Buckled beam structure is a component widely used in MEMS as a simple bistable mechanism that combines the advantages of passive holding and compliant mechanisms. The internal stress of the beam generated after deformation ensures the bistability of the structure. Curved beams can be classified in three categories based on the fabrication process [136]:

- Precompressed curved beams where the beam is fabricated rectilinear then it is compressed [9, 10].
- Prestressed curved beams where during fabrication, the beam is buckled due to residual stress which is added by heating or oxidation [101].
- Preshaped curved beams where the beam is directly fabricated at the first buckling shape mode without residual stresses [102, 106].

The mechanical behavior of the precompressed curved beam is symmetric between two sides of buckling. However, the monolithic constraint in the microfabrication process and the difficulty to set accurately the required buckling dimensions after fabrication make this solution difficult to use in MEMS.

The prestressed curved beam makes the integration into a monolithic device easier, but the residual stress is difficult to control by fabrication [136]. For the pre-shaped curved beam, despite the fact that symmetry is lost and that bistability exists under some conditions, fabrication and integration are simpler.

A solution used in literature to improve the symmetry property of preshaped curved beams [62, 106] is to use a hinged preshaped curved beam structure. In this category, the thickness of a part of the beam is kept very low as compared to the overall beam thickness. This part is usually called the elastic hinge.

One digital system is presented for each one of these configurations. Zaidi in his thesis [136] have developed a bistable system based on the use of a precompressed curved beam as a bistable mechanism and two SMA actuators for the switching (Figure 1.12(a)). The switching is made by heating up the SMA actuator using a laser source. Charlot et al. [15] have used the electrostatic parallel plate configuration to realize a micromechanical memory (Figure 1.12(b)). It consists of a prestressed beam nanowire placed between two adjacent electrodes. Binary data are stored as the mechanical position of the beam.

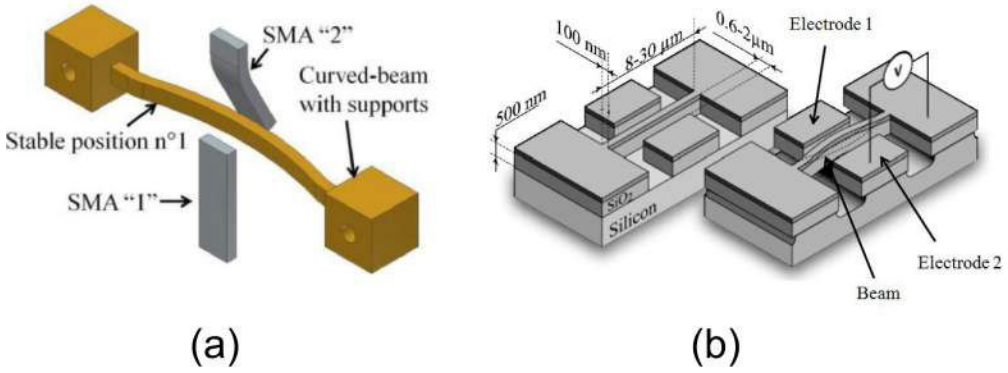

FIGURE *1.12: Precompressed curved beam actuated using two SMA actuators [136] (a), prestressed beam nanowire as micromechanical memory [15] (b).*

Liao et al. [79] have proposed a 2x2 MEMS optical switch with two bistable actuators. Each bistable actuator consists of a pair of preshaped curved beams which are switched using two V-shaped actuators as shown in Figure 1.13(a). Kwon et al. [72] have proposed a bistable actuator operated by electrostatic comb drive (Figure 1.13(b)). The mechanism is a pair of hinged preshaped curved beams with two stable positions. Fingers of the comb drive are designed to generate a switching force in the switching direction with respect to each stable position.

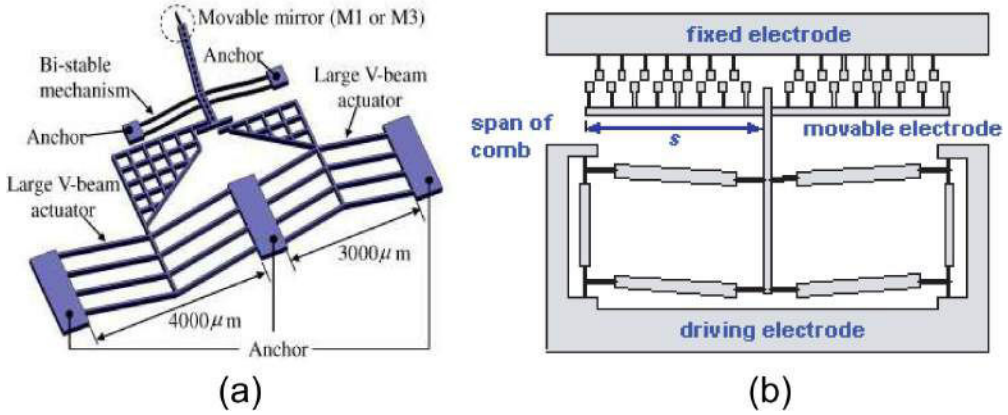

FIGURE *1.13: 2x2 MEMS optical switch using preshaped curved beams [79] (a), comb drive bistable actuator using hinged preshaped curved beams [72] (b).*

The buckled beam structure is used mechanically in two forms: free or constrained. The free structure consists generally of a single curved beam, while the constrained structure consists of two or more curved beams that are connected in the middle by a shuttle which is the moving part. This mechanical constraint serves for guiding a rectilinear displacement of the shuttle, it prevents unsymmetrical buckling modes from occurring during displacement and improves the bistability feature.

The principle of the buckled beam structure can be illustrated using the example of the ball on a surface. Figure 1.14 shows this example on a path with two stable positions (A & B). These two positions are at a local minimum of the potential energy. All the positions in between are considered as unstable positions of the ball. The potential energy is equivalent to the height of the ball, thereby, its evolution with the different positions seems like the path of the surface. The driving force applied on the ball due to the gravity is equivalent to the first derivative of the potential energy with respect to the position. Evolution of the driving force with respect to the ball position on the path is also shown.

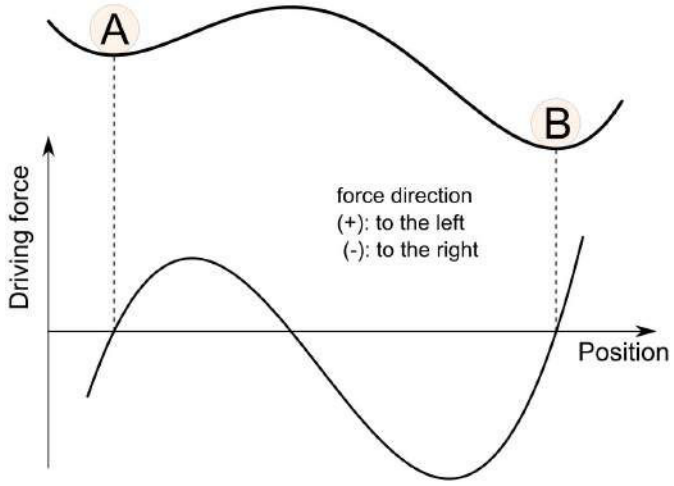

FIGURE *1.14: The example of the ball on a surface in analogy with the buckled beam structure principle. The driving force curve is shown in the bottom with respect to the ball position.*

The stability of the positions A and B is more obvious in the driving force curve. It is characterized by two features: The first one is that the driving force in these positions is equivalent to zero, the second one is that if the ball moves locally in any direction, the driving force will appear in the contrary direction. This is not the case in the upper position where the driving force is equivalent to zero but it push out the ball following any minimal disturbance.

This is similar to the case of the buckled beam structure. The analogy between the two cases is in the evolution form of the energy and the force after displacement/deformation. The driving force in the case of the buckled beam structure is called ”snapping force”. The energy in the case of the ball is the potential energy, while the energy in the buckled beam structure is its internal deformation energy in the post-buckling phase where the beam deflects between the two sides of buckling.

Stop blocks

In result, the discrete positions of a buckled beam structure are considered as stable, but not maintained positions. No holding force are applied on the moving part in these discrete positions. A solution used in the bistable module of the DiMiBot to add holding forces is the use of stop blocs. Figure 1.15 shows the same example in Figure 1.14 but with the use of stop blocs. Two stop blocs are placed between the two initial stable sides of the path. The ball is then placed in between, and its position is bounded between the two stop blocs.

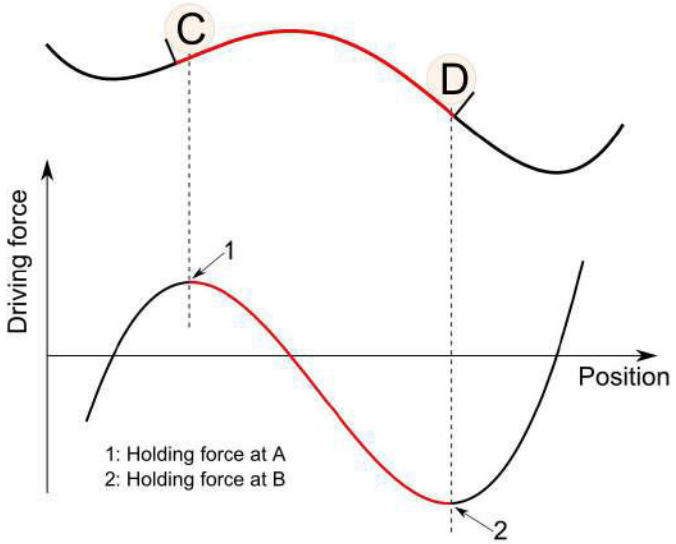

FIGURE *1.15: The example of the ball on a surface with stop blocks.*

The new discrete positions of the ball in the new configuration (C & D) are then the adjacent positions to the stop blocks. These positions are maintained due to the presence of a holding force which is equivalent to the driving force in these positions. These positions does not change unless an external force is applied in the switching direction that is higher than the holding force.

Exactly the same principle is used in the buckled beam structure. Two stop blocs are used in the bistable modules in the DiMiBot. Figure 1.16 shows a zoom on these stop blocs and their configurations in three different states (as-fabricated, at position 1 and at position 2). In the as-fabricated state, no residual stress or deformation energy is present, therefore, the shuttle is only stable without holding forces.

Identically to the case of the ball which is placed between two stop blocks, the shuttle in the case of the buckled beam structure must be placed between the two stop blocs after fabrication. This operation is called ”activation” of the bistable module. In the activation phase, the stroke is pushed manually to enter between the two stop blocs. Stop block 0 is simply a mechanical stop which blocks the displacement in the second side of buckling at position 2.

However, the monolithic structure and in-plane displacement of the curved beam complicate the design of stop block 1. Its design consists of triangular heads placed on horizontally flexible structure. This design allows the displacement in a direction in order to insert the shuttle inside its working stroke, and it blocks the displacement in the other direction which is the main

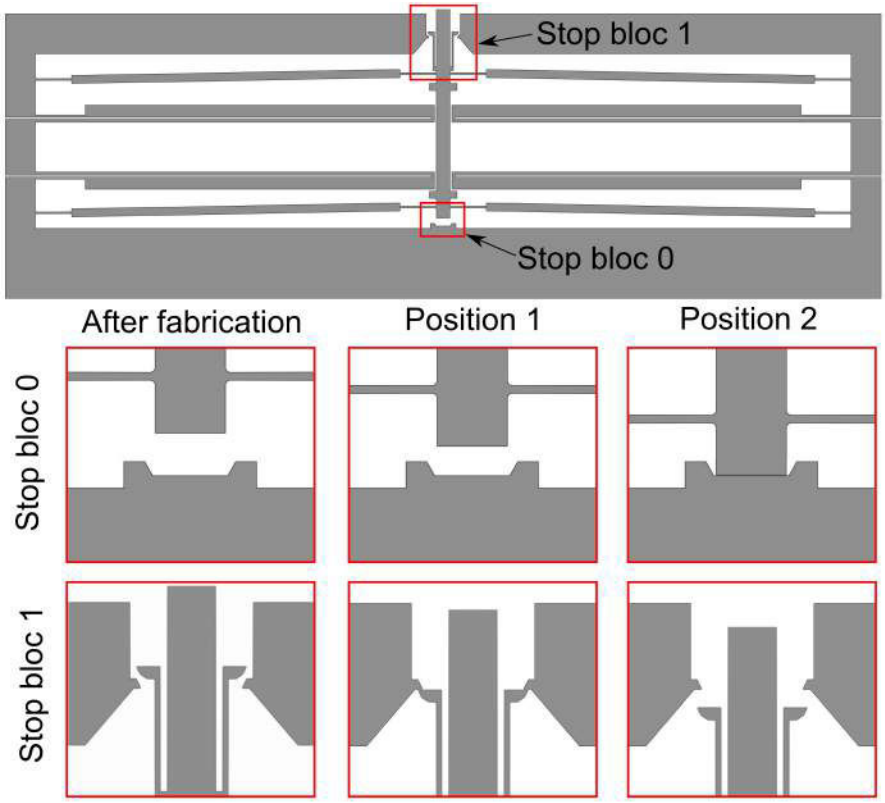

FIGURE *1.16: Configurations of the stop blocs of the bistable module, in the DiMiBot, in three different states: as-fabricated, at position 1 and at position 2.*

function of the stop block. In this way, positions 1 and 2 of the shuttle can be considered as maintained, and a holding force is added for each position.

1.3.2.3 Synthesis

The holding principles used in literature for digital systems including active and passive principles have been presented. Active holding principles include ”continuous switching function” and ”active locking actuator”, while passive holding principles include ”passive locking actuator”, ”permanent magnet” and ”buckled beam structure”. The active holding is useful for low holding time applications and high switching frequency. The holding with a locking actuator requires additional components to realize the holding. The magnetic holding function provides a contactless holding function with no external energy, however, permanent magnets, ferromagnetic materials or magnetic circuits have to be integrated. The buckled beam structure is based on the deformation properties to realize the holding function in two stable positions. Stop blocks can be used to add holding forces in each stable position of the buckled beam structure.

Hinged preshaped curved beams were used in the bistable module in the old generation of the DiMiBot. However, we took the choice of using uniform preshaped curved beams in the new structures for two reasons, firstly, the hinged structure create weak points at the elastic hinges

which are susceptible to fail in the fabrication process, secondly, the symmetrical behavior can be obtained by adjusting positions of stop blocks.

In addition, in the new generation of the DiMiBot, several internal systems are switched temporally. The holding in these internal systems is made using continuous switching function method in order to simplify the design and reduce the number of actuators.

1.3.3 Multistable mechanisms

A multistable mechanism has many stable force-balanced positions within its range of motion which allows relying on the stable states to have confidence in the positions after switching from one state to the other without need of sensors. The different solutions found in literature to realize the multistable mechanisms can be classified in three main categories.

- Elementary multistable mechanism
- Assembly of elementary modules
- Stepping microactuators

The number of stable positions is limited in the first category (bistable, tristable quadristable, etc.), while it is not limited (unlimited) in principle in the two other categories where more positions are added either by adding more elementary modules in the architecture of the mechanism or by extending the range of motion of the moving part. Thereby, the number of stable positions can be changed in each prototype with respect to the design requirements. Each category is detailed with examples in the following.

1.3.3.1 Elementary multistable mechanism

The design of elementary multistable systems/mechanism is dedicated for switching between limited number of stable positions. Most of the multistable digital systems found in literature are from this category. Bistable systems are the most widespread [5, 22, 36, 56, 61, 85, 102, 107, 112, 132, 133, 135, 136, 137] (including the bistable module used in the DiMiBot). Tristable [16, 18, 95, 128, 139], quadristable [97, 50, 96, 103, 104, 105] and pentastable designs [17, 140] are also investigated. Several examples of these mechanisms can be found in the previous sections.

1.3.3.2 Assembly of elementary modules

Several applications can be cited that uses elementary digital systems in a large scale without collaboration in their local specific task, including the braille display systems [86, 127], optical switch arrays [29, 63], mechanical memories array [15, 125], etc.. However, the concerned applications in this category are the application where the elementary modules contribute together to move one end effector.

Assembly of several digital actuators as elementary modules is a solution to add discrete states to a digital system. In addition to the advantages of the digital concept, the advantage of the elementary architecture is the ability to reach high number of stable positions by simply

adding digital modules. In the other side, the main drawback in these systems is that for high number of discrete positions, a large number of digital systems is needed. This increases the size of the device, complicates its integration and connectivity, and increases the possibility of failure in the fabrication process.

Macroscale At the macroscale, several designs of digital positioning systems with elementary modules were proposed previously. These designs include the VGT (variable geometry trusses) manipulator which allows reaching positions in a tridimensional workspace [120], the BRAID (Binary Robotic Articulated Intelligent Device) where the different modules are connected in series [119], and the digital robotic platform developed by Wang et al. [130] which consists of six elementary modules that are connected in parallel.

Microscale This concept is also used at the microscale where different designs with elementary modules were presented in literature. These designs include displacement tables [14, 104, 103], multistable microrobots with elementary modules distributed in series [42] and the DiMiBot with elementary modules distributed in parallel [12].

1.3.3.3 Stepping microactuators

The principle of stepping microactuators is based on making consecutive steps in order to reach a desired position. The stepping principle is very close to the digital concept. However, the focus in these designs is generally on the step realization, not on the holding in a defined discrete position, which implies that, in contrast to digital actuators, sensors are always required for repeatable and accurate positioning.

Microactuators based on the stepping motion have a potential to satisfy the contradictory requirements for micropositioning. They allows realizing high-resolution positioners that fit in a small volume and are able to produce large stroke and large force while using little power. Various principles for making a step are developed in literature and used widely in commercial products. A brief description and example for each principle is given in the following

Inchworm actuators Various designs and concepts for the inchworm actuation is presented in literature [2, 35, 73, 77, 116, 35]. The most common design comprises three independently driven actuators, two for latching (LA1 and LA2) and one for driving (DA) with six steps of actuation. This is the case of the inchworm developed by Erismis et al. [35] and shown in Figure 1.17.

Stick-slip actuators The functioning of stick-slip actuator consists mainly of two steps (Figure 1.18(a)). In the first step, a slow deflection of a driving object moves the body of the device along the actuation direction due to a static friction (stick effect). In the second step, a rapid deflection slides the driving object towards its initial position (slip effect). The repetition of this sequence allows unlimited strokes and submicrometric resolutions.

Based on this principle, Rakontondrabe et al. [108] have developed a 2-DoF stick-slip device which moves around and along a tube (Figure 1.18(b)). The device consists of three microac-

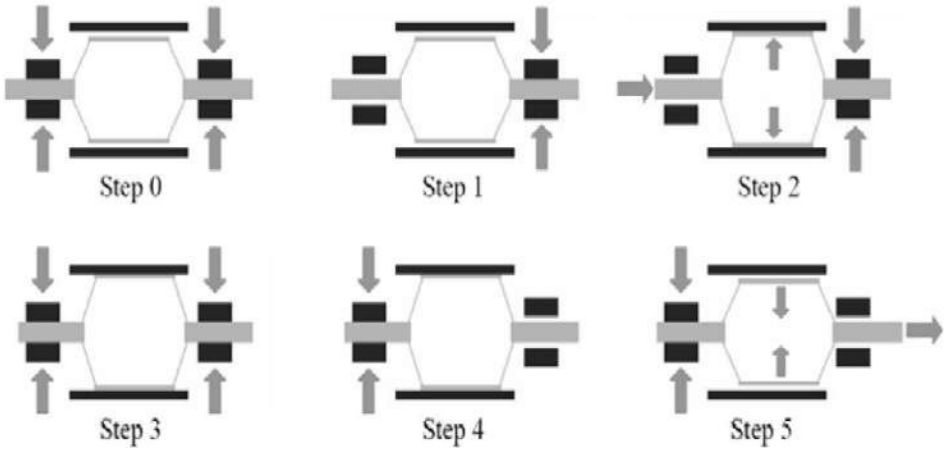

FIGURE *1.17: Functioning principle of an electrostatic inchworm actuator [35]. LA1 and LA2 latch the two shuttles (step 0), LA1 unlatch the first shuttle (step 1), DA is activated which moves the first shuttle ahead (step 2), LA1 latch the first shuttle (step3), LA2 unlatch the second shuttle (step 4), finally, DA is disactivated which moves the second shuttle ahead.*

tuators assembled together, each one have a piezoelectric leg that is able to deflect in the four directions, two of wich are used for the translation and two other are used for the rotation.

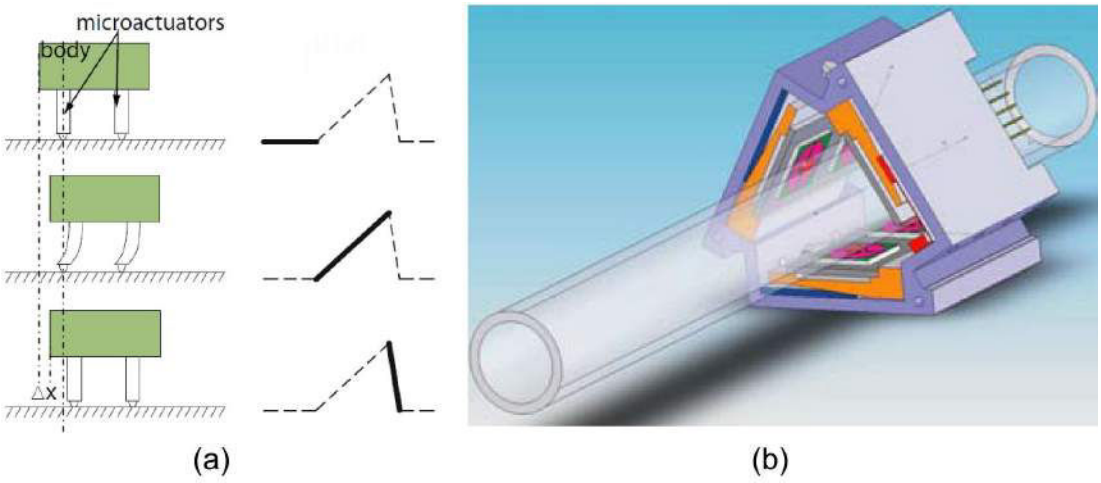

FIGURE *1.18: Functioning principle of stick-slip actuators (a), drawing of stick-slip device working around and along a tube [108] (b).*

Friction-inertia actuators The functioning of these actuators (Figure 1.19(a)) is very close in concept to stick-slip actuators. The operation cycle consists of two steps, in the first step, a slow expansion of active material (actuator) drags the inertial mass to be moved relative to the ground. The slow motion ensures the adhesion of the main object with the ground. In the second step, a fast contraction accelerate the inertial mass towards the main object. Thereby, an inertial

force appears in the reverse direction and pushes the whole body a step forward. An example of a $XY\theta$ microrobot [94] based on the friction-inertia principle is presented in Figure 1.19(b).

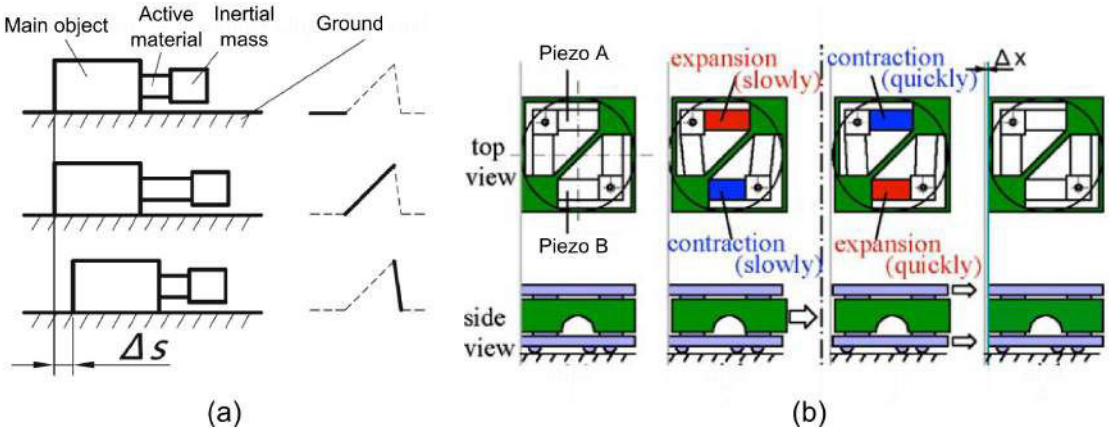

FIGURE *1.19: Principle of friction-inertia actuators (a), a friction-inertia microrobot [94] (b).*

Ultrasonic actuators An ultrasonic actuator uses the inverse piezoelectric effect to obtain oscillation in an elastic body (stator) at one of its resonant frequencies in the form of either stationary or traveling waves. These waves are transmitted in conjunction with a smooth frictional contact to the moving part. The working principle of these actuators is shown in Figure 1.20(a). An example of a XY drive [30] that works on the ultrasonic principle is shown in Figure 1.20(b).

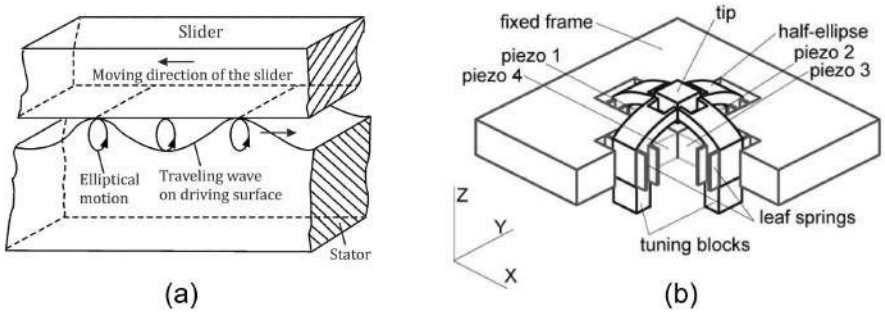

FIGURE *1.20: Principle of ultrasonic actuators [65] (a), XY drive which uses ultrasonic principle [30] (b).*

1.3.3.4 Synthesis

A classification of the different solutions found in literature to realize the multistable mechanisms was presented in this section. Bistable, tristable, quadristable and pentastable mechanisms were presented as elementary multistable mechanisms, while the unlimited mechanisms are realized generally in two ways: either using several elementary digital modules or using the stepping principles. The old generation of the DiMiBot uses elementary digital modules in a

spatial distribution. However, the stepping principle shows important advantages that may overcome some limitations of the old DiMiBot. New multistable systems for the DiMiBot which combine the advantages of the digital concept and stepping microactuators are proposed in the thesis as clarified in the next section.

1.4 Thesis objectives and working axes

In the previous sections, digital microrobotics and the DiMiBot were presented, including challenges for a new generation of the DiMiBot. The different solutions to realize discrete positioning were also presented, which allows sorting the alternatives that may improve the functioning of the DiMiBot. The objectives and working axes of the thesis are presented in this section. The following chapters of the thesis are subsequently introduced.

The global context of the thesis is to continue the previous works made in the laboratory on digital microrobotics with the objectives of making the DiMiBot more accurate, more controllable and smaller.

- **More accurate** by improving the fabrication process and providing solutions to compensate the fabrication tolerances and to improve the reliability.
- **More controllable** by proposing new architecture of the DiMiBot that allows generating complex trajectories without feedback in the workspace.
- **Smaller** by proposing new architectures that enable more positions with a smaller space and by optimizing the structure of the different components and defining their miniaturization limits.

In order to achieve these objectives, two working axes were followed in the thesis. The first one is by optimizing the structure of the main components in the DiMiBot, the second one is by proposing novel architectures for the DiMiBot.

The purpose of the first axis is to answer an important question which was proposed at the early stages: How far can we go in the miniaturization of the DiMiBot with keeping the same characteristics at the workspace?

Therefore, we launched a comprehensive study on the optimization of the main components in the DiMiBot: the curved beams and the actuators. The design of the other components (connecting beams, hinges, etc.) is simple and already treated in the previous thesis.

Two ways are possible to make this study: either numerically or analytically. The analytical path was preferred for several reasons. The numerical optimization provides the dimensions for a specific design while the analytical modeling shows clearly the influence of each dimension on the behavior of the curved beam/actuator and allows choosing the optimal dimensions that ensure the desired outputs and characteristics. In addition, analytical modeling and design of the curved beams and U-shaped actuators is a general need for MEMS due to the few works that cover these issues in literature. The design of these structures is still paying the price for the lack of physical intuition by resorting to FEM modeling. That's why the focus in the works was on the modeling and design in a general case, while the optimization of the components in the DiMiBot is simply an application.

The second working axis is to propose new architectures that improve the performance of the DiMiBot. A new idea was proposed during the thesis which consists in replacing all the bistable modules in a side of the DiMiBot by only one multistable stepper module. This does not cancel the need for the first working axis since the curved beams and bistable modules are also used in the multistable module.

The use of multistable modules in the DiMiBot has many advantages. Its principle is a combination between the bistable module and the stepping microactuators. It combines the advantages of stepping actuation in the sense of generating an infinite number of positions simply by extending the range of motion but with accuracy in the positioning and it keeps most of the advantages of the previous DiMiBot structure. Further, it makes the system more compact, it allows generating complex trajectories in the workspace and agrees with the objectives of the thesis to make the DiMiBot more accurate, more controllable and smaller.

The second working axis contains several parts which have been treated in turns in the thesis, starting with the principle, the design, the fabrication (including layouts, process and realization), and ending with the connectivity and characterization. Loops of improvements were made in and between these parts which allowed obtaining operational prototypes at the end.

1.4.1 First axis: Analytical design optimization

Preshaped curved beam

In a previous analytical model presented by Qiu et al. [106], analytical solution of the snapping force in the postbuckling phase was provided with an approximation of neglecting high modes of buckling, this model was approved by experiments. However, no studies were found in literature for calculating evolution of the internal stress during deflection between two sides of buckling.

In Chapter 2, modeling of the snapping forces and internal stresses is presented with considering high modes of buckling. A comparison of the results with FEM simulations shows that the consideration of high modes of buckling in the calculation of the snapping forces is slightly more accurate while the calculation of stress without high modes does not correspond to FEM results.

After that, design and optimization of the curved beam are investigated in the second part of the chapter based on the analytical expressions obtained in the modeling. The influence of the beam dimensions and material properties on the mechanical behavior of the beam is clarified. A design method is provided subsequently that define the optimal dimensions of the beam that provide the desired snapping force and stroke of deflection while respecting the design specifications and limitations. Limits of miniaturization are investigated finally.

Electrothermal U-shaped actuator

The modeling of the electrothermal U-shaped actuator is treated by a sequence of two analytical models: electro-thermal and thermo-mechanical. The first one concerns the computation of the evolution of the thermal distribution in the actuator, while the second one allows computing the displacement resulting from the thermal distribution.

No exact analytical solutions were found in literature for the electrothermal problem in the case of U-shaped actuators. In Chapter 3, an exact solution of the electrothermal problem is presented using a novel calculation method. The comparison of the results between the electrothermal modeling and FEM simulations shows to be in excellent agreement.

Afterwards, a thermomechanical model is presented which output the displacement of the actuator with respect to the thermal distribution (obtained from the previous model), and the external loads on the actuator. The combination of the two models allows getting the displacement in function of the electrical input and external loads. A comparison of the displacement results with the FEM simulations and experiments showed a similar behavior with slight differences which are acceptable.

After that, the influence of the different dimensions and electro-thermo-mechanical properties of the material on the electrical, thermal and mechanical behavior of the actuator is investigated based on the analytical models. A design method is presented subsequently to choose optimal actuator dimensions that provide desired outputs in terms of displacement and carried loads.

1.4.2 Second axis: DiMiBot with multistable modules

The focus here is on the development and fabrication of a new generation of the DiMiBot with multistable modules as shown in Figure 1.21. The principle of the new multistable module is based on the use of an unlimited multistable mechanism based on the stepping principle. The moving part of each module can be placed in several stable positions on a rectilinear axis. The moving part of the two modules are connected to the end effector using the same top head mechanism as in the old DiMiBot in order to form a square workspace.

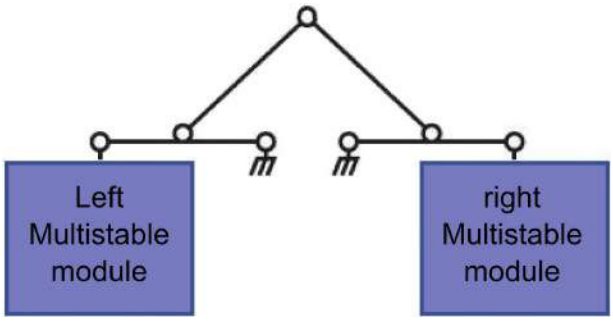

FIGURE *1.21: Architecture of the DiMiBot with multistable modules.*

The advantage of this module with respect to the other stepping microactuators presented previously is that the positions are defined accurately and maintained at rest in front of external loads and disturbances. Thereby, the multistable module combines simultaneously the advantages of the digital concept and stepping microactuators.

This new configuration of the DiMiBot helps to overcome several disadvantages that were presented in the old configuration with bistable modules. The first advantage is that only two elementary modules are used with unlimited positions that can be added by extending the range of motion. This allows obtaining more positions and going further in miniaturization simulta-

neously, and avoids the drawbacks related to the large size of the DiMiBot, such as lowering the failure possibilities in the fabrication process, limiting the number of metal lines for the electrical connectivity and solidifying the structure.

Further, the transition in one side of the DiMiBot with multistable modules is made incrementally step by step and not by binary steps. This means that the transition in the workspace of the DiMiBot is now between the adjacent positions. This means also that the DiMiBot is able to realize any complex trajectory with an open loop control.

In the other side, an accurate positioning mechanism was designed and used in the multistable module in order to ensure accurate maintained positions. The novel idea in this mechanism is the compensation of fabrication tolerances by playing on the excess/shortage in the width of the openings and patterns of the device layer obtained in the fabrication. As the case of stop blocks, this mechanism is used around the shuttle of a pair of preshaped curved beams in the multistable module. It places the shuttle between two discrete positions which are accurately defined by compensation of the fabrication tolerances. This adds also holding forces on the stable positions which improves the positioning robustness in front of external loads and disturbances.

However, The binary feature of the bistable DiMiBot is not a feature of the new structure. The positions in the workspace are reached by incremental stepping and no absolute states of the modules are assigned to each position. The positions in this case are determined relatively to the first initial position by counting the steps made to reach the current state.

The principle and the design of the multistable module is presented in Chapter 4. The stepping principle is based on a specific sequence of bistable displacement and opening normally closed latch arms in a part and closing other normally open latch arms in the other part. The design of the internal systems in the module, the global structure of the module and the DiMiBot are subsequently presented.

In Chapter 5, the fabrication process, difficulties encountered and different runs are presented. The fabrication was made in the clean room MIMENTO of the institute Femto-st. Major changes were made in the fabrication process and layouts with respect to the previous thesis in order to obtain more proper, more accurate and more homogeneous structures and to reduce the failure possibilities in the fabrication as possible. Finally, the experiments on some fabricated tests and operational prototypes of the multistable module are presented. The experiments showed a proper functioning of the stepping principle and accurate positioning on prototypes of multistable modules. All the difficulties encountered and solutions provided in the fabrication and the experiments are detailed.

1.5 Conclusion

After introducing digital microrobotics and the old generation of the DiMiBot, challenges for a new generation were presented in the first part. These challenges include proposing new structures/mechanisms of the DiMiBot that reduce the size, allows complex trajectories and improve the accuracy. Also, the challenges include improving the fabrication process and developing models for designing the main components in the DiMiBot.

Solutions found in literature, that allow realizing the switching and holding functions and the multistable mechanisms of a digital system, are then classified. This classification shows the possibilities that can be adopted for improving the concept and functioning of the DiMiBot. In this context, the reasons behind choosing the solutions used in the DiMiBot are clarified.

Finally, the thesis objectives and working axes are presented and the next chapters are introduced. Two working axes were followed in parallel in the thesis. The first one is the analytical modeling and design of preshaped curved beam and U-shaped actuator. We have succeeded in the development of these models and the definition of design methods with respect to general design requirements, limitations and desired outputs. The contribution is original in the literature and the design methods are useful for MEMS applications. The second axis focus on the development of a new generation of the DiMiBot with multistable modules. Also, we have succeeded, after following all the steps, in fabricating operational prototypes. The following chapters deal with the works in these two axes as shown in Figure 1.22.

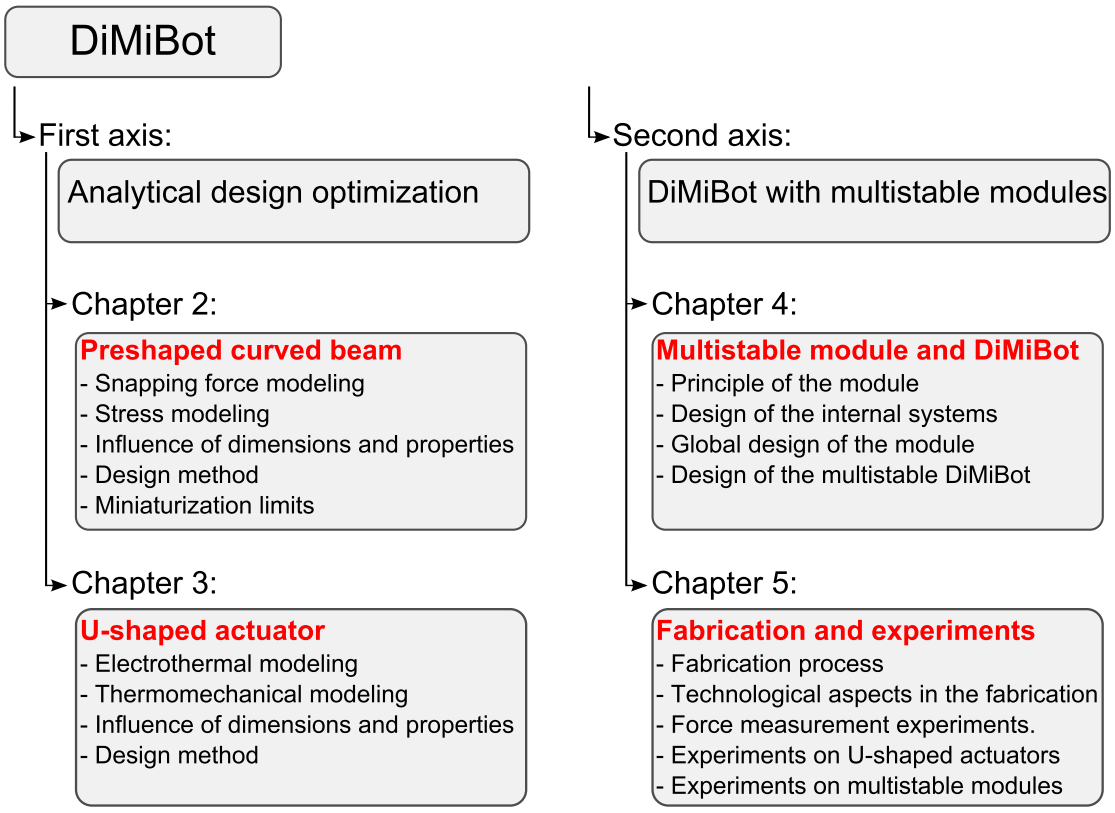

FIGURE *1.22: Woking axes and the following chapters of the thesis.*

Chapter 2

Curved beam bistable mechanism

This chapter deals with the modeling, stress analysis and design of a preshaped curved beam. In a first stage, the presented modeling develops further the snapping force solution and bistability conditions without and with including high modes of buckling. In a second stage, we develop the analytical solution of the stresses inside the beam during deflection between the two sides of buckling. The analytical expressions obtained in the modeling and stress analysis define the mechanical behavior of the curved beam during deflection and include the effects of high modes of buckling. The analytical results are then compared with FEM simulations and have shown to be in excellent agreement. The results show the importance of high modes of buckling in the calculation of stresses and snapping force. In the final stage, design and optimization of the curved beam are investigated based on the analytical expressions obtained in the modeling. Design elements are provided in order to achieve the best integration of the curved beam in a complete microstructure.

Chapter contents

2.1 Introduction

Few works are found in literature that cover the modeling, stress analysis and design of a preshaped curved beam. Modeling of the precompressed curved beam was more investigated. Based on Lagrangian approach, Vangbo et al. [126] carried out one of the first studies on precompressed curved beams that takes compressibility into account for small deformations. The obtained expressions consider high modes of buckling. Self buckling behavior of microbeams in response to resistive heating was investigated by Chiao et al. [25]. Emam and Nayfeh examine in their studies [33, 92] the vibration and dynamics of postbuckling configurations of a precompressed beam. Cazottes in his thesis [10] has studied the bistability of a precompressed beam when it is actuated either by force or by moment. Elastica models for static and dynamic analysis with solutions and experiments are investigated by Camescasse in his thesis [9]. Chen et al. [19] showed the importance of extensible elastica theory in the modeling of a curved beam.

As for the case of preshaped curved beam, Qiu et al. in [106] have calculated analytically the snapping forces by neglecting high modes of buckling and they provide an approximation of the solution with high modes for high values of the initial height-to-thickness ratio. They noticed a bifurcation of solutions and appearance of some buckling modes when the axial stress exceeds some limits. This will be explained in details in the chapter. Their analytical results were approved by FEM simulations and experiments. In the other side, Park et al. [102] have presented analytical modeling of a preshaped curved beam when it is actuated by Laplace force distributed throughout the beam. The load-displacement curve was calculated analytically without high modes and numerically with high modes of buckling and was compared with experiments. However, this study does not notice any bifurcation of solutions (i.e. several cases of solution) depending on the stress state.

However, as far as we know, no studies are found in literature for calculating evolution of the internal stress in the post-buckling phase. Calculation of the stress is important in order to define the limits on dimensions that must be respected in the design to avoid exceeding the stress limit in the curve beam during deflection.

In this chapter, snapping forces and internal stress in the post-buckling phase were calculated analytically with and without high modes of buckling. FEM simulation showed the importance of considering high modes of buckling in the calculation. Afterwards, variation of the preshaped curved beam behavior with respect to different dimensions and material properties were studied, and a design method is presented based on the analytical expressions that allows optimizing the dimensions with respect to the design requirements and limitations. Miniaturization limits are investigated finally.

In Section 2.2, the buckling model and its general solution are presented. The model, in this section, is based on the formalism implemented by Qiu et al. in [106] including three major points : normalization of the variables, superposition of the buckling modes and calculation of the mode constants by minimizing the variation of the total energy.

In Section 2.3, solution of the snapping forces without considering high modes of buckling is recalled. The solution with considering high modes of buckling is then developed. The analytical expressions obtained with high modes implicitly include the effects of all modes of buckling on the curved beam behavior.

In Section 2.4 existence and margin of bistability are discussed with respect to the snapping force solution.

In Section 2.5, the internal stresses in the curved beam are investigated with and without considering high modes of buckling. The calculated stress expressions show evolution of their maximum value during deflection. Knowing the stress state in the curved beam is important for optimizing its dimensions under elastic or failure limits.

In Section 2.6, the analytical results with and without high modes of buckling are compared with FEM simulations. This comparison shows the importance of considering high modes of buckling in the modeling of the curved beam behavior.

Finally, in Section 2.7, the influence of the dimensions and material properties on the main elements of the design are investigated and a design method is proposed in order to obtain the optimal dimensions with respect to the design requirements.

2.2 Buckling of a beam

2.2.1 Buckling model

Buckling a beam is defined as a sudden deformation which occurs when the excess of compression energy stored in the beam is converted into bending energy. In other words, transverse deflection occurs when the compressive force P exceeds a critical value P_0, the beam enters in the first buckling mode (Figure 2.1).

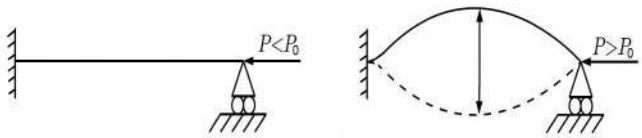

FIGURE *2.1: Buckling of a beam before and after a critical axial compression.*

The postbuckling configuration of the beam can be considered as a compliant mechanism that shows bistability. The buckled beam shows stability of its position at two possible configurations which are distributed symmetrically in the two buckling sides (Figure 2.2).

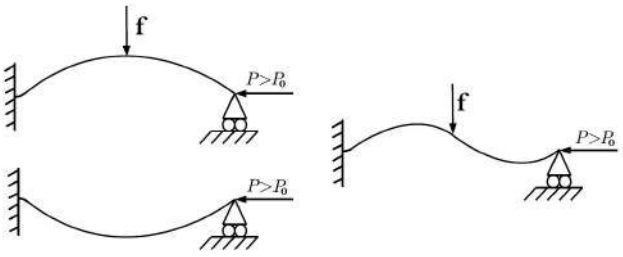

FIGURE *2.2: Transition between the two stable positions of a buckled beam as a result of a lateral force applied in the middle of the beam.*

In most cases, and in our case, the action is a lateral force applied at the middle of the beam. Otherwise, the action can be also a force applied in different points [9], an electromagnetic field [102], an electrostatic field [69, 122] or moments applied in determined locations on the beam [10, 118].

There are two possible approaches to deal with the post-buckling problem, based on static and dynamic models. In dynamic modeling, there are two types of modes, buckling modes that depend on the axial stress and resonance modes that depend on the system frequency. In contrast, since it does not consider the time, static modeling exhibits only buckling modes.

Generally, the resonance frequency of a curved beam is higher while reducing the beam dimensions. MEMS devices generally range in size from $20\mu m$ to few millimeters. Thus, the dynamic behavior of the curved beams is considered to be quasistatic in our application and only the static modeling is investigated in our study. An interest to dynamic modeling can be referred to studies in [9, 10, 33, 92, 122].

The curved beams used in our systems are preshaped (Section 1.3.2.2). One preshaped curved beam has the following characteristics as presented in Figure 2.3: axial force P, thickness t, depth b, span l, deflection d, beam shape $w(\mathrm{x})$, initial height of buckling h and the applied lateral force at the middle f.

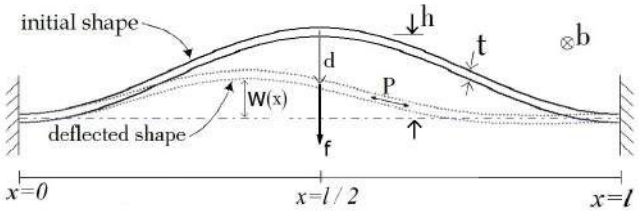

FIGURE *2.3: Clamped-clamped curved bistable beam at the initial position and after deflection.*

The deflection d is defined as the lateral deflection in the middle with respect to the initial configuration:

$$d = \overline{w}\left(\frac{l}{2}\right) - w\left(\frac{l}{2}\right) \tag{2.1}$$

where $\overline{w}(x)$ is the initial beam shape.

Since the height h is generally very small compared to the span l of the beam, the hypothesis of small deformations is taken. The length s of the beam is then calculated with respect to the slope dw/dx with considering the small deformation hypothesis.

$$s = \int_0^l \sqrt{1 + \left(\frac{\mathrm{d}w}{\mathrm{dx}}\right)^2}\,\mathrm{dx} \approx l + \frac{1}{2}\int_0^l \left(\frac{\mathrm{d}w}{\mathrm{dx}}\right)^2 \mathrm{dx} \tag{2.2}$$

The axial force P which is the resultant of the axial stress over the section area is calculated using Hook's law:

$$P = Ebt\left(\frac{\overline{s} - s}{\overline{s}}\right) \tag{2.3}$$

where $\overline{s}$ is the initial length, and bt is the section area.

2.2.2 Buckling equation

A beam in bending has a radius of curvature R that can be variable throughout the beam length. The curvature indicates the presence of two zones of strains, contraction and expansion within the thickness section which are the results of compression and traction stresses respectively. These two zones are separated by a neutral line where there are no strain. By convention, traction is positive and compression is negative.

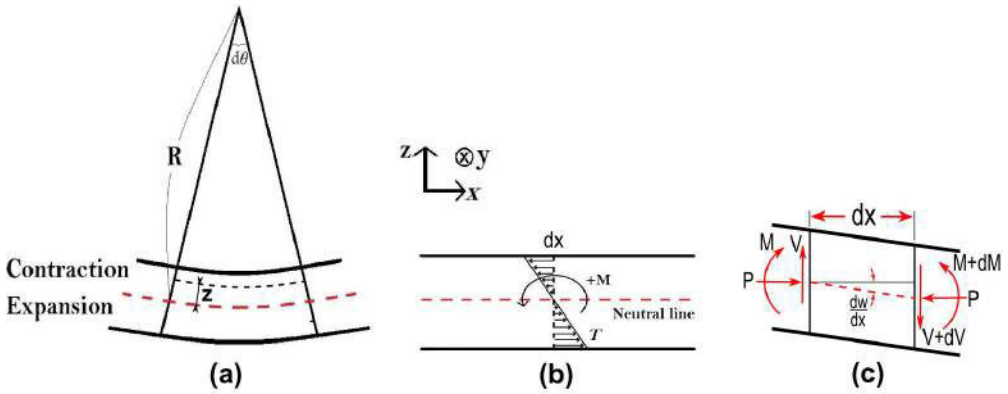

FIGURE *2.4: A beam in bending (a), bending stress distribution along the thickness and bending moment in a section (b) forces and moments equilibrium in a section of a buckled beam(c).*

In Figure 2.4.a, the distance between arc lines throughout the thickness and the neutral line is equivalent to z. The length of the arc lines variates with z, so the bending strain S_b is equivalent to:

$$S_b = \frac{(R-(R-z))\mathrm{d}\theta}{R\mathrm{d}\theta} = \frac{z}{R} \tag{2.4}$$

The radius of curvature R is equivalent to:

$$R = \frac{\sqrt{\left(1+\left(\frac{\mathrm{d}w}{\mathrm{dx}}\right)^2\right)^3}}{\frac{\mathrm{d}^2w}{\mathrm{dx}^2}} \tag{2.5}$$

Taking account of small deformations, the slope $\frac{\mathrm{d}w}{\mathrm{dx}}$ is relatively negligible. Moreover, according to elastic theory, the stress T of an elastic material is proportional to the strain S_b with respect to Young's modulus E:

$$T = ES_b = E\frac{z}{R} = Ez\frac{\mathrm{d}^2w}{\mathrm{dx}^2} \tag{2.6}$$

As shown in Figure 2.4.b, the bending moment M around the neutral line is the average of the bending stress T multiplied by the distance z:

$$M = -\iint Tz\mathrm{dydz} = -EI\frac{\mathrm{d}^2 w}{\mathrm{dx}^2} \tag{2.7}$$

where $I = \iint z^2 \mathrm{dydz}$ is the quadratic moment.

However, based on the forces and moments equilibrium equations, Timoshenko in his famous book [124] developed the buckling equation of a beam. The forces and moments acting on buckled beam cross section including the shear force V, axial force P and bending moment M are shown in Figure 2.4.c. Applying the force and moment equilibrium, we obtain the following equations:

$$\begin{aligned} \frac{dV}{dx} &= 0 \\ V &= \frac{dM}{dx} - P\frac{dw}{dx} \end{aligned} \tag{2.8}$$

Combining (2.7) and (2.8), the buckling equation is obtained:

$$\frac{\mathrm{d}^2}{\mathrm{dx}^2}\left(EI\frac{\mathrm{d}^2 w}{\mathrm{dx}^2}\right) + P\frac{\mathrm{d}^2 w}{\mathrm{dx}^2} = 0 \tag{2.9}$$

Generally, the material is the same and sections do not change their shapes in the beam, E and I are constants:

$$EI\frac{\mathrm{d}^4 w}{\mathrm{dx}^4} + P\frac{\mathrm{d}^2 w}{\mathrm{dx}^2} = 0 \tag{2.10}$$

The general solution of (2.10) has the following form:

$$w(\mathrm{x}) = C_1 \sin k\mathrm{x} + C_2 \cos k\mathrm{x} + C_3\mathrm{x} + C_4 \tag{2.11}$$

where $k = \sqrt{\frac{P}{EI}}$, and C_1, C_2, C_3 and C_4 are constants.

The boundaries in our case are constrained in terms of the displacement $w(\mathrm{x}=0 \;\&\; \mathrm{x}=l)=0$ and the rotation $\frac{\mathrm{dw}}{\mathrm{dx}}(\mathrm{x}=0 \;\&\; \mathrm{x}=l)=0$. Applying the boundary conditions, the constants C_1, C_2, C_3 and C_4 are determined with respect to N where the values of N are obtained from the following equation:

$$\sin\frac{N}{2}\left(\tan\frac{N}{2} - \frac{N}{2}\right) = 0 \tag{2.12}$$

where $N = \sqrt{\frac{PI^2}{EI}}$ is the normalized axial force.

The trigonometric equation in (2.12) has infinity of solutions which justifies the modal nature of the final solution:

$$w(\mathrm{x}) = \sum_{j=1}^{\infty} a_j w_j(\mathrm{x}) \tag{2.13}$$

The term a_j in (2.13) is the j^{th} constant mode which reflects the contribution of each mode in the total solution, and $w_j(\mathrm{x})$ is the j^{th} buckling shape mode:

$$\left.\begin{array}{r} w_j = 1-\cos N_j \frac{\mathrm{x}}{l} \\ N_j = (j+1)\pi \end{array}\right\} j = 1,3,5... \qquad \left.\begin{array}{r} w_j = 1-2\frac{\mathrm{x}}{l}-\cos N_j \frac{\mathrm{x}}{l}+\frac{2\sin N_j \frac{\mathrm{x}}{l}}{N_j} \\ N_j = 2.86\pi, 4.92\pi, 6.94\pi, 8.95\pi... \end{array}\right\} j = 2,4,6... \tag{2.14}$$

where N_j is the j^{th} mode of normalized axial forces (j^{th} solution of N).

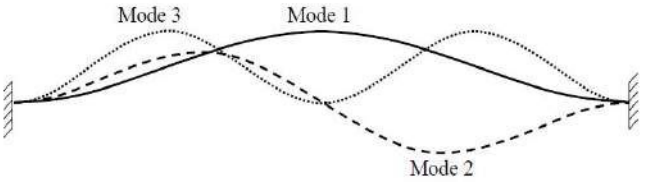

FIGURE *2.5: The first three buckling shape modes*

The length s in (2.2) is then recalculated using (2.14):

$$s = l + \sum_{j=1}^{\infty} \frac{a_j^2 N_j^2}{4l} \tag{2.15}$$

2.2.3 Bifurcation of solutions

Equation (2.13) is the general solution of the problem. Qiu et al. in [106] have calculated the constants a_j by minimizing the variation of the total energy u_t. The variational principle stipulates that a system is in equilibrium when every variation in one of its parameters will create tendency to increase its level of energy. Thus, the variation of the normalized total energy must respect the following condition:

$$\delta(u_t) \geq 0 \tag{2.16}$$

The total energy u_t, in this case, is the sum of the bending, compression and actuation energy. Bending energy u_b is the result of the deformation of the beam during deflection, compression energy u_s is the result of the axial force in the curved beam after deflection, and actuation energy u_f is the result of the lateral force f.

The bending energy starts evolution from the initial position. The variation of the bending energy is equivalent to:

$$\delta(u_b) = \frac{EI}{2}\delta\left[\int_0^l \left(\frac{\mathrm{d}^2\overline{w}}{\mathrm{dx}^2} - \frac{\mathrm{d}^2 w}{\mathrm{dx}^2}\right)^2 \mathrm{dx}\right] \tag{2.17}$$

The variation of the compression energy is equivalent to:

$$\delta(u_s) = -P\delta(s) \tag{2.18}$$

The variation of the actuation energy is equivalent to:

$$\delta(u_f) = -f\delta(d) \tag{2.19}$$

In order to simplify the solution and the presentation, the following parameters are normalized as follows:

$$X = \frac{x}{l} \quad W_j(X) = w_j(x) \quad W(X) = \frac{w(x)}{h} = \sum_{j=1}^{\infty} A_j W_j(X) \tag{2.20}$$

The applied force, deflection, length and energy are also normalized:

$$F = \frac{fl^3}{EIh}; \qquad \Delta = \frac{d}{h}; \qquad S = \frac{sl}{h^2}; \qquad U_t = \frac{u_t l^3}{EIh^2} \tag{2.21}$$

The variation of the normalized total energy has then the following form:

$$\begin{aligned} \partial(U_t) = \left(\frac{N_1^4 - N^2N_1^2}{2}A_1 - \frac{N_1^4}{4} + 2F\right)\partial A_1 + \sum_{j=5,9,13\ldots}\left(\frac{N_j^4 - N^2N_j^2}{2}A_j + 2F\right)\partial A_j \\ + \sum_{j=2,3,4,6,7\ldots}\left(\frac{N_j^4 - N^2N_j^2}{2}\right)\partial A_j^2 \end{aligned} \tag{2.22}$$

Minimizing energy variation in (2.22) in order to satisfy (2.16) brings out bifurcation of solutions. The bifurcation is based on the value of the axial stress inside the curved beam.

In fact, the behavior of the beam is decomposed by the compression ability. When $N < N_2$, the beam is in a compressible phase and N is able to be increased, the modes 2,3,4,6,7,8,10... do not appear, and the terms A_j for $j = 2,3,4,6,7,8,10...$ are equivalent to zero. At $N = N_2$, the system enters in the incompressible phase where no more axial stress N or extra length S is allowed. Mode 2 is the manner used by the system to stop evolution of the axial stress and length contraction. A_2 appears with the other constants A_j ($j = 1,5,9,13...$) in a way that S and N remain constants. Furthermore, N is not able to exceed N_2 unless the mode 2 is constrained. So, for $j = 2,3,4,6,7,8,10...$:

$$A_j = \begin{cases} \text{Mode 2 is unconstrained} & N \leq N_2 \\ \text{Mode 2 is constrained} & N \leq N_3 \\ 0 & N < N_j \\ A_j \text{ appear} & N = N_j \end{cases} \tag{2.23}$$

The other terms A_j, for $j = 1,5,9,13...$, are calculated by setting to zero the variation of the total energy:

$$A_1 = -\frac{1}{2}\frac{N_1^2}{N^2 - N_1^2} + \frac{4F}{N_1^2(N^2 - N_1^2)} \tag{2.24}$$

$$A_j = \tfrac{4F}{N_j^2(N^2 - N_j^2)} \quad \text{for } j = 5,9,13... \tag{2.25}$$

The normalized deflection Δ can be recalculated from (3.50) and (2.21) in function of the mode constants as follows:

$$\Delta = 1 - 2 \sum_{j=1,5,9...} A_j \tag{2.26}$$

Idem, the normalized axial stress N in function of the mode constants can be concluded from (2.2) and (2.21) as follows:

$$\frac{N^2}{12Q^2} = \frac{N_1^2}{16} - \sum_{j=1}^{\infty} \frac{A_j^2 N_j^2}{4} \tag{2.27}$$

where Q is the height-to-thickness ratio $Q = h/t$.

Usually, in the case of a preshaped curved beam, a simple one curved beam shows bistability only for high values of Q. The bistability, in this case, is highly asymmetric between the two sides of buckling. However, it is possible to mechanically prevent asymmetrical bending relatively to the middle of the beam and consequently preventing mode 2 from occurring.

Connecting two beams by a shuttle, as shown in Figure 2.6, can eliminate mode 2 and all asymetrical modes. In this case, mode 2 is canceled into calculation, the force is doubled with the same displacement and the normalized axial stress N can increase to the new critical value N_3.

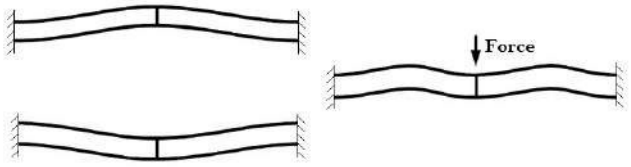

FIGURE *2.6: Transition between the two stable positions of two curved beams connected in the middle, mode 3 appears during transition.*

Based on the above, we can distinguish three kinds of solutions. The first kind is when the curved beam is in the compressible phase:

$$\begin{cases} F = F_1 \\ N < \begin{cases} N_2 & \text{mode 2 is not constrained} \\ N_3 & \text{mode 2 is constrained} \end{cases} \\ A_j \neq 0; \qquad j = 1,5,9,13... \end{cases} \tag{2.28}$$

The second kind is when N reaches N_2 without mechanical constraints:

$$\begin{cases} F = F_2 \\ N = N_2 \\ A_j \neq 0; \quad j = 1,2,5,9,13... \end{cases} \tag{2.29}$$

The third kind is when mode 2 is constrained and N reaches N_3 :

$$\begin{cases} F = F_3 \\ N = N_3 \\ A_j \neq 0; \quad j = 1,3,5,9,13... \end{cases} \tag{2.30}$$

In our applications, curved beams are used at least as a couple of two curved beams connected in the middle in order to improve the bistability, guide the displacement and avoid rotation. The calculation steps in the rest are shown only for the first and third kinds of solutions. The results for the second kind are similar in calculation to those of the third kind.

2.3 Snapping force

2.3.1 Without high modes of buckling

Evolution of the normalized snapping force F and axial stress N in (2.28), (2.29) and (2.30) during deflection Δ are calculated by introducing the values of the mode constants A_j presented in (2.24) and (2.25) in the Δ (2.26) and N (2.27) equations.

Qiu et al. in [106] have calculated the snapping force taking an approximation of neglecting high modes of buckling (mode 5 and above). In this case, the calculation is highly simplified where no infinite sum have to be calculated. Solution for the normalized axial stress is obtained by introducing A_1 obtained from (2.26) in (2.27):

$$N^2 = 3\pi^2 Q^2(-\Delta^2 + 2\Delta) \tag{2.31}$$

Solution of the snapping force F_1 for the first kind is obtained from (2.26) and (2.27):

$$F_1 = \frac{3\pi^4 Q^2}{2}\Delta\left(\Delta - \frac{3}{2} + \sqrt{\frac{1}{4} - \frac{4}{3Q^2}}\right)\left(\Delta - \frac{3}{2} - \sqrt{\frac{1}{4} - \frac{4}{3Q^2}}\right) \tag{2.32}$$

For the third kind, the solution is obtained by setting $N = N_3$:

$$F_3 = 6\pi^4(\frac{4}{3} - \Delta) \tag{2.33}$$

Equation (2.33) exhibits a perfect linear interaction between force and displacement in the third kind of solution.

The third mode of buckling only appears for $Q > \sqrt{(16/3)}$ as can be concluded from (2.31). Also, F_1 has three zeros only for $Q > \sqrt{(16/3)}$ as can be concluded from (2.32). Figure 2.7 shows evolution of the snapping force F during deflection Δ for Q $< \sqrt{(16/3)}$, Q $= \sqrt{(16/3)}$ and Q $> \sqrt{(16/3)}$ respectively.

As shown in Figure 2.7, for $Q > \sqrt{(16/3)}$, the third mode of buckling appears during deflection and the evolution of the snapping force becomes linear with deflection. The snapping force is equivalent to zero at Δ_{zero1}, Δ_{zero2}, Δ_{zero3}. (Δ_{top},F_{top}) are the coordinates where the third mode of buckling appears in the first side of buckling. (Δ_{bot},F_{bot}) are the coordinates where the third mode of buckling appears in the second side of buckling. (Δ_{end},F_{end}) are the coordinates where the deflection is at the end, after that, the axial stress is oriented towards traction.

The values of Δ_{zero1}, Δ_{zero2}, Δ_{zero3}, Δ_{top}, Δ_{bot}, Δ_{end}, F_{top}, F_{bot}, F_{end} in Figure 2.7 can be concluded from (2.31), (2.32) and (2.33):

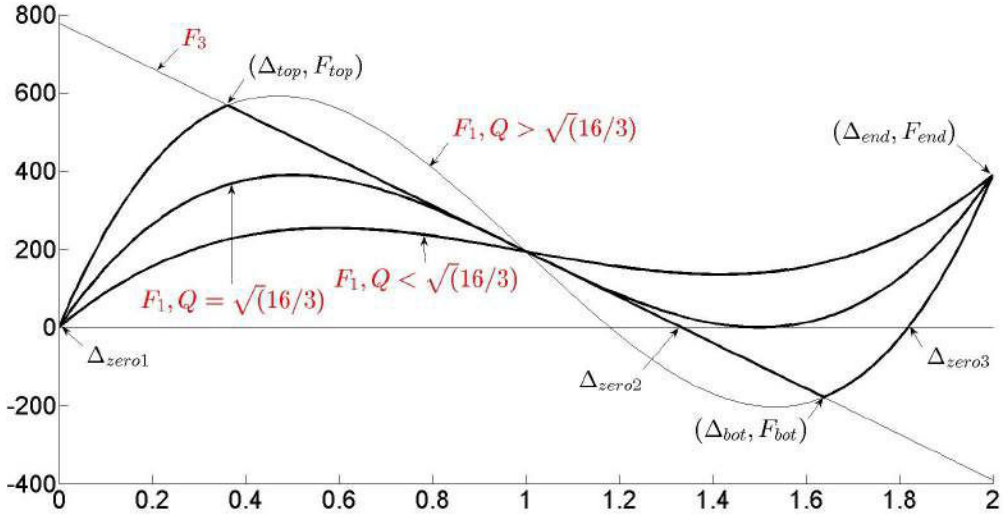

FIGURE 2.7: *Snapping force solutions without considering high modes of buckling for* $Q < \sqrt{(16/3)}$, $Q = \sqrt{(16/3)}$ *and* $Q > \sqrt{(16/3)}$ *respectively.*

$$\begin{aligned} \Delta_{zeros} &= \left\{0, \frac{4}{3}, \frac{3}{2} + \sqrt{\frac{1}{4} - \frac{4}{3Q^2}}\right\} & \Delta_{end}, F_{end} &= \left\{2, 4\pi^4\right\} \\ \Delta_{top}, \Delta_{bot} &= 1 \pm \sqrt{1 - \frac{16}{3Q^2}} & F_{top}, F_{bot} &= 6\pi^4 \left(\frac{1}{3} \mp \sqrt{1 - \frac{16}{3Q^2}}\right) \end{aligned} \tag{2.34}$$

2.3.2 Considering high modes of buckling

In this section, we develop the solution of the snapping forces taking into account the high modes of buckling. The first step is to calculate the infinite sums in (2.26) and (2.27). Introducing equations (2.24) and (2.25) in (2.26) and (2.27), the two infinite sums become:

$$\sum_{j=1,5,9\ldots} A_j = -\frac{1}{2} \frac{N_1^2}{N^2 - N_1^2} + 4F \cdot Sum_1 \tag{2.35}$$

$$\sum_{j=1}^{\infty} A_j^2 N_j^2 = \frac{1}{4} \frac{N_1^2 (N_1^4 - 16F)}{(N^2 - N_1^2)^2} + 16F^2 \cdot Sum_2 \tag{2.36}$$

where Sum_1 and Sum_2 have the following forms:

$$Sum_1 = \sum_{j=1,5,9\ldots}^{\infty} \frac{1}{N_j^2 (N^2 - N_j^2)} \qquad Sum_2 = \sum_{j=1,5,9\ldots}^{\infty} \frac{1}{N_j^2 \left(N^2 - N_j^2\right)^2} \tag{2.37}$$

Imposing $j = 4k+1$, Sum_1 can be then decomposed in two infinite sums:

$$Sum_1 = \frac{1}{4\pi^2 N^2} \left[\sum_{k=0}^{\infty} \frac{1}{(2k+1)^2} - \sum_{k=0}^{\infty} \frac{1}{(2k+1)^2 - (\frac{N}{2\pi})^2}\right] \tag{2.38}$$

The first sum in (2.38) is equal to:

$$\sum_{k=0}^{\infty} \frac{1}{(2k+1)^2} = \frac{\pi^2}{8} \tag{2.39}$$

The second sum can be concluded from the following equation [111]:

$$\pi \tan(\frac{\pi}{2}x) = \sum_{k=0}^{\infty} \frac{4x}{(2k+1)^2 - x^2} \tag{2.40}$$

Then, Sum_1 is equal to:

$$Sum_1 = \frac{1}{8N^3}\left[\frac{N}{4} - \tan(\frac{N}{4})\right] \tag{2.41}$$

Introducing (2.41) in (2.26), a new equation is derived:

$$F = \frac{N^3}{\frac{N}{4} - \tan\frac{N}{4}}\left(\frac{N^2}{N^2 - 4\pi^2} - \Delta\right) \tag{2.42}$$

In addition, $Sum2$ can be obtained by deriving Sum_1 with respect to N:

$$\frac{\partial(Sum_1)}{\partial N} = -2N \cdot Sum_2 \tag{2.43}$$

Then, Sum_2 is equivalent to:

$$Sum_2 = \frac{3}{64N^4}\left[1 - \frac{\tan(\frac{N}{4})}{\frac{N}{4}} + \frac{\tan^2(\frac{N}{4})}{3}\right] \tag{2.44}$$

Introducing (2.44) in (2.27), the following equation is obtained for the first kind of solution:

$$\frac{3}{16N^4}\left(1 + \frac{\tan^2\frac{N}{4}}{3} - \frac{\tan\frac{N}{4}}{\frac{N}{4}}\right)F_1^2 - \frac{4\pi^2}{(N^2-4\pi^2)^2}F_1 + \frac{N^2}{12Q^2} - \frac{\pi^2N^2\left(N^2-8\pi^2\right)}{4\left(N^2-4\pi^2\right)^2} = 0 \tag{2.45}$$

Equations (2.42) and (2.45) are the characteristic equations that allow defining the relations between F, N and Δ.

For the first kind of solution, the problem can be solved by numerical method. The idea is to change N in (2.45) from 0 to the point where there are no real solutions. Then, 2 values of F are obtained for each value of N. Then, introducing these values in (2.42) , the relations $N-\Delta$ and $F-\Delta$ are obtained.

Figure 2.8 shows evolution of N in function of Δ for different values of Q. Shapes of the curved beam during snapping between two sides of buckling are shown in Figure 2.8 with first, second and third kinds of solution. Noting that the normalized axial stress N is equivalent to 0 at ($\Delta = 0$,$F = 0$) and at ($\Delta = 20/\pi^2$,$F = 3840/\pi^2$). The normalized displacement at the end of deflection is close to 2, but not exactly as it is for the precompressed curved beam where the mechanical behavior is symmetric between two sides of buckling.

Figure 2.8 illustrates the values of Q providing the transitions between the first, second and third kinds of solution with considering high modes of buckling. In the first kind of solution, the

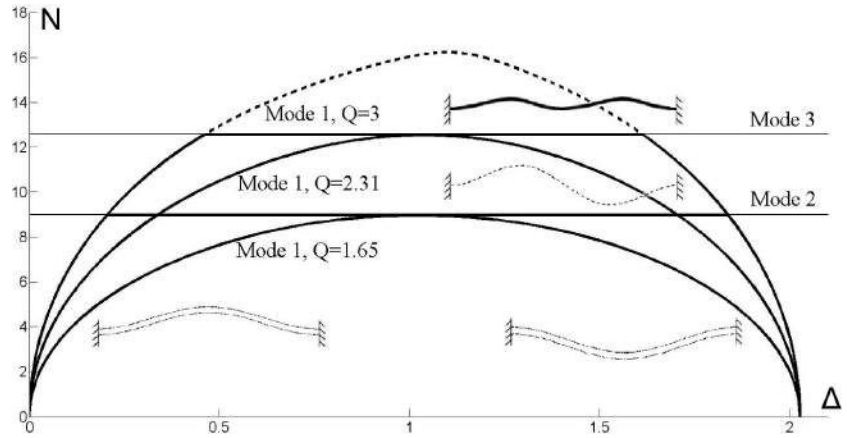

FIGURE *2.8: Evolution of the normalized axial stress N in the first kind of solution in function of Q ratio. N is constant in the second and third kinds of solution. The shape of the curved beam in the first, second and third case.*

maximum value of N that can be reached during snapping increases with increasing the value of Q. N exceeds N_1 only for:

$$Q \geq \sqrt{\frac{64\pi^2}{117-7\pi^2}} \approx 1.16 \tag{2.46}$$

Noting that at $N = N_1$, the normalized force has a unique value $F = 2\pi^4$.

On the other side, the third kind of solution is simpler. Making N constant at $N_3 = 4\pi$, the third kind simplify the previous equations. Evolution of the force can be then directly concluded from (2.42):

$$F_3 = 64\pi^2\left(\frac{4}{3}-\Delta\right) \tag{2.47}$$

Figure 2.9 shows evolution of the snapping force F in function of Δ for different values of Q with constraining mode 2 and considering high modes of buckling.

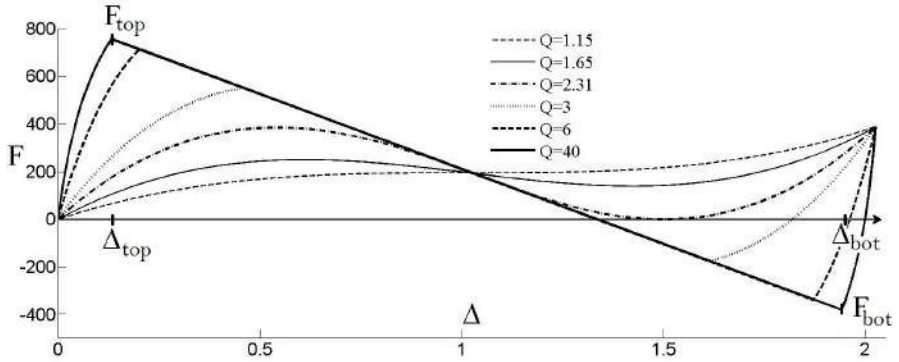

FIGURE *2.9: Evolution of the normalized applied force F for the curved beam for different Q values when mode 2 is constrained.*

The mode constant A_3 which appears in the third kind of solution is obtained by recalculating (2.45) without canceling A_3, then introducing (2.42) in the new equation:

$$A_3^2 = -\frac{3}{4\pi^2}\Delta^2 + \frac{14}{9\pi^2}\Delta + \frac{1}{18} - \frac{20}{27\pi^2} - \frac{1}{3Q^2} \tag{2.48}$$

Noting that the sign of A_3 changes with the direction of deflection.

In light of the equation of A_3, the third mode cannot appear unless Q respects the following condition:

$$Q \geq \sqrt{\frac{162\pi^2}{27\pi^2+32}} \approx 2.314 \tag{2.49}$$

Further, Δ_{top}, Δ_{bot} (Figure 2.9), which are the exact positions where the third mode appears, and F_{top}, F_{bot} which are the value of F at these positions can be concluded from (2.47) and (2.48) respectively:

$$\begin{aligned} \Delta_{top},\Delta_{bot} &= \frac{28}{27} \pm \frac{2\pi}{3}\sqrt{\frac{1}{6} + \frac{16}{81\pi^2} - \frac{1}{Q^2}} \\ F_{top},F_{bot} &= 64\pi^2\left(\frac{8}{27} \mp \frac{2\pi}{3}\sqrt{\frac{1}{6} + \frac{16}{81\pi^2} - \frac{1}{Q^2}}\right) \end{aligned} \tag{2.50}$$

Equation 2.50 shows the analytical expressions of the coordinates of the main snapping points. These expressions show clearly the influence of the different parameters on the snapping force behavior. The influence of these parameters will be investigated in Section 2.7.

2.4 Bistability conditions

Physically, the curves in Figure 2.9 represent the amount of the lateral force produced by the beam in the center point after deflection. In this context, the bistability that we look for is provided by the negative portions of F produced by the beam that will push to the other buckling side.

As we can conclude from Figure 2.9, the value of the snapping force is not symmetric between two sides of buckling. This comes from the bending energy which starts its evolution from the as-fabricated initial shape.

The shift-up of the curves in Figure 2.9 affects the bistability behavior. Mechanical conditions must be considered in order to involve bistability, while the greater margin of stability remains in the first side of buckling.

In the other side, canceling F in (2.45) for the first kind of solution, three values of N are obtained. Putting these values in (2.42), three values of Δ are obtained:

$$\Delta = \left\{0, \frac{3}{2} \pm \sqrt{\frac{1}{4} - \frac{4}{3Q^2}}\right\} \tag{2.51}$$

We conclude from (2.51) and Figure 2.9 that the beam exhibits two stable positions, only for $Q > \sqrt{\frac{16}{3}} \approx 2.31$.

Moreover, when $Q \geq \sqrt{6} \approx 2.45$, F is equivalent to zero in one position in the third solution domain. The new values of Δ where F is equal to zero are equivalent to:

$$\Delta = \left\{ 0, \frac{4}{3}, \frac{3}{2} + \sqrt{\frac{1}{4} - \frac{4}{3Q^2}} \right\} \tag{2.52}$$

The stable positions are the points where F is equivalent to zero and the beam tends to return to its position after a small displacement. Thus, the second Δ is unstable position because every variation of its state will create a tendency to move away. The first and last Δ values in (2.52) are the two stable positions:

$$\Delta = \left\{ 0, \frac{3}{2} + \sqrt{\frac{1}{4} - \frac{4}{3Q^2}} \right\} \tag{2.53}$$

Unlike the first case where high modes of buckling are canceled in the calculation, the beam exhibits the bistability without the third mode of buckling for $\sqrt{\frac{16}{3}} < Q < \sqrt{6}$.

In the other side, the Δ positions which cancel F for the second kind of solution are:

$$\Delta = \left\{ 0, 1.96, \frac{3}{2} + \sqrt{\frac{1}{4} - \frac{4}{3Q^2}} \right\} \tag{2.54}$$

A curved beam where the second mode of buckling is not constrained will never show bistability unless $Q > 5.65$. This value is obtained in the second kind of solution which can be calculated using the same calculation method of the third kind of solution. The bistability in this case is very limited and no important force is obtained in the second side of buckling.

Table 2.1 summarizes the conditions on Q in order to reach N_1, N_2, N_3 and the bistability features. The normalized axial stress N inside the curved beam reaches N_1 during deflection between the two sides of buckling only for $Q > 1.16$ and reaches N_2 for $Q > 1.65$. In the other side, N reaches N_3 for $Q > 2.31$ when mode 2 is constrained. The bistability exists only for $Q > 5.65$ when mode 2 isn't constrained and for $Q > 2.31$ when mode 2 is constrained.

TABLE *2.1: Conditions on Q in order to reach mode 1, mode 2, mode 3 and the bistability feature for the preshaped curved beam.*

	Mode 2 unconstrained	Mode 2 constrained
Mode 1	$Q \geq 1.16$	$Q \geq 1.16$
Mode 2	$Q \geq 1.65$	does not appear
Mode 3	does not appear	$Q \geq 2.31$
Bistability	$Q \geq 5.65$	$Q \geq 2.31$

2.5 Stress State

Axial and bending stresses are calculated in this section with and without considering high modes of buckling. This allows obtaining the evolution of the maximal total stress inside the curved beam during deflection.

2.5.1 Without high modes of buckling

Stresses inside the beam are decomposed into axial and bending stresses. Axial stress is constant along the beam and has a maximum when the deflection is around the middle while bending stress changes along the beam sections and increases as far as the deflection is closer to the other side. Further, axial stress p is equivalent to:

$$p = \frac{Et^2}{12l^2}N^2 \tag{2.55}$$

The bending stress T given in (2.6) starts evolution from the initial shape, T becomes:

$$T = Ez\left(\frac{\mathrm{d}^2\overline{w}}{\mathrm{dx}^2} - \frac{\mathrm{d}^2w}{\mathrm{dx}^2}\right) \tag{2.56}$$

The approximation of neglecting high modes of buckling simplifies the calculation [106]. The following equations summarize the first and third solution kinds with eliminating high modes. For the first kind of solution:

$$\begin{cases} F_1 = \dfrac{3\pi^4Q^2}{2}\Delta\left(\Delta^2 - 3\Delta + 2 + \dfrac{4}{3Q^2}\right) \\ N^2 = 3\pi^2Q^2(-\Delta^2 + 2\Delta) \\ W(X) = A_1W_1(X);\ \ A_1 = \dfrac{1-\Delta}{2} \end{cases} \tag{2.57}$$

For the third kind of solution:

$$\begin{cases} F_3 = 6\pi^4(\dfrac{4}{3} - \Delta) \\ N = N_3 \\ W(X) = A_1W_1(X) + A_3W_3(X) \\ A_1 = \dfrac{1-\Delta}{2}; A_3^2 = -\dfrac{1}{16}\left(\Delta^2 - 2\Delta + \dfrac{16}{3Q^2}\right) \end{cases} \tag{2.58}$$

For the first kind of solution, axial stress is simply concluded from (2.55) and (2.57):

$$p = \pi^2\frac{Eth}{l^2}\frac{Q}{4}(-\Delta^2 + 2\Delta) \tag{2.59}$$

Also, bending stress is obtained using (2.56) and (2.57):

$$T = \frac{2\pi^2Ezh}{l^2}\Delta\cos 2\pi\frac{x}{l} \tag{2.60}$$

The same for the third kind of solution, axial and bending stresses are calculated from (2.55), (2.56) and (2.58):

$$p = \pi^2\frac{Eth}{l^2}\frac{4}{3Q} \tag{2.61}$$

$$T = \frac{2\pi^2Ezh}{l^2}\left(\Delta\cos 2\pi\frac{x}{l} - 2\sqrt{-\Delta^2 + 2\Delta - \frac{16}{3Q^2}}\cos 4\pi\frac{x}{l}\right) \tag{2.62}$$

The total stress inside the beam is simply the sum of the axial and bending stresses. However, analyzing (2.60) and (2.62), the extremums of the bending stress are noticed at the midpoint $x = \frac{l}{2}$ and at boundaries $x = \{0, l\}$ when the first kind of solution is present and only at the midpoint when mode 3 appears. Also, the stress is maximized when z is at the limits $z = |\frac{t}{2}|$. Putting these values in the stress equations, the absolute value of the maximal total stress during deflection can be written as follows, for the first kind of solution:

$$\sigma_{max}^{\Delta} = \pi^2 \frac{Eth}{l^2} \left(-\frac{Q}{4}\Delta^2 + \left(1 + \frac{Q}{2}\right)\Delta \right) \tag{2.63}$$

And for the third kind of solution:

$$\sigma_{max}^{\Delta} = \pi^2 \frac{Eth}{l^2} \left(\Delta + 2\sqrt{-\Delta^2 + 2\Delta - \frac{16}{3Q^2}} + \frac{4}{3Q} \right) \tag{2.64}$$

Analyzing the last two equations, we notice the presence of 3 different forms of evolution curves for the maximal stress during deflection, as shown in Figure 2.10.

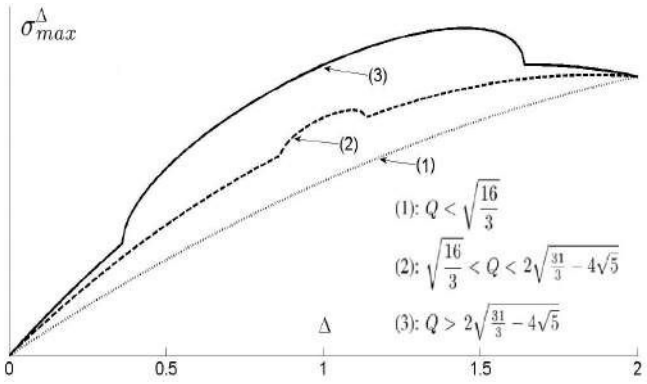

FIGURE *2.10: Evolution of the maximal stress in the beam during deflection depending on Q.*

The first form of stress is when only the first kind of solution exists. The second form is when the third kind of solution appears during deflection. The third form is when the maximal stress point is higher in the third kind of solution domain.

The first form exists for $Q < \sqrt{\frac{16}{3}} \approx 2.31$, while the third one appears for $Q > 2\sqrt{\frac{31}{3} - 4\sqrt{5}} \approx 2.36$. The second form of stress exists between the last two values of Q. Noting that there is a small difference between the last two values of Q, which means that the second form of stress is a rare case.

The maximal stress point in the first two forms is at $\Delta = 2$ when $Q \leq 2$ and at $\Delta = 1 + 2/Q$ when $Q \geq 2$.

Then, for $Q \leq 2$, the maximal stress σ_{max} is equivalent to:

$$\sigma_{max} = 2\pi^2 \frac{Eth}{l^2} \tag{2.65}$$

When Q is between $[2; 2.36]$, σ_{max} is equivalent to:

$$\sigma_{max} = \pi^2 \frac{Eth}{l^2} \left(1 + \frac{1}{Q} + \frac{Q}{4}\right) \tag{2.66}$$

In the third form, the maximal stress point is at:

$$\Delta = 1 + \frac{1}{\sqrt{5}} \sqrt{1 - \frac{16}{3Q^2}} \tag{2.67}$$

Then, for $Q > 2.36$, σ_{max} is equivalent to:

$$\sigma_{max} = \pi^2 \frac{Eth}{l^2} \left(1 + \frac{4}{3Q} + \sqrt{5}\sqrt{1 - \frac{16}{3Q^2}}\right) \tag{2.68}$$

Noting that the maximum of σ_{max} in the last form is for $Q = 16/\sqrt{3}$. However, based on the previous equations, σ_{max} is ranging between:

$$\sigma_{max} = \pi^2 \frac{Eth}{l^2} \cdot \begin{cases} 2 & Q < 2 \\ [2;2.01] & Q \in [2;2.36[\\ [2.01;3.31[& Q \in [2.36;\infty[\end{cases} \tag{2.69}$$

These values of σ_{max} in (2.69) are calculated when Δ is ranging between 0 and 2. Although, the end of deflection can be considered at the second stable position that corresponds to a transversal displacement Δ lower than 2. In this case, the new range of σ_{max} is as follows:

$$\sigma_{max} = \pi^2 \frac{Eth}{l^2} \cdot \begin{cases} [1.93;1.97] & Q \in [2.31;2.34] \\ [1.97;3.31[& Q \in [2.34;\infty[\end{cases} \tag{2.70}$$

2.5.2 Considering high modes of buckling

In the other side, the problem with high modes is complex and hard to handle without approximations. Difficulty lies in the fact that the maximal stress point is difficult to determine analytically.

Axial stress (2.55) remains the same, while bending stress changes with the consideration of high modes. Bending stress in this case is concluded by introducing (2.14) into (2.13) and (2.13) into (2.56):

$$T = \pi^2 \frac{Ezh}{l^2} \left[2\cos 2\pi X - \sum_j A_j (j+1)^2 \cos{(j+1)\pi X}\right] \tag{2.71}$$

The index j in the previous equation refers to $j = 1,5,9...$ for the first kind of solution, and to $j = 1,3,5,9...$ for the third kind of solution.

Drawing equations with changing Δ, N, and Q variables along the beam shows that the midpoint at $x = \frac{l}{2}$ is a local maximum point, and in some cases, the global maximum will not remain at the midpoint but rather a point beside it. However, there are no big difference between stress values at the local and global maximum points. An approximation to suppose

the midpoint as the global maximum point is taken. The infinite sum in (2.71) can be calculated by referring to the second sum in (2.38). Then, the maximal total stress for the first kind of solution is concluded:

$$\sigma_{max}^{N,\Delta} = E\left(\frac{t}{l}\right)^2\left[\frac{\pi^2N^2Q}{N^2-4\pi^2}+\frac{N^2}{12}+N^2Q\left(\frac{N^2}{N^2-4\pi^2}-\Delta\right)\frac{\tan\frac{N}{4}}{4\left(\frac{N}{4}-\tan\frac{N}{4}\right)}\right] \tag{2.72}$$

The maximum of the stress in the first kind of solution is at the final point. Noting that the final point where N is equivalent to zero is at $\Delta = 20/\pi^2$ when considering high modes of buckling. Then, introducing these values in (2.72), the maximal stress becomes:

$$\sigma_{max} = E\left(\frac{t}{l}\right)^2 \times \frac{240}{\pi^2}Q \tag{2.73}$$

Idem for the third kind of solution, the maximal total stress can be obtained by setting the value of N and taking into account the constant A_3:

$$\sigma_{max}^{\Delta} = E\left(\tfrac{t}{l}\right)^2 \tfrac{4\pi^2}{3}\left[1+Q+Q\sqrt{\tfrac{-27}{\pi^2}\Delta^2+\tfrac{56}{\pi^2}\Delta+2-\tfrac{80}{3\pi^2}-\tfrac{12}{Q^2}}\right] \tag{2.74}$$

The maximum of the third solution of stress is remarked at $\Delta = 28/27$. Introducing this Δ value in (2.74), we obtain the total maximum stress for the third solution of stress:

$$\sigma_{max} = E\left(\frac{t}{l}\right)^2\frac{4\pi^2}{3}\left(1+Q+Q\sqrt{\frac{64}{27\pi^2}+2-\frac{12}{Q^2}}\right) \tag{2.75}$$

We should note here that the global maximum point is at $x = l/2$ when the deflection Δ is at the two specific positions taken in (2.73) and (2.75). Then, in this context, (2.73) and (2.75) are exact.

Based on the above, the maximal stress with considering high modes of buckling is ranging between:

$$\sigma_{max} = \pi^2\frac{Eth}{l^2}\cdot\begin{cases} 2.46 & Q < 2.419 \\ [2.46,3.41[& Q \in [2.419,\infty[\end{cases} \tag{2.76}$$

Noting that the maximum for the maximal stress in the third kind of solution is for $Q = \sqrt{\frac{156}{2+\frac{64}{27\pi^2}}} \approx 8.345$.

Figure 2.11 shows evolution of the maximal stress inside the curved beam during deflection in 3 cases. The first case is for $Q = 2$ where the third mode doesn't appear during deflection, the second case is for $Q = 2.4$ where the third mode appears but the maximal stress value remains in the first solution domain and the third case is for $Q = 3$ where the maximal stress value is in the third solution domain.

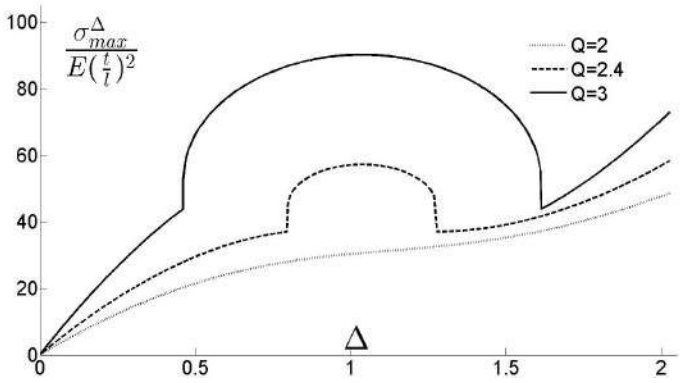

FIGURE *2.11: Evolution of the maximal total stress during deflection for* $Q = 2$*,* $Q = 2.4$ *and* $Q = 3$*.*

2.6 FEM simulations and comparison

The results obtained in the previous sections for the snapping force and stresses, with and without neglecting high modes of buckling, are compared in this section with FEM simulations that are made using ANSYS.

Simulations are made on a mechanism of two curved beams connected in the middle in order to prevent unsymmetrical buckling modes from occurring. In theory, the snapping force f will be doubled with the number of beams while the deflection d and stresses inside the beam remain the same.

A comparison between the snapping force theory with and without high modes of buckling and the FEM simulation of a silicon curved beam with $5mm$ length, $20\mu m$ thickness, $10mm$ depth, $80\mu m$ height and a Young's modulus of 169 GPa is presented in Figure 2.12.

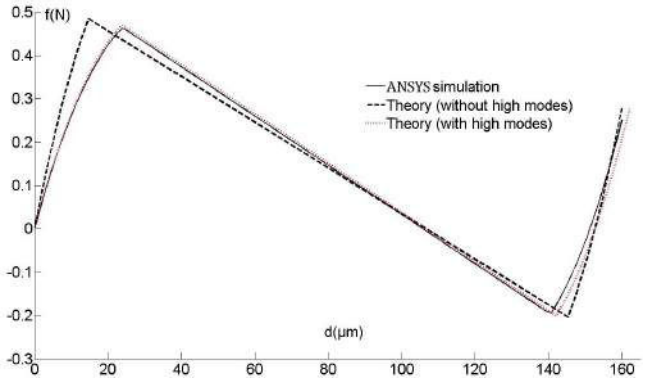

FIGURE *2.12: Comparison of the snapping-force behavior during deflection between theory and FEM simulation.*

Curves in Figure 2.12 show a good agreement between the presented theory and FEM simulation. The presented theory with high modes is more similar to the simulation while the theory without high modes shows some differences.

The presented modeling with high modes of buckling allows obtaining the expressions of the different values of Q and the main snapping points (Δ_{top},F_{top},Δ_{bot},F_{bot}) that include the effects of all modes of buckling. In the example given in Figure 2.12, the relative difference between the negligence and the consideration of high modes of buckling for the values of the snapping points (Δ_{top}, F_{top}, Δ_{bot}, F_{bot}) is equivalent to $(38.53\%, 2.93\%, 2.32\%, 1.39\%)$ respectively.

The quite large error on the Δ_{top} parameter could be a problem for the design of a bistable system. Reminding that the bistable system, as we assume , is composed of a preshaped curved beam bistable mechanism and actuators for switching between both stable positions. The snapping points in terms of displacements and forces respectively define the stroke and the force that the actuators have to provide. Thus, the accurate knowledge of the relations between the snapping points and the preshaped curved beam dimensions is very important in order to achieve the best integration of the complete bistable system.

In the other side, Figure 2.13 shows a comparison of the evolution of the maximal stresses, between the theory with and without high modes of buckling and FEM simulation on a curved beam with the same dimensions and properties.

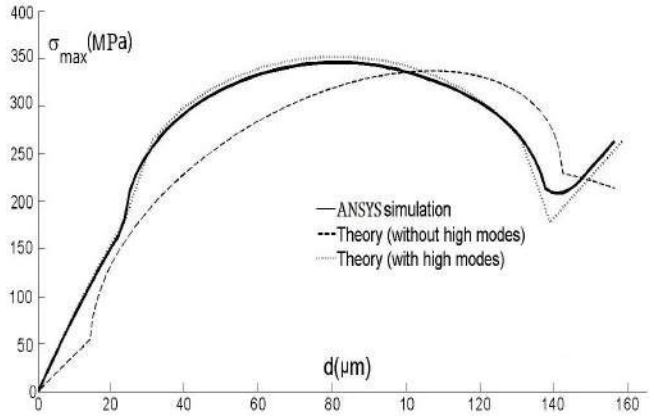

FIGURE *2.13: Comparison between the maximal stress value during deflection between theory ans FEM simulation.*

The importance of high modes of buckling is more obvious in the calculation of stresses. As shown in Figure 2.13, neglecting high modes makes a significant difference between the calculated stress and the simulation. Differences appear in the shape of the stress curves and in the highest stress point position.

Figure 2.14 shows the evolution of the maximal bending stress in the two cases, with and without high modes of buckling.

Comparing the results in Figure 2.13 and 2.14, we conclude that the bending stress has the main contribution in the total stress value. The bending and total stress curves have almost the same shape. Then, the contribution of high modes of buckling is more important in the calculation of the bending stresses.

In the first kind of solution, the axial stress evolves after deflection from the two sides of buckling to the middle (Figure 2.8), while the maximal bending stress is higher when the curved beam is far away from its initial position (Figure 2.14, parts *AB & CD*).

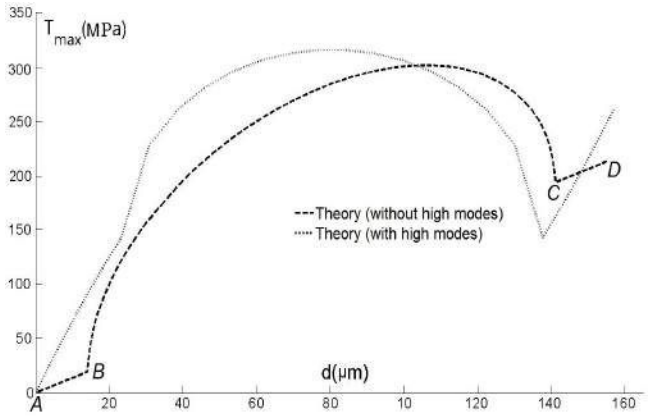

FIGURE *2.14: Comparison between the bending maximal stress value during deflection with and without high modes of buckling.*

In the third kind of solution, the axial stress is constant along the beam (Figure 2.8), while the bending stress has a maximum around the middle of deflection (Figure 2.14, part *BC*).

Calculating internal stresses in the curved beam is important for design purposes, particularly for miniaturization and for determining the design limits under elastic and/or failure limits. The accurate determination of the relation between the beam dimensions and the stress state allows identifying the limits of miniaturization and avoiding the fracture of a miniature curved beam.

2.7 Design and optimization

Evolution of the snapping forces and the internal stresses during deflection between two sides of buckling and the bistability aspects was investigated in the previous sections. Analytical models were presented and showed a good agreement with FEM simulations. The analytical expressions show the influence of all the parameters and dimensions on the behavior of the curved beam.

In this section, the design of the preshaped curved beam is investigated based on the analytical elements provided in the modeling. Generally, several criteria can be considered in the design. In our approach, we aim to define the optimal dimensions that allows obtaining a defined force and stroke of displacement.

The miniaturization is considered as well in the design where the dimensions have two main limitations in terms of the fabrication and strength limits. Concerning the fabrication limits, a minimal feature size or a maximal aspect ratio are generally defined with respect to the fabrication process. Concerning the strength limits, the dimensions are limited in terms of the stress where shorter length of the curved beam, higher height or wider thickness leads to important stresses that may lead to the failure.

Some other specifications can be defined in a design such as defining previously a dimension or the presence of stop blocks in the possible margin of displacement or define a symmetrical behavior between the two sides of buckling. The stop blocks are used to define the stroke and to add holding forces on each stable side [12].

In the following, in a first part, the influence of the different dimensions and properties on the main parameters that define the behavior of the curved beam is investigated. These parameters are the internal stress, the strength limits, the snapping force and the stroke of displacement.

The influence is presented for the stress in terms of its maximal value. A strength criterion S is defined in terms of the different dimensions and properties, which must remain lower than 1 to avoid exceeding the stress limit. As for the snapping force, the influence is presented on its top value. The distance between the two stable positions is considered as an image of the stroke. However, the influence of the dimensions and properties, that is visualized on a specific point for calculation purposes, is the same or very similar to the general behavior of the concerned parameter.

After that, a design method is proposed and presented step by step in order to define the dimensions that allows obtaining a defined force and displacement. As specifications, stop blocks are used to define the stroke, an equal holding force is desired at the two stable positions and the miniaturization is concerned.

The final part concerns the miniaturization limits and evolutions of the important parameters and maximal/minimal dimensions at the strength limits.

The elements provided in this section constitute a basis for the design of the curved beam and provide a clear view on how optimizing the dimensions in order to get the desired performance while still respecting the limitations and specifications.

2.7.1 Influence of the dimensions and properties on the mechanical behavior

The influence of the different dimensions (b, t, h, l and Q) and material properties (E, σ_{crit}) on the main parameters that define the mechanical behavior of the curved beam (stress, strength limits, snapping force, stroke) is investigated in this part.

Evolution of the different parameters is visualized in terms of $Q = h/t$, since the presentation with Q allows summarizing the influence of all the dimensions and properties in one curve. As shown in the previous sections, Q is an internal parameter that defines the general behavior of the curved beam including the snapping force, bistability aspects and stress state. However, the value of Q is not necessarily a parameter that must be strictly defined in a design. That's why in the design part, Q is not considered.

2.7.1.1 Stresses and strength limits

Strength limits are defined as the limits on the curved beam dimensions where the internal stresses remain in an acceptable margin. Designing above these dimensions leads to exceeding the critical limits of the stress σ_{crit}.

As we conclude from the stress equations (2.73) and (2.75), the maximal stress value is related proportionally to the Young's modulus, inversely proportional to the square of the span and is dependent of the ratio Q according to $f_1(Q)$ and $f_2(Q)$ as follows:

$$\sigma_{max} = E\left(\frac{t}{l}\right)^2 f_1(Q) = E\left(\frac{h}{l}\right)^2 f_2(Q) \tag{2.77}$$

where $f_1(Q)$ and $f_2(Q)$ have the following forms:

$$f_1(Q) = \begin{cases} \frac{240}{\pi^2} Q & Q < 2.419 \\ \frac{4\pi^2}{3}\left(1 + Q + Q\sqrt{\frac{64}{27\pi^2} + 2 - \frac{12}{Q^2}}\right) & Q > 2.419 \end{cases} \qquad f_2(Q) = \frac{f_1(Q)}{Q^2} \tag{2.78}$$

Changing the thickness t has two contradictory influences in two parts of the equation of σ_{max}. By increasing the thickness, σ_{max} increases proportionally to the square of the thickness in a part. In the other side, Q is inversely proportional to the thickness. Thus, σ_{max} decreases inversely proportional to $f_1(Q)$ by increasing the thickness.

In addition, changing the height h has two contradictory influences in two parts of the equation of σ_{max} which increases proportionally to the square of the height in a part and decreases according to $f_2(Q)$ in the other part by increasing the height.

Figure 2.15 shows evolution of the maximal stress value in the curved beam with respect to the critical ratio Q according to $f_1(Q)$ (left axis) and to $f_2(Q)$ (right axis). The importance of Figure 2.15 is that it allows determining directly the maximal stress reached in the curved beam for all dimensions and it shows the influence of variating each beam dimension on the maximal stress value.

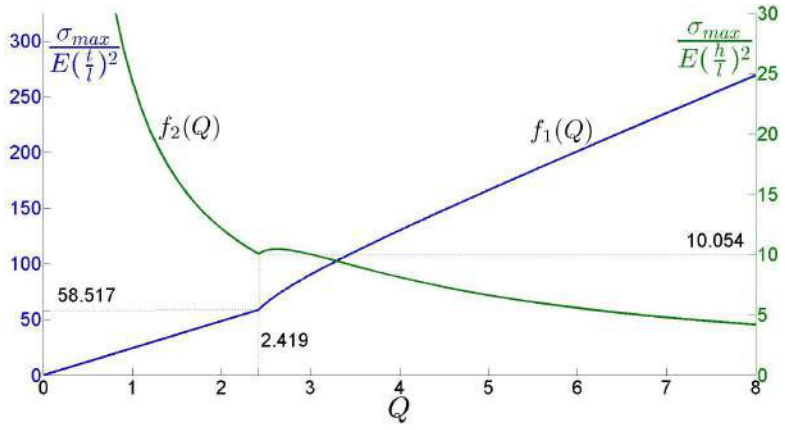

FIGURE *2.15: Evolution of the maximal stress in function of the critical ratio Q according to $f_1(Q)$ (blue curve left axis) and to $f_2(Q)$ (green curve right axis).*

For constant values of Q, the thickness and the height can be changed simultaneously in a proportional way while $f_1(Q)$ and $f_2(Q)$ remain constant. This means that σ_{max} evolves proportionally to the square of the thickness or the height for constant values of Q.

In the design, an important requirement is that the maximum value of the internal stress σ_{max} must remain under a critical limit σ_{crit}.

$$\sigma_{max} < \sigma_{crit} \tag{2.79}$$

The critical limit σ_{crit} can be determined according to the design preferences, it can be the yield strength, the fatigue limit, the fracture limit, etc.. Introducing (2.77) in (2.79) leads to the following condition that can be written in two forms:

$$K_1 \frac{t}{l} < \sqrt{\frac{1}{f_1(Q)}} \qquad K_1 \frac{h}{l} < \sqrt{\frac{1}{f_2(Q)}} \tag{2.80}$$

where $K_1 = \sqrt{E/\sigma_{crit}}$ is a material constant.

Based on (2.80), Figures 2.16 and 2.17 show evolution of the conditions on $K_1 t/l$ and $K_1 h/l$ respectively with respect to Q. The gray parts include the dimensions where stresses remain acceptable during deflection.

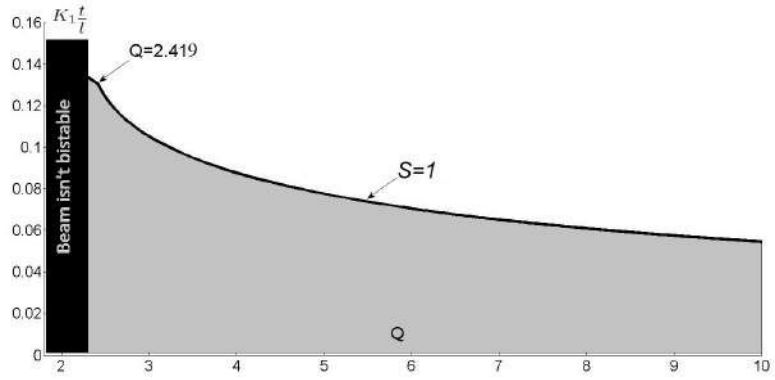

FIGURE *2.16: Evolution of the condition on $K_1 t/l$ with respect to Q.*

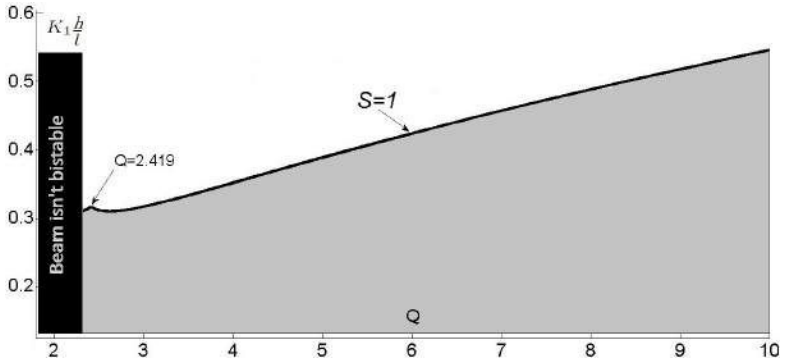

FIGURE *2.17: Evolution of the condition on $K_1 h/l$ with respect to Q.*

The results are shown for $Q > 2.31$ where the curved beam shows bistability. Figures 2.16 and 2.17 are explicit and allow choosing the curved beam dimensions under the strength limits and identifying the miniaturization limits of dimensions.

A strength criterion S can be defined in light of (2.80). The strength criterion S is dependent of the beam dimensions and material properties, it must be less than one in order to respect the stress limits.

$$S = K_1 \frac{t}{l}\sqrt{f_1(Q)} = K_1 \frac{h}{l}\sqrt{f_2(Q)} \leq 1 \tag{2.81}$$

In the gray parts of Figures 2.16 and 2.17, the strength criterion S is less than one $S < 1$. The lines that limit the gray parts represent the dimensions and parameters at the strength limits $S = 1$.

The strength criterion S is dependent of the material and the three dimensions t, h and l. Regarding the material properties, S is lower when the material is tougher ($\sigma_{crit} \nearrow$) and/or

more flexible ($E \searrow$). The span l is the main dimension in terms of size. Miniaturizing l leads to higher values of the internal stresses and to reduce the security margin before reaching the strength limits.

In terms of miniaturization, the thickness t is generally limited due to the microfabrication limitations (feature size, aspect ratio, etc.). Increasing the value of the thickness has two contradictory influences on the strength criterion S. In this case, S increases proportionally to the thickness in a part while it decreases according to $\sqrt{f_1}$ in the other part.

Idem, changing the height has two contradictory influences. By increasing the height, S increases proportionally to the height in a part while it decreases proportionally to $\sqrt{f_2}$ in the other part.

2.7.1.2 Snapping force, bistable distance and summary of the parameters influences

The relation between the snapping force f and its normalized value F is given in (2.21). The expressions of the normalized snapping force F are given in (2.45), (2.42) and (2.47). In order to define a standard of comparison, we suggest that the force criterion that can be used to evaluate the snapping force f is its top value f_{top} (Figure 2.9). The expression of f_{top} is given in the following equation:

$$\begin{aligned} f_{top} = \frac{Ebt^3h}{12l^3}F_{top} &= \frac{Ebt^4}{l^3}\left(\frac{448\pi^2}{81}Q + \frac{32\pi^3}{9}Q\sqrt{\frac{1}{6}+\frac{16}{81\pi^2}-\frac{1}{Q^2}}\right) = \frac{Ebt^4}{l^3}f_3(Q) \\ &= \frac{Ebh^4}{l^3}\left(\frac{448\pi^2}{81Q^3} + \frac{32\pi^3}{9Q^3}\sqrt{\frac{1}{6}+\frac{16}{81\pi^2}-\frac{1}{Q^2}}\right) = \frac{Ebh^4}{l^3}f_4(Q) \end{aligned} \tag{2.82}$$

Based on (2.82), Figure 2.18 shows evolution of f_{top} according to $f_3(Q)$ (left axis) and to $f_4(Q)$ (right axis). As can be concluded, the snapping forces are related proportionally to the Young's modulus and to the depth and inversely proportional to the cube of the span. As for the thickness, f_{top} increases proportionally to the fourth power of the thickness in a part while it decreases according to f_3 in the other part. For the height, f_{top} increases proportionally to the fourth power of the height in a part while it decreases with respect to f_4 in the other part. For constant values of Q, f_3 and f_4 are constants and changing t and h has only the fourth power influence on the value of f_{top}.

Another important element in the design is the distance between the two stable positions. This distance is equivalent to the stroke of deviation when there are no applied forces at the stable positions. The normalized bistable distance Δ_{stab} is equivalent to the second stable position in (2.53). Noting that the bistable distance $d_{stab} = h \cdot \Delta_{stab}$.

$$\Delta_{stab} = \frac{3}{2} + \sqrt{\frac{1}{4} - \frac{4}{3Q^2}} \tag{2.83}$$

Figure 2.19 shows evolution of the bistable distance Δ_{stab} in function of Q. The bistable distance evolves from $\Delta_{stab} = 1.5$ when the bistability appear (for $Q = \sqrt{(16/3)}$) and tend to $\Delta_{stab} = 2$ by increasing the value of Q.

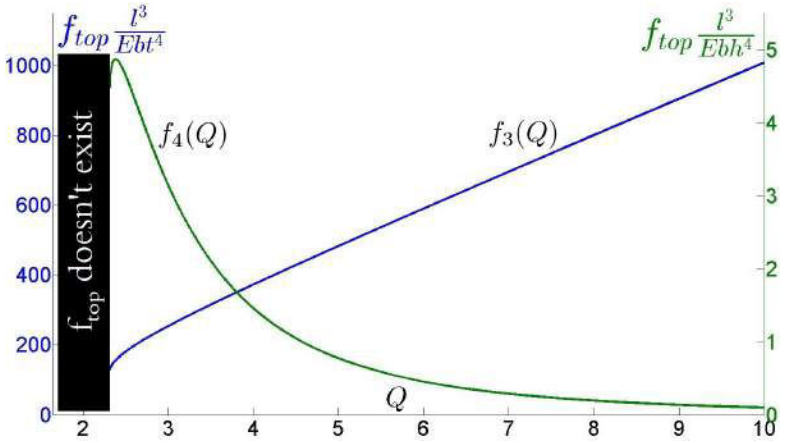

FIGURE *2.18: Evolution of the top of the snapping forces f_{top} with respect to Q according to $f_3(Q)$ (blue curve left axis) and to $f_4(Q)$ (green curve right axis).*

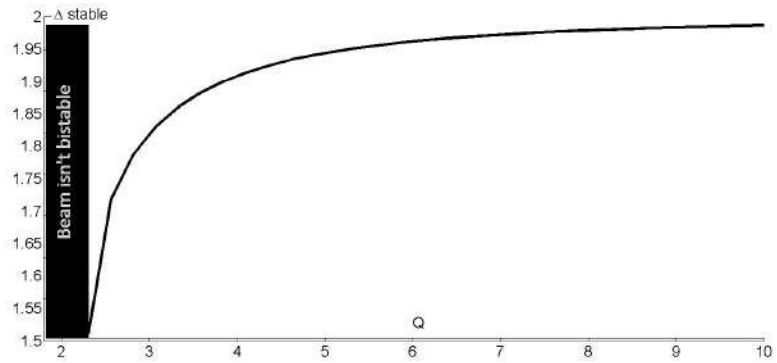

FIGURE *2.19: Evolution of the distance between the two stable positions with respect to Q.*

Noting that the stroke of deflection can be defined also by the use of stop blocks which allow defining a stop position in each side of buckling [20]. The importance of stop blocks is that they allow controlling the stroke precisely without being constrained by the dimensions of the beam and adding a clamping force at the rest positions in order to stabilize the curved beam against undesired noise and vibrations.

Consequently, it is noticed that changing Q has an influence on the snapping force (Figure 2.18) and the bistable distance (Figure 2.19). In order to obtain an overview of these two criteria simultaneously, Figure 2.20 shows evolution of f_{top} in front of the bistable distance Δ_{stab}.

Based on the above, the internal stress, strength criterion, snapping force and stroke of deflection are dependent of the material properties and of the beam dimensions. Table 2.2 summarizes the effect of changing these properties and dimensions on σ_{max}, S, f_{top} and d_{stab}.

The arrow $\nearrow$ means that the concerned characteristic in the column increases when increasing the dimension or property in the row. The arrow $\searrow$ means that it evolves in the reverse direction. The power index means that the concerned characteristic evolves proportionally to the index power (1/2,1,2,3,4) of the dimension or property. Noting that evolution of strength

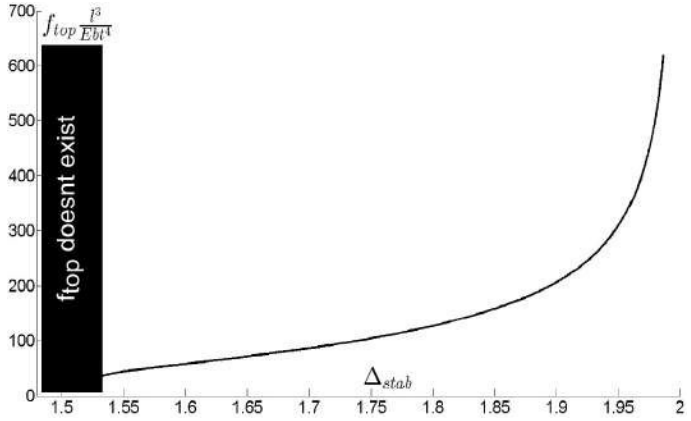

FIGURE 2.20: *Evolution of f_{top} in front of the bistable distance Δ_{stab}.*

TABLE 2.2: *Influence of the material properties and the curved beam dimensions on the top of the snapping force f_{top}, the strength criterion S, the maximal stress σ_{max} and the stroke of deflection d_{stab}.*

Dimensions	σ_{max}	S	f_{top}	d_{stab}
E	$\nearrow^{1}$	$\nearrow^{\frac{1}{2}}$	$\nearrow^{1}$	—
σ_{crit}	—	$\searrow^{\frac{1}{2}}$	—	—
b	—	—	$\nearrow^{1}$	—
l	$\searrow^{2}$	$\searrow^{1}$	$\searrow^{3}$	—
t (Q constant)	$\nearrow^{2}$	$\nearrow^{1}$	$\nearrow^{4}$	$\searrow^{1}$
h (Q constant)	$\nearrow^{2}$	$\nearrow^{1}$	$\nearrow^{4}$	$\nearrow^{1}$
Q (t constant)	$\nearrow(f_1)$	$\nearrow(\sqrt{f_1})$	$\nearrow(f_3)$	$\nearrow^{1}_{(h\nearrow)} \cdot \nearrow$ (Fig. 2.19)
Q (h constant)	$\searrow(f_2)$	$\searrow(\sqrt{f_2})$	$\searrow(f_4)$	$\nearrow$ (Fig. 2.19)
$t \sim (1/Q)$	$\nearrow^{2} \cdot \searrow(f_1)$	$\nearrow^{1} \cdot \searrow(\sqrt{f_1})$	$\nearrow^{4} \cdot \searrow(f_3)$	$\searrow$ (Fig. 2.19)
h	$\nearrow^{2} \cdot \searrow(f_2)$	$\searrow^{1} \cdot \nearrow\sqrt{(1/f_2)}$	$\nearrow^{4} \cdot \searrow(f_4)$	$\nearrow^{1} \cdot \nearrow$ (Fig. 2.19)

limits with the different parameters shown in Table 2.2 refers to the curves evolution in Figures 2.16 and 2.17.

2.7.2 Curved beam design

In a design generally, designers are seeking to determine a set of dimensions which allows providing the desired performance with a set of specifications and limitations. In this part, the design of a preshaped curved beam is investigated. A design method is presented and seeks to determine the range of dimensions which allows defining two stable positions with a desired holding force at each position and stroke of displacement (the stroke is equivalent to the distance between the two stable positions). The same characteristics of the old bistable module are targeted in terms of the stroke and holding forces (stroke=30μm, holding force=0.5mN) [12].

Noting that the design is made with considering that the curved beam is connected with other similar curved beams in the middle by a shuttle in order to avoid unsymmetrical buckling

and guide the displacement. In the other side, the value of the holding force is considered in the design for one curved beam.

Two main limitations are considered in the design, fabrication limit and stress limit. A minimal feature size is allowed in the fabrication process while the stress must not exceed its limit during deflection.

A set of specifications is chosen to be considered in the design, the material and the depth are the same as in our wafers (Chapter 5), the miniaturization of the different dimensions is concerned and the stable positions are defined using stop blocks.

As for the stop blocks, other specifications are defined relatively. A symmetrical snapping force behavior between the two stable sides is concerned, the stable positions are held with the same holding force value, and the distance between the initial position and the first stop block must be higher than a defined distance.

The design method, limitations and specifications are summarized in the block diagram in Figure 2.21.

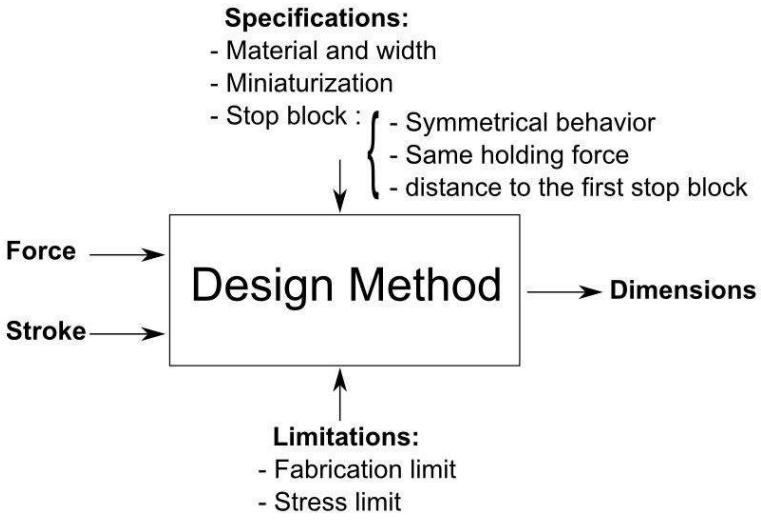

FIGURE *2.21: Block diagram representing the design method.*

The specifications and limitations may vary between a design and the other and each one leads to a condition on the dimensions or the material properties.

In the following, each specification and limitation is presented with its corresponding condition. The field of possibilities for the dimensions reduces with each condition which leads in a final stage to define the field of possibilities for the dimensions that allows reaching the desired performance with respecting the limitations and specifications.

2.7.2.1 Specifications

As just mentioned, several specifications are chosen to be considered in the design, concerning the material, the depth, the miniaturization and the stop blocks.

As for the material, often, it is chosen regarding the fabrication process or defined in the design specifications. In our case, the material is the silicon ($E = 169GPa$, $\sigma_{crit} = 0.5GPa$)

which is a common material widely used in MEMS and has many important properties that are clarified in Chapter 5.

However, the parameters that are related to the material are the Young's modulus E and the stress limit σ_{crit}. In terms of the stress, materials with higher σ_{crit}/E ratio lead to lower values of the strength criterion S and more important margin of dimensions. In terms of the snapping force, materials with higher values of E generate more important forces.

Concerning the depth, this dimension is defined to be equivalent to the thickness of the device layer in our SOI wafers $b = 100\mu m$ (Chapter 5). Otherwise, the depth has only an influence on the value of the snapping force produced by the beam. Thus, this dimension can be used to adjust the value of the forces in cases that is not defined previously.

In addition, the miniaturization is concerned. After, defining the field of possibilities for the dimensions, the smallest possible dimensions are selected.

In the other side, stop blocks are used to define the stable positions. Their relative specifications are defined in the following.

2.7.2.2 Stop blocks

Stop blocks were used in the previous design of the bistable module developed by Qiao Chen in his thesis [20], and subsequently in the bistable modules of the bistable DiMiBot [12]. The stop blocks are placed in the two stable sides of the curved beam and have two main functions, defining the two stable positions and adding holding force at each stable position.

In this chapter, we are not interested to the design of the stop blocks but to their functions. Figure 2.22 shows the main snapping points that are used in the design of the curved beams.

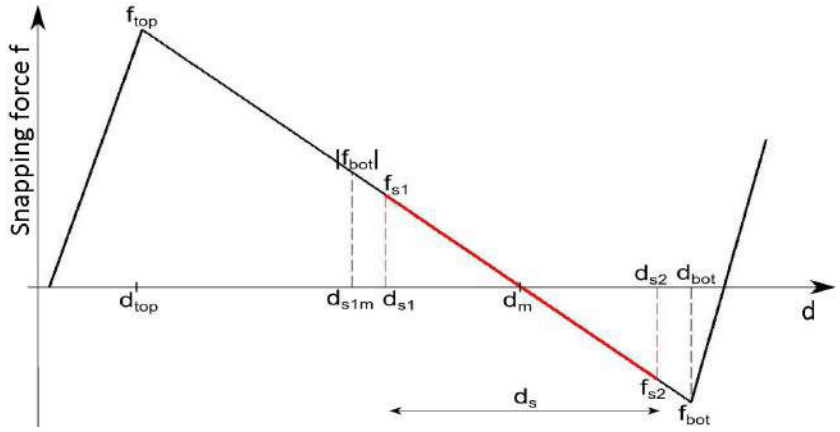

FIGURE 2.22: *Important snapping points for the design of curved beams in the bistable module.*

After fabrication, in an activation phase, the curved beam is pushed beyond the first stop block, after that, the position of the curved beam is bounded between the two stop blocks. The positions of the 2 stop blocks in the snapping curves is at the distances d_{s1} and d_{s2} while the red line between them is the evolution of the snapping forces along the stroke of deflection. In these conditions, the stable positions are at the stop blocks while the holding force is equivalent to the snapping force at the stop blocks.

The stroke d_s is the distance between the two stop blocks ($d_s = d_{s2} - d_{s1}$). The positions of the stop blocks (at d_{s1} and d_{s2}) are chosen symmetrically between the positive and negative sides of the snapping forces (with respect to $d_m = 4h/3$).

$$\begin{cases} d_{s1} = \dfrac{4}{3}h - \dfrac{d_s}{2} \\ d_{s2} = \dfrac{4}{3}h + \dfrac{d_s}{2} \end{cases} \tag{2.84}$$

In this context, the value of the holding force f_h at the stop blocks can be defined using (2.21), (2.47) and (2.84).

$$f_h = \frac{8\pi^2}{3}\frac{Ebd_s t^3}{l^3} \tag{2.85}$$

Considering that the snapping forces must remain linear during deflection, the maximal stroke that can be defined is when the second stable position d_{s2} is at d_{bot}, the first stable position d_{s1} is at d_{s1m} in this case ($d_{smax} = d_{bot} - d_{s1m}$). The maximal stroke d_{smax} is then expressed as follows:

$$d_{smax} = -\frac{16}{27}h + \frac{4\pi}{3}h\sqrt{\frac{1}{6} + \frac{16}{81\pi^2} - \frac{1}{Q^2}} \tag{2.86}$$

In light of the above, the stroke d_s is limited by the value of d_{smax}:

$$d_s \leq d_{smax} \tag{2.87}$$

The condition in the last equation leads to a condition on the height h with respect to the thickness t and the stroke d_s.

$$h \geq h_{dsmax} = \frac{2d_s}{\pi^2} + \sqrt{\left(\frac{4}{\pi^4} + \frac{27}{8\pi^2}\right)d_s^2 + 6t^2} \tag{2.88}$$

Another specification for the stop blocks is related to the position of the first stop block. The distance d_{s1} must be higher than a distance $d_{s1min} = 45\mu m$ at least for feasibility reasons (minimal distance for activating stop blocks). This leads to the following condition:

$$d_{s1} \geq d_{s1min} \tag{2.89}$$

Introducing the expression of d_{s1} in the last condition leads to another condition on the height h with respect to d_s and d_{s1min}.

$$h \geq h_{ds1min} = \frac{3}{4}d_{s1min} + \frac{3}{8}d_s \tag{2.90}$$

2.7.2.3 Limitations

Two main limitations are considered in the design, the fabrication limit and the stress limit. As for the fabrication limit, a minimal feature size of $10\mu m$ is allowed in the fabrication process.

Besides, as the thickness is normally the smallest dimension, this leads to a condition on the thickness that must be equivalent or higher than $t_{min} = 10\mu m$.

$$t \geq t_{min} \tag{2.91}$$

Concerning the stress limit, as explained previously, the strength criterion S which is defined in function of the dimensions and material properties must be lower than 1 in order to respect the stress limit.

$$S \leq 1 \tag{2.92}$$

The expression of S is dependent of t, h, l, Q and the material properties. The ratio Q can be expressed in function of t and h while the expression of l is determined from (2.85) to adjust the value of the holding force:

$$l = t\sqrt[3]{\frac{8\pi^2}{3}\frac{Ebd_s}{f_h}} \tag{2.93}$$

Replacing the expressions of Q and l in (2.92) leads to the following condition on h with respect to thickness t and the other parameters that are already defined.

$$h \leq h_S = \frac{t}{1+\frac{64}{27\pi^2}}\left(1-\frac{3}{4\pi^2}\left(\frac{8\pi^2}{3}\frac{Ebd_s}{K_1^3 f_h}\right)^{\frac{2}{3}}+\sqrt{(2+\frac{64}{27\pi^2})\left(1-\frac{3}{4\pi^2}\left(\frac{8\pi^2}{3}\frac{Ebd_s}{K_1^3 f_h}\right)^{\frac{2}{3}}\right)^2+12}\right) \tag{2.94}$$

2.7.2.4 Defining the dimensions

The dimensions that remain to define are the thickness t, the height h and the span l. A field of possibilities for t and h is defined with respect to the previous defined conditions:

$$\begin{cases} t \geq t_{min} \\ h \geq h_{dsmax} \\ h \geq h_{ds1min} \\ h \leq h_S \end{cases} \tag{2.95}$$

Figure 2.23 shows the field of possibilities for the value of the thickness and the height concluded from the previous conditions. These dimensions allow reaching the desired performance and respecting limitations and specifications.

As the miniaturization is concerned, the smallest possible values of t and h are selected. Smaller values of the thickness lead to miniaturizing the span l of the beam as can be concluded from (2.93).

The values of t, h and l are then equivalent to $t = 10\mu m$, $h = 45\mu m$ and $l = 4.5mm$ respectively. In result, the position of the first stop block is at $d_{s1} = 45\mu m$ and of the second stop block is at $d_{s2} = 75\mu m$ while the holding force is equivalent to $f_h = 0.483mN$.

In result, all the dimensions are obtained. These dimensions are defined based on the desired stroke, holding force, the specifications and the limitations.

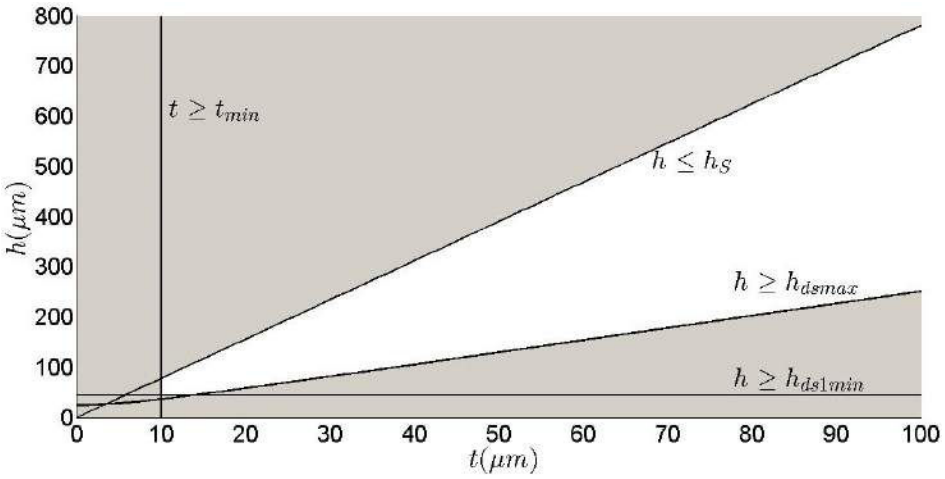

FIGURE *2.23: Field of possibilities for the value of the thickness and the height that is concluded from the conditions extracted from the specifications and limitations. The possible dimensions are in the white part.*

The design methods are proposed for a design with some specific constraints, these constraints vary from one design to another. The same methodology can be adopted for other designs with other limitations and specifications, where the corresponding conditions must be extracted firstly and the range dimensions and the material are defined subsequently. The design method can be changed to suit each design requirement based on the design elements provided hereinbefore in the chapter.

2.7.3 Limits of the miniaturization

So how much can we reduce the size of the curved beam?
This question was asked at the beginning of the thesis, and it was one of the reasons behind the works on the pre-shaped curved beam presented in this chapter.

As far as the miniaturization is concerned, we find that the design is limited by the dimension of the thickness t which must remain higher than the minimal feature size allowed by the fabrication process.

In the other side, the dimensions must be chosen under the strength limits. A maximal thickness is allowed before exceeding the stress limit, this maximum can be concluded from (2.80) as follows:

$$t_{max} = l\sqrt{\frac{\sigma_{crit}}{E}\frac{1}{f_1(Q)}} \tag{2.96}$$

The maximal thickness is then only dependent of the span l, the ratio Q and the material properties E and σ_{crit}. Choosing a length $l = 1mm$, and the silicon as material, the maximal thickness can be concluded from (2.96) for the different values of Q.

Table 2.3 shows, for different Q ratios, the maximal thickness t_{max} allowed before reaching a stress limit of $\sigma_{crit} = 0.5GPa$ for a $1mm$ span $100\mu m$ depth silicon curved beam ($E = 169GPa$).

In addition, the maximal height h_{max}, the main distances that may define the stroke (d_{top}, d_{bot}, d_{stab} and d_{smax}) and the main snapping force values (f_{top} and f_{bot}) are also calculated in the table.

The values of the different dimensions and parameters in Table 2.3 can be recalculated for other dimensions of l and b and other material properties (E and σ_{crit}) by simply multiplying them by the values of the new dimension with respect to the old one as follows.
For the thickness, the height and the distances, the values must be multiplied by:

$$\frac{\text{new } l}{1mm} \cdot \sqrt{\frac{169GPa}{\text{new } E} \frac{\text{new } \sigma_{crit}}{0.5GPa}}$$

For the forces, the values must be multiplied by:

$$\frac{\text{new } l}{1mm} \frac{\text{new } b}{100\mu m} \frac{169GPa}{\text{new } E} \left(\frac{\text{new } \sigma_{crit}}{0.5GPa}\right)^2$$

Thereafter, we can define directly the limits of miniaturization of the curved beam. We have an upper limit for the thickness t due to the strength limit and a lower limit due to fabrication constraints. On this basis, we can change the length of the beam to determine the minimal possible length l_{min} at which the maximal thickness imposed by the stress is equivalent to the minimal feature size allowed by the fabrication.

The values of h_{max}, d_{top}, d_{bot}, d_{stab}, d_{smax}, f_{bot}, and f_{top} in the table are calculated from the following expressions obtained in the chapter:

$$h_{max} = Qt_{max} \tag{2.97a}$$

$$d_{top} = h_{max}\left(\frac{28}{27} - \frac{2\pi}{3}\sqrt{\frac{1}{6} + \frac{16}{81\pi^2} - \frac{1}{Q^2}}\right) \tag{2.97b}$$

$$d_{bot} = h_{max}\left(\frac{28}{27} + \frac{2\pi}{3}\sqrt{\frac{1}{6} + \frac{16}{81\pi^2} - \frac{1}{Q^2}}\right) \tag{2.97c}$$

$$d_{stab} = h_{max}\left(\frac{3}{2} + \sqrt{\frac{1}{4} - \frac{4}{3Q^2}}\right) \tag{2.97d}$$

$$d_{smax} = h_{max}\left(-\frac{16}{27} + \frac{4\pi}{3}\sqrt{\frac{1}{6} + \frac{16}{81\pi^2} - \frac{1}{Q^2}}\right) \tag{2.97e}$$

$$\lim_{S\to 1} f_{top} = \frac{Ebt_{max}^3 h_{max}}{12l^3} F_{top} = \frac{\sigma_{crit}^2}{E} bl \frac{1}{f_1^2(Q)}\left(\frac{448\pi^2}{81}Q + \frac{32\pi^3}{9}Q\sqrt{\frac{1}{6} + \frac{16}{81\pi^2} - \frac{1}{Q^2}}\right) \tag{2.97f}$$

$$\lim_{S\to 1} f_{bot} = \frac{Ebt_{max}^3 h_{max}}{12l^3} F_{bot} = \frac{\sigma_{crit}^2}{E} bl \frac{1}{f_1^2(Q)}\left(\frac{448\pi^2}{81}Q - \frac{32\pi^3}{9}Q\sqrt{\frac{1}{6} + \frac{16}{81\pi^2} - \frac{1}{Q^2}}\right) \tag{2.97g}$$

The parameters were presented with respect to the values of Q in order to simplify the calculation. We notice that t_{max} decreases for higher values of Q which means that the minimal

TABLE 2.3: *Evolution of t_{max}, h_{max}, d_{top}, d_{bot}, d_{stab}, d_{smax}, f_{bot}, and f_{top} at the strength limits for constant values of $l = 1mm$, $b = 100\mu m$, $E = 169GPa$ and $\sigma_{crit} = 0.5GPa$. The values in the table can be recalculated directly for other constant dimensions and materials by multiplying them by the amount mentioned below the columns.*

	$l = 1mm, b = 100\mu m, E = 169GPa, \sigma_{crit} = 0.5GPa$							
Q	$t_{max}(\mu m)$	$h_{max}(\mu m)$	$d_{top}(\mu m)$	$d_{bot}(\mu m)$	$d_{stab}(\mu m)$	$d_{smax}(\mu m)$	$f_{bot}(mN)$	$f_{top}(mN)$
2.5	6.76	16.91	11.75	23.32	28.6	1.55	0.21	2.97
2.8	6.04	16.92	8.93	26.16	30.16	7.21	0.71	2.67
3.1	5.59	17.34	7.54	28.42	31.79	10.6	0.83	2.42
3.4	5.26	17.88	6.69	30.4	33.38	13.11	0.85	2.22
3.7	4.99	18.47	6.11	32.2	34.92	15.14	0.84	2.05
4	4.77	19.08	5.7	33.87	36.41	16.86	0.81	1.9
4.3	4.58	19.69	5.4	35.43	37.84	18.36	0.78	1.78
4.6	4.41	20.3	5.18	36.92	39.22	19.72	0.75	1.67
4.9	4.26	20.89	5	38.33	40.56	20.95	0.72	1.58
5.2	4.13	21.49	4.87	39.69	41.85	22.09	0.69	1.49
5.5	4.01	22.07	4.77	41	43.11	23.15	0.66	1.42
5.8	3.9	22.64	4.69	42.26	44.34	24.15	0.64	1.35
6.1	3.8	23.2	4.63	43.48	45.53	25.1	0.61	1.29
6.4	3.71	23.75	4.59	44.66	46.69	26	0.59	1.23
6.7	3.62	24.29	4.56	45.81	47.83	26.86	0.57	1.18
7	3.55	24.82	4.54	46.93	48.94	27.68	0.55	1.13
7.3	3.47	25.34	4.53	48.02	50.02	28.48	0.53	1.09
7.6	3.4	25.85	4.53	49.09	51.09	29.24	0.51	1.05
7.9	3.34	26.35	4.53	50.13	52.13	29.98	0.5	1.01
8.2	3.27	26.85	4.53	51.15	53.15	30.7	0.48	0.98
8.5	3.22	27.33	4.55	52.15	54.15	31.4	0.46	0.94
8.8	3.16	27.81	4.56	53.12	55.14	32.08	0.45	0.91
9.1	3.11	28.28	4.58	54.09	56.11	32.75	0.44	0.89
9.4	3.06	28.75	4.6	55.03	57.06	33.39	0.42	0.86
9.7	3.01	29.21	4.62	55.95	57.99	34.02	0.41	0.83
10	2.97	29.66	4.65	56.86	58.91	34.64	0.4	0.81

For other values of l, b, E and σ_{crit}, we have just to multiply by:

$\cdot \frac{l}{1mm} \cdot \sqrt{\frac{169GPa}{E} \cdot \frac{\sigma_{crit}}{0.5GPa}}$	$\cdot \frac{l}{1mm} \cdot \frac{b}{100\mu m} \cdot \frac{169GPa}{E} \cdot \left(\frac{\sigma_{crit}}{0.5GPa}\right)^2$

length, allowed before exceeding the stress limits, is higher for high values of Q. In the other side, the values of h_{max} and the different distances d_{top}, d_{bot}, d_{stab} and d_{smax} increase when the value of t_{max} decreases. As for the snapping force, it is lower for high values of Q while f_{bot} tends to be equivalent to $f_{top}/2$.

2.8 Conclusion

In conclusion, analytical modeling and stress analysis of the postbuckling behavior of a pre-shaped curved beam were presented in this chapter. The snapping force solution was investigated without and with high modes of buckling. Bistability conditions were subsequently deduced from the snapping force solution. An analytical model was then developed (with and without high modes of buckling), which describes the internal stress evolution during deflection. The presented modeling showed a good agreement with FEM simulations and revealed the importance of considering high modes of buckling in the modeling in contrast to the previous works in literature. After that, design and optimization of the curved beam was investigated based on the analytical expressions obtained in the modeling. The influence of the different dimensions and properties on the mechanical behavior was firstly presented, a design method was then presented that allows choosing the dimensions and providing the desired performance, the limit of miniaturization for the curved beam was discussed in the final part. Originality of the works made in this chapter lies in considering high modes of buckling in the modeling, stress analysis which is useful for the design, investigating the impact of the dimensions and material properties on the beam behavior, proposing a design method and finally investigating the miniaturization limits.

The other main component in the DiMiBot and in the multistable module is the U-shaped electrothermal actuator. The modeling and design of this actuator are investigated in details in Chapter 3.

Chapter 3

U-shaped electrothermal actuators

This chapter deals with the modeling of the electro-thermo-mechanical behavior of a U-shaped electrothermal actuator. The problem is treated by a sequence of two analytical models: electro-thermal and thermo-mechanical. The first one concerns the computation of the evolution of the thermal distribution in the actuator, while the second one allows computing the displacement resulting from the thermal distribution. The electrothermal model provides an exact solution of the hybrid PDEs that describe the electrothermal behavior in the three arms of the actuator. The relation between the displacement and the thermal distribution is then provided in the thermo-mechanical model. FEM simulations and experiments are run on doped silicon actuators. The analytical models show a good agreement with the results of the FEM simulations and experiments in terms of the thermal distribution and the displacement. The influence of the different dimensions and electro-thermo-mechanical properties on the electrical, thermal and mechanical behavior of the actuator is then investigated based on the analytical models. The analytical expressions provide very important key tools for the design and optimization of U-shaped actuators.

Chapter contents

3.1 Introduction

The U-shaped electrothermal actuator known as the Guckel [47], U-beam, folded or pseudobimorph actuator is well known and widespread in MEMS. Many advantages can be cited with respect to other kinds of actuators [115].

Its high output force with a wide range of displacement, the repeatability and long life time [68], the small footprint and simple design, the tolerance to working conditions (dust, moisture...), the monolithic structure and the compliance with standard MEMS-based fabrication processes, all of those are advantages that make the U-shaped actuator an attractive solution in a wide variety of MEMS applications (Microgrippers [75, 131], stepper motors [27], micromanipulator [90], nanopositioner [24], bistable module [59], the DiMiBot [13], etc.).

The U-shaped actuator is fabricated with a monolithic single material. It consists of three connected lineshaped beams (hot arm, cold arm and flexure), in a folded configuration as can be seen in Figure (3.1). The electrothermal heating of different arms with variable sections leads to non-equivalent expansions between two sides of the folded actuator. The slight expansion of those arms is amplified by the structure to generate a considerable displacement at the tip of the actuator.

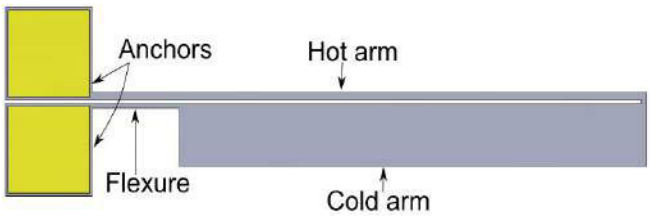

FIGURE *3.1: U-shaped electrothermal micoractuator.*

This design is being widely exploited during the last two decades especially in MEMS due to its obvious advantages which pushed research towards ameliorating the design and the performance of the actuator.

Modeling the behavior of the actuator is a diverse task since it is an interaction of several domains: electro-thermal heating, heat exchange and thermal distribution, thermo-elastic expansion and structural behavior. The problem of electrothermal actuators is usually treated by a sequence of two models: electro-thermal and thermo-mechanical. The first one concerns the computation of temperature distribution along the actuator as a result of Joule heating, while the second one allows computing the displacement at the actuator's tip resulting from the thermal distribution.

Analytical models for the U-shaped actuator are generally one dimensional and include simplifying assumptions. For example, it is difficult to include nonlinear terms such as temperature-dependent properties (electrical conductivity, thermal conductivity, thermal expansion coefficient, specific heat, resistivity). These simplifications led to some deviation between the analytical and experimental results in previous works [4, 54, 57].

Numerous electrothermal [54, 57, 71, 89, 91] and thermomechanical [54, 57, 89, 91] models have been presented in previous works on the U-shaped actuator.

In the other side, experiments and simulations on the actuator showed a dynamic behavior/displacement which is related to the dynamic of the temperature distribution while the elastic response is quasistatic relatively. Therefore, dynamic electrothermal model and static thermomechanical models are needed. Few studies [40, 52, 55, 75, 89, 121] are found that have addressed the dynamic response of the U-shaped actuator.

As far as we know, no exact analytical solution of the transient electrothermal response of the actuator was found in literature. In the case of a simple beam, solving the electrothermal equation revolves around the recognition of a Fourier series form of the general solution after introducing boundary and initial conditions. This is not the case for the U-shaped actuator.

The difficulty in the case of the actuator lies in the fact that the arms are differently heated, and temperature evolution in each arm is described by an equation. This leads to a general solution in the form of a hybrid function with three sub-functions, each one concerns one arm of the actuator. In result, the hybrid function cannot be recognized as a Fourier series, and no solution can be obtained with this method.

An analytical formulation of the steady state and transient solutions of the electrothermal response of a line-shape microstructure is presented in [80]. For the U-shaped actuator case, the steady state solution was investigated in [58]. As for the transient solution, the problem was solved numerically in [89] using Laplace transformation. The dynamic response of the actuator for a sine wave electrical input is investigated experimentally in [55, 121]. Lerch et al. [75], Geisberger et al. [40] and Henneken et al. [52] have investigated the transient behavior of their U-shaped devices with a pulse electrical input. An overshoot of displacement of the actuator is reported in their experiments which is similar to the findings of our experiments. In their works, a normal speed camera is used where the sampling rate is too low and the dynamic behavior is not analyzed in details.

An exact analytical solution of the electrothermal problem of the actuator is presented in this chapter using a novel calculation method that allows presenting an integrable function by a hybrid function, where sub-functions consist of infinite sum of sines and cosines. Expression of the temperature final solution is an infinite sum of periodic functions where all the parameters are determined. This analytical expression describes evolution of the temperature distribution inside the actuator in response to an electrical input.

As for the thermo-mechanical model, in previous works, several approaches were considered to estimate the displacement at the tip using mainly the length thermal expansion in each arm. The difference of enthalpy approach was used in [91], Castiglianos theory approach as in [55] and Euler-Bernoulli equation was derived to estimate the displacement in [34]. As in the validated model [57] where the virtual works method was used, in our proposed model we calculate the displacement using the same method but we have chosen not to make any of the simplifications done previously (such as the same width between hot arm and flexure or the consideration of axial stresses) in order to obtain a solution of a more general case with regard to the actuator dimensions. In addition, the effect of the external loads on the displacement is also considered in the calculation.

The importance of the new models (electrothermal and thermomechanical), lies not only in the estimation of the displacement and temperature distribution; but to its capability of showing the effects of different parameters and dimensions on the response, a key tool for the design and optimization.

In Section 3.2, the electrothermal model and solutions are investigated, as we begin by recalling the calculation method of the electrothermal response for a lineshaped structure, the calculation method is developed and the actuator's electrothermal new solution is obtained.

In Section 3.3, the thermomechanical model is investigated. The displacement expression is obtained in this section as a result of the Joule heating and external loads.

In Section 3.4, the analytical solutions are discussed and compared to FEM modeling and experimental results. The dynamic behavior is analyzed and the evolution of the physical aspects in the actuator (temperature distribution, arms expansions, deformation, etc.) during displacement is clarified.

In Section 3.4, the influence of the different dimensions and properties on the performance the actuator is analyzed providing very important key tools for the design and optimization of U-shaped actuators.

3.2 Electrothermal model

3.2.1 Electrothermal equation

At microscale, the heat transfer mechanisms have some differences from macroscales [64, 100]. Conduction is dominant on the free convection [100] while radiation showed a negligible influence in several studies [54, 57, 71]. Conduction should be treated as the only mode of heat transfer in the lack of forced convection [100]. Furthermore, the temperature is considered to be uniform in the cross section for microactuators [24, 54].

In our model, convection and radiation effects are neglected in the electrothermal part and a one dimensional simplification is considered. The electrothermal partial differential equation (PDE) that describes the temperature T behavior in terms of the space dimension x and the time t is as follows:

$$\rho_d C_p \frac{\partial T}{\partial t} = J^2 \rho_0 + K_p \frac{\partial^2 T}{\partial x^2} \tag{3.1}$$

ρ_d: density in $\frac{kg}{m^3}$
C_p: specific heat in $\frac{J}{K.kg}$
J: electrical current density in $\frac{A}{m^2}$
ρ_0: electrical resistivity in $\Omega.m$
K_p: thermal conductivity in $\frac{W}{K.m}$

The term on the left of (3.1) represents the density of heat added due to thermal variation. The first term on the right represents the heat generation by Joule effect, the one next concerns the conduction between sections.

3.2.2 Lineshaped beam electrothermal response

In this section, the calculation method for the electrothermal response in the case of a lineshaped microbeam is recalled. A schema for the lineshaped beam is shown in Figure 3.2.

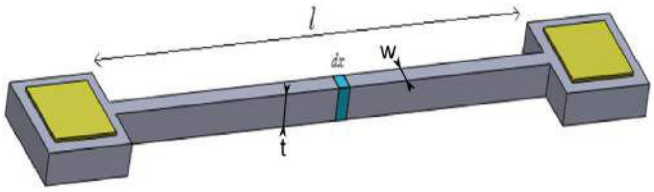

FIGURE *3.2: Schema of lineshaped microbeam.*

Considering a constant temperature at the borders that is equivalent to the ambient temperature T_∞ and an initial temperature distribution as follows:

$$T(0,t) = T_\infty \quad T(l,t) = T_\infty \quad T(x,0) = T_0(x) \tag{3.2}$$

Normally, after a long cooling time, the initial temperature distribution $T(x,0)$ is equivalent to the ambient temperature T_∞. Introducing the boundary conditions in (3.1), the steady state temperature in the lineshaped beam has the following distribution:

$$\lim_{t\to\infty} T(x,t) = T_{ss}(x) = -\frac{J^2\rho_0}{2K_p}x^2 + \frac{J^2\rho_0}{2K_p}lx + T_\infty \tag{3.3}$$

In order to obtain the transient solution, the temperature is decomposed in two parts:

$$T(x,t) = u(x) + v(x,t) \tag{3.4}$$

where $u(x)$ is the steady state solution $u(x) = T_{ss}(x)$.

This decomposition allows assigning to zero the boundary conditions of $v(x,t)$. The boundary and initial conditions for $v(x,t)$ are then as follows:

$$v(0,t) = 0 \quad v(l,t) = 0 \quad v(x,0) = T_0(x) - T_{ss}(x) \tag{3.5}$$

Introducing (3.4) in the electrothermal equation (3.1), the PDE of $v(x,t)$ can be written as follows:

$$\frac{\partial^2 v}{\partial x^2} = \frac{1}{\alpha_p}\frac{\partial v}{\partial t} \tag{3.6}$$

where $\alpha_p = \frac{K_p}{\rho_d C_p}$ is the thermal diffusivity.

Using the method of separation of variables (Fourier method), $v(x,t)$ can be decomposed in two functions with separated variables:

$$v(x,t) = X(x)\Gamma(t) \tag{3.7}$$

Introducing the separated functions (3.7) in the PDE (3.6) allows obtaining the PDEs of $\Gamma(t)$ and $X(x)$:

$$\begin{cases} \dfrac{\partial \Gamma}{\partial t} + \alpha_p \lambda^2 \Gamma = 0 \\ \dfrac{\partial^2 X}{\partial x^2} + \lambda^2 X = 0 \end{cases} \tag{3.8}$$

where λ is a positive non-zero constant assigned to $X(x)$ and $\Gamma(t)$.

The general solutions of $\Gamma(t)$ and $X(x)$ have the following forms:

$$\begin{cases} \Gamma(t) = e^{-\alpha_p \lambda^2 t} \\ X(x) = a\sin(\lambda x) + b\cos(\lambda x) \end{cases} \tag{3.9}$$

where a, b and λ are the unknowns.

Introducing the boundary conditions, we conclude that the unknowns have infinity of solutions with a periodic form: $a = a_n$, $b = b_n$ and $\lambda = \lambda_n$, where n is a positive integer. In result, according to the superposition principle:

$$v(x,t) = \sum_{n=1}^{\infty} X_n(x)\Gamma_n(t) \tag{3.10}$$

where X_n and Γ_n are equivalent to X and Γ respectively for $a = a_n$, $b = b_n$ and $\lambda = \lambda_n$.

For the boundary conditions in 3.2, the constants b_n and λ_n are equivalent to: $b_n = 0$, $\lambda_n = n\pi/l$. Afterwards, the transient solution of the temperature has the following form:

$$T(x,t) = T_{ss}(x) + \sum_{n=1}^{\infty} a_n \sin\left(\frac{n\pi}{l}x\right) e^{-\frac{\alpha_p n^2 \pi^2}{l^2}t} \tag{3.11}$$

Introducing the initial temperature condition, we recognize a Fourier series form, enabling to determine the expression of a_n.

$$a_n = \frac{2}{l}\int_0^l (T_0(x) - T_{ss}(x)) \sin\left(\frac{n\pi}{l}x\right) \tag{3.12}$$

Thereby, all the unknowns are determined and the solution is obtained.

3.2.3 Actuator electrothermal response

In this section, the exact solution of the electrothermal equations in the case of a U-shaped actuator is obtained. The system is modeled using three electrothermal PDEs that are continuous in temperature and heat flux density, one for each arm of the actuator.

The actuator is considered unfolded in order to match the one dimension 1D hypothesis. Coordinates and dimensions of the actuator are shown in Fig. 3.3.

The temperature distribution $T(x,t)$ in the case of the actuator is a hybrid function with three sub-functions that represent the temperature in each of the three arms.

$$T(x,t) = \begin{cases} T_h(x,t) & x \in [0; l_1] \\ T_c(x,t) & x \in [l_1; l_2] \\ T_f(x,t) & x \in [l_2; l_3] \end{cases} \tag{3.13}$$

where the indexes h, c and f refer to the hot arm, cold arm and flexure respectively.

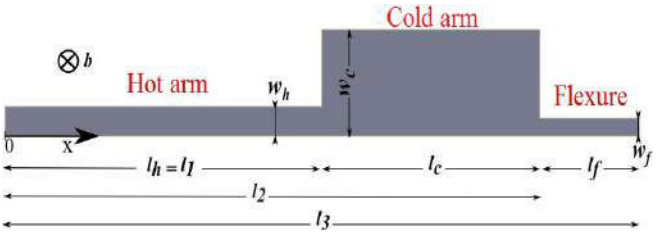

FIGURE *3.3: Unfolded actuator*

In order to simplify the presentation of the model, the index k refers to the three different arms as follows:

$$\{\text{equation}_k\} \equiv \begin{cases} \text{equation}_{k\equiv h} & x \in [0;l_1] \\ \text{equation}_{k\equiv c} & x \in [l_1;l_2] \\ \text{equation}_{k\equiv f} & x \in [l_2;l_3] \end{cases} \tag{3.14}$$

Three different equations allow defining the electrothermal behavior of each arm taking in consideration the thermal exchanges in all three as follows:

$$\left\{ \frac{\partial^2 T_k}{\partial x^2} = \frac{1}{\alpha_p}\frac{\partial T_k}{\partial t} - \frac{J_k^2 \rho_0}{K_p} \right\} \tag{3.15}$$

The steady state temperature solution has the following distribution in all three arms:

$$\left\{ T_{kss}(x) = -\frac{J_k^2 \rho_0}{2K_p}x^2 + d_{k1}x + d_{k2} \right\} \tag{3.16}$$

where d_{h1}, d_{h2}, d_{c1}, d_{c2}, d_{f1} and d_{f2} are constants.

In addition to the boundary conditions at both ends of the actuator, there are also continuity conditions between adjacent arms in temperature and heat flux density. The boundary and continuity conditions are as follows:

$$\begin{array}{ll} T_h(0,t) = T_\infty & T_f(l_3,t) = T_\infty \\ T_h(l_1,t) = T_c(l_1,t) & A_h\frac{\partial T_h}{\partial x}(l_1,t) = A_c\frac{\partial T_c}{\partial x}(l_1,t) \\ T_c(l_2,t) = T_f(l_2,t) & A_c\frac{\partial T_c}{\partial x}(l_2,t) = A_f\frac{\partial T_f}{\partial x}(l_2,t) \end{array} \tag{3.17}$$

where A_h, A_c and A_f are the arms section areas.

Considering the boundary and continuity conditions allows determining the values of d_{k1} and d_{k2} in (3.16).

As for the transient solution, as in the lineshaped beam case, the temperature solution is a sum of the steady state solution and a sum of separated variables functions as follows:

$$\left\{ T_k(x,t) = T_{kss}(x) + \sum_{n=1}^{\infty} X_{kn}(x)\Gamma_{kn}(t) \right\} \tag{3.18}$$

The general solutions of $\Gamma_{kn}(t)$ and $X_{kn}(x)$ have the following forms:

$$\left\{\begin{array}{l} \Gamma_{kn}(t) = e^{-\alpha_p \lambda_n^2 t} \\ X_{kn}(x) = a_{kn}\sin(\lambda_n x) + b_{kn}\cos(\lambda_n x) \\ \qquad\quad = C_{kn}\sin(\lambda_n x + \varphi_{kn}) \end{array}\right\} \tag{3.19}$$

Introducing the boundary and continuity conditions in (3.17) allows obtaining the following conditions on X_{kn}:

$$\begin{array}{ll} X_{hn}(0) = 0 & X_{fn}(l_3) = 0 \\ X_{hn}(l_1) = X_{cn}(l_1) & A_h \frac{\partial X_{hn}}{\partial x}(l_1) = A_c \frac{\partial X_{cn}}{\partial x}(l_1) \\ X_{cn}(l_2) = X_{fn}(l_2) & A_c \frac{\partial X_{cn}}{\partial x}(l_2) = A_f \frac{\partial X_{fn}}{\partial x}(l_2) \end{array} \tag{3.20}$$

Applying the conditions in (3.20) on X_{kn} allows obtaining the equation of λ_n and defining the relation between a_{hn} and the other constants. The relations between a_{hn} and the other constants are as follows:

$$\begin{array}{l} b_{hn} = 0 \\ \frac{b_{cn}}{a_{hn}} = \left(1 - \frac{A_h}{A_c}\right)\sin(\lambda_n l_h)\cos(\lambda_n l_h) \\ \frac{a_{cn}}{a_{hn}} = \sin^2(\lambda_n l_h) + \frac{A_h}{A_c}\cos^2(\lambda_n l_h) \\ \frac{b_{fn}}{a_{hn}} = -\frac{a_{fn}}{a_{hn}}\tan(\lambda_n l_3) \\ \frac{a_{fn}}{a_{hn}} = \cos(\lambda_n l_c)\left(\frac{A_h}{A_f}\cos(\lambda_n l_2)\cos(\lambda_n l_1) + \sin(\lambda_n l_2)\sin(\lambda_n l_1)\right) \\ + \sin(\lambda_n l_c)\left(\frac{A_h}{A_c}\sin(\lambda_n l_2)\cos(\lambda_n l_1) - \frac{A_c}{A_f}\cos(\lambda_n l_2)\sin(\lambda_n l_1)\right) \end{array} \tag{3.21}$$

Noting that the lengths have different indexes in order to reduce the expressions inside the sine and cosine functions as possible.

Besides, the equation of λ_n concluded from (3.20) is as follows:

$$\begin{array}{l} A_h A_c \cos(\lambda_n l_h)\cos(\lambda_n l_c)\sin(\lambda_n l_f) + \\ A_h A_f \cos(\lambda_n l_h)\sin(\lambda_n l_c)\cos(\lambda_n l_f) + \\ A_c A_f \sin(\lambda_n l_h)\cos(\lambda_n l_c)\cos(\lambda_n l_f) - \\ A_c^2 \sin(\lambda_n l_h)\sin(\lambda_n l_c)\sin(\lambda_n l_f) = 0 \end{array} \tag{3.22}$$

Unlike the case of a lineshaped beam, the trigonometric equation (3.22) doesn't allow obtaining a simple analytical form of λ_n. The values of λ_n for the actuator must be then calculated numerically from (3.22).

Yet, a kind of periodicity for the values of λ_n is noticed. If the total length of the arms can be written as a positive integer after scaling, then λ_{K_l} is the $K_l th$ solution of λ_n:

$$\lambda_{K_l} = \frac{K_l \pi}{l_3} \tag{3.23}$$

K_l is a least common multiple between lengths of arms:

$$K_l = LCM\left(\frac{LCM(l_h,l_3)}{l_h}, \frac{LCM(l_c,l_3)}{l_c}, \frac{LCM(l_f,l_3)}{l_f}\right) \tag{3.24}$$

Accordingly, the solutions of λ_n are periodic as follows:

$$\lambda_{K_l+n} = \lambda_{K_l} + \lambda_n \tag{3.25}$$

In our case, $l_3 = 2l_h$, then the first part in (3.24) is equivalent to 2 and K_l is always an even number. In this case, $\lambda_{K_l/2} = \frac{(K_l\pi)}{2l_3}$ is also a solution of λ_n. The first K_l solutions of λ_n are also symmetric as follows:

$$\lambda_{K_l-n} = \lambda_{K_l} - \lambda_n \tag{3.26}$$

Therefore, it is sufficient to calculate only the first λ_n for $\lambda_n \leq \frac{(K_l\pi)}{2l_3}$. the other λ_n are obtained by symmetry and periodicity.

Returning to the modeling, the second representation of $X_{kn}(x)$ in (3.19) with C_{kn}, λ_n and φ_{kn} is adopted in order to present the developed solution hereinafter:

$$C_{kn} = \sqrt{a_{kn}^2 + b_{kn}^2} \quad \varphi_{kn} = \begin{cases} -\tan^{-1}\left(\frac{b_{kn}}{a_{kn}}\right) & a_{kn} > 0 \\ \pi - \tan^{-1}\left(\frac{b_{kn}}{a_{kn}}\right) & a_{kn} < 0 \end{cases} \tag{3.27}$$

The values of φ_{kn} can be concluded from (3.21) and (3.27). The relations of C_{cn}, C_{fn} with respect to C_{hn} are as follows:

$$\begin{aligned} C_{hn} &= |a_{hn}| \\ \frac{C_{cn}}{C_{hn}} &= \left| \begin{array}{l} \frac{A_h}{A_c}\sin^2(\lambda_n l_h) + \cos^2(\lambda_n l_h) \\ + \left(\frac{A_h}{A_c} - 1\right)\sin(\lambda_n l_h)\cos(\lambda_n l_h) \end{array} \right| \\ \frac{C_{fn}}{C_{hn}} &= \left| \frac{a_{fn}}{a_{hn}} \frac{1}{\cos(\lambda_n l_3)} \right| \end{aligned} \tag{3.28}$$

Among the 7 unknown constants in (3.19), λ_n is obtained from (3.22) and all others are defined according to only one constant C_{hn} (3.28). This constant can be calculated by introducing the initial distribution of temperature:

$$\left\{ \sum_{n=1}^{\infty} C_{kn}\sin(\lambda_n x + \varphi_{kn}) = T_{k_0}(x) - T_{k_{ss}}(x) \right\} \tag{3.29}$$

The recognition of a Fourier series form allows calculating the unknown constants in the case of a lineshaped beam. Fourier series allows representing any integrable function by an infinite sum of sine waves. The sine waves are periodic on a determined range while the sine and cosine constants are continuous throughout the period.

These conditions are satisfied in the case of the lineshaped beam, while the hybrid and aperiodic nature of the temperature distribution along the actuator prevents the application of the same principle for calculating the constants of the actuator electrothermal response.

A solution for the unknown constant in (3.29) is presented in the following using a novel calculation method to present an integrable function by a sum of hybrid sine and cosine functions. In order to calculate the values of the constants C_h, C_c, C_f, φ_h, φ_c and φ_f that correspond to $\lambda_n = \lambda$, we multiply the first row in (3.29) by $C_h A_h \sin(\lambda x + \varphi_h)$, the second row by

$C_c A_c \sin(\lambda x+\varphi_c)$ and the third row by $C_f A_f \sin(\lambda x+\varphi_f)$ and integrate the result over the length of the actuator:

$$\begin{aligned}&\int_0^{l_3}\sum_{n=1}^{\infty}\{C_{kn}C_kA_k\sin(\lambda_n x+\varphi_{kn})\sin(\lambda x+\varphi_k)\}\,dx\\&=\int_0^{l_3}\{C_kA_k\left(T_{k_0}(x)-T_{k_{ss}}(x)\right)\sin(\lambda x+\varphi_k)\}\,dx\end{aligned}\tag{3.30}$$

Noting that:

$$\begin{aligned}&\int_0^{l_3}\{\text{equation}_k\}\,dx=\\&\int_0^{l_1}\text{equation}_{k\equiv h}dx+\int_{l_1}^{l_2}\text{equation}_{k\equiv c}dx+\int_{l_2}^{l_3}\text{equation}_{k\equiv f}dx\end{aligned}\tag{3.31}$$

The first side in (3.30) can be decomposed in two parts:

$$\begin{aligned}&\int_0^{l_3}\sum_{n=1}^{\infty}\{C_{kn}C_kA_k\sin(\lambda_n x+\varphi_{kn})\sin(\lambda x+\varphi_k)\}\,dx\\&=\int_0^{l_3}\sum_{\lambda_n\neq\lambda}\{C_{kn}C_kA_k\sin(\lambda_n x+\varphi_{kn})\sin(\lambda x+\varphi_k)\}\,dx\\&\qquad+\int_0^{l_3}\left\{C_k^2A_k\sin^2(\lambda x+\varphi_k)\right\}dx\end{aligned}\tag{3.32}$$

Considering boundary and continuity conditions allows canceling the first part of (3.32) for $\lambda_n\neq\lambda$:

$$\int_0^{l_3}\sum_{\lambda_n\neq\lambda}\{C_{kn}C_kA_k\sin(\lambda_n x+\varphi_{kn})\sin(\lambda x+\varphi_k)\}\,dx=0\tag{3.33}$$

Considering boundary and continuity conditions, the other part of (3.32) is equivalent to:

$$\int_0^{l_3}\left\{C_k^2A_k\sin^2(\lambda x+\varphi_k)\right\}dx=\frac{1}{2}(C_h^2A_hl_h+C_c^2A_cl_c+C_f^2A_fl_f)\tag{3.34}$$

Introducing (3.32), (3.33) and (3.34), equation (3.30) becomes:

$$\begin{aligned}&\int_0^{l_3}\{C_kA_k\left(T_{k_0}(x)-T_{k_{ss}}(x)\right)\sin(\lambda x+\varphi_k)\}\,dx\\&\qquad=\tfrac{1}{2}(C_h^2A_hl_h+C_c^2A_cl_c+C_f^2A_fl_f).\end{aligned}\tag{3.35}$$

Applying integration by parts two times to the first part in (3.35) and considering boundary and continuity conditions, the first part in (3.35) becomes:

$$\begin{aligned}&\int_0^{l_3}\{C_kA_k\left(T_{k_0}(x)-T_{k_{ss}}(x)\right)\sin(\lambda x+\varphi_k)\}\,dx\\&=\tfrac{1}{\lambda^2}\int_0^{l_3}\left\{C_kA_k\tfrac{d^2}{dx^2}\left(T_{k_0}(x)-T_{k_{ss}}(x)\right)\sin(\lambda x+\varphi_k)\right\}dx\end{aligned}\tag{3.36}$$

Equations (3.35) or/and (3.36) allow defining the value of the unknown constants for a determined initial temperature distribution. In the case of an initial uniform distribution of temperature, $\frac{d^2}{dx^2}\left(T_{k_0}(x)-T_{k_{ss}}(x)\right)$ is equivalent to:

$$\left\{\frac{d^2}{dx^2}\left(T_{k_0}(x)-T_{k_{ss}}(x)\right)=-\frac{I^2\rho_0}{K_pA_k^2}\right\} \tag{3.37}$$

The integral in (3.35) is then equivalent to:

$$\begin{aligned}&\int_0^{l_3}\left\{C_kA_k\left(T_{k_0}(x)-T_{k_{ss}}(x)\right)\sin(\lambda x+\varphi_k)\right\}dx\\&=\frac{I^2\rho_0}{\lambda^3K_p}\left[-\frac{C_h}{A_h}\cos(\varphi_h)+C_hA_h\cos(\lambda l_1+\varphi_h)\left(\frac{1}{A_h^2}-\frac{1}{A_c^2}\right)\right.\\&\left.+C_cA_c\cos(\lambda l_2+\varphi_c)\left(\frac{1}{A_c^2}-\frac{1}{A_f^2}\right)+\frac{C_f}{A_f}\cos(\lambda l_3+\varphi_f)\right]\end{aligned} \tag{3.38}$$

where I is the electrical current.

Combining (3.35) and (3.38) allows obtaining the value of the unknown constant C_h with respect to the actuator dimensions, material properties and the corresponding λ, φ_k and C_k:

$$\begin{aligned}C_h=&\frac{2I^2\rho_0}{\lambda^3K_p\left(l_h+l_c\frac{A_c}{A_h}(\frac{C_c}{C_h})^2+l_f\frac{A_f}{A_h}(\frac{C_f}{C_h})^2\right)}\\&\left[-\frac{1}{A_h^2}\cos(\varphi_h)+\cos(\lambda l_1+\varphi_h)\left(\frac{1}{A_h^2}-\frac{1}{A_c^2}\right)\right.\\&\left.+\frac{A_c}{A_h}\frac{C_c}{C_h}\cos\left(\lambda l_2+\varphi_c\right)\left(\frac{1}{A_c^2}-\frac{1}{A_f^2}\right)+\frac{1}{A_hA_f}\frac{C_f}{C_h}\cos(\lambda l_3+\varphi_f)\right]\end{aligned} \tag{3.39}$$

Consequently, the solution of the electrothermal problem is obtained. The expression of the temperature with respect to time t and position x in the case of the actuator is as follows:

$$\left\{T_k(x,t)=T_{kss}(x)+\sum_{n=1}^{\infty}C_{kn}\sin(\lambda_nx+\varphi_{kn})e^{-\alpha_p\lambda_n^2t}\right\} \tag{3.40}$$

The steady state temperature distribution $T_{kss}(x)$ is obtained in (3.16). The values of λ_n are calculated from (3.22) and the corresponding constants C_{kn} and φ_{kn} are obtained in (3.27), (3.28) and (3.39).

The obtained expression (3.40) allows obtaining directly the evolution of the temperature distribution inside U-shaped actuators with determined dimensions and material properties. In addition, this expression allows identifying the influence of all dimensions and parameters on the evolution of the temperature distribution inside the actuator.

3.3 Thermo-mechanical model

In this section, the displacement at the tip of the actuator is calculated based on the superposition and virtual work principles. The displacement is seen as an image of the evolution of the thermal distribution inside the actuator. The mechanical inertia of the micro-actuator is neglected due to its high natural frequency.

Generally, the natural frequency of a structure is higher as far as the miniaturization is concerned. Taking the example of a beam, the equation that governs its dynamic is the Euler-Bernoulli equation.

$$E_b I_b \frac{d^4 y_b}{dx_b^4} + \rho_b A_b \frac{d^2 y_b}{dt^2} = 0 \tag{3.41}$$

where E_b is the Young's modulus, $I_b = b_b t_b^3/12$ is the second moment of area, b_b is the depth, t_b is the thickness, y_b is the deflection, x_b is the position, ρ_b is the density, $A_b = b_b t_b$ is the section area and t is the time.

The general solution of (3.41) shows that the natural frequency f_b of the beam is equivalent to:

$$f_b = \frac{1}{2\pi} \frac{\beta_n}{l_b^2} \sqrt{\frac{E_b I_b}{\rho_b A_b}} = \frac{\beta_n}{4\pi} \sqrt{\frac{E_b}{3\rho_b}} \frac{t_b}{l_b^2} \tag{3.42}$$

where l_b is the length of the beam and β_n is a constant that can be determined in function of the boundary conditions.

As shown in (3.42), the natural frequency is proportional to the ratio t_b/l_b^2. However, scaling the beam means that the ratio t_b/l_b is constant, which leads to conclude that the natural frequency of the beam is inversely proportional to its length. Generalizing this result, the natural frequency of a structure is inversely proportional to its characteristic length. Thus, the natural frequency is more important in microstructures.

In addition, simulations and experiments showed that the natural frequency of the actuator is of several KHz, which implies that the structural dynamic response is much faster than the electrothermal dynamic response. Thus, the mechanical inertia is considered to be quasi-static in our model.

The structure of the actuator allows amplifying the thermal expansion difference between two sides of the actuator. In the other side, thermal expansion in a beam evolves due to a temperature rise with respect to the following equation:

$$\Delta l(t) = \int_0^l \alpha \left(T(x,t) - T_0\right) dx \tag{3.43}$$

where Δl is the length expansion and α is the thermal expansion coefficient.

Figure 3.4 shows distribution of the surface forces N and bending moments M_b in the actuator anchored at the flexure after applying virtual unit forces and moment at the free border of the hot arm and at the tip of the actuator.

The efforts X, Y and M in Figure 3.4 are the efforts needed to cancel vertical and horizontal displacements and rotation at the free border of the hot arm after an action.

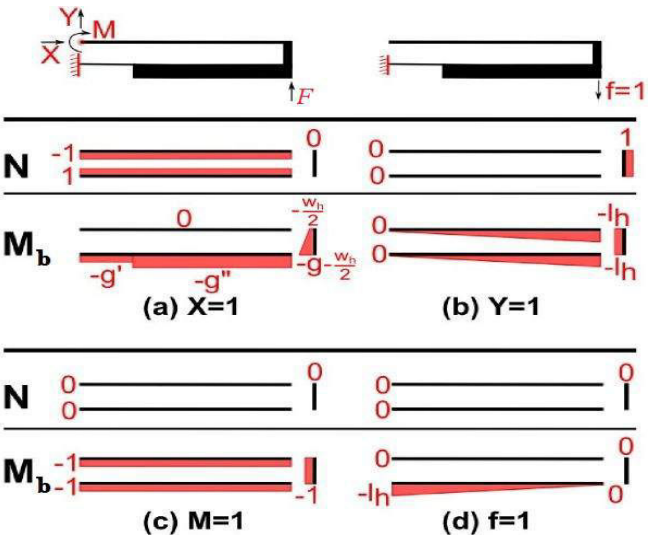

FIGURE *3.4: Distribution of the surface forces N and bending moments M_b in the actuator when it is anchored at the flexure end and free in the other side after applying virtual unit forces and moment at the free border of the hot arm, (a), (b) and (c), and at the tip of the actuator (d).*

In our case, two different types of actions are applied on the actuator, the first one concerns the thermal expansion of the different arms due to Joule heating while the other one concerns the mechanical load that must be handled by the actuator. The load is represented by a vertical force F at the tip of the actuator in the reverse direction of displacement (Figure 3.4). In result, the anchor efforts X, Y and M consist of two parts, one is for the thermal expansion and the other is for the load:

$$\begin{cases} X = X_\Delta + X_F \\ Y = Y_\Delta + Y_F \\ M = M_\Delta + M_F \end{cases} \tag{3.44}$$

The efforts X_Δ, Y_Δ and M_Δ are the efforts produced by the support of the hot arm after expansion. These efforts are calculated as follows:

$$\begin{pmatrix} \delta_{XX} & \delta_{XY} & \delta_{XM} \\ \delta_{YX} & \delta_{YY} & \delta_{YM} \\ \delta_{MX} & \delta_{MY} & \delta_{MM} \end{pmatrix} \begin{pmatrix} X_\Delta \\ Y_\Delta \\ M_\Delta \end{pmatrix} = \begin{pmatrix} \Delta \\ 0 \\ 0 \end{pmatrix} \tag{3.45}$$

where Δ denotes the arms expansion difference between hot and cold sides: $\Delta = \Delta l_h - \Delta l_c - \Delta l_f$.

The displacements and rotations after applying unit forces and moments $\delta_{XX}, \delta_{XY}...$ are obtained by applying the virtual works principle with respect to the following equation:

$$\delta_{12} = \int_0^l \left(\frac{N_1 N_2}{EA} + \frac{M_1 M_2}{EI_y} \right) dx \tag{3.46}$$

δ_{12}: Displacement or rotation in the direction of the virtual unit effort 1 after applying the real effort 2.
N_1: Surface forces with the virtual effort.
N_2: Surface forces with the real effort.
M_1: Bending moments with the virtual effort.
M_2: Bending moments with the real effort.
$I_y = \frac{bw^3}{12}$: Second moment of area of section with respect to the midline.
E: Young's modulus.

Based on (3.46), expressions of δ coefficients in (3.45) are as follows:

$$\delta_{XX} = \frac{g'^2 l_f}{EI_{yf}} + \frac{g''^2 l_c}{EI_{yc}} + \frac{2g^3 + 3gw_h(g + \frac{w_h}{2})}{6EI_{yg}} + \frac{l_f}{ES_f} + \frac{l_c}{ES_c} + \frac{l_h}{ES_h} \tag{3.47a}$$

$$\delta_{YY} = \frac{l_f^3}{3EI_{yf}} + \frac{l_h^3 - l_f^3}{3EI_{yc}} + \frac{gl_h^2}{EI_{yg}} + \frac{l_h^3}{3EI_{yh}} + \frac{g}{ES_g} \tag{3.47b}$$

$$\delta_{MM} = \frac{l_f}{EI_{yf}} + \frac{l_c}{EI_{yc}} + \frac{g}{EI_{yg}} + \frac{l_h}{EI_{yh}} \tag{3.47c}$$

$$\delta_{XY} = \delta_{YX} = \frac{g' l_f^2}{2EI_{yf}} + \frac{g''(l_h^2 - l_f^2)}{2EI_{yc}} + \frac{g^2 l_h + l_h g w_h}{2EI_{yg}} \tag{3.47d}$$

$$\delta_{XM} = \delta_{MX} = \frac{g' l_f}{EI_{yf}} + \frac{g'' l_c}{EI_{yc}} + \frac{g(g + w_h)}{2EI_{yg}} \tag{3.47e}$$

$$\delta_{YM} = \delta_{MY} = \frac{l_f^2}{2EI_{yf}} + \frac{l_h^2 - l_f^2}{2EI_{yc}} + \frac{gl_h}{EI_{yg}} + \frac{l_h^2}{2EI_{yh}} \tag{3.47f}$$

Given that:
g: Gap width
g': Distance between hot arm and flexure mid-lines; $g' = g + \frac{w_h + w_f}{2}$
g'': Distance between hot and cold arm mid-lines; $g'' = g + \frac{w_h + w_c}{2}$

In the other side, U-shaped actuators work generally with loads in MEMS. The efforts X_F, Y_F and M_F are the anchor efforts produced to face displacements and rotation resulting from the applied load:

$$\begin{pmatrix} \delta_{XX} & \delta_{XY} & \delta_{XM} \\ \delta_{YX} & \delta_{YY} & \delta_{YM} \\ \delta_{MX} & \delta_{MY} & \delta_{MM} \end{pmatrix} \begin{pmatrix} X_F \\ Y_F \\ M_F \end{pmatrix} = - \begin{pmatrix} \delta_{XF} \\ \delta_{YF} \\ \delta_{MF} \end{pmatrix} F \tag{3.48}$$

where δ_{XF}, δ_{YF} and δ_{MF} are the displacements and rotations at the free border of the hot arm after applying a unit load $F = 1$.

The terms δ_{XF}, δ_{YF} and δ_{MF} are equivalent to $-\delta_{Xf}$, $-\delta_{Yf}$ and $-\delta_{Mf}$ respectively. In the other side, δ_{Xf}, δ_{Yf} and δ_{Mf} are equivalent to the vertical displacement at the tip of the actuator after applying a unit effort on the free border X,Y and $M = 1$ respectively:

$$\delta_{Xf} = \frac{g'}{EI_{yf}}\left(l_h l_f - \frac{l_f^2}{2}\right) + \frac{g''}{EI_{yc}}\left(\frac{l_h^2}{2} - l_h l_f + \frac{l_f^2}{2}\right) \tag{3.49a}$$

$$\delta_{Yf} = \frac{1}{EI_{yf}}\left(\frac{l_h l_f^2}{2} - \frac{l_f^3}{3}\right) + \frac{1}{EI_{yc}}\left(\frac{l_h^3}{6} - \frac{l_h l_f^2}{2} + \frac{l_f^3}{3}\right) \tag{3.49b}$$

$$\delta_{Mf} = \frac{1}{EI_{yf}}\left(l_h l_f - \frac{l_f^2}{2}\right) + \frac{1}{EI_{yc}}\left(\frac{l_h^2}{2} - l_h l_f + \frac{l_f^2}{2}\right) \tag{3.49c}$$

Calculation of the anchor efforts (X_Δ, Y_Δ and M_Δ in (3.45)) and (X_F, Y_F and M_F in (3.48)) allows computing the displacement d at the tip of the actuator after applying the Joule heating and the load F:

$$d = X\delta_{Xf} + Y\delta_{Yf} + M\delta_{Mf} + F\delta_{Ff} \tag{3.50}$$

The term δ_{Ff} corresponds to the displacement at the tip of the actuator (clamped-free) after applying a unit force $F = 1$ (Figure 3.4):

$$\delta_{Ff} = \frac{1}{EI_{yf}}\left(-l_h l_c l_f - \frac{l_f^3}{3}\right) + \frac{1}{EI_{yc}}\left(-\frac{l_c^3}{3}\right) \tag{3.51}$$

Analyzing the analytical expression of the displacement d in (3.50) shows that the displacement is directly proportional to the arms expansion difference and the load:

$$d = K_1\Delta + K_2 F \tag{3.52}$$

where K_1 and K_2 are calculated as follows

$$K_1 = \begin{pmatrix} 1 & 0 & 0 \end{pmatrix} \begin{pmatrix} \delta_{XX} & \delta_{YX} & \delta_{MX} \\ \delta_{XY} & \delta_{YY} & \delta_{MY} \\ \delta_{XM} & \delta_{YM} & \delta_{MM} \end{pmatrix}^{-1} \begin{pmatrix} \delta_{Xf} \\ \delta_{Yf} \\ \delta_{Mf} \end{pmatrix} \tag{3.53a}$$

$$K_2 = \begin{pmatrix} \delta_{Xf} & \delta_{Yf} & \delta_{Mf} \end{pmatrix} \begin{pmatrix} \delta_{XX} & \delta_{YX} & \delta_{MX} \\ \delta_{XY} & \delta_{YY} & \delta_{MY} \\ \delta_{XM} & \delta_{YM} & \delta_{MM} \end{pmatrix}^{-1} \begin{pmatrix} \delta_{Xf} \\ \delta_{Yf} \\ \delta_{Mf} \end{pmatrix} + \delta_{Ff} \tag{3.53b}$$

3.4 Simulations, Experiments and discussion

The analytical models in this section are compared with FE simulations and experiments and the evolution of the physical aspects (such as the temperature distribution and displacement) is discussed.

Modeling, simulations and experiments are run on a doped silicon U-shaped actuator with the dimensions in Figure 3.5. These dimensions are the same used later for the actuators in the new digital microrobot.

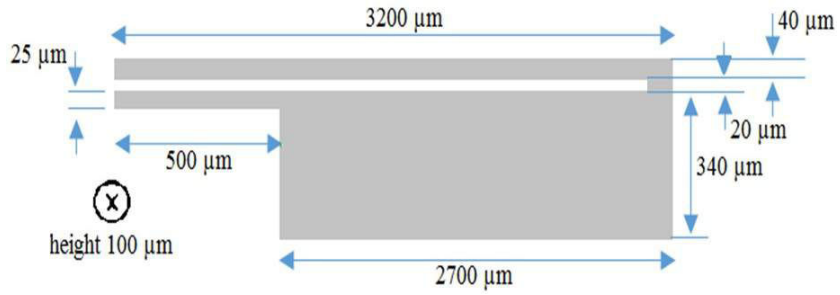

FIGURE *3.5: Dimensions for the U-shaped actuator in the modeling, simulations and experiments.*

Most of the physical properties of doped silicon are dependent on the temperature and the doping concentration. The thermal conductivity K_p of silicon decreases with temperature [45]. It also decreases for thin layers and for high impurity concentration [3]. The specific heat C_p of silicon increases with temperature [99]. The electrical resistivity ρ_0 of silicon is also thermally dependent, its evolution with doping concentration and temperature is clarified in [78].

A simplifying assumption considering a constant value for these properties is taken. This hypothesis allowed using the analytical solution of the electrothermal model to simulate the temperature distribution in the actuator.

In the other side, the expansion coefficient α is considered to be thermally dependent in the analytical calculation (3.43) and FEM simulations. This consideration was taken into account because of the large variation of the expansion coefficient of silicon with temperature (from $2.568\mu m/(m\cdot K)$ at $300K$ to $4.258\mu m/(m\cdot K)$ at $1000K$). Yokada et al. in [98] have defined an equation for the thermal expansion coefficient of silicon with respect to temperature:

$$\alpha = 10^{-6}\left(3.725\left(1-e^{-5.88\cdot 10^{-3}(T-124)}\right)+5.548\cdot 10^{-4}T\right) \tag{3.54}$$

The physical properties used in the modeling and simulations have the following values: $T_s = 298.15\ K$, $\rho_d = 2330\ kg/m^3$, $C_p = 712\ J/K\cdot kg$, $K_p = 149\ W/m\cdot K$, $\rho_0 = 0.265\ \Omega mm$.

3.4.1 Electrothermal response

Introducing these dimensions and properties in the electrothermal model (3.40) allows calculating the temperature values at each point in the actuator with respect to time. Figure 3.6 shows evolution of the temperature distribution after applying a voltage difference of $15V$ at the anchors. The temperature distributions in Figure 3.6 is obtained directly from the analytical solution in (3.40).

Figure 3.7 shows the profile of the temperature distribution in the actuator at several instants between 0 and 1s. Analyzing Figures 3.6 and 3.7, different evolution rates of the temperature are observed in the three arms of the actuator. Figure 3.8 shows evolution of the average temperature of the hot arm, cold arm and flexure with respect to time.

Due to the lower width, the local Joule heating is higher in the flexure at the beginning. Thus, the initial temperature evolution is faster in the flexure, than in the hot and cold arms respectively. However, the temperature evolution rate of the flexure is limited by the cold temperature

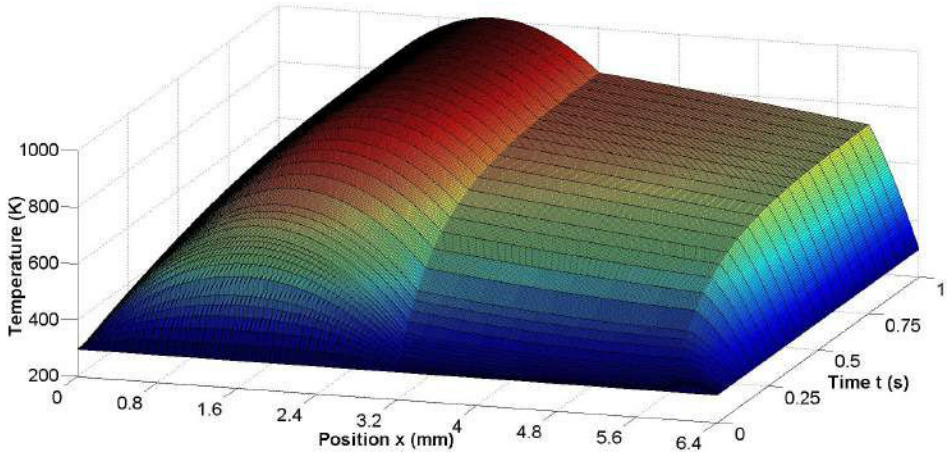

FIGURE *3.6: Evolution of the temperature distribution in the actuator obtained from the analytical solution after applying* 15*V voltage at the anchors.*

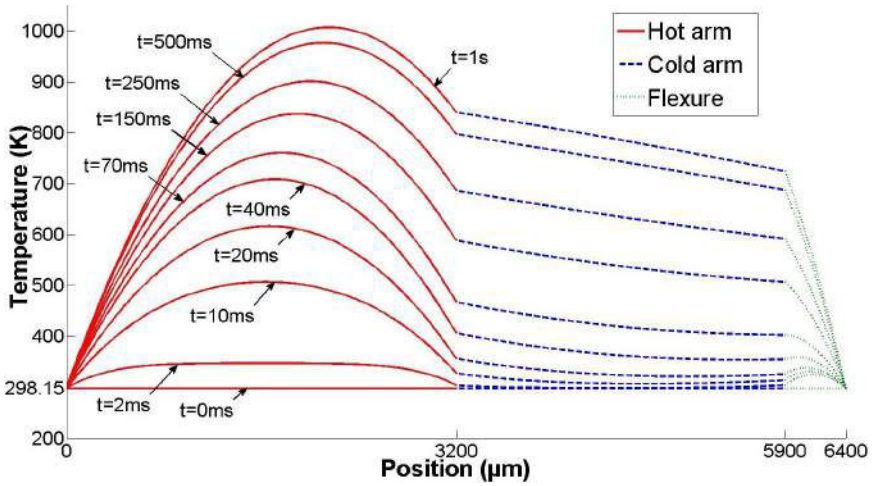

FIGURE *3.7: Temperature profiles in the actuator obtained analytically at 0, 2, 10, 20, 40, 70, 150, 250, 500 and 1000ms after applying* 15*V*.

of the anchor and the cold arm and its evolution rate starts to slow down (zoom in Fig. 3.8) consequently. From the beginning, the temperature in the hot arm grows rapidly and despite a larger width than the flexure arm, the temperature in the hot arm becomes quickly higher. After around 100 ms, the temperature in the hot arm is closer to the steady state and its evolution rate becomes highly reduced whereas the temperatures in the cold and the flexure arms continue to rise until their steady state.

In result, the evolution rate of the temperature in the hot arm is higher than the cold side (cold and flexure arms) at the beginning while it is slower while getting closer to the steady state.

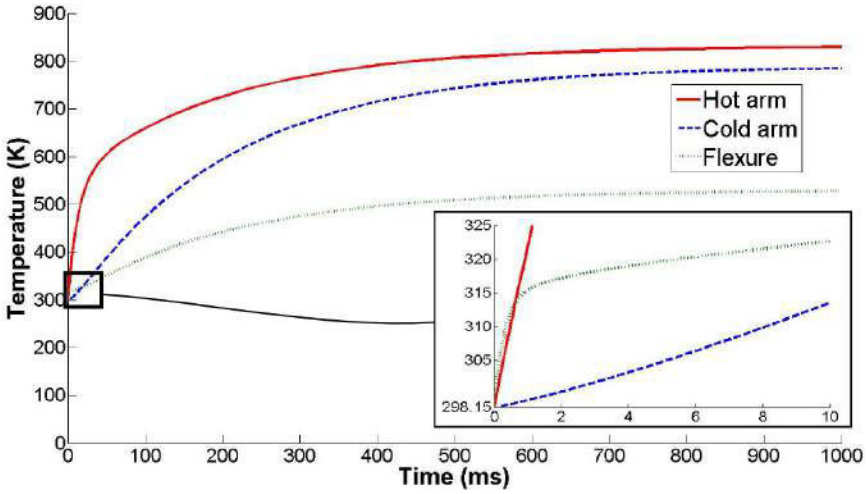

FIGURE *3.8: Evolution of the average temperature with time in the three arms of the actuator after applying* 15*V voltage.*

A 3D FEM modeling is made using ANSYS and allows simulating the thermal distribution and the structural deformation of the actuator after applying electrical voltage. The element used in the simulation SOLID226 is selected to allow a thermal-electric-structural analysis. Convection and radiation are neglected and the physical properties and boundary conditions are the same as in the analytical modeling.

Evolution of the average temperature in the hot arm is considered as a comparison parameter of the electrothermal response between the analytical solution and FEM simulation. Figure 3.9 shows a comparison between the average temperature in the hot arm obtained from the analytical model and ANSYS for two applied voltages (15 and 18V).

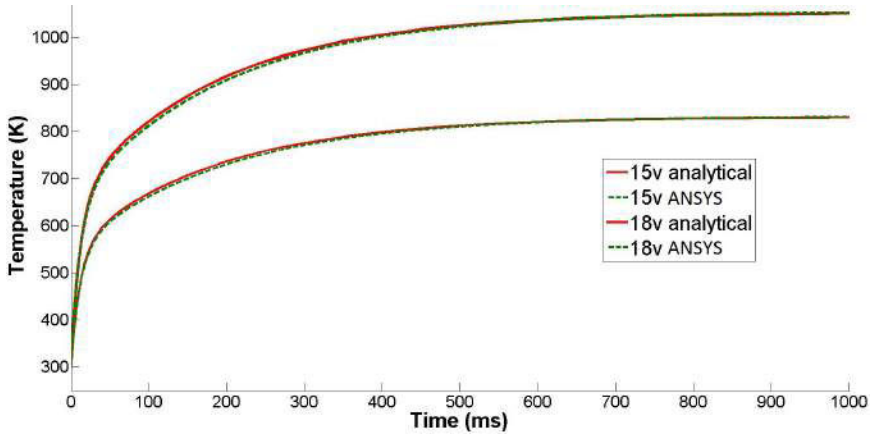

FIGURE *3.9: Comparison between the analytical model and ANSYS for the evolution of the average temperature in the hot arm.*

Figure 3.9 shows a very good agreement between the presented electrothermal solution and FEM simulations. The temperature distribution in the 3D FEM simulation is remarked to be homogeneous in the cross section along each arm while it is slightly non-homogeneous at the borders. This validates the one-dimensional simplifying assumption used in the electrothermal analytical model.

3.4.2 Mechanical response

In addition to FEM simulations, experiments are made on microfabricated actuators in order to validate the electro-thermo-mechanical models and coupling. The actuators are fabricated using the fabrication process explained later in Chapter 5. Displacement of the actuators in the experiments after applying voltages are recorded using a high speed camera. The experimental setup is explained in Chapter 5.

The shape of the actuator after fabrication is shown in Figure 3.10. The active parts of the actuator are realized in the device layer while the handle layer serves as a support of the whole device. The intermediate SiO_2 layer is an electrical insulator, it allows separating the anchor pads electrically.

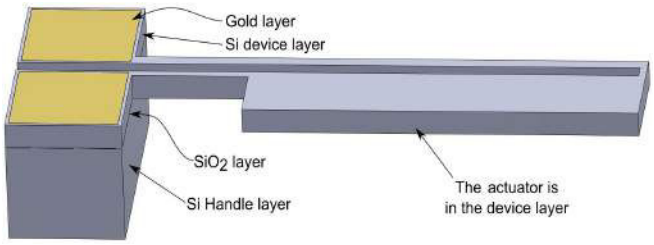

FIGURE *3.10: Layers of the microfabricated actuator.*

The displacement of the actuator after applying the different voltages is recorded on videos, and is then measured using Phantom cine viewer software. Figure 3.11.a shows the top of a fabricated U-shaped actuator in the experiments, where the actuator is in the rest position where no electrical input is applied. Figure 3.11.b shows the actuator during displacement after applying electricity. The displacement is then measured with respect to the reference position defined at rest.

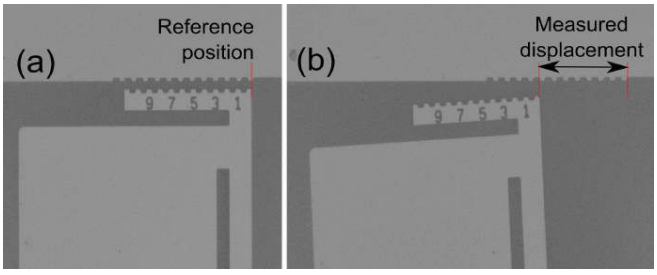

FIGURE *3.11: Shape of the actuator at the rest position (a) and during displacement (b) in the videos.*

Figure 3.12 shows the displacement curves of the actuator with respect to time obtained from the analytical models, FEM simulations and experiments. Displacement curves are shown for two applied voltages ($15V$ and $18V$).

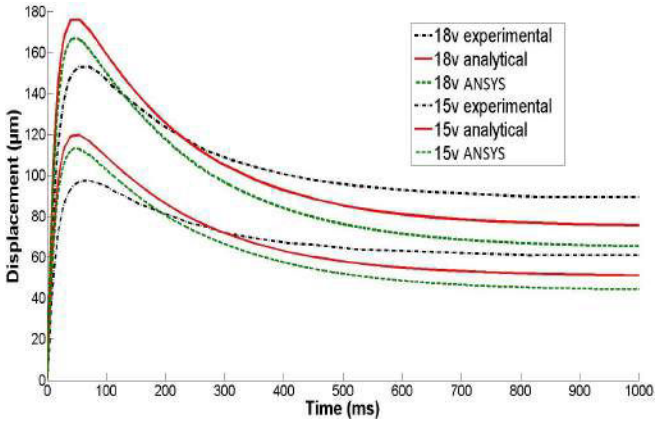

FIGURE *3.12: Comparison between the analytical model, ANSYS and experiments for the displacement curves at the tip of the actuator.*

Figure 3.12 shows an important overshoot of displacement of the actuator before reaching a steady state position. The transient shape of displacement is due to the variation of the evolution rate of temperature distribution on the two sides of the actuator as shown in Figure 3.6, 3.7 and 3.8.

Furthermore, the thermal expansion in each side is related to the temperature distribution (3.43) and the displacement is an image of the expansion difference (3.52). Figure 3.13 shows evolution of the thermal expansion calculated analytically in each arm, in the cold side (cold arm & flexure) of the actuator and the expansion difference between hot and cold sides.

As shown in Figure 3.13, the expansion difference has the same overshoot behavior as the displacement which implies that the dynamic behavior is related to the temperature evolution and not to the mechanical part.

In the other side, Figure 3.12 showed slight differences between the curves of the analytical models, simulations and experiments. The displacement curves of the analytical models and the FEM simulations have the same shapes but with a small shift between the two theoretical curves (less than 15%). Consequently, as there's a good agreement in terms of the electrothermal response as shown in Figure 3.9 and as the displacement is equivalent to the expansion difference (Figure 3.13) which is an image of the temperature distribution, then the difference in the calculated displacement returns mostly to the thermo-mechanical model.

This difference may return to the negligence of the shear force and the one dimensional simplification in the analytical calculation. The different arms in the actuator are considered as lines and there is an uncertainty in the calculation particularly at the connection between arms. In addition, the slightest difference in the electrothermal model is amplified in the displacement calculation due to the amplifying effect of the structure.

In the other side, there is a difference in the shape of the displacement curves between the calculated and experimental results as shown in Figure 3.12. Experiments show a less signif-

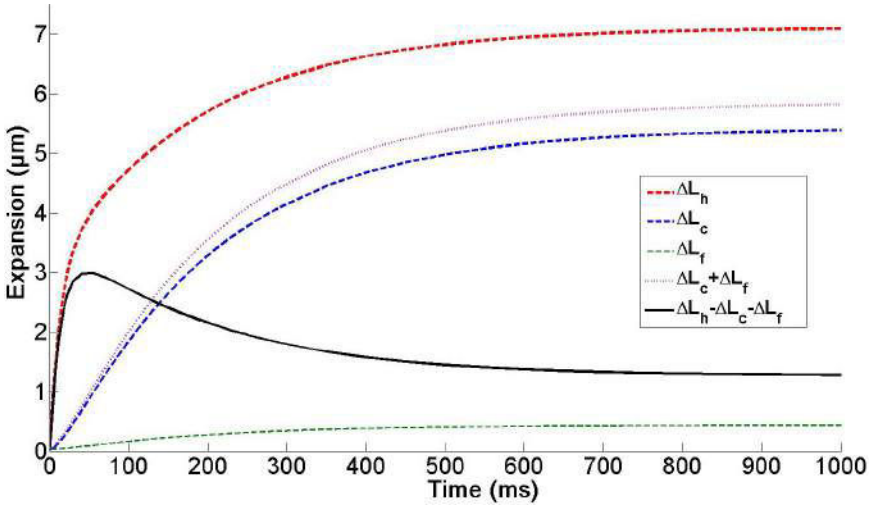

FIGURE *3.13: Thermal expansion of the hot, cold and flexure arms, cold side and expansion difference between both sides of the actuator after applying a voltage of* $15V$.

icant difference between the overshoot and the final position. This difference may exist due to the assumptions taken in the calculation (negligence of convection and radiation, boundary conditions etc.), the uncertainty in the physical properties and the thermal dependence of the physical properties of silicon especially in the steady state where the actuator is overheated.

In result, the analytical models presented in this paper show a good agreement with the results of the FEM simulations and experiments. An almost perfect agreement is noted in terms of the transient electrothermal response between the analytical solution and FE simulation despite the 1D simplification of the analytical model.

Less agreement is noted in the calculated displacement. A small shift between the displacement curves is noted with the FEM simulation results and a slight difference in the shape of these curves is noted with the experimental results.

Originality of the electrothermal analytical model is that it provides an exact solution of the hybrid PDEs that describe the electrothermal behavior of the three arms of the actuator. The calculation method can be extended to any number of connected hybrid PDEs and evidently for other defined boundary conditions. The cooling cycle can be modeled also using the analytical modeling by canceling the Joule heating term in the electrothermal equation and introducing the final temperature distribution in the heating cycle as the initial temperature distribution in the cooling cycle.

The presented modeling opens up important perspectives in terms of the modeling, design and optimization of the actuator. For the modeling, several development axes are possible such as the modeling of the cooling cycle, free and charged displacements with external forces, consideration of phenomena neglected in the present approach (convection or radiation, different boundary conditions, temperature dependence of the properties, etc).

3.5 Design and optimization

The dynamic behavior of the U-shaped actuator was investigated in the previous sections. Analytical models was presented which relate the electrical input and the applied load to the displacement passing by the temperature distribution. These models was validated by comparing it with the FEM simulations and experiments. The obtained expressions show clearly the influence of the different dimensions and properties on the electrothermal behavior and the displacement of the actuator. These expressions can be used for the design and the dimensioning of the U-shaped actuator.

The purpose of this section is to provide key elements for the design of the U-shaped actuator based on the analytical models. Firstly, the maximal voltage that can be applied on the actuator is calculated based on the maximal temperature allowed to be reached. After that, a new formulation of the dimensions is adopted in order to present more clearly their influence and the characteristic curve of the actuator. The influence of the different properties and dimensions on the performance of the actuator is then clarified. Finally, a design method is proposed that ensures obtaining the desired performance of the actuator in terms of the force and displacement.

3.5.1 Maximal voltage

As it has been recognized that the displacement of the actuator is related to the temperature distribution, the higher is the temperature, the higher is the displacement. However, the temperature in the actuator must not exceed a maximal limit that is defined with respect to the material. Otherwise, high temperature leads to a degradation of the material properties, a plastic deformation of the actuator, fracture at the weak points, etc..

Introducing the boundary and continuity conditions (3.17) in the steady state temperature expressions (3.16), the different constants d_{h1}, d_{h2}, d_{c1}, d_{c2}, d_{f1} and d_{f2} are determined and the steady state temperature distribution is obtained. These expressions show clearly the influence of the different parameters on the temperature distributions (including the dimensions, voltage, resistivity and conductivity).

Analyzing these expressions, an important conclusion is noticed. The maximal temperature T_{max} reached in the steady state for an applied voltage is independent of the actuator dimensions. The expression of T_{max} is as follows:

$$T_{max} = T_\infty + \frac{V^2}{8\rho_0 K_p} \tag{3.55}$$

In contrast, position of the maximal temperature point at the steady state x_{max} is dependent only on the actuator dimensions. This point exists generally in the hot arm while it's possible to exist in the cold arm in some extreme cases. The expression of x_{max} in the two cases is as follows:

$$\begin{cases} x_{max} = \dfrac{l_h}{2} + \dfrac{A_h}{2}\left(\dfrac{l_c}{A_c} + \dfrac{l_f}{A_f}\right) & \dfrac{l_f}{A_f} + \dfrac{l_c}{A_c} < \dfrac{l_h}{A_h} \\ x_{max} = l_h + \dfrac{A_c}{2}\left(-\dfrac{l_h}{A_h} + \dfrac{l_c}{A_c} + \dfrac{l_f}{A_f}\right) & \dfrac{l_f}{A_f} + \dfrac{l_c}{A_c} > \dfrac{l_h}{A_h} \end{cases} \tag{3.56}$$

Based on the above, the maximal temperature expression allows defining a limitation V_{max} on the voltages, where V_{max} is the maximal voltage allowed before reaching the maximal temperature T_{max}.

$$V_{max} = \sqrt{8\rho_0 K_p (T_{max} - T_\infty)} \tag{3.57}$$

The value of V_{max} must be respected in the cases where the actuator is powered on for long time and the feeding time may exceed the response time.

In the other side, the feeding time is related to the task requirement and the responsiveness and capacity of the actuator. An optimal feeding time is when the actuator can do the task in the time between the start of feeding and the peak of displacement. In this case, the actuator can output a maximum of performance without overheating the different arms. During this time, the temperature has not yet reached its maximum, thus, we can increase the voltage above the limits imposed at the steady state. This allows reaching higher performance of the actuator.

3.5.2 Characteristic curve of the actuator

Improvement of the performance of the actuator is related to the improvement of its output, which is expressed in terms of the displacement in the models. The expression of the displacement is developed in the following in order to extract the characteristic curve of the actuator and to show clearly the influence of the different dimensions and properties on the performance of the actuator.

The expression of the displacement is given in (3.52). The constants K_1 and K_2 can be expressed using another formulation which allows separating the general length l and width w of the arms from the ratios of widths and length c, f, γ and a. The different lengths and widths in this case have the following values:

$$\begin{array}{llll} l_h = l & l_c = (1-a)l & l_f = a \cdot l & \\ w_h = w & w_c = c \cdot w & w_f = f \cdot w & g = \gamma \cdot w \end{array} \tag{3.58}$$

Considering the new variables, the displacement can be expressed as follows:

$$d = \frac{l}{w} K_1' \Delta - \frac{1}{E} \frac{l^3}{bw^3} K_2' F \tag{3.59}$$

where K_1' and K_2' are dependent only on a, c, γ and f. K_1' and K_2' are obtained as follows:

$$K_1' = \begin{pmatrix} 1 & 0 & 0 \end{pmatrix} \begin{pmatrix} \delta_{XX}' & \delta_{YX}' & \delta_{MX}' \\ \delta_{XY}' & \delta_{YY}' & \delta_{MY}' \\ \delta_{XM}' & \delta_{YM}' & \delta_{MM}' \end{pmatrix}^{-1} \begin{pmatrix} \delta_{Xf}' \\ \delta_{Yf}' \\ \delta_{Mf}' \end{pmatrix} \tag{3.60a}$$

$$K_2' = -12 \begin{pmatrix} \delta_{Xf}' & \delta_{Yf}' & \delta_{Mf}' \end{pmatrix} \begin{pmatrix} \delta_{XX}' & \delta_{YX}' & \delta_{MX}' \\ \delta_{XY}' & \delta_{YY}' & \delta_{MY}' \\ \delta_{XM}' & \delta_{YM}' & \delta_{MM}' \end{pmatrix}^{-1} \begin{pmatrix} \delta_{Xf}' \\ \delta_{Yf}' \\ \delta_{Mf}' \end{pmatrix} - 12\delta_{Ff}' \tag{3.60b}$$

The different terms δ' in (3.60) (δ'_{XX}, δ'_{YY}, δ'_{MM}, δ'_{XY}...) are equivalent to the terms δ (δ_{XX}, δ_{YY}, δ_{MM}, δ_{XY}...) in (3.47), (3.49) and (3.51). The terms δ' are related only to the ratios a, c, γ and f. Some terms are neglected in the δ' expressions due to the relative difference between the length and the width.

$$\delta'_{XX} = \frac{(1+2\gamma+f)^2 a}{4f^3} + \frac{(1+2\gamma+c)^2(1-a)}{4c^3} + \frac{a}{12f} + \frac{1-a}{12c} + \frac{1}{12} \tag{3.61a}$$

$$\delta'_{YY} = \frac{a^3}{3f^3} + \frac{1-a^3}{3c^3} + \frac{1}{3} \tag{3.61b}$$

$$\delta'_{MM} = \frac{a}{f^3} + \frac{1-a}{c^3} + 1 \tag{3.61c}$$

$$\delta'_{XY} = \frac{(1+2\gamma+f)a^2}{4f^3} + \frac{(1+2\gamma+c)(1-a^2)}{4c^3} \tag{3.61d}$$

$$\delta'_{XM} = \frac{(1+2\gamma+f)a}{2f^3} + \frac{(1+2\gamma+c)(1-a)}{2c^3} \tag{3.61e}$$

$$\delta'_{YM} = \frac{a^2}{2f^3} + \frac{1-a^2}{2c^3} + \frac{1}{2} \tag{3.61f}$$

$$\delta'_{Xf} = \frac{(1+2\gamma+f)(2a-a^2)}{4f^3} + \frac{(1+2\gamma+c)(1-a)^2}{4c^3} \tag{3.61g}$$

$$\delta'_{Yf} = \frac{3a^2-2a^3}{6f^3} + \frac{1-3a^2+2a^3}{6c^3} \tag{3.61h}$$

$$\delta'_{Mf} = \frac{2a-a^2}{2f^3} + \frac{(1-a)^2}{2c^3} \tag{3.61i}$$

$$\delta'_{Ff} = \frac{-3a(1-a)-a^3}{3f^3} - \frac{(1-a)^3}{3c^3} \tag{3.61j}$$

Equation (3.59) shows that the displacement is related linearly to the two actions: arms expansion difference Δ and applied load F. In the other side, the different arms expansion Δl_h, Δl_c and Δl_f are calculated by introducing the temperature expressions (3.40) in the expansion equation (3.43).

$$\Delta l_h(t) = \Delta l_{hss} - \alpha \sum_{n=1}^{\infty} \frac{C_{hn}}{\lambda_n} \left(\cos(\lambda_n l_1 + \varphi_{hn}) - \cos(\varphi_{hn})\right) e^{-\alpha_p \lambda_n^2 t} \tag{3.62a}$$

$$\Delta l_c(t) = \Delta l_{css} - \alpha \sum_{n=1}^{\infty} \frac{C_{cn}}{\lambda_n} \left(\cos(\lambda_n l_2 + \varphi_{cn}) - \cos(\lambda_n l_1 + \varphi_{cn})\right) e^{-\alpha_p \lambda_n^2 t} \tag{3.62b}$$

$$\Delta l_f(t) = \Delta l_{fss} - \alpha \sum_{n=1}^{\infty} \frac{C_{fn}}{\lambda_n} \left(\cos(\lambda_n l_3 + \varphi_{fn}) - \cos(\lambda_n l_2 + \varphi_{fn})\right) e^{-\alpha_p \lambda_n^2 t} \tag{3.62c}$$

Noting that α is considered to be constant in the calculation in order to simplify the problem.

The terms Δl_{hss}, Δl_{css} and Δl_{fss} correspond to the length expansions of the different arms at the steady state. They are obtained by introducing the steady state temperature expressions (3.16) in the expansion equation (3.43).

$$\Delta l_{hss} = \frac{\alpha V^2 l}{12\rho_0 K_p} \frac{cf\,(3ac+cf+3f(1-a))}{(ac+cf+f(1-a))^2} \tag{3.63a}$$

$$\Delta l_{css} = \frac{\alpha V^2 l}{12\rho_0 K_p} \frac{f^2(1-a)^3+3(acf+cf^2)(1-a)^2+6ac^2f(1-a)}{(ac+cf+f(1-a))^2} \tag{3.63b}$$

$$\Delta l_{fss} = \frac{\alpha V^2 l}{12\rho_0 K_p} \frac{a^2c\,(ac+3fc+3f(1-a))}{(ac+cf+f(1-a))^2} \tag{3.63c}$$

In result, the arms expansion difference consists of a steady state part and a transient part:

$$\Delta(t) = \Delta_{ss} + \Delta_t(t) \tag{3.64}$$

The transient part $\Delta_t(t)$ is equivalent to:

$$\begin{aligned}\Delta_t(t) = \alpha \sum_{n=1}^{\infty} \Bigg[&\frac{C_{hn}}{\lambda_n} \left(\cos(\varphi_{hn}) - (1+\frac{A_h}{A_c})\cos(\lambda_n l_1 + \varphi_{hn}) \right) \\ &+ \frac{C_{fn}}{\lambda_n} \left(\cos(\lambda_n l_3 + \varphi_{fn}) + (\frac{A_f}{A_c} - 1)\cos(\lambda_n l_1 + \varphi_{fn}) \right) \Bigg] e^{-\alpha_p \lambda_n^2 t}\end{aligned} \tag{3.65}$$

The steady state part Δ_{ss} is equivalent to:

$$\Delta_{ss} = \frac{\alpha}{\rho_0 K_p} l K_3' V^2 \tag{3.66}$$

where K_3' is only dependent on a, c, and f and is equivalent to:

$$K_3' = \frac{a^3(f^2-c^2) - 3(a^2-a)(f+cf)(f-c) + c^2f^2 - f^2}{12\,(ac+cf+f(1-a))^2} \tag{3.67}$$

Introducing (3.64) in the displacement equation (3.59), the displacement consists also of a transient part and steady state part:

$$d(t) = d_{ss} + d_t(t) \tag{3.68}$$

The transient part of the displacement $d_t(t)$ is equivalent to:

$$d_t(t) = \frac{l}{w} k_1' \Delta_t(t) \tag{3.69}$$

The steady state displacement d_{ss} is equivalent to:

$$d_{ss} = \frac{\alpha}{\rho_0 K_p} \frac{l^2}{w} K_1' K_3' V^2 - \frac{1}{E} \frac{l^3}{bw^3} K_2' F \tag{3.70}$$

Equations (3.68), (3.69) and (3.70) show that the displacement is transient in response of a voltage step, while the impact of the force is quasistatic if static forces are applied.

Figure 3.14 shows evolution of the force-displacement characteristic curve of the U-shaped actuator at several instants after applying a constant voltage.

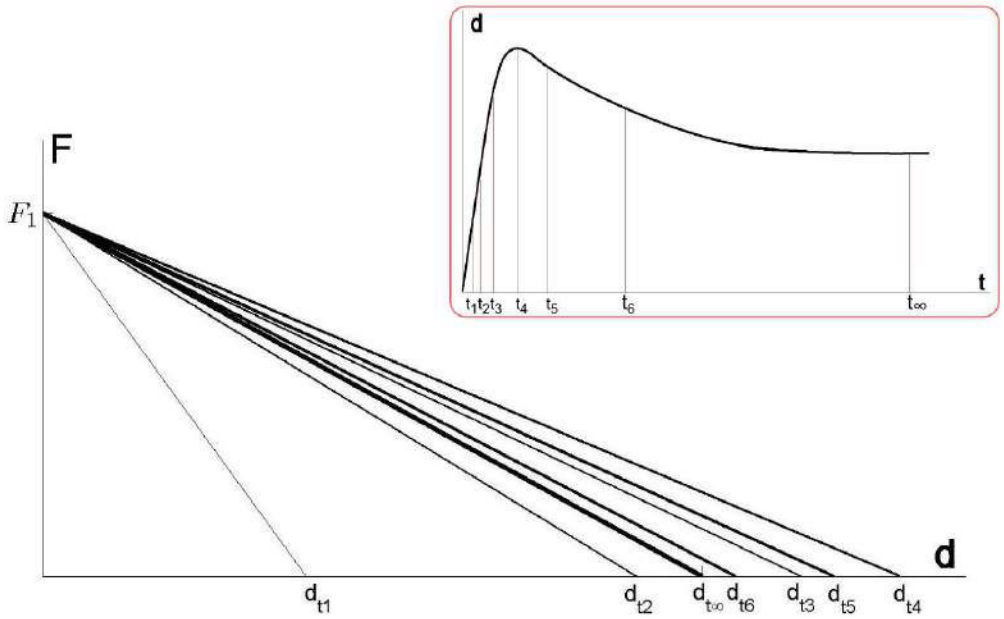

FIGURE *3.14: Evolution of the characteristic curves of the actuator at several instants after applying a constant voltage.*

The term F_1 in Figure 3.14 corresponds to the blocking force of the actuator at zero displacement while d_{t1} is the free displacement at $t = t_1$. For the other terms of the free displacement, $t_1 < t_2 < t_3 < t_4 < t_5 < t_6 < t_\infty$ as shown in the dynamic displacement curve.

From the modeling perspective, the output of the actuator is the displacement while the load is an input to the system beside the applied voltages. Due to the elastic structure of the actuator, the applied load generates a reverse displacement of the actuator according to its mechanical stiffness. In the cases where the elastic properties are not related to the temperature, the stiffness is related only to the Young's modulus and actuator dimensions. This conclusion is justified in the expression of the stiffness in (3.70) in the direction of the applied load ($E\frac{bw^3}{l^3}\frac{1}{K_2'}$).

This conclusion is verified also in Figure 3.14 where the blocking force remains constant during the transient phase. The dynamic of the actuator is related only to the dynamic of the temperature distribution in the different arms while the structure has an amplifying effect for the displacement and the stiffness is related only to the structure.

3.5.3 Influence of the parameters on the actuator's performance

The free displacement d_{free} and the blocking force F_{block} at the steady state are the two main characteristics of the actuator's performance. According to (3.70), d_{free} and F_{block} are equivalent to:

$$d_{free} = \frac{\alpha}{\rho_0 K_p}\frac{l^2}{w}K_1' k_3' V^2 \tag{3.71}$$

$$F_{block} = \frac{\alpha E}{\rho_0 K_p} b \frac{w^2}{l} \frac{K_1' K_3'}{K_2'} V^2 \tag{3.72}$$

Figure 3.15 shows the characteristic curve of the actuator at the steady state including the blocking force and free displacement expressions.

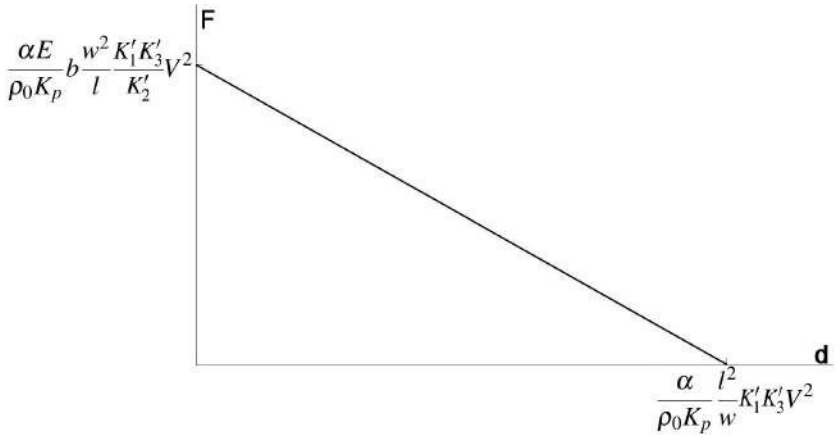

FIGURE *3.15: The characteristic curve of the actuator at the steady state including the blocking force and free displacement expressions.*

The expressions of d_{free} and F_{block} show clearly the influence of the different parameters on the actuator's performance. These parameters can be classified in 4 categories depending on their nature: electrical voltage (V), material properties (α, ρ_0, K_p and E), general dimensions (b, l and w) and the dimension ratios (a, c, γ and f).

In the following, the influence of each parameter on the main characteristics of the actuator (d_{free} and F_{block}) in the steady state is investigated.

In the other side, the main parameters characterizing the transient solution are the value of the displacement at the peak during overshoot of displacement d_{peak}, the time needed to reach the peak t_{peak} and the time needed to reach the steady state t_{ss}. Noting that, according to our simulations, the dimensions that optimize the steady state performance are not necessary the same that optimize the transient performance.

Regarding the complexity of the transient solution, the values of the transient parameters are obtained only numerically for a well defined dimensions and properties. Thus, the influence of the different parameters on the transient performance is not investigated in this chapter. This work is left for future developments.

3.5.3.1 Voltage and material properties

Returning to d_{free} and F_{block} expressions, the voltage V, the thermal expansion coefficient α, the resistivity ρ_0 and the conductivity K_p affect d_{free} and F_{block} in an equivalent way while the other parameters affect d_{free} and F_{block} differently.

The output of the actuator is related proportionally to the thermal expansion coefficient α. Thus, materials with higher α will have a better performance.

Idem, the output of the actuator is related proportionally to the square of the voltage and inversely proportional to the resistivity and conductivity. In contrast, this doesn't mean that the actuator has a better performance for lower resistivity and conductivity because the maximal allowable voltage V_{max} is proportional to the root square of ρ_0 and K_p as shown in (3.57). In result, the performance is the same for variable values of ρ_0 and K_p while the variation is in the voltage margin.

The Young's modulus E and the depth b have only an influence on the value of the blocking force. Higher Young's modulus for the material and depth for the actuator allow a higher proportionally blocking force. Noting that for high values of the Young's modulus E, the internal stresses are higher and the failure limits can be early reached.

3.5.3.2 General dimensions

The general length l and width w have an inverse influence on d_{free} and F_{block} values. The free displacement d_{free} is proportional to the square of l and inversely proportional to w while the blocking force F_{block} is proportional to the square of w and inversely proportional to l.

Figure 3.16 shows the influence of changing the general dimensions of the actuator (l, w, and b) on the characteristic curves. Noting that when changing l and w with the same ratio, the characteristic curve evolves in parallel with the same ratio.

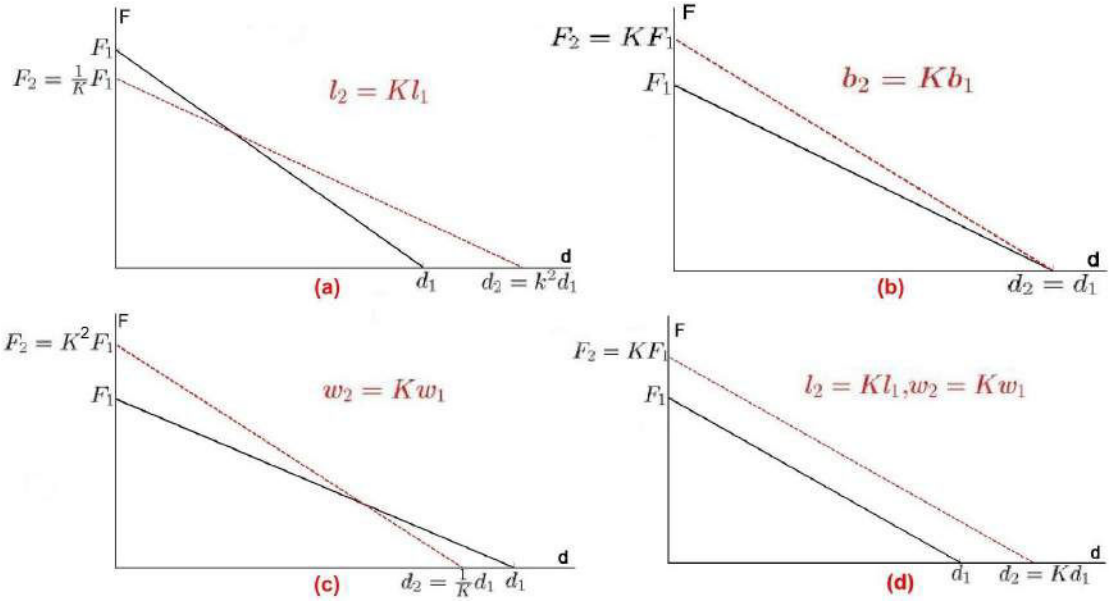

FIGURE *3.16: Influence of changing the general dimensions on the characteristic curve of the actuator: including the general length l (a), the depth b (b), the general width w (c) and l and w simultaneously with the same ratio of changing (d).*

Furthermore, relating the influence of the general length l on the free displacement and on the response time, we note that the two are proportional to the square of l. That means that

for higher length, the displacement is higher and the response time is higher but the speed of displacement is the same.

In the other side, one remark can be noted for the response time. As shown in (3.65), the transient solution is an infinite sum of exponentials with a time constant τ_n equivalent to:

$$\tau_n = \frac{1}{\alpha_p \lambda_n^2} \tag{3.73}$$

Further, analyzing the λ_n equation (3.22), we conclude that λ_n is inversely proportional to the general length l and is related to the dimension ratios a, c and f. Thus, the time response of the actuator is proportional to the square of the general length l and inversely proportional to the thermal diffusivity α_p. Physically, this means that the actuator is slower for higher length dimensions while it is faster for materials with higher thermal diffusivity.

3.5.3.3 Dimensions ratios

The last parameters that affect the actuator's performance are the dimension ratios. The influence of the dimension ratios is represented by K_1', K_2', K_3' in d_{free} and F_{block} expressions. The free displacement evolves with respect to $K_1'K_3'$ and the blocking force evolves with respect to $K_1'K_3'/K_2'$. The ratio γ is not considered hereinafter in order to simplify the problem (γ is set to zero).

The dependency of K_1', K_2' and K_3' on three parameters (a, c and f) makes difficult the representation of the state of $K_1'K_3'$ and $K_1'K_3'/K_2'$ in a single plot. In the following, 3 plots are presented showing evolution of the free displacement (or $K_1'K_3'$) with respect to the dimension ratios a, c and f, each plot represents the evolution $K_1'K_3'$ with respect to two dimension ratios for a constant value of the third one. Figures 3.17, 3.18 and 3.19 show evolution of $K_1'K_3'$ for a constant ratio $f = 1$, $a = 0.1$ and $c = 10$ respectively.

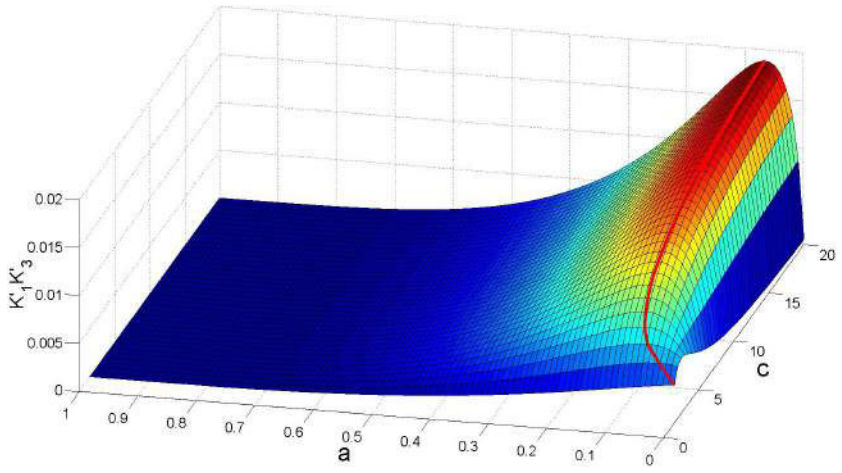

FIGURE *3.17: Evolution of $K_1'K_3'$ with respect to c and a for a constant ratio $f = 1$.*

Figures 3.17 and 3.18 show that the free displacement is always higher for higher c values. This conclusion is logical since higher width of the cold arm with respect to that of the hot arm

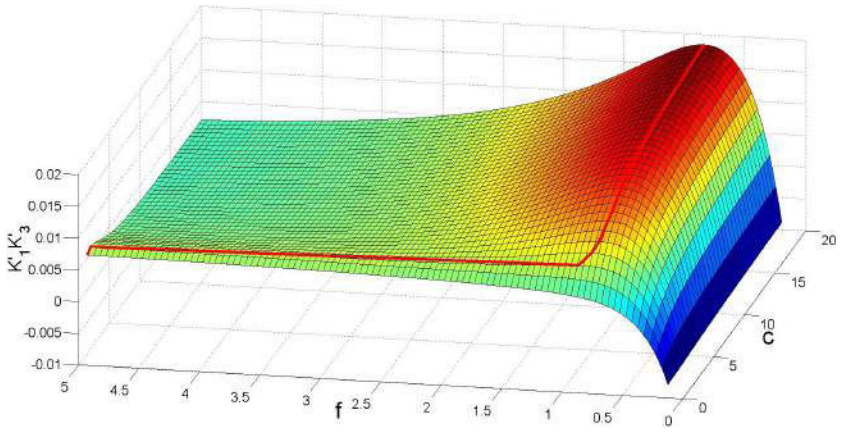

FIGURE *3.18: Evolution of $K_1'K_3'$ with respect to c and f for a constant ratio $a = 0.1$.*

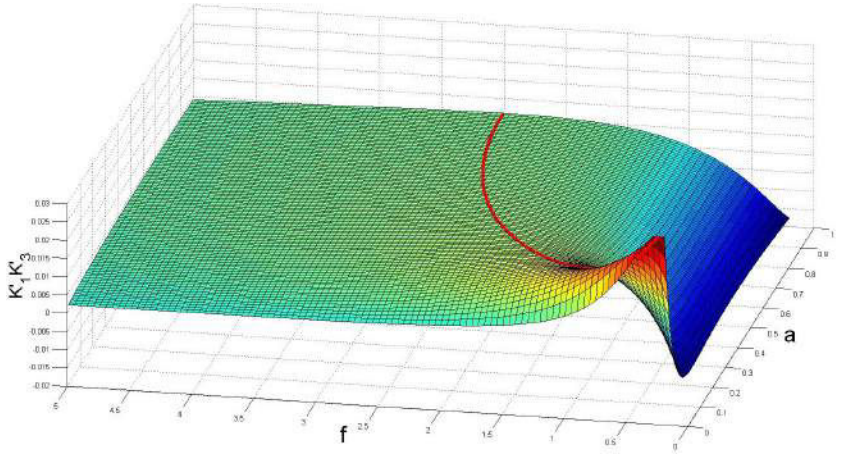

FIGURE *3.19: Evolution of $K_1'K_3'$ with respect to a and f for a constant ratio $c = 10$.*

implies that the cold side of the actuator is less heated and the length expansion becomes higher in the hot arm.

Figures 3.17, 3.18 and 3.19 show that for each value of c, there are some determined values of a and/or f that maximize the displacement. This maximum is represented by the red line in the three figures. The red line in Figure 3.17 represents the maximum of $K_1'K_3'$ for $f = 1$, the line in Figure 3.18 represents the maximum for $a = 0.1$ while the line in Figure 3.19 represents the maximum with respect to a and f simultaneously for $c = 10$.

Figure 3.20 shows the values of a and f that allow reaching the maximum of displacement for different values of c. The curves of Figure 3.20 correspond to the projection for the red line in Figure 3.19 on the $a - f$ plane but for different values of c.

As shown in Figure 3.20, the curves are nearly similar where a slight difference is remarked between the curves for the different values of c. These curves constitute a key element for optimizing the design of the actuator in order to obtain a maximal free displacement at the steady state. These dimensions are called the max-free dimensions in the following.

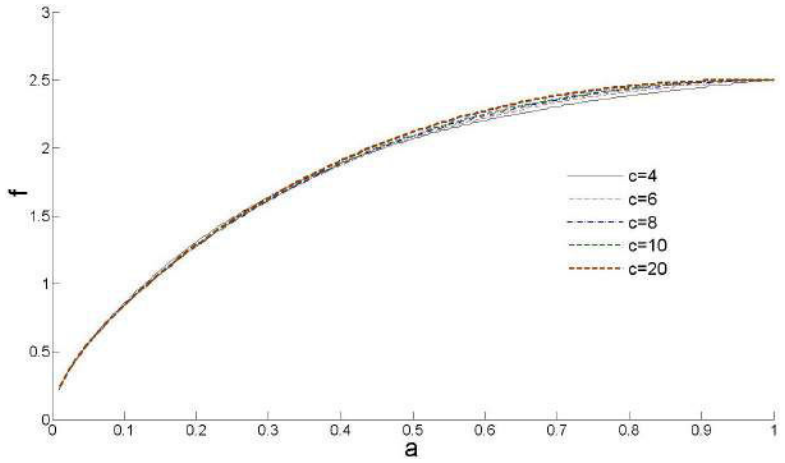

FIGURE *3.20: Values of the ratios f and a maximizing the free displacement d_{free} for different values of c ratio.*

However, the values of the free displacement at the max-free dimensions are not the same for the different values of c. Figure 3.21 shows evolution of $K_1'K_3'$ at the max-free dimensions for different values of c. The curves are visualized with respect to a while the value of the corresponding f is concluded from the max dimensions.

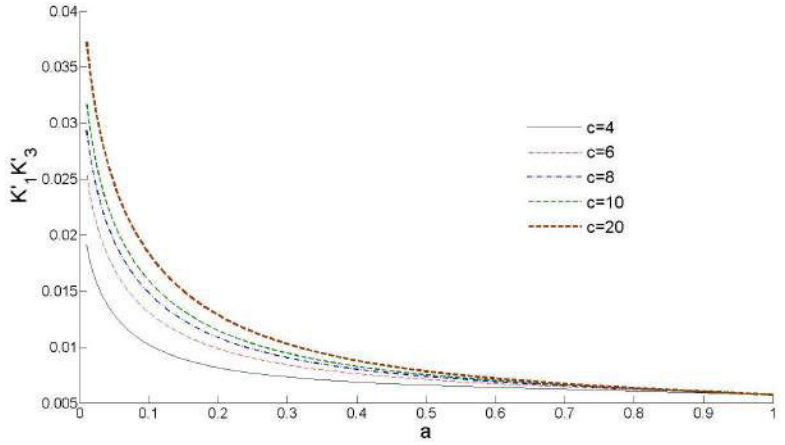

FIGURE *3.21: Evolution of $K_1'K_3'$ at the max-free dimensions for different values of c and with respect to a.*

Two conclusions can be extracted from Figure 3.21. The first one is that the free displacement is higher for higher values of c which confirms the previous conclusion from Figures 3.17 and 3.18.

The second conclusion is that the free displacement is higher for lower values of a and f consequently. This means that the free displacement is higher when the length and width of the flexure have the smallest possible values. However, the reduction of the flexure dimensions increase the possibility of failure at the flexure due to the fragility with too small dimensions.

In the other side, the blocking force is related proportionally to $K'_1K'_3/K'_2$. Idem, 3 plots are presented hereinafter that show evolution of the blocking force (or $K'_1K'_3/K'_2$) with respect to the dimension ratios a, c and f. Figures 3.22, 3.23 and 3.24 show evolution of $K'_1K'_3/K'_2$ for a constant ratio $f = 1$, $a = 0.1$ and $c = 10$ respectively.

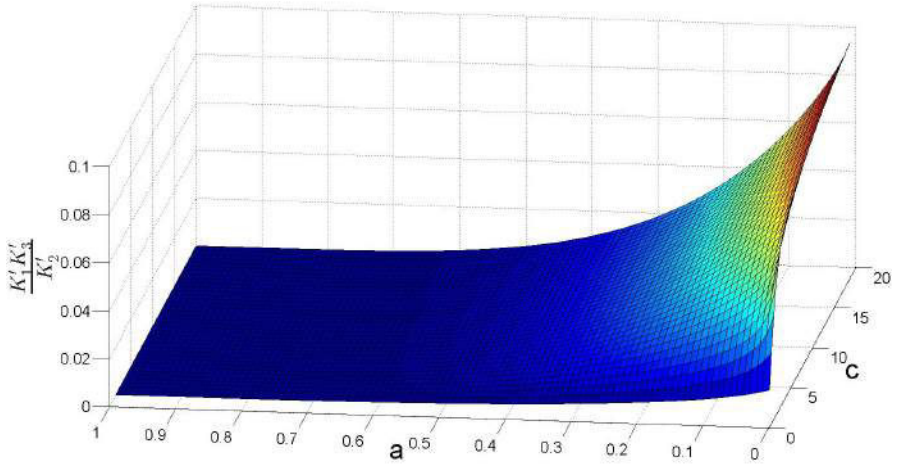

FIGURE *3.22: Evolution of $K'_1K'_3/K'_2$ with respect to c and a for a constant ratio $f = 1$.*

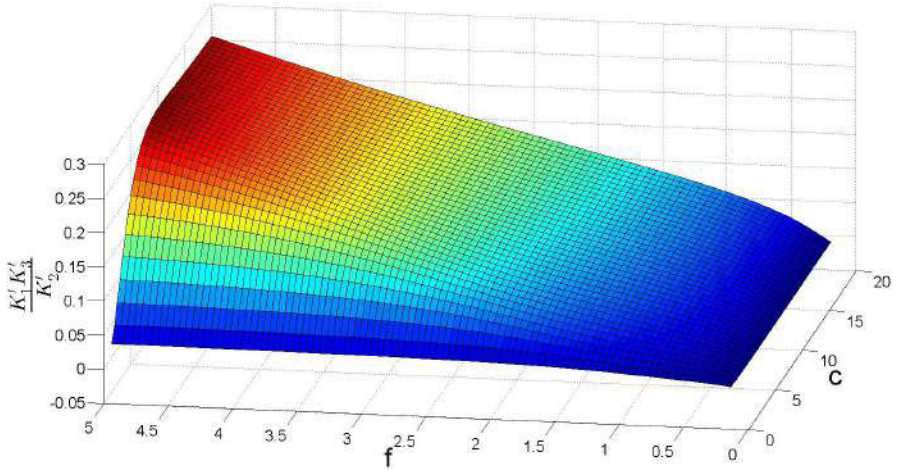

FIGURE *3.23: Evolution of $K'_1K'_3/K'_2$ with respect to c and f for a constant ratio $a = 0.1$.*

Analyzing these figures, we conclude that the blocking force is more important for higher values of c as shown in Figures 3.22 and 3.23, for higher values of f as shown in Figures 3.23 and 3.24 and for lower values of a as shown in Figures 3.22 and 3.24. This implies that the stiffness at the tip of the actuator is more important when the flexure is shorter and wider.

In result, d_{free} and f_{block} are more important when the cold arm is wider and the flexure is shorter. In contrast, the width of the flexure has an inverse influence on the blocking force and free displacement: d_{free} is more important for lower flexure width while f_{block} is more important for higher flexure width.

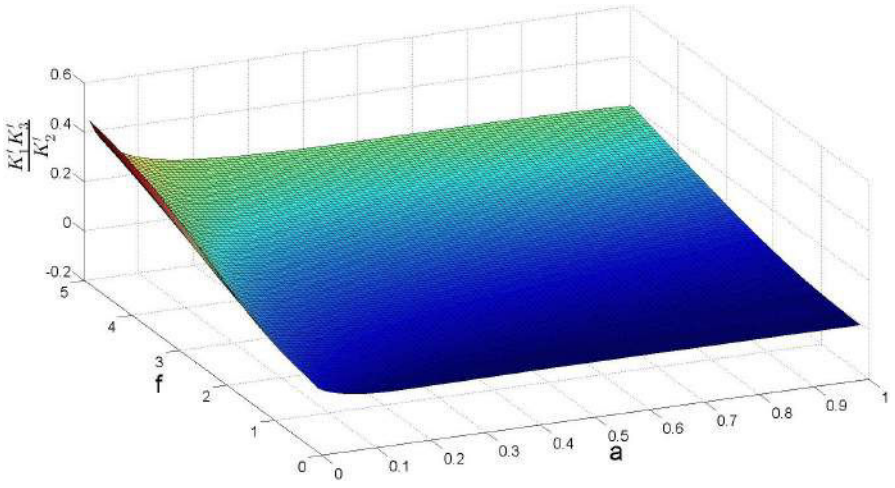

FIGURE *3.24: Evolution of $K_1' K_3' / K_2'$ with respect to a and f for a constant ratio $c = 10$.*

Table 3.1 summarizes the influence of the different parameters and dimensions of the actuator on its performance at the steady state. The arrows ↗ and ↘ and the power index have the same significance as in Table 2.2.

TABLE *3.1: Influence of the different parameters and dimensions of the actuator on its performance at the steady state.*

		d_{free}	F_{block}
E		—	$\nearrow^1$
α		$\nearrow^1$	$\nearrow^1$
ρ_0		$\searrow^1$	$\searrow^1$
K_p		$\searrow^1$	$\searrow^1$
V		$\nearrow^2$	$\nearrow^2$
b		—	$\nearrow^1$
l	a, c & f are constants	$\nearrow^2$	$\searrow^1$
w		$\searrow^1$	$\nearrow^2$
l+w		$\nearrow^1$	$\nearrow^1$
l+w+b		$\nearrow^1$	$\nearrow^2$
c		↗ Fig. 3.17 & 3.18	↗ Fig. 3.22 & 3.23
a		max Fig. 3.20	↘ Fig. 3.22 & 3.24
f			↗ Fig. 3.23 & 3.24
(a & f) max Fig. 3.20		↘ Fig. 3.21	

3.5.4 Design methodology of the actuator

General key elements for the design of the actuator are presented in the following. These elements allow choosing the various dimensions and providing the desired performance. An un-

certainty range must be taken on the obtained dimensions due to the uncertainty in the material properties and their thermal dependency. After that, a design methodology is presented to choose the dimensions of the actuator in the multistable module (Chapter 4).

The function of the actuator is to provide the desired force and displacement. These two properties define the performance of the actuator. The design must ensure that the actuator is able to output the needed force and the desired displacement d_d at a defined instant t_d. As the effect of the load F is considered in the expression of the displacement d ((3.68) and (3.70)), the design condition can be expressed as follows:

$$d \geq d_d \tag{3.74}$$

This design condition is visualized in Figure 3.25 in terms of the characteristic curves. The characteristic curve after $t = t_d$ must be above the desired performance.

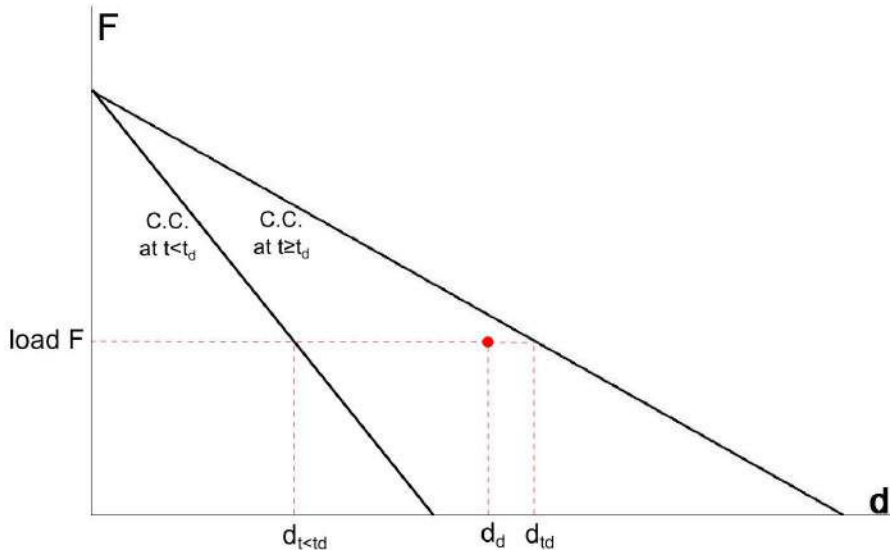

FIGURE *3.25: Characteristic curves of the actuator before and after $t = t_d$. The loaded displacement after $t = t_d$ must be more important than the desired displacement d_d.*

Putting the expression of the displacement at a defined instant in the last equation (3.74) leads to a condition on the different parameters and dimensions that allow obtaining the desired force and displacement. The instant at which the actuator must output the desired performance vary between a system and the other with respect to the specific task. In our design, we consider that the actuator must provide the desired properties at the steady state.

$$d_{ss} \geq d_d \tag{3.75}$$

As explained before, the actuator output higher performance before reaching the steady state without overheating the different arms. Afterwards, if the task needs a feeding time less than the time before reaching the steady state, the design can be calculated on the basis of a higher performance in terms of the arms expansion difference and the maximal voltages as clarified in Figure 3.26.

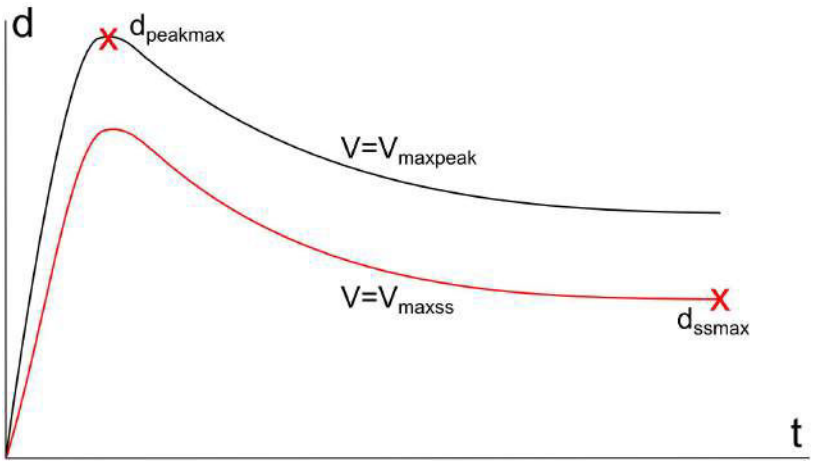

FIGURE *3.26: The maximal performance that can be reached in terms of the displacement. When the output is considered at the steady state, the voltage that can be applied is lower and the performance is less important. When the output is considered at the peak of the overshoot, the maximal allowable voltage is higher due to the lower temperature and the performance is more important.*

Until now, the design in the transient phase relies on the complex expressions of the temperature and displacement obtained in the modeling. The design in the transient phase constitutes a part of the future works.

However, despite that the influence of the different parameters and the design are investigated only in the steady state, the performance at the steady state gives a very good idea about the performance of the actuator and its evolution in the transient phase.

Returning to the design, the output of the actuator is dependent of the electrical input. The maximal performance at the steady state is reached when the maximal voltage V_{max} is applied (3.57). The maximal voltage V_{max} is defined with respect to the maximal temperature ΔT_{max} allowed to be reached. The design is investigated when V_{max} is applied in order to reduce the parameters, in this case, the expression of d_{ss} is as follows:

$$d_{ss} = 8\alpha \frac{l^2}{w} k_1' k_3' \Delta T_{max} - \frac{l^3}{Ebw^3} K_2' F \tag{3.76}$$

where $\Delta T_{max} = T_{max} - T_{\infty}$.

Introducing the expression of d_{ss} in (3.75) leads to the following condition:

$$l^2 \frac{8\alpha k_1' k_3' \Delta T_{max}}{w} - l^3 \frac{K_2' F}{Ebw^3} - d_d \geq 0 \tag{3.77}$$

The last equation is very important in terms of the design. It allows defining some constraints on the dimensions, after which, the actuator is able to output the desired force and displacement. It allows also defining the expression of the length that maximizes the output. In order to clarify the problem, Figure 3.27 shows evolution of $(d_{ss} - d_d)$ in terms of the length.

The expression of $(d_{ss} - d_d)$ is a 3^{rd} degree polynomial function in terms of the length l. It has 2 extremums at $l = 0$ and $l = l_{max}$. The mathematical expression $(d_{ss} - d_d)$ leads to two

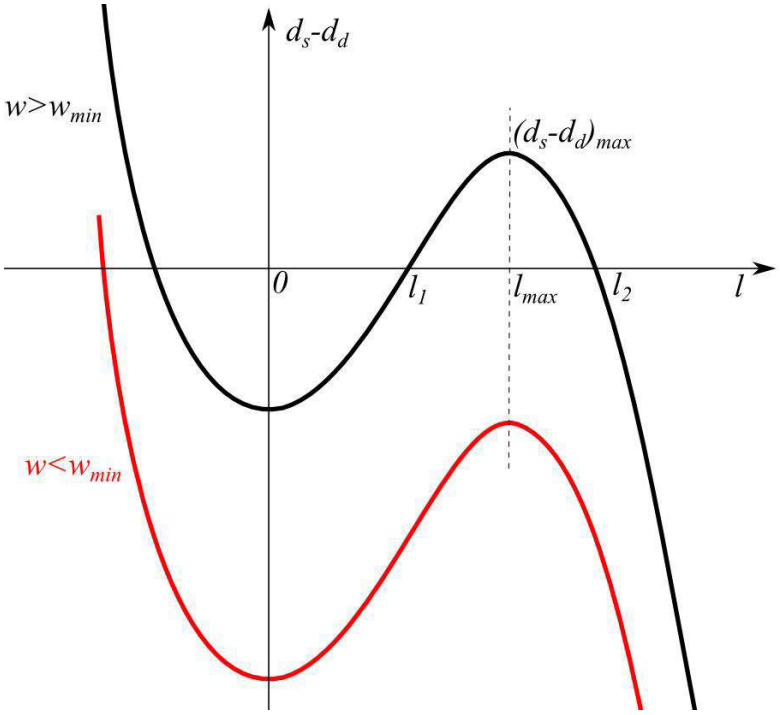

FIGURE 3.27: *Evolution of* $(d_{ss} - d_d)$ *with respect to the length* l.

cases in terms of its evolution as shown in Figure 3.27. If the general width w is smaller than w_{min}, then, whatever is the length, the actuator is not able to output the desired performance. In the other case, if w is higher than w_{min}, the actuator can reach the desired performance if l is between l_1 and l_2, where l_1 and l_2 are the positive zeros of $(d_{ss} - d_d)$. In result, the general width w must be always higher than w_{min}:

$$w \geq w_{min} \tag{3.78}$$

The expression of w_{min} is as follows:

$$w_{min} = \frac{3}{8\alpha\Delta T_{max}} \frac{\sqrt[3]{K_2'^2}}{K_1' K_3'} \sqrt[3]{\frac{1}{4}\frac{F^2 d_d}{E^2 b^2}} \tag{3.79}$$

The length l_1 is the minimal length after which the actuator output the desired performance. As clarified in the previous section, the free displacement evolves with respect to the square of the length while the blocking force is inversely proportional to the length. That's why evolution of the curve after $l = l_1$ is concave where the free displacement increases but the stiffness in front of the load decreases. After $l = l_2$, the stiffness is too small to handle the external load. The output of the actuator is then maximal when l is equivalent to l_{max}. The expression of l_{max} is as follows:

$$l_{max} = \frac{16}{3} E b \alpha w^2 \frac{K_1' K_3'}{K_2'} \frac{\Delta T_{max}}{F} \tag{3.80}$$

In the design, the length l must be equivalent or around l_{max}. The expression of the displacement when $l = l_{max}$ is as follows:

$$d_{ssmax} = \frac{2048}{27} E^2 b^2 \alpha^3 \frac{K_1'^3 K_3'^3}{K_2'^2} \frac{\Delta T_{max}^3}{F^2} w^3 \tag{3.81}$$

The design in the following is based on (3.81), the dimensions and the material must be chosen in order to maximize the value of d_{ssmax} as possible. Noting that there is another parameter, that must be always observed in any design, which is the stress limits. The stress evolution in the actuator is not studied in the thesis, this work is left for the perspectives. However, the stress evolution can be calculated numerically with FEM simulations. Generally, in cases that the stress exceeds its limits during functioning, higher widths in the weakest points must be chosen.

As for the material, as mentioned before, it can be chosen regarding the fabrication process or defined in the design specifications. In our case, we use the silicon as mentioned before. However, the parameters that are related to the material in the expression of d_{ssmax} (3.81) are the Young's modulus E, thermal expansion coefficient α and the maximal allowable temperature T_{max}. A better material for the actuator is when the value of $E^2\alpha^3\Delta T_{max}^3$ is more important.

In terms of the dimensions, d_{ssmax} evolves proportionally to the square of the depth b and to the cube of the general width w. As for the dimensions ratios (a, f, c and γ), in contrast to the free displacement (3.71), the charged displacement must be maximized with respect to $(K_1'^3 K_3'^3 / K_2'^2)$ when the length is equivalent to l_{max}.

In light of the above, a design methodology is given in the following as example on the actuators of system 1 in the multistable module shown in Chapter 4. The needed force and displacement for these actuators are equivalent to $d_d = 73\mu m$ and $F = 2.2mN$.

Regarding the complexity of $(K_1'^3 K_3'^3 / K_2'^2)$ and its dependency of 4 parameters, the design is made in two steps: in the first step, constant values of a, f, c and γ are chosen which allows defining an initial value of $K_1'^3 K_3'^3 / K_2'^2$ and choosing a width w above w_{min}. In the second step, the dimension ratios can be changed in order to optimize the output.

Choosing arbitrarily the following dimension ratios: $a = 0.1$, $f = 1$, $c = 10$ and $\gamma = 1$. The value of $K_1'^3 K_3'^3 / K_2'^2$ is then equivalent to $4.9286 \cdot 10^{-5}$. The other parameters in the expression of d_{ssmax} are chosen as follows: $b = 100\mu m$ (equivalent to the thickness of the device layer in the wafer, Chapter 5), $E = 169GPa$, $\Delta T_{max} = 650K$ and average value of $\alpha = 3.728 \cdot 10^{-6}\mu m/(m \cdot K)$ (α average is calculated from (3.54)). Putting these values in (3.79), the value of w_{min} is equivalent to:

$$w_{min} = 28.8\mu m \tag{3.82}$$

The value of w is set at $30\mu m$. In the following, the other dimensions are chosen in order to reach the minimal actuator length allowing reaching the desired performance.

As shown in (3.80), the length that maximizes the displacement is proportional to $K_1' K_3' / K_2'$. This quantity is inversely proportional to f as clarified in the previous section. Thus, the width of the flexure is chosen at the minimum possible in order to reduce the length of the actuator. In the other side, the flexure and the connexion between hot and cold arms are the weakest points

in the actuator due to the high stress with the presence of the heat. Thus, the width of the flexure is limited at $w_f = 20\mu m$ in order to avoid the failure, the value of f is then equivalent to $2/3$.

On the other hand, the gap width g is equivalent to $20\mu m$ which is the width of the openings in our fabrication process, δ is then equivalent to $2/3$. Concerning the value of c, in a first moment, we can choose an arbitrary value of $c = 20$.

The only dimension that remains is the ratio a. Figure 3.28 shows evolution of d_{ssmax} and l_{max} with respect to a. The values of d_{ssmax} and l_{max} are calculated with all the dimensions and parameters defined previously and an arbitrary value of $c = 20$.

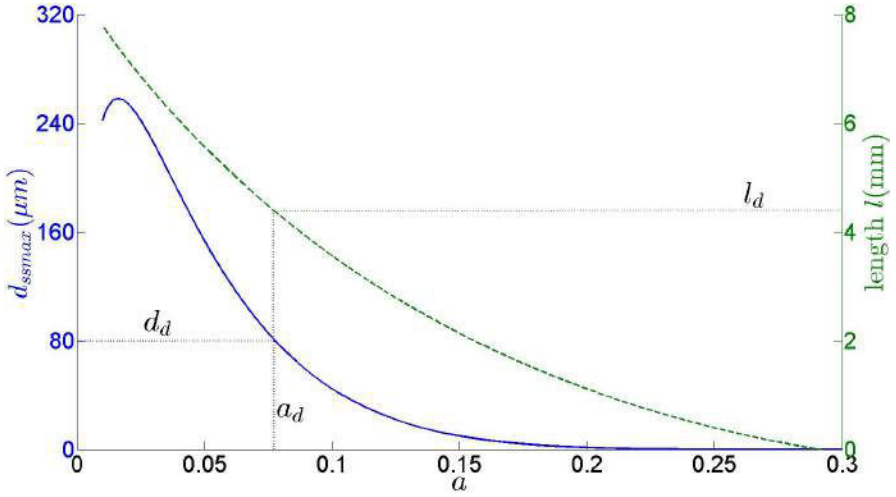

FIGURE *3.28: Evolution of d_{ssmax} (left column) and l_{max} (right column) with respect to a. These values are calculated for $c = 20$.*

The length l_{max} shows to be higher with low values of a. The value of d_{ssmax} decreases after a maximum at low values of a. Our goal is to reach the desired performance (which is revealed in terms of the displacement in Figure 3.28) with the lowest length possible. Let define a desired displacement $d_d = 80\mu m$ (Higher than $73\mu m$ as a security margin). This allows obtaining the value of the corresponding a_a from the curve of d_{ssmax} and of the corresponding length l_d. Calling these points (a_d, d_d, l_d) the desired points.

In the following, the desired points are recalculated for different values of c. Figure 3.29 shows evolution of the desired length l_d with respect to c allowing obtaining a desired displacement $d_d = 80\mu m$.

The evolution of l_d with respect to c shows to have a minimum around $c = 11$. The value of the corresponding ratio a_a is around 0.055 and of the corresponding length is around $l_d = 4.33\mu m$. In light of the above, the length of the flexure is chosen to be equivalent to $240\mu m$.

In result, all the dimensions of the actuator are obtained ($w_h = 30\mu m$, $w_c = 330\mu m$, $w_f = 20\mu m$, $g = 20\mu m$, $l_h = 4.33mm$, $l_c = 3.93mm$, $l_f = 0.24mm$). In summary, the design method consists of several steps, defining initial dimension ratios allowed choosing a width above the minimal width. After that the gap width was defined with respect to the fabrication process and the flexure width was minimized as possible in order to reduce the length of the actuator. After

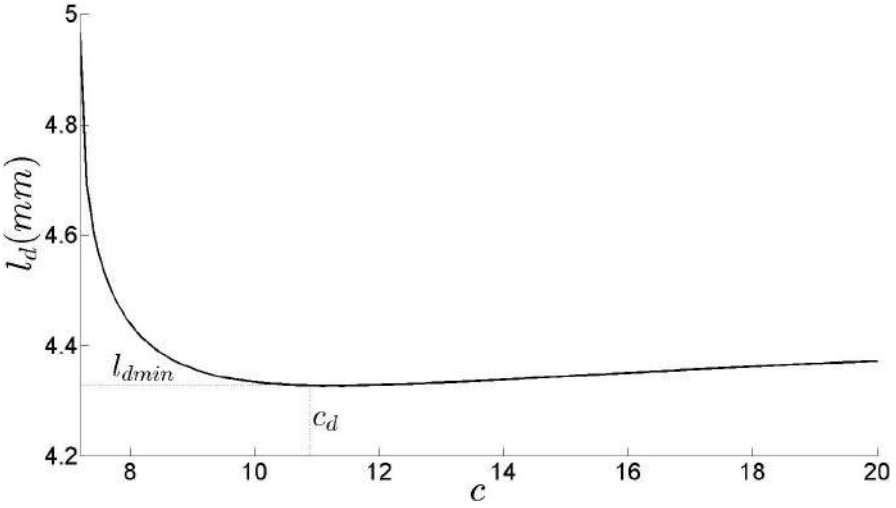

FIGURE *3.29: Evolution of the desired length l_d with respect to c allowing obtaining a desired displacement $d_d = 80\mu m$.*

that, scanning the values of the length with respect to *a* and *c* allowed defining the minimal value of the length and the corresponding *a* and *c* that allows reaching the desired performance.

3.6 Conclusion

The modeling and design of the U-shaped actuator were investigated in this chapter. An exact solution was presented for the electrothermal PDEs in the case of the actuator. The displacement was then calculated by a thermomechanical model with respect to the temperature distribution obtained from the electrothermal model and an external load. The two models showed a good agreement with FEM simulations and experiments.

The design of the actuator was investigated subsequently. The impact of the different dimensions and properties on the actuator behavior was studied. A design method was then proposed that allows choosing and optimizing the dimensions that ensure reaching a required performance at the steady state in terms of the force and displacement.

The studies in this chapter and Chapter 2 provide key elements for understanding the behavior and improving the design of the main components (curved beams and U-shaped actuators) in the DiMiBot and the multistable module which are presented in the next chapter.

Noting that the dimensions of the actuator obtained in this section are not the same in the multistable module since this work was made at a late stage of the thesis. The length of the actuator and its "steady state" capacity is lower in the multistable module since the actuator is designed to provide the desired performance near to the overshoot as clarified previously in the chapter. The perspectives for the works on the U-shaped actuator are cited later in the final conclusion of the thesis.

Chapter 4

Multistable module and DiMiBot

In this chapter, the principle and the design of a novel multistable module are presented. The multistable module has a monolithic and compliant structure and allows switching its moving part between several stable positions linearly in a one dimensional direction back and forth. The number of stable positions can be increased by increasing the range of displacement of the moving part. Transition is made by an upward or downward step to one of the nearest two stable positions. Upward and downward steps are made by a specific sequence of moving and opening normally closed latch arms and closing other normally open latch arms. An accurate positioning mechanism is used in order to ensure accurate steps and to compensate the fabrication tolerances.

The design of the different components and each system in the multistable module is presented in this chapter. The design of the global structure of a multistable module is then presented. Finally, the design of the multistable DiMiBot, which consists of two multistable modules, is presented.

Chapter contents

4.1 Introduction

A new generation of the DiMiBot is proposed and developed in the thesis. The new DiMiBot consists of two multistable modules instead of the bistable modules in the old design. In this chapter, the principle and design of the multistable module and the DiMiBot are presented. The advantages of the multistable module and the importance of using it in the new DiMiBot were clarified previously in Chapter 1. Figure 4.1 shows a drawing of the new generation of the DiMiBot.

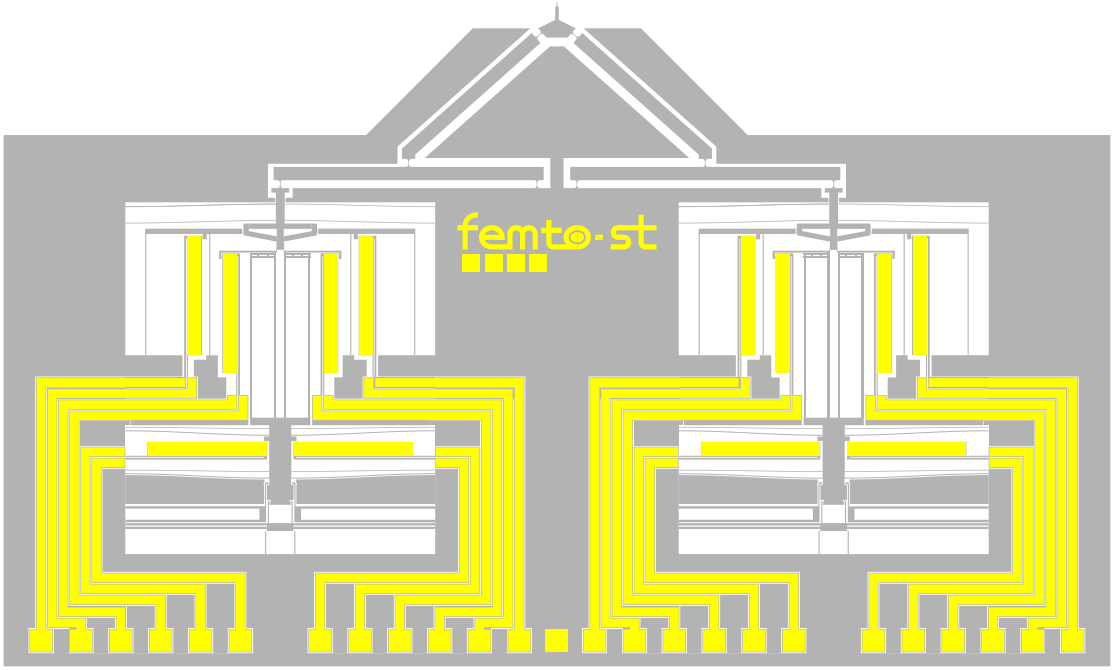

FIGURE *4.1: Drawing of the new generation of the DiMiBot.*

The structure of the new DiMiBot is more compact. It consists of the top head mechanism as in the previous DiMiBot, and one multistable module in each side. Gold is used instead of aluminum for the electrical connectivity due to a fabrication purpose which is presented later in Chapter 5.

The multistable module used in the DiMiBot allows switching its moving part between several stable positions in a straight line back and forth. It consists of three systems with two latches and the moving part. At least, one of the two latches holds the moving part at rest and during functioning. The first latch is normally closed, it holds the moving part at rest and during switching, while the second latch is normally open and it holds the moving part temporary during switching. The holding is ensured by interconnecting some teeth between the latches and the moving part.

The displacement of the moving part is guided with a couple of curved beams. The stepping is performed by a sequence of moving, opening and/or closing the latches with and without the moving part. Changing the sequence order allows making either upward or downward steps of

the moving part. Figure 4.2 shows a drawing of the different systems and components in the multistable module.

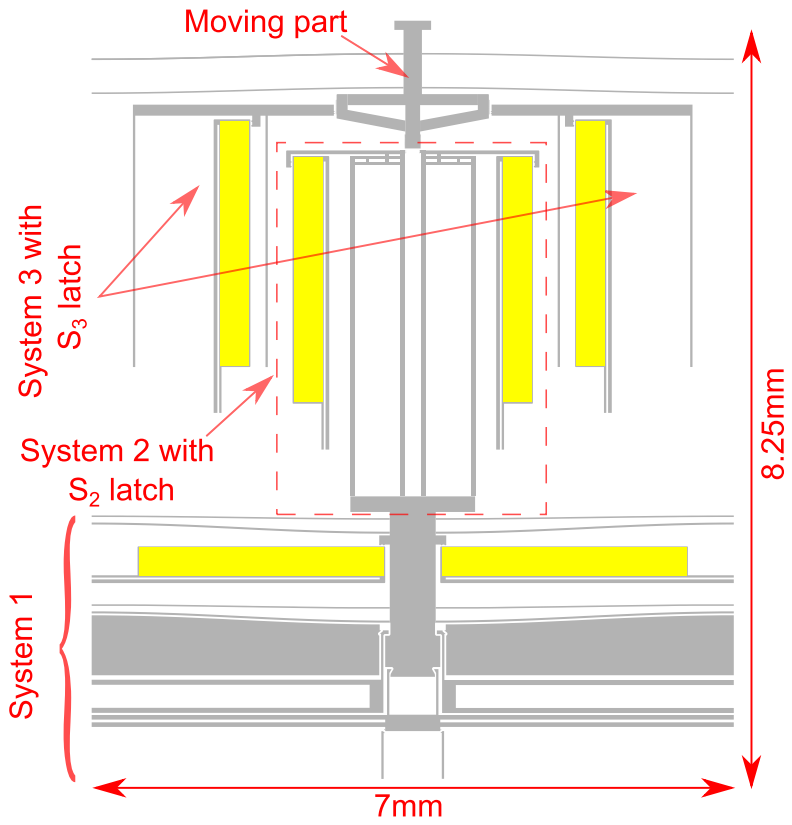

FIGURE *4.2: A drawing of the different systems and components in the multistable module..*

Each system in the multistable module allows switching the latches between two states (up-down or close-open). The first system (S_1) is a bistable system that allows switching accurately the latch of system 2 between two stable positions. The accuracy is ensured using an accurate positioning mechanism which compensates the fabrication tolerances. The second system is a set of two U-shaped actuators that allow opening a latch from the two sides simultaneously. The third system consists also of two U-shaped actuators in order to close another latch from the two sides simultaneously.

The principle of the multistable module, the design of the different systems, the design of the multistable module and of the new DiMiBot are presented in the following sections.

In Section 4.2, the mechanism principle of the multistable module and the different steps to make upward and downward steps of the moving part are presented.

In Section 4.3, the fabrication tolerances are presented and discussed before presenting the principle of an accurate positioning mechanism. This mechanism is used in the design of the first system which is presented subsequently.

In Sections 4.4 and 4.5, the designs of systems 2 and 3 are presented respectively. Two configurations are used for the teeth between the latches and the moving part in the two systems.

In Section 4.6, the global structure of a multistable module prototype is presented and the holding forces at each stable position are calculated. The design of the new DiMiBot is finally presented in section 4.7.

4.2 Principle of the multistable mechanism

The principle of the multistable mechanism revolves around a specific sequence of several simple steps of activating the internal systems to switch the moving part from a stable state to another one. Two specific sequence orders allow upward and downward steps of the moving part. Figure 4.3 shows a schematic of the moving part with the two latches. This representation is used to present the stepping principle. The configuration in the figure is at rest where S_2 latch is closed on the moving part and is in its bottom position, while S_3 latch is in its open state.

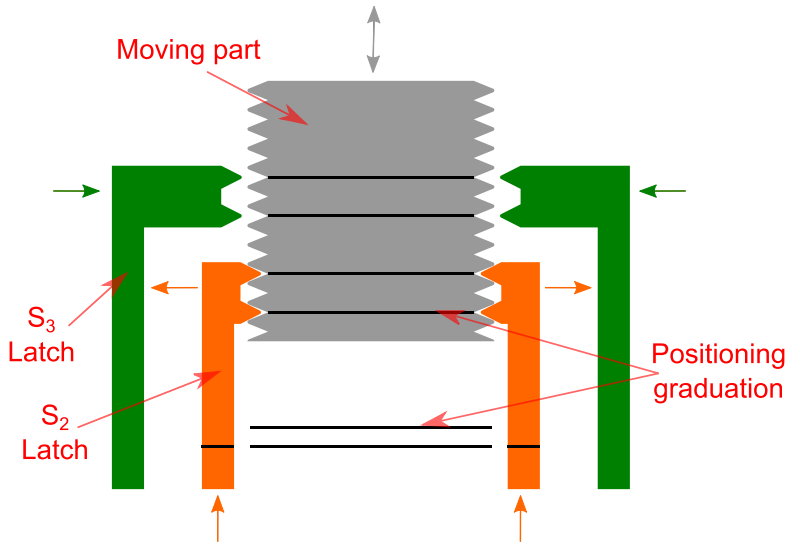

FIGURE *4.3: Schema of the rest configuration of the multistable mechanism including the latches and the moving part.*

In order to simplify the design and reduce number of actuators, each system in the multistable module is designed to switch between one passively and another actively stable states. System 1 allows moving up S_2 latch which is normally at the bottom position. Dimension of the step is well defined using an accurate positioning mechanism. U-shaped actuators in system 2 allow opening S_2 latch which is normally closed. U-shaped actuators in system 3 allow closing S_3 latch which is normally open.

The first state is maintained passively using curved beams in system 1 and the stiffness of the latches in systems 2 and 3. The second state of the three systems is maintained actively by supplying U-shaped electrothermal actuators continuously.

The sequence orders for making an upward and downward steps are presented in Figures 4.4 and 4.5 respectively.

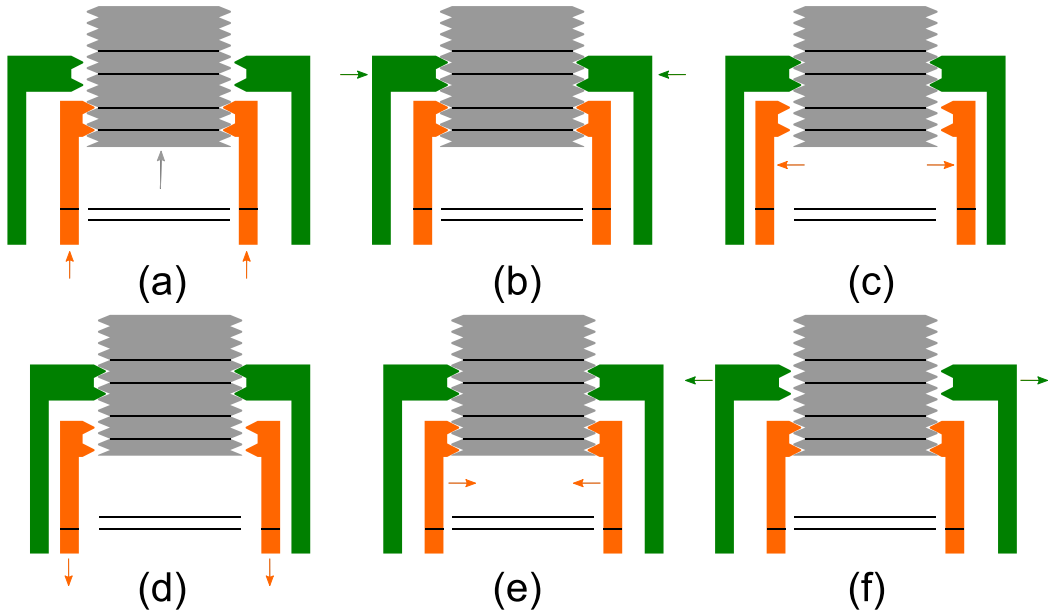

FIGURE 4.4: *Sequence order to make an upward step. Firstly, S_2 latch move upwards with holding the moving part (a), S_3 latch holds the moving part (b), S_2 latch releases the moving part (c), moves downwards (d) and holds the moving part in a bottom position (e), finally, S_3 latch releases the moving part (f).*

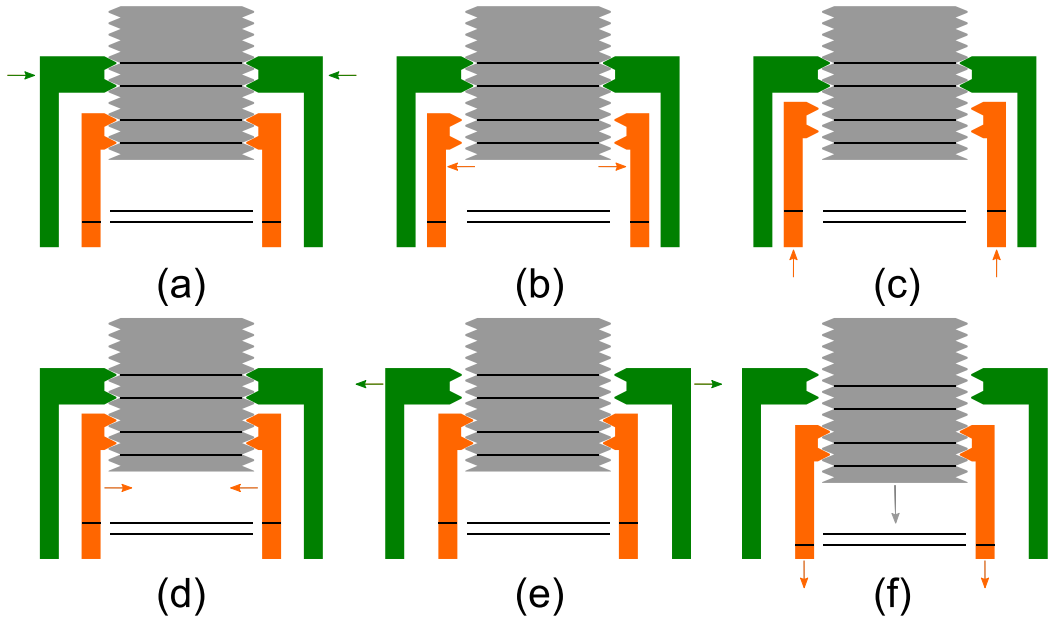

FIGURE 4.5: *Sequence order to make a downward step. Firstly, S_3 latch holds the moving part (a), S_2 latch releases the moving part (b), moves upwards (c) and closes in the upper position (d), S_3 latch releases then the moving part (e), finally, S_2 latch moves downwards with holding the moving part (f).*

The use of teeth for the holding between the moving part and the latches could create problems in the design. The teeth alone do not ensure accurate positioning at this scale, and a perfect engagement of the teeth requires an accurate positioning of the teeth in the two sides. As explained in the principle of the multistable module, the positions in the direction of motion are defined by system 1. The design of system 1 is investigated in the following, where an accurate positioning mechanism is used to compensate the fabrication tolerances and ensure accurate steps.

4.3 System 1: an accurate bistable mechanism

In this section, the design of the first system and its different components is presented. Regardless of its function in the multistable module, system 1 can be classified as a bistable module which combines advantages of the digital concept, monolithic structures and compliant mechanisms.

Figure 4.6 shows a drawing of system 1 and its different components. System 1 consists of a shuttle which is guided vertically using curve beams, electrothermal actuators and an accurate positioning mechanism. The structure of the shuttle from the top is related to S_2 latch in the global design of the multistable module.

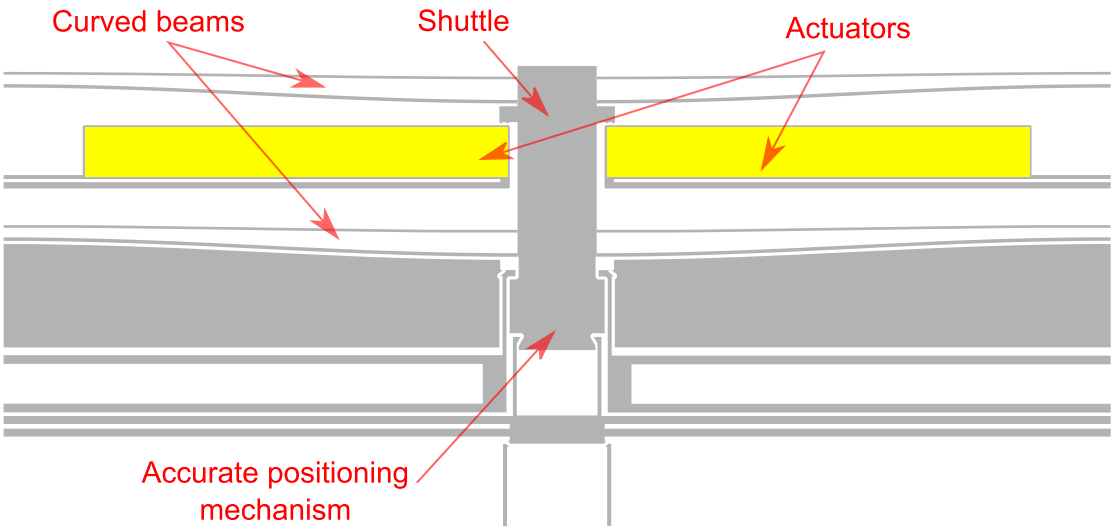

FIGURE *4.6: Drawing of system 1 and its different components.*

The accurate positioning mechanism compensates the tolerances resulting from the fabrication process and defines accurately the two discrete positions of system 1.

In the following, the fabrication tolerances are presented and discussed, the principle of the accurate positioning mechanism is presented where an hypothesis is considered that the tolerances are homogeneous throughout the sidewalls of the device layer. The design of the different components of system 1 is then presented.

4.3.1 Microfabrication tolerances

Selection of the fabrication process depends upon the specific application, material, tolerance, size of features and aspect ratio. The device in our fabrication process is realized using a classical bulk micromachining of a single-crystalline silicon substrate (Chapter 5).

Many parameters affect the patterns final form and the resulting tolerances in each step of fabrication. The active parts of the bistable module are realized in the device layer. Figure 4.7 shows the main steps for etching the device layer.

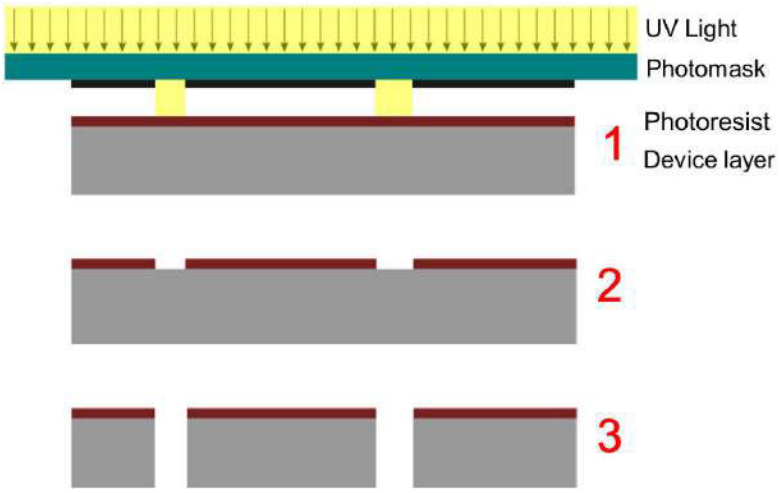

FIGURE *4.7: Usual etching process steps. Photoresist deposition and UV light exposure using a photomask (1), photoresist developing (2), DRIE of the silicon layer (3).*

In the first step (Figure 4.7), the wafer is covered with positive photoresist layer by spin coating, then, the photoresist is exposed to a pattern of UV light through the photomask.

Manufacturing the photomask involves unavoidable tolerances. The photomask is a patterned chromium coated glass, the pattern information is created in a CAD software and transferred to the photomask using a laser or e-beam writer. The patterns in the photomask shows some differences from the design due to the influence of some parameters (laser or electron density, etcher concentration, etching time of the chromium layer etc.).

In the second step, the imaged pattern of the photoresist on the device layer is developed. The tolerances in this step are related to several parameters (photoresist quality, developing time, developer concentration, bake recipes etc.).

In the third step, the device layer is etched using DRIE process. DRIE process is one of the most popular fabrication techniques for silicon bulk micromachining. It is characterized by a high etch rate, high selectivity to silicon dioxide and etching photoresist, high aspect ratio microstructures and vertical sidewalls.

DRIE is done using the Bosch process with alternating passivation (C_4F_8) and etching (SF_6) steps. However, this fabrication technique induces various fabrication tolerances such as microloading effect [51, 134], notching or footing effect [60], lag effect in the small openings [123], slanted profiles and undercut [46, 76].

These tolerances may affect the mechanical stiffness, displacement, performance of devices in MEMS and would induce a mismatching between the measured dimensions and the designed values.

The various tolerances are dependent of the process parameters (gas flowrate, electrode power, pressure, temperature, cycling time, etc.) but also to the feature sizes. In fact, the etching tolerances evolve with the width of the openings [46, 51, 60, 76, 123, 134].

In order to obtain a uniform and homogeneous etching throughout the photomask, the photoresist and the wafer, the silicon layers are etched with a unified opening width in the fabrication process. This allows considering an hypothesis that the fabrication tolerances have the same form and dimensions throughout the sidewalls of the patterns in the device layer.

4.3.2 Accurate positioning mechanism

As we consider that the microfabrication tolerances have the same shape and dimensions on the patterns' sidewalls, especially in a local area, then, gain or loss in the sidewalls dimensions have the same value throughout the microdevice.

Figure 4.8 shows the variation in the width and the distance between the sidewalls of two parallel patterns in the design and after fabrication. Δ is the value of gain or loss in each sidewall dimension after fabrication. Positive values of Δ are considered when there is a loose in the width of patterns.

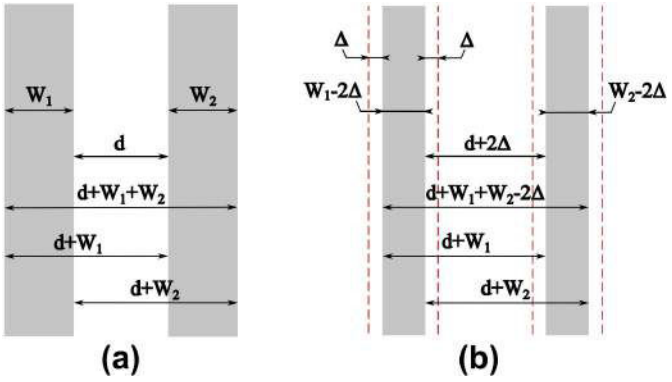

FIGURE *4.8: Distances between the sidewalls of two parallel patterns in the design (a) and after fabrication (b).*

As shown in Figure 4.8, due to the uncertainty of dimensions after fabrication, 2Δ is added to the distance between two faced sidewalls ($d \rightarrow d + 2\Delta$) and is subtracted from the distance between two opposite sidewalls ($d + w_1 + w_2 \rightarrow d + w_1 + w_2 - 2\Delta$). Another important feature is that the distance between two sidewalls from the same side (right or left) remains the same after fabrication.

In the design of the accurate positioning mechanism, we take advantage of the effect that the distance between two parallel patterns sidewalls in the design increases or decreases after fabrication according to the different sidewalls.

The accurate positioning mechanism is designed in order to move the shuttle initially an accurate distance d during the activation phase and to ensure an accurate stroke s between the two stable positions of the moving part.

Figure 4.9.a shows the components of the accurate positioning mechanism, it consists of bottom and upper locks, bottom and upper movable parts and the shuttle. The important distances d_1, d_2, d_3 and d_4 between the different components are shown in Figure 4.9.a with considering the fabrication tolerances.

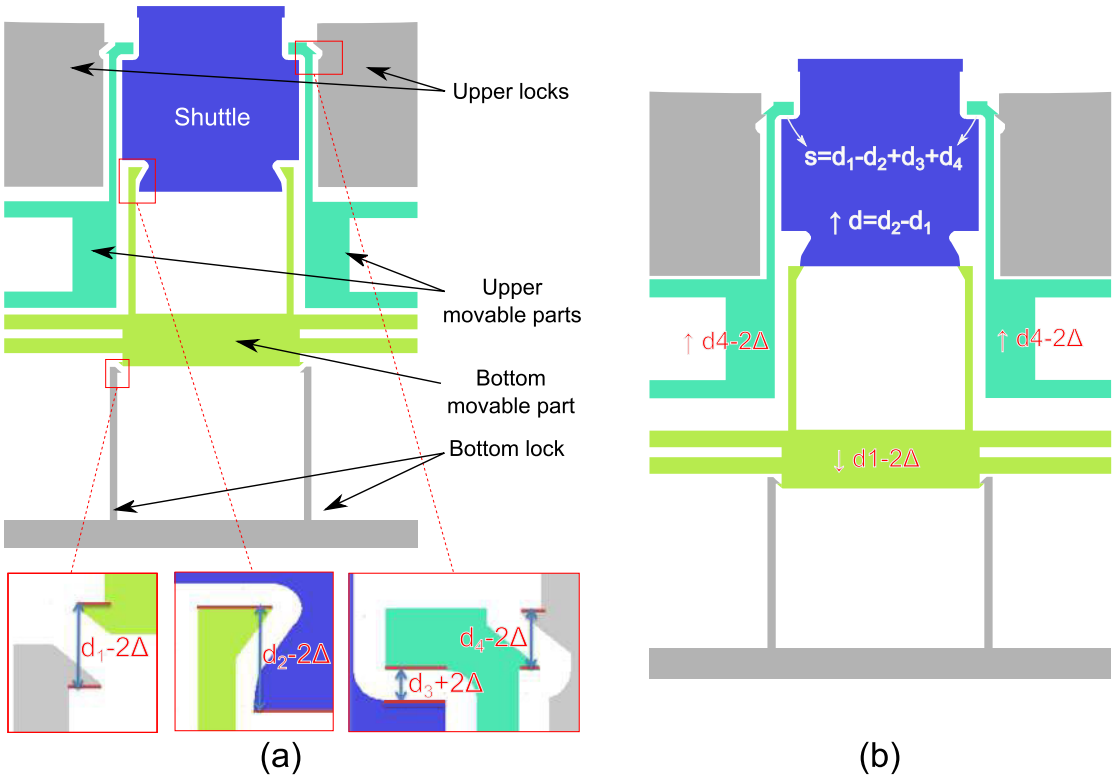

FIGURE *4.9: Drawing of the accurate positioning mechanism in the design, the important distances between the different components are shown with considering the fabrication tolerances (a). Drawing of the accurate positioning mechanism after activation where the movable parts are suspended to their locks and the moving part is in the initial position (b).*

The bottom and upper locks are designed to hold the bottom and upper movable parts respectively after suspension in the activation phase. These components are suspended using the triangular-shaped head which allows sliding from a side and blocking displacement from the other side.

The deformable beams in the bottom lock and movable parts are used due to their horizontal flexibility during suspension of the different components. The handle layer under the upper locks was not etched in order to improve its stiffness while the other components are only in the device layer.

The activation phase is a sequence of several steps which are made manually after fabrication. In the first step, the upper movable parts are suspended to the upper locks by moving them upwards a distance $d_4 - 2\Delta$. In the second step, the bottom movable part is suspended to the bottom locks by moving it downwards a distance $d_1 - 2\Delta$. In the last step, the shuttle is pushed beyond the head of the deformable beams in the bottom movable part. Its position is then limited between the bottom and upper movable parts.

The shuttle is connected to several curved beams as shown in Figure 4.6. The stiffness of the curved beams ensures that the shuttle remains in contact with the bottom movable part (first stable position). The second stable position is when the shuttle becomes in contact with the upper movable parts. The shuttle is normally stable at the first position and reach the second position using the actuators.

Figure 4.9.b shows the accurate positioning mechanism after activation. As shown in Figure 4.9.b, the initial displacement d of the moving part and the stroke s between the two stable positions show to be independent from the fabrication tolerances:

$$\begin{aligned} d &= -d_1 + d_2 \\ s &= d_1 - d_2 + d_3 + d_4 \end{aligned} \tag{4.1}$$

The principle of the accurate positioning mechanism is illustrated in Figure 4.10. Firstly, after fabrication, the shuttle must be activated by moving it a distance d to its first position. In order to compensate the fabrication tolerances related to this distance d, the bottom movable part is suspended to the bottom lock, then the shuttle is moved to its first position by suspending it to the bottom movable part (Figure 4.10.a & 4.10.b). The fabrication tolerances in this case are compensated by subtracting the tolerances of two pairs of opposite sidewalls.

In the other side, the step size s is the distance between the faced sides of the shuttle and the upper movable parts. After inserting the shuttle in its first position (moving a distance d), in order to compensate the fabrication tolerances related the step size s, the upper movable parts are suspended to the upper locks (Figure 4.10.c & 4.10.d). The fabrication tolerances in this case are compensated by adding the tolerances of opposite and faced sidewalls. In result, the initial activation distance d and the step size s are independent from the fabrication tolerances.

In conclusion, the accurate positioning mechanism has several functions: compensate the fabrication tolerances, place the shuttle accurately in its first position and define accurately the stroke between the 2 stable positions. In the first position of S_2 latch (defined by the shuttle of system 1), teeth of the S_2 latch become engaged to those of the moving part of the module as shown later in Section 4.4.

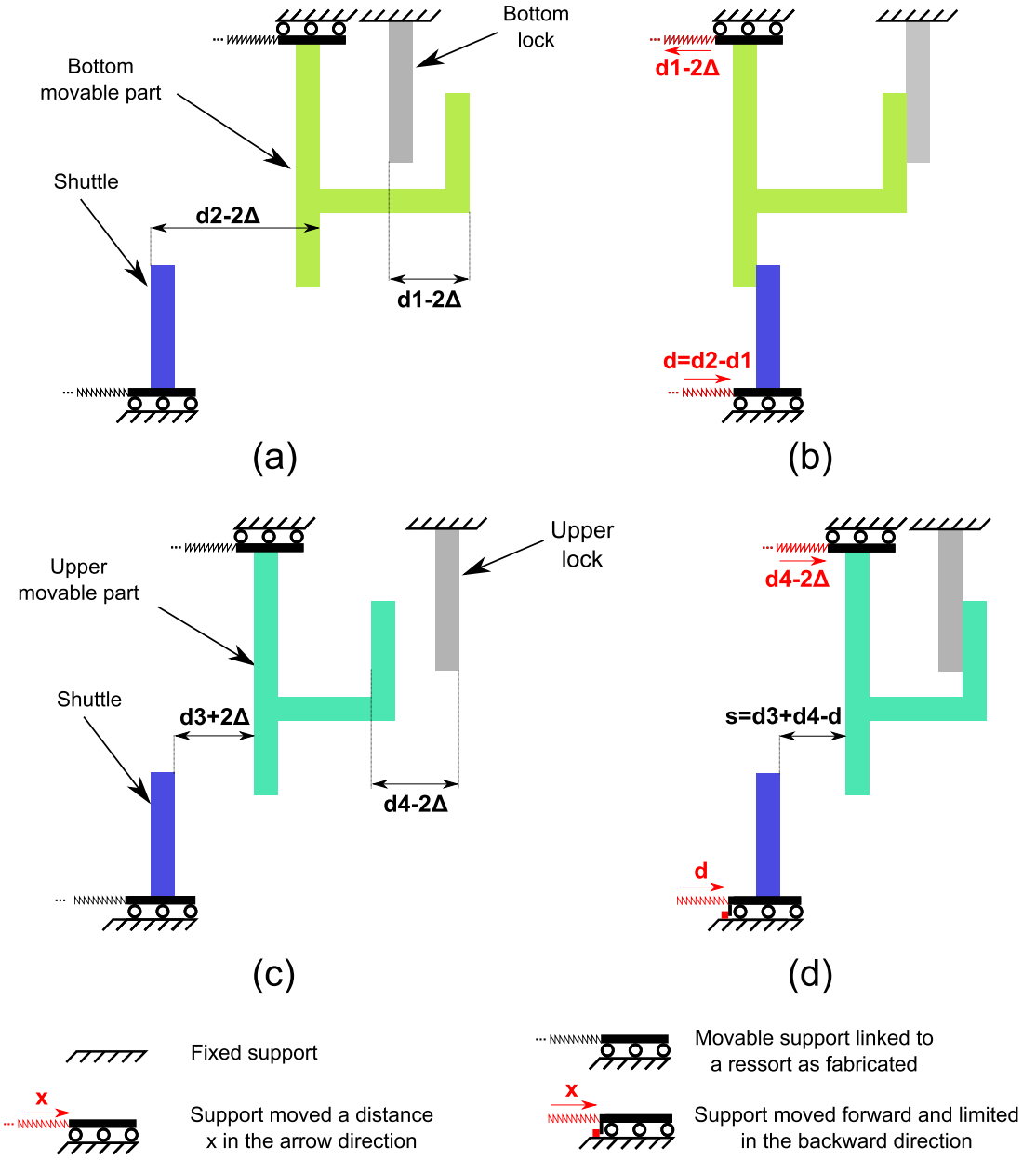

FIGURE *4.10: Configuration of the mechanism to compensate the fabrication tolerances. The mechanism to realize the initial activation distance d as fabricated (a) and after the initial activation (b). The mechanism to define the step size s as fabricated (c) and after the initial activation (d).*

4.3.3 Design of the different components in system 1

Design of the different components in system 1 is presented hereinafter. As for the accurate positioning mechanism, its design allows defining any dimensions for the stroke. The stroke s in the fabricated prototype is equivalent to $10\mu m$. The distance d_3 is equivalent to the unified

opening width in the device layer. The opening width is equivalent to $20\mu m$ in our fabrication process. The distances d_1 and d_4 must contain 2 triangular heads which are separated by the width of the opening between them. d_1 and d_4 are chosen to be equivalent to $40\mu m$ in the prototype. Higher values of d_1 and d_4 allow higher size of the triangular heads which increases and enhances the contact surface between them. Afterwards, the distances d and d_2 are calculated from (4.1) ($d = 50\mu m$ and $d_2 = 90\mu m$).

In the other side, dimensions of the different components in the accurate positioning mechanism are chosen in order to obtain a suspension force of $14.5mN$ in the bottom movable part and $7.5mN$ for each one of the upper movable parts. Thus, total forces on the shuttle must not exceed $14.5mN$ in the downward direction and $15mN$ in the upward direction.

Four curved beams were used in order to guide a vertical displacement robustly and reduce the possibility of rotating the moving part due to external forces. The curved beams are used instead of simple straight beams because of the exponential nature of the force evolution of clamped-clamped straight beams after deflection in their middle. Otherwise, the actuators must provide an important force in order to switch the shuttle between the two stable positions.

Behavior and design of preshaped curved beams was investigated in 2. Figure 4.11 shows the snapping force-displacement curves after deflection of curved beams for $Q < 2.31$ and $Q > 2.31$.

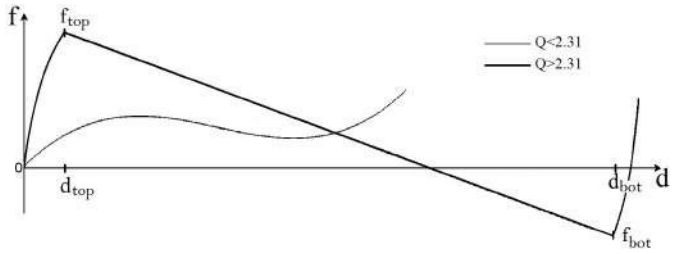

FIGURE *4.11: Evolution of the snapping force of preshaped curved beams during deflection for* $Q < 2.31$ *and* $Q > 2.31$.

The curved beams dimensions are chosen to ensure a significant holding force in the first stable position and to avoid high loads on the actuators in the second stable position. Two different dimensions are chosen for the curved beams where each set of dimensions is for two curved beams. In the first couple, dimensions are chosen to ensure that the first position at $50\mu m$ is after d_{top} (Figure 4.11). In this way, the snapping force which is a load on the actuators will decrease during transition to the second position at $60\mu m$. Dimensions of the first couple are as follows ($l = 6.5mm$, $h = 100\mu m$, $t = 20\mu m$, $b = 100\mu m$). Dimensions of the second couple of curved beams are chosen in order to get a nearly constant load on the actuator and to reduce the snapping forces as possible. The dimensions are chosen under $Q = 2.31$ ($l = 6.5mm$, $h = 30\mu m$, $t = 15\mu m$, $b = 100\mu m$).

Evolution of the snapping forces of the four curved beams together is shown in Figure 4.12. The value of the snapping force at the first position ($50\mu m$) is equivalent to $4.4mN$ and at the second position ($60\mu m$) is equivalent to $4.15mN$. Noting that the values of the forces in this paper are obtained using FEM simulations on Ansys.

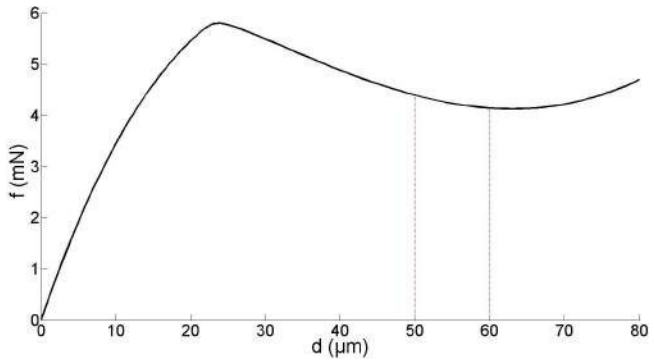

FIGURE *4.12: Snapping force evolution of the curved beams in system 1 during deflection.*

The holding forces on the moving part in the first position are then equivalent to $10.1mN$ in the downward direction and $4.4mN$ in the upward direction. Any external force must exceed these holding barriers before disturbing the position of the moving part.

As for the electrothermal actuators, their role is to ensure the switching function and to hold the moving part in the second stable position. Dimensions of the actuators in system 1 and the other systems are the same shown in Figure 3.5. A gold layer is deposited on the cold arm in order to reduce the expansion in the cold side and improve the performance of the actuator.

As the two actuators are placed in parallel and supplied simultaneously with the same voltage, the conducting force is twice the force produced by one actuator. Each actuator must then move $73\mu m$ ($60\mu m$ + distance between actuators and shuttle at rest: $13\mu m$) and provide a force of $2.2mN$ (i.e. $4.4mN/2$) at least. The force produced by the actuator must not exceed $9.58mN$ (i.e. $(15mN + 4.15mN)/2$), otherwise, the upper movable parts in the accurate positioning mechanism will loose their positions and the second stable position of system 1 is no more accurate. All of these distances and forces are clarified in Figure 4.13.

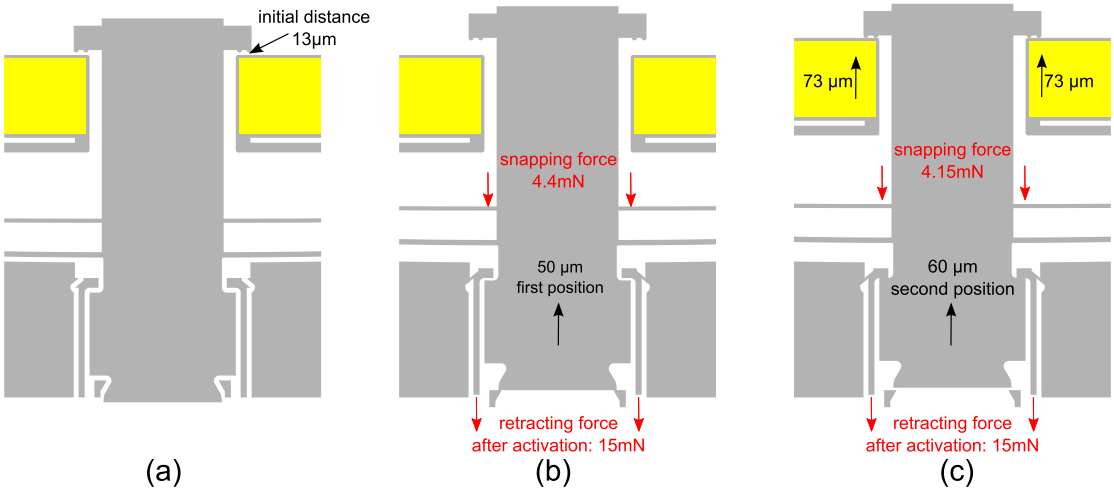

FIGURE *4.13: Important distances and elastic forces in the as-fabricated configuration of system 1 (a), after activation (b) and after switching to the second position (c).*

4.4 System 2 and the teeth configurations

4.4.1 Functioning

As explained previously, system 2 allows opening the S_2 latch which is designed to be normally closed after activation. System 2 consists of two actuators and the structure of S_2 latch as shown in Figure 4.14.

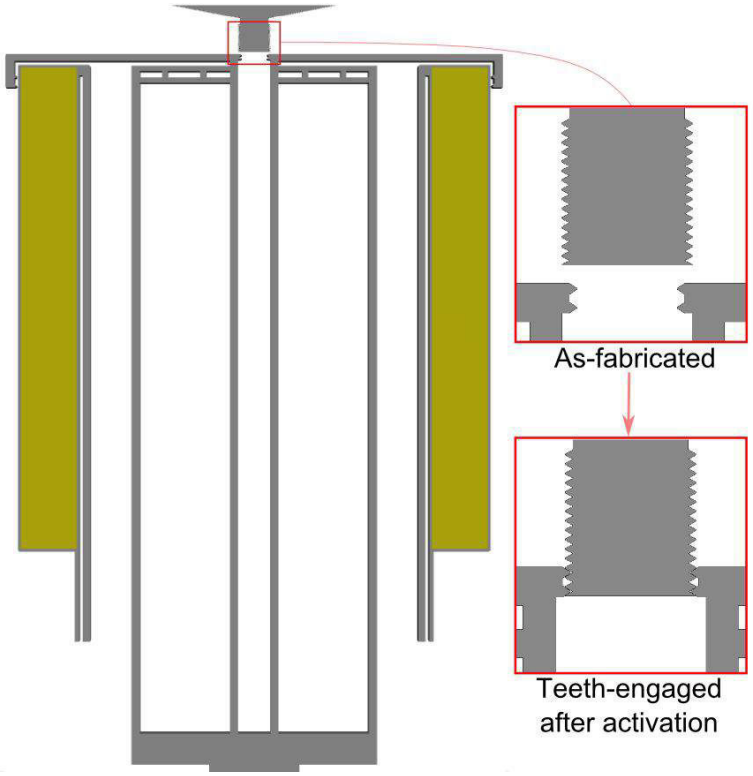

FIGURE *4.14: Drawing of system 2 including S_2 latch and two electrothermal actuators, and a zoom on the teeth of the latch and the moving part before and after activation.*

During activation, S_2 latch is opened manually, moved vertically the distance $d = 50\mu m$ (activation distance) and then closed where the couples of teeth on the head of each side of the latch become engaged to the first couples of teeth in the moving part as shown in Figure 4.14. The horizontal distance between the as-fabricated and the teeth-engaged configurations of S_2 latch is equivalent to $d_{s2} = 12\mu m$. The retracting force of each side of the latch and the teeth engagement allows maintaining the moving part at rest.

In order to ensure a proper functioning in the multistable module, the actuators must open the latch a sufficient distance to ensure no contact between the teeth during vertical transition of the moving part, let say that this distance is at least $30\mu m$ (regarding teeth dimensions).

Each side of the latch is designed as a gantry in order to ensure horizontal entry and exit of the teeth. Figure 4.15 shows evolution of the retracting force of each gantry after deflection.

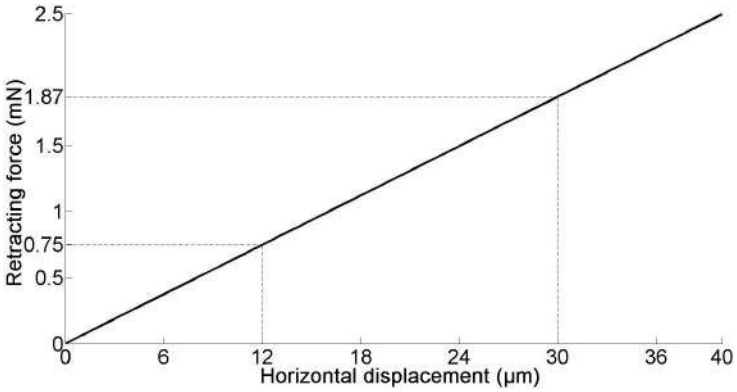

FIGURE *4.15: Evolution of the retracting force after deflection of the gantry in each side of the latch in system 2.*

The loads on the actuators of system 2 are decomposed in two parts. After supplying, each actuator will move without loads a distance of $25\mu m$ (initial free distance between one actuator and one gantry + d_{s2}). After that, the load on the actuator is the retracting force of the gantry shown in Figure 4.15, starting after d_{s2}. All these distances are clarified in Figure 4.16.

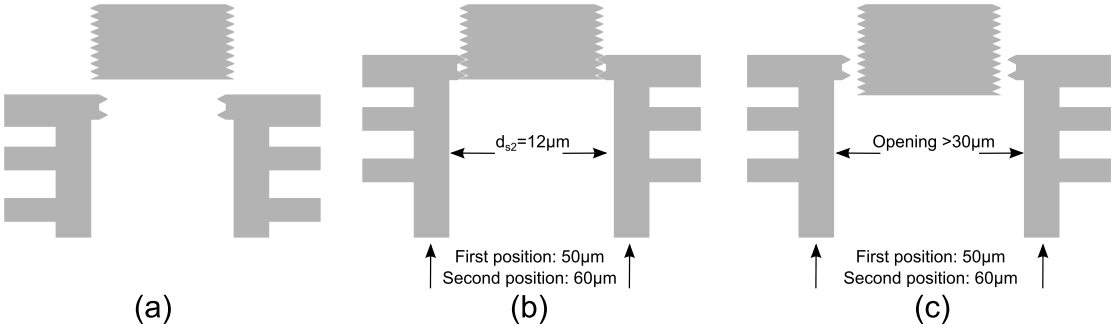

FIGURE *4.16: Zoom on the contact zone between the moving part and S_2 latch in the as-fabricated configuration (a), when the latch holds the moving part (b) and when it releases the moving part (c).*

4.4.2 Teeth configurations

Two teeth are used for each arm of the latch in order to ensure the holding of the moving part. The number of teeth in the moving part define the number of its stable positions. Two configurations were considered for the teeth in the design that allow engaging the teeth at each step. One smaller configuration is used which is somewhat traditional where the step of displacement (s) between the stable positions is equivalent to the distance between two consecutive teeth, this configuration limits the teeth size to the step size. In addition, one wider configuration is used where the teeth in a side is separated by a distance of 3s and in the other side by a distance of 2s, in this way, wider teeth can be used for making the same step size of displacement. The wide configuration is used to anticipate any problem that may occur due to the tiny size of teeth in

the small configuration (etching quality, weak structure, etc.). Figure 4.17 shows dimensions of the teeth in the two configurations with respect to the step size (s).

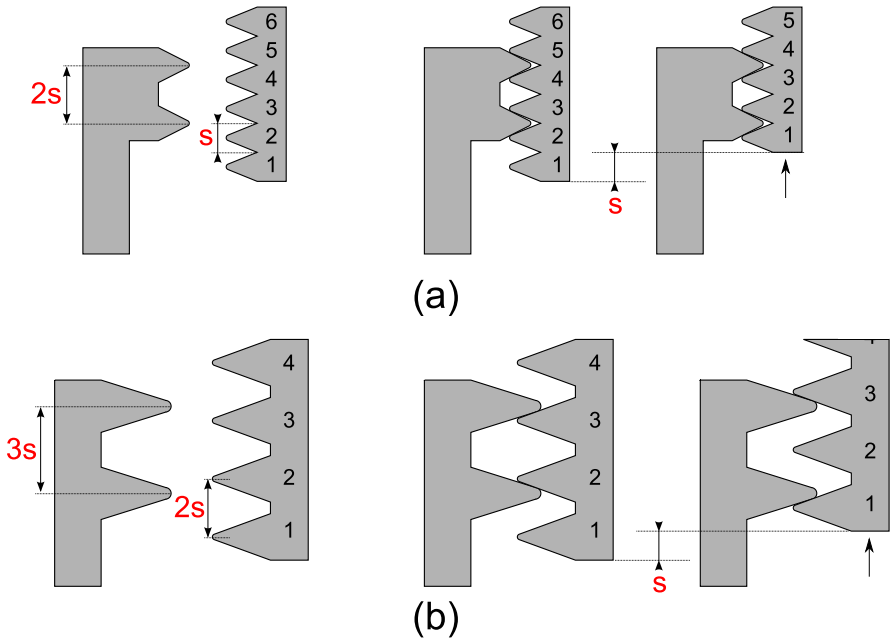

FIGURE *4.17: Two possible configurations of the teeth dimensions allowing engaging the teeth at each step. Small (a) and wide (b) teeth configurations. The teeth dimensions are shown at the left while the engagement shape of the teeth between two consecutive positions of the moving part is shown at the right.*

In the small teeth configuration, teeth of the latch become engaged at the middle between two consecutive teeth of the moving part. In the wide teeth configuration, the holding is done using the border of the teeth in two possible ways. Internal borders of the latch teeth push on the external borders of the moving part teeth in some stable positions. In the next stable position, external borders of the latch teeth push on the internal borders of the moving part teeth as shown in Figure 4.17.

As will be shown later, the experiments showed a drawback for the small teeth configuration for small step sizes ($s = 10\mu m$ in our prototypes). Due to the small size of the teeth, their structure is too weak and they was broken after several steps through them. This problem appears mainly in system 2 where the moving part moves back and forth during holding.

The existence of the teeth is for improving the holding of the moving part. Otherwise, the holding can be ensured by relying on the friction between the latch and moving part sidewalls, especially for a small step size. In this case, the horizontal stiffness of the latch must be improved.

4.5 System 3 and the moving part

As for system 3, it works on the same principle as system 2 but in the reverse direction. It consists of two actuators and S_3 latch which is a set of two gantries as shown in Figure 4.18.

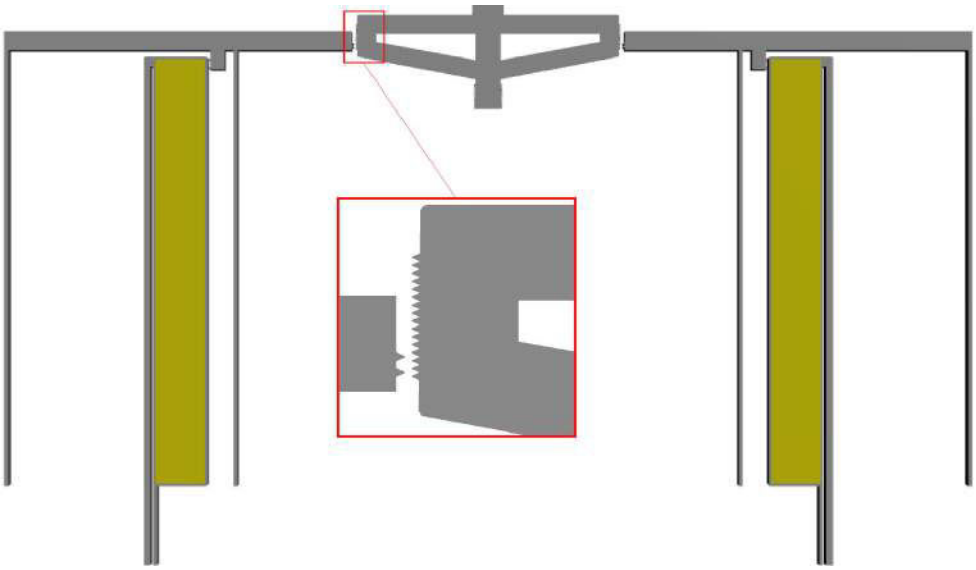

FIGURE *4.18: Drawing of system 3 including S_3 latch, two electrothermal actuator, and a zoom on the teeth between the latch and moving part.*

The activation phase doesn't concerns system 3 where S_3 latch is normally open. Figure 4.19 shows evolution of the retracting forces in each gantry of S_3 latch after deflection.

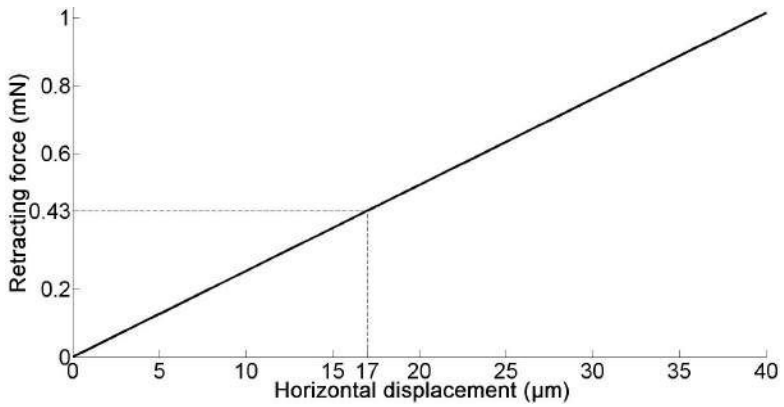

FIGURE *4.19: Evolution of the retracting force after deflection of the gantry of the latch in system 3.*

The gantries dimensions were chosen in order to reduce the retracting forces as possible. An horizontal distance of around $d_{s3} = 17\mu m$ exists between the open and closed configurations for each gantry. The loads on the actuator in system 3 are decomposed in three parts: firstly, the actuator will move a free distance, then it will push the gantry until closing on the moving part,

after that, the actuator is blocked in displacement. The retraction force constitutes a load on the actuator during closing and is the driving force for opening the latch.

As for the moving part, its butterfly shape allows reducing the horizontal extension of the gantries. Longer extensions can amplify minimal rotations in the displacement of the teeth during closing and opening.

In the other side, curved beams are used in order to maintain the moving part and to guide a vertical displacement as shown in Figure 4.20.

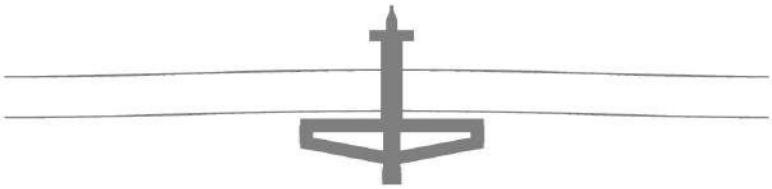

FIGURE *4.20: Moving part of the multistable module connected to curved beams.*

Dimensions of the curved beams are as follows ($l = 6.8mm$, $h = 60\mu m$, $t = 15\mu m$, $b = 100\mu m$). These dimensions are chosen, with the help of the works made in Chapter 2, to define the stroke of the moving part and to reduce the snapping forces as possible.

The stroke of the moving part is equivalent to $120\mu m$ decomposed to 12 steps of $10\mu m$ and 13 stable positions. Thus, the teeth are designed to have 13 engaged positions with the latches. The as-fabricated curved beams form is buckled upwards, the as-fabricated position of the moving part is the initial position while the other positions are in the downward direction. Figure 4.21 shows evolution of the snapping forces (calculated analytically) of the curved beams during deflection and after each step.

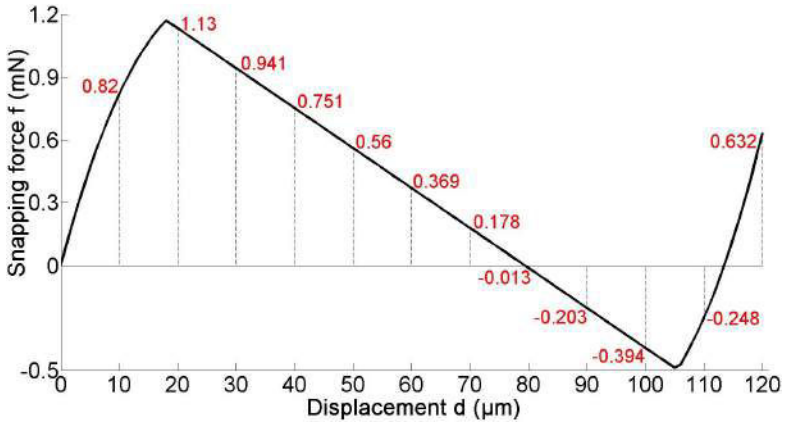

FIGURE *4.21: Evolution of the snapping forces of the curved beams connected to the moving part after deflection and their values at each stable position.*

Positive values of the snapping forces in Figure 4.21 are helpful when the actuators in system 1 are pushing the moving part upwards and have an opposite contribution when the curved beams of system 1 are pushing the moving part downwards. Thus, the greatest loads on the

actuators of system 1 exists during transition between 100 and 110μm while the lowest driving force of the curved beams of system 1 in the downward direction is between 10 and 20μm.

4.6 Multistable module global design

The stable positions of the moving part are robust due to the robustness in the positioning of S_2 latch in its first position. The holding forces on the moving part in both upward and downward directions at each stable position are shown in Table 4.1. Position 1 in the table is the higher one and position 13 is the lower one.

TABLE *4.1: Holding forces on the moving part in the upward and downward directions at each stable position.*

Position number	holding force (mN) upward direction	holding force (mN) downward direction
1	4.39	10.10
2	3.57	10.92
3	3.26	11.23
4	3.45	11.04
5	3.64	10.85
6	3.83	10.66
7	4.02	10.47
8	4.21	10.28
9	4.40	10.09
10	4.59	9.90
11	4.78	9.71
12	4.64	9.85
13	3.76	10.73

The holding forces in Table 4.1 are calculated with respect to the holding force of the S_2 latch in its first position and to the snapping forces of the curved beams at each position (Figure 4.21).

The retention force is defined as the maximal vertical force that can be applied on the moving part before loosing retention with the latches at the engaged teeth. This force is difficult to be estimated previously since the roughness of the sidewalls in the device layer variates with the fabrication parameters, and especially with complicated geometries such as the juxtaposed teeth as in our case. The holding forces in Table 4.1 are calculated with considering that the retention force is more important than the holding forces.

Figure 4.22 shows a drawing of a prototype of the multistable module. The total planar dimension of the multistable module is equivalent to 12×11 mm including the support, conductive lines and the active parts.

The different electrothermal actuators are connected electrically to the pads at the bottom edge of the multistable module through conductive lines in the gold layer as shown in Figure 4.22. Each conductive line with its correspondent pad are separated electrically from the device

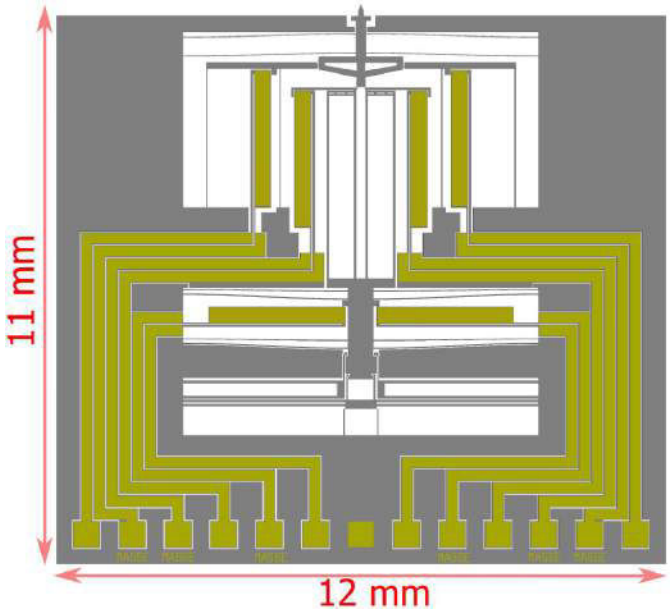

FIGURE *4.22: Drawing of the multistable module including the support, conductive lines and the different systems.*

by etching their borders till the buried oxide layer which is an electrical insulator. One other pad is deposited in the middle between the other pads in order to impose the electrical potential of the device. The electrical connectivity with the external circuit is made through wire bonding as explained in Chapter 5.

The design of the multistable module combines advantages of digital microrobotics, monolithic structures, compliant and unlimited multistable mechanisms. The multistable module can be used for accurate positioning applications in MEMS. The module is able to be integrated in more complex systems for more advanced tasks and the design can be changed for other number of stable positions and other step dimensions.

4.7 Multistable modules in the DiMiBot

The principle and the design of the multistable module was shown in the previous sections. In this section, the global design of the multistable DiMiBot is investigated. The multistable module is used in the design of the new DiMiBot as explained previously in Chapter 1. Figure 4.23 shows a drawing of the multistable DiMiBot.

Two multistable modules are used in the structure of the DiMiBot. The actuators in each module are connected to the pads at the bottom through conductive lines. An additional pad in the middle is used to impose the electrical potential of the structure. The moving part of each module are connected to the end effector through beams and compliant hinges. This head mechanism allows transmitting the displacement between the modules and the end effector. Its kinematics was investigated by Chalvet in his thesis [12] and was used in the old DiMiBot.

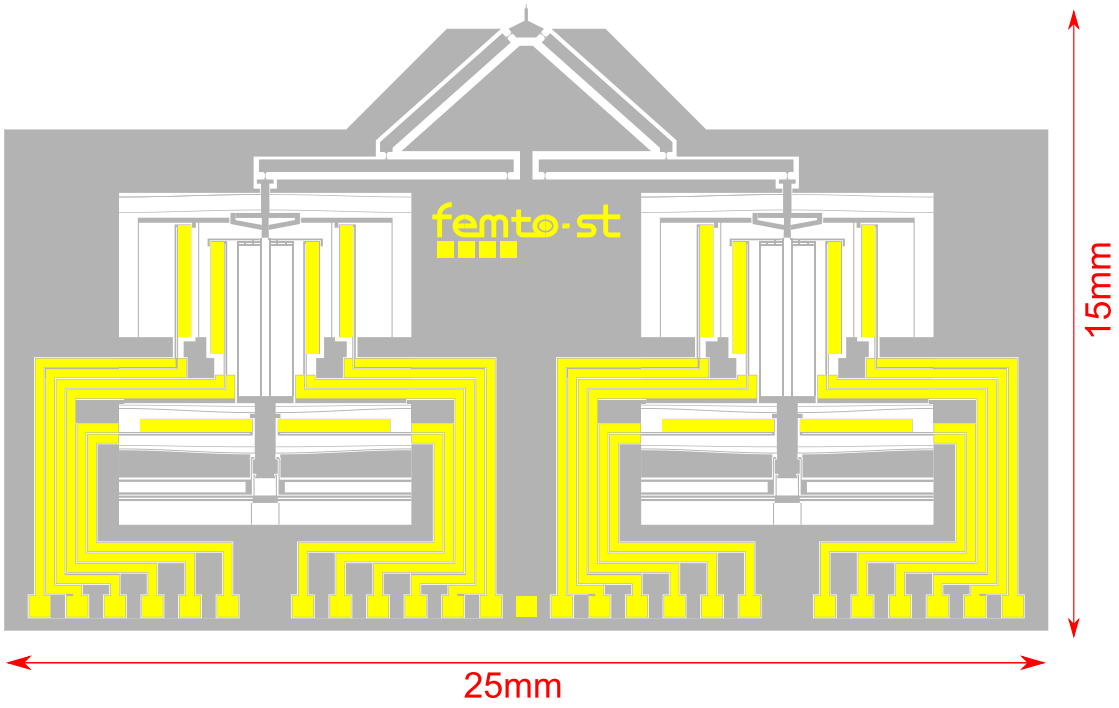

FIGURE *4.23: Drawing of the multistable DiMiBot including the multistable modules, the support, the conductive lines, and the top head mechanism relating the moving parts to the end effector.*

In contrast to the old DiMiBot, the support is extended as shown in Figure 4.23 to protect the structure of the head mechanism. Figure 4.24 shows a drawing of the head mechanism, the hinges dimensions and the end effector.

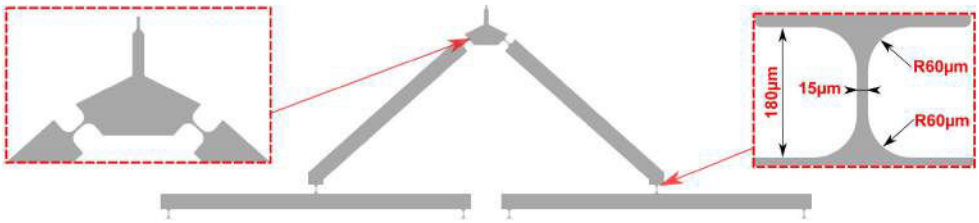

FIGURE *4.24: Drawing of the head mechanism at the head of the DiMiBot including the end effector, the beams and the compliant hinges.*

The two middle hinges in the bottom of the head mechanism are clamped to the structure while the hinges at the sides are related to the multistable modules. The other hinges relate the beams and the end effector. The mechanism is symmetric between the two sides of the DiMiBot. All the hinges have the same dimensions shown in Figure 4.24.

The beams are wide enough to neglect their elastic deformation during functioning. Dimensions of the hinges and of the beams, and the structure of the end effector are chosen in

order to reduce the stiffness of the mechanism as possible and to obtain a square and symmetric workspace.

Figure 4.25 shows the workspace of the DiMiBot that is obtained with the chosen dimensions in the prototype.

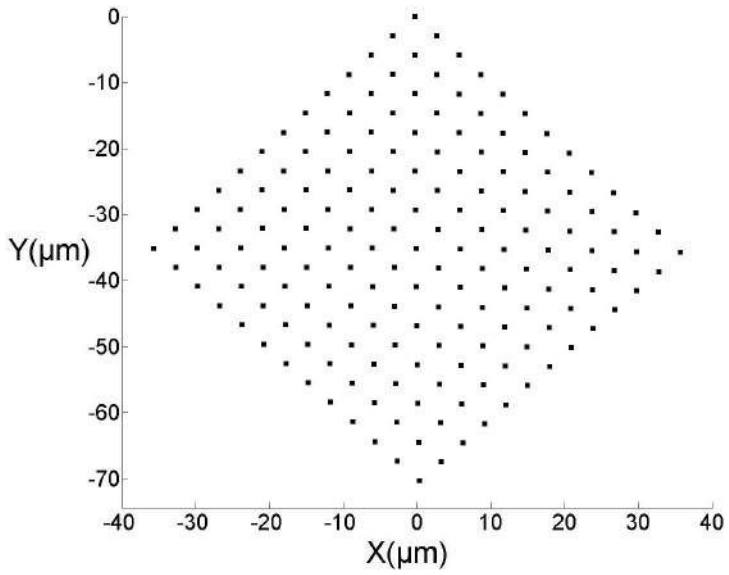

FIGURE *4.25: Workspace of the DiMiBot which consists of 169 discrete positions.*

The workspace consists of $13 \times 13 = 169$ discrete positions which are obtained with respect to the different stable positions of the multistable modules. Dimensions of the workspace is around $50 \times 50 \mu m$.

The head mechanism adds another load on the moving part of each multistable module. FEM simulations showed a linear evolution of the retracting forces with the vertical displacement of a bottom hinge at a side when the other bottom hinges are constrained. The displacement of the hinge corresponds to the displacement of the moving part of the multistable modules. The stiffness of the displacement at one side is not the same when the moving part in the other side is at the different stable positions. Figure 4.26 shows evolution of the retracting force in the bottom left hinge (Figure 4.24) when the left and right modules are in the different stable positions.

As shown in Figure 4.26, the retracting force increases linearly with the displacement in the two sides. The retracting force is at the maximum when the moving parts in the two sides are in the farthest positions from the initial state. Dimensions of the head mechanism allowed reducing the retracting force to less than $0.6mN$ at its maximum. Table 4.2 shows the minimal holding forces at each position of the moving part of each multistable module in the DiMiBot.

The retracting force of the head mechanism plays a negative role for the holding forces in the upward direction while it plays a positive role in the downward direction. Thus, the minimal holding forces in Table 4.2 are calculated differently between the two directions. In the upward direction, they are calculated with considering that the moving part in the other side is in the last position. In contrast, the holding forces in the downward direction are calculated when the moving part in the other side is in the first position.

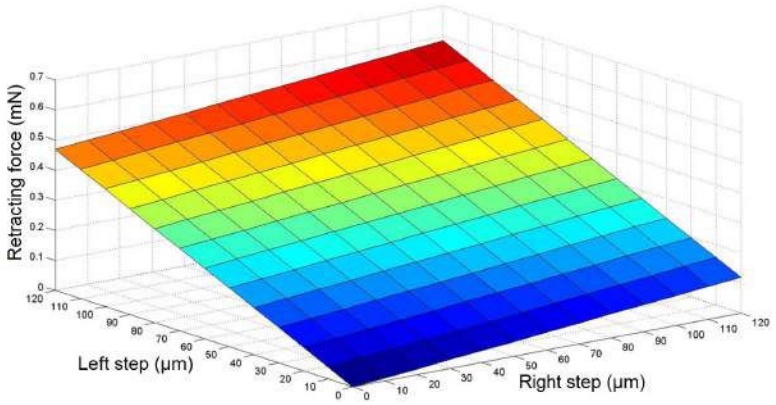

FIGURE *4.26: Evolution of the retracting force in the bottom left hinge when the left and right modules are in the different stable positions.*

TABLE *4.2: Minimal holding forces of the stable positions of the multistable module in the DiMiBot.*

Position number	holding force (mN) upward direction	holding force (mN) downward direction
1	4.27	10.10
2	3.41	10.96
3	3.06	11.31
4	3.21	11.16
5	3.36	11.01
6	3.52	10.86
7	3.67	10.71
8	3.82	10.55
9	3.97	10.40
10	4.12	10.25
11	4.27	10.10
12	4.09	10.28
13	3.17	11.20

In addition, a vertical force applied to the end effector will be divided approximately 4 times on the bottom hinges of the head mechanism. Thus, the real force applied to the moving part of each multistable module is approximately the external force divided 4 times.

In my thesis, the works has focused on the design of the multistable module with the different components. The structure of the head mechanism is the same as in the old DiMiBot. Some drawbacks of this mechanism still exist, including the lack of holding forces at the end effector and the square workspace distribution which is related to small displacement conditions. The improvement of these drawbacks was not a part of my thesis, this part of the work is left for the prospects.

The robustness of the multistable module is loosen in the DiMiBot due to the use of the head mechanism. As explained in this chapter, the multistable module is designed to hold positions

of the moving part in front of external loads with some limits of robustness. The positioning robustness is characterized by the holding forces calculated in Table 4.1. However, considering that the bottom hinges of the head mechanism are totally constrained, the structure of the head mechanism doesn't allows keeping stable the discrete positions of the end effector after applying external loads, especially in the horizontal direction.

In addition, the kinematics of the head mechanism is calculated with considering a small deformation hypothesis [12]. For large deformation, the discrete positions in the workspace are not distributed uniformly and the shape of workspace is not a square with rectilinear sides but mostly a quadrilateral with arc sides. Thus, for higher workspace dimensions, the length of the beams in the head mechanism must be increased sufficiently to consider the small deformation hypothesis.

The dimensions of the head mechanism that allow defining a step dimension in the workspace can be chosen using the inverse geometric model in [12]. However, the geometrical model is not sufficiently precise due to the small deformation hypothesis, it remains difficult to ensure an accurate and uniform step dimension in the workspace.

Further, the compliant hinges are the weakest points in the structure. Many prototypes of the multistable DiMiBot were broken at the hinges, either in the fabrication process or during manipulation. In the other side, the retracting force evolves rapidly with larger hinge dimensions. In the design, a compromise must be made in terms of the hinge dimensions by accepting higher in order to strengthen the structure of the hinges.

4.8 Conclusion

The principle and design of a new generation of a multistable module and the DiMiBot was presented in this chapter. The design of the different components and each system in the multistable module, and the global structure of the module and the DiMiBot was presented. The multistable module allows switching its moving part between several stable positions linearly in a one dimensional direction. An accurate positioning mechanism is used in order to ensure accurate steps and to compensate the fabrication tolerances. Only two multistable modules are used in the new generation of the DiMiBot to realize planar positioning. The fabrication process and the experiments made on some operational multistable module prototypes are presented in the next chapter.

Chapter 5

Fabrication and experiments

This chapter deals with the fabrication process followed in the thesis and the experiments made on the fabricated prototypes. The general steps in the fabrication process are cited, each fabrication step is detailed and the layout of the prototypes in the wafers are presented. The experiments are then presented, they include force measurement experiments, the experiments on U-shaped actuators and finally experiments on some operational prototypes of the multistable module. All the difficulties encountered and solutions provided in the fabrication or the experiments are detailed in the chapter.

Chapter contents

5.1 Introduction

In the previous chapters, the theoretical works were presented including the state of the art, the modeling and design of the preshaped curved beams and U-shaped actuators, and the design of the new multistable module and DiMiBot. In this chapter, the fabrication and experiments are presented.

In this thesis, two runs of fabrication were made in the clean room MIMENTO. The fabrication is made on SOI wafers using bulk micromachining fabrication techniques. Some differences are made in the fabrication process in order to avoid the problems encountered in the previous thesis. Fabrication tests (lithography, etching, metal deposition, etc.) were made before and during the fabrication runs to validate the process and to define the different parameters for each fabrication step.

The fabrication process is clarified in the first section. Layout of the prototypes fabricated and used in the experiments are then presented. The technical aspects, difficulties and solutions for each step in the fabrication are subsequently presented.

The experiments are presented in the second part of the chapter. Force measurement experiments were made for identifying the stiffness and geometric parameters of the fabricated structures and for measuring the snapping forces of the bistable curved beams. Experiments on the U-shaped actuators were also made in situ in a micromanipulation station under a microscope and a high speed camera.

The final section concerns the experiments made on some operational multistable modules. The different aspects of the experiments are presented including the wire bonding, the electronic circuit, the sequence orders, and the experimental functioning. The fabricated prototypes of the multistable module showed a proper functioning in the experiments, this validates the principle and design of the new multistable module.

5.2 Fabrication process

5.2.1 General process flow

Various prototypes were fabricated in the thesis either for testing the behavior of several components or for realizing operational prototypes for the new generation of the DIMIBOT and the multistable modules. The fabrication is realized on SOI wafers, the silicon device layer has a single-crystalline form with (100) orientation . This material is used due to its important properties previously cited. The device layer is highly doped (p-type) in order to reduce the electrical resistivity and to supply the actuators with low voltages.

Some improvements were made in the fabrication process with respect to the previous thesis to avoid previously encountered problems. The fabrication steps in the previous thesis are recalled and the difficulties encountered are clarified in this section, followed by our fabrication process and the improvements being made. Figure 5.1 shows the main steps in the previous fabrication process.

The silicon etching in the previous process was made with non homogeneous openings which have common areas between the two sides. The non homogeneous openings lead to non homogeneous etching speed of the silicon layers and different patterns quality and tolerances

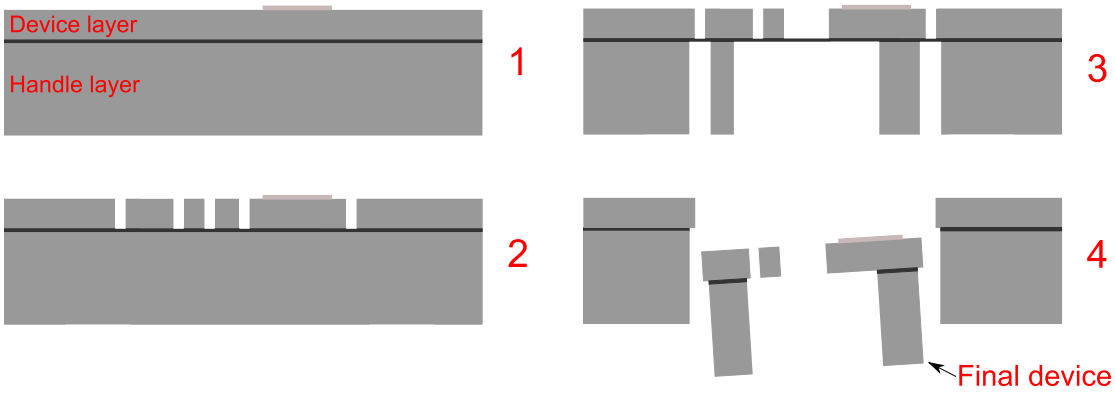

FIGURE *5.1: Fabrication process steps in the thesis of Vincent Chalvet [12]. Aluminum layer deposition and patterning (1), device and handle layers etching using DRIE process (2-3), structure releasing from the wafer using RIE of the buried oxide (4).*

throughout the wafer. The wide openings are etched faster than the smaller ones, this means that when the small openings are totally etched, an excess of etching occurs in the wider ones.

Further, a large volume of silicon is etched which is not effective for the etching process where generally the etching area must be less than 30% of the total wafer area. In addition, the wide and opposite common openings in the two sides of the wafer leave a lot of portions suspended by solely a very thin layer of oxide. All of these factors make the structure of the wafer weaker in the etching and is susceptible to explode or to fail in the weak points.

In the last step, where the buried oxide is etched (RIE process) from the bottom, the clamping and the poor cooling conditions during RIE etching add constraints on the wafer which is already fragile, leading to the loss of most of the devices.

For these reasons, we have made some variations in the fabrication process in order to improve the fabrication conditions, reduce the fabrication tolerances and failure risk. Figure 5.2 illustrates the main steps in our fabrication process. These steps are shown to fabricate the same device as in Figure 5.1.

In the first step, the hard mask in the backside is lithographically patterned and etched using a photomask (Photomask A). In the second step, a gold layer is sputtered, then patterned using wet etching through a photoresist layer which is patterned with a second photomask (Photomask B). In the third step, the device layer is patterned lithographically through a third photomak (Photomask C) and then etched using a deep reactive ion etching (DRIE) process. In the fourth step, the handle layer is etched by DRIE through the backside SiO_2 layer. Finally, the last step consists in releasing devices from the wafer using HF wet etching. Useless parts fall into the HF solution during etching.

The main differences with respect to the previous process include the HF releasing, homogeneous etching and backside hard mask. The HF releasing is chosen in order to avoid the problems related to RIE releasing previously encountered. However, the aluminum (which is compatible with the previous process) peels off directly with HF solution, therefore, it is replaced by gold which is resistant to HF.

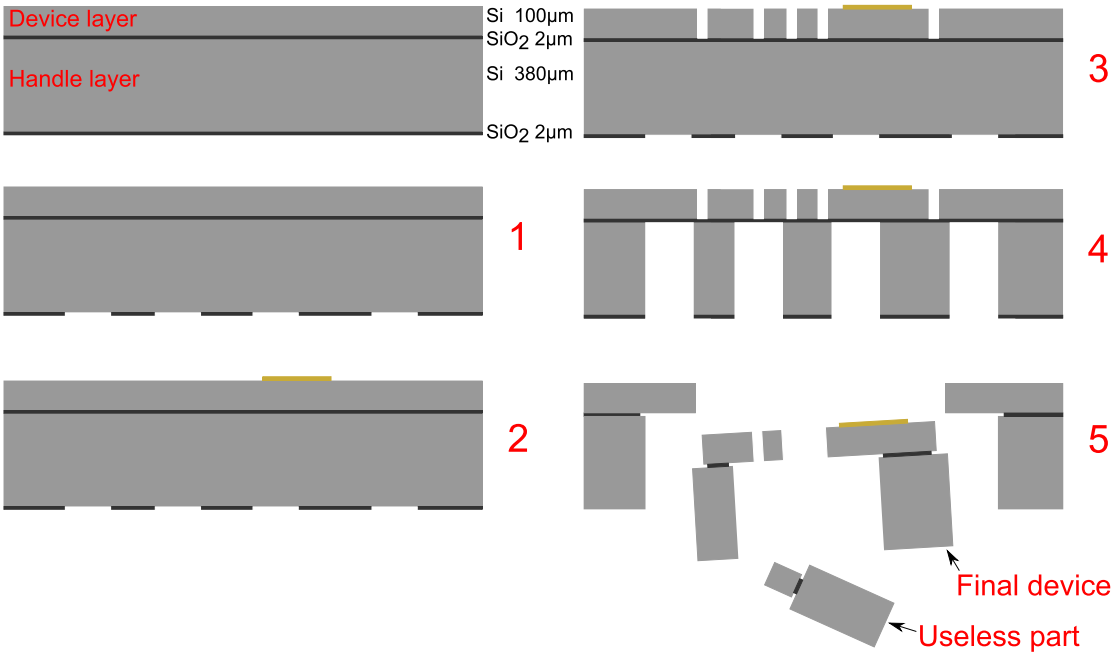

FIGURE 5.2: *Fabrication process steps. SiO_2 hard mask etching on the backside (1), gold layer deposition (2), device and handle layers etched using DRIE process (3-4), structure releasing from the wafer using HF wet etching (5).*

In addition, the opening width of silicon layers is unified in our process ($20\mu m$ in the device layer and $100\mu m$ in the handle layer) in order to ensure an homogeneous etching throughout the wafer. In result, a great number of useless parts (parts which must be removed but are not etched) are released in the HF solution while they were etched totally in the previous process.

Further, the openings in the two sides of the wafer have no common areas but are separated by a releasing distance. The buried oxide along this distance is transversally etched by the HF solution in the releasing step. This distance is unified in the wafer in order to ensure that all the structures in the wafer are released at the same time approximately.

Furthermore, the higher thickness of oxide layer ($2\mu m$ instead of $1\mu m$ in the previous process) and the added backside layer in the new wafer serve for improving the hardness of the wafer during silicon etching.

5.2.2 Layout

After choosing the process and creating the design, the first step in the fabrication is to realize the photomasks. The photomask is a patterned chromium coated glass, the pattern information (layout) is created in a CAD software and transferred to a laser or e-beam writer, then printed in a layer of photoresist coated onto the chromium plate. The imaged pattern on the photomask is then developed and the chromium is etched away where the resist is clear.

Three photomaks are used in the fabrication process steps (Photomasks A, B & C) as shown previously. The layouts are created in the same CAD file but in different layers, each layer

corresponds to a photomask. The different prototypes or components to be fabricated are drawn in a cell individually, then all the cells are distributed in the main wafer layout. In this way, variating the design of several prototypes from the same type can be made one time at the cell level. Figure 5.3 shows an example of the layout in the cell of a multistable module.

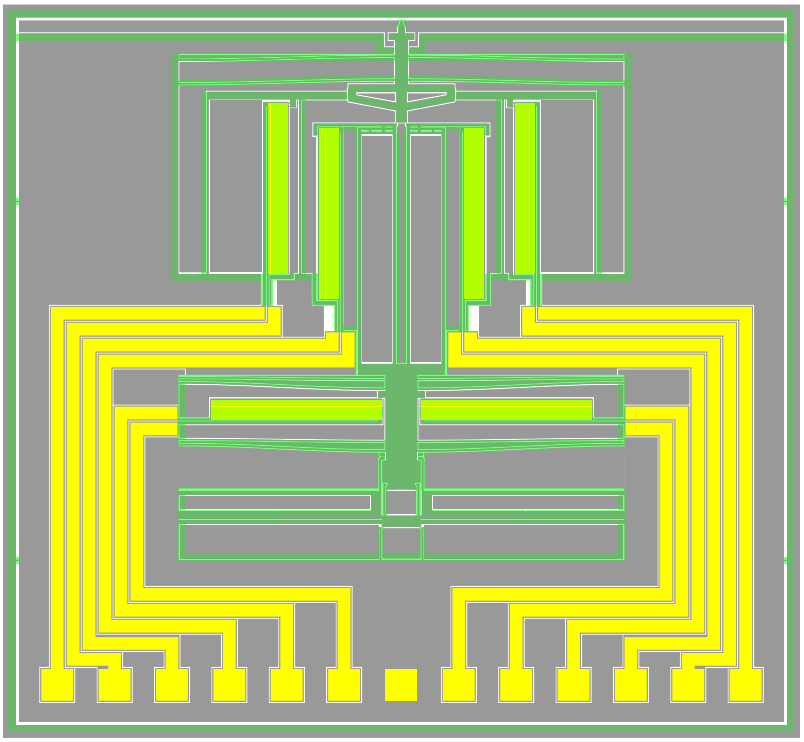

FIGURE *5.3: Example of the layout in the cell of a multistable module.*

The different layouts are differentiated by color. The green part is patterned on photomask A, it corresponds to the openings in the backside hard mask (step 1 in the fabrication process) and then etched in the handle layer (step 4). The yellow part is patterned on photomask B, it corresponds to the gold layer that is deposited and patterned on the top of the device layer (step 2). The gray part corresponds to the layout of the device layer (Photomask C). The openings in this part correspond to the openings in the device layer of the wafer (step 3).

Using these cad layouts, Figure 5.4 shows evolution of the state of the prototype in the SOI wafer during various fabrication steps. A top view of the prototype at its initial state is shown in (a), the gold patterns are deposited on the top of the device layer (after step 2) (b), the device layer is etched (step 3) (c), the handle layer is etched and the useless parts are released (steps 4 & 5) (d).

After that, the prototype is separated from the wafer by simply pressing mechanically on the thin links with the substrate using an external tool (probe, tool). A top and bottom views of the multistable prototype after releasing are shown in (e) and (f) respectively. The color of the handle layer is dark just to distinguish it. However, in other cases, the prototype is made to make

in-situ experiments directly on the wafer. The substrate of these prototypes is not separated from the substrate of the wafer.

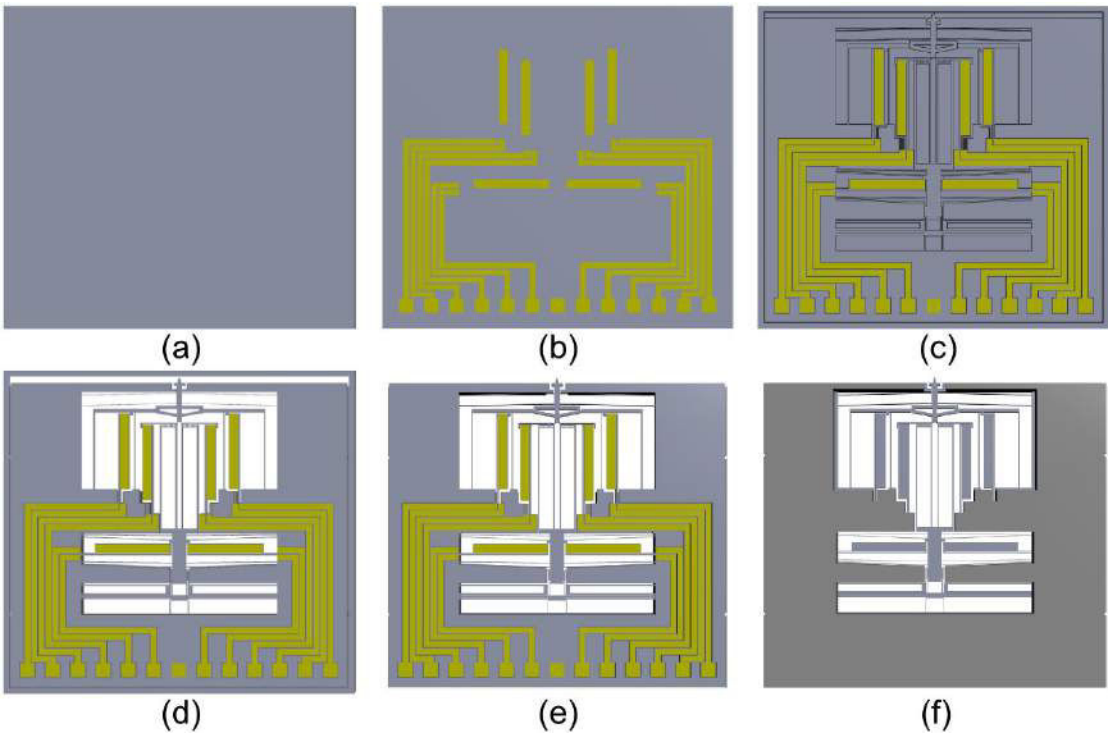

FIGURE *5.4: States of a multistable prototype in the wafer during the fabrication process. top view at the initial state (a), after deposition of the gold patterns (b), after etching the device layer (c), after releasing the useless parts (d), after releasing the prototype from the wafer, top view (e) bottom view (f).*

The fabrication process and layout principles were demonstrated in the case of a multistable module. However, various designs of the multistable module were inserted in the layout. These designs are different in a local feature such as the teeth dimensions, shuttle of system 1, modules with elastic loads etc.. The variation in these designs is made to test the functioning of these features.

The same for the other prototypes (DiMiBot, bistable beams, actuators, etc.) where several designs for the same prototype are placed in the wafer. A quick illustration of the layout of the different prototypes used in the experiments is presented in the following without details. The layouts presented are for the final prototype where the useless parts and backside etching are not shown.

DiMiBot

Layout of the new generation of the DiMiBot with multistable modules is shown in Figure 5.5. Its structure was presented in Chapter 4.

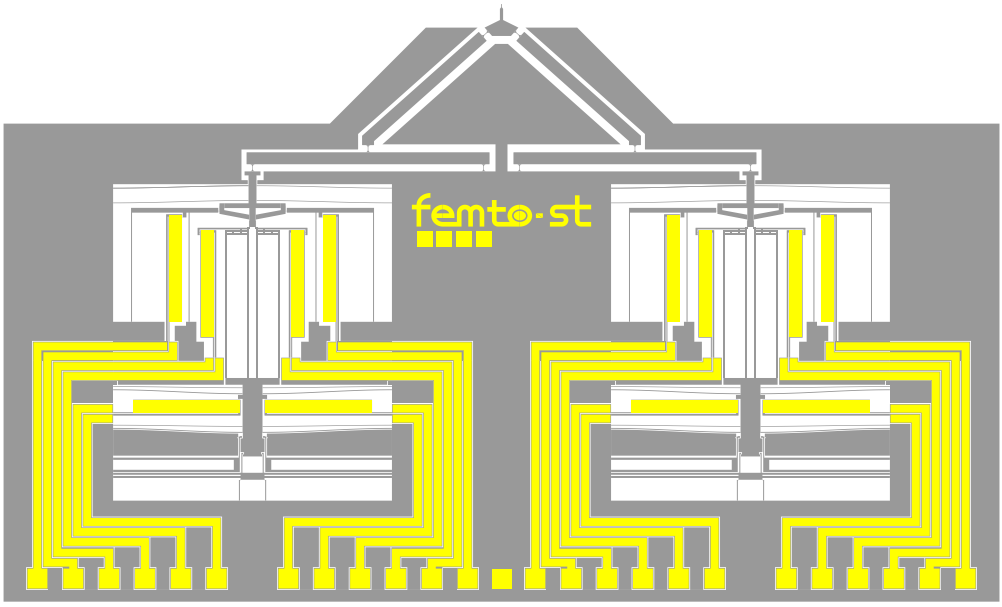

FIGURE *5.5: Layout of the DiMiBot with multistable modules.*

Bistable module

Figure 5.6 shows the layout of an accurate bistable module. This module corresponds to the first system in the multistable module. These prototypes are fabricated to make tests for the functioning of the different systems in the multistable module before testing the multistable module.

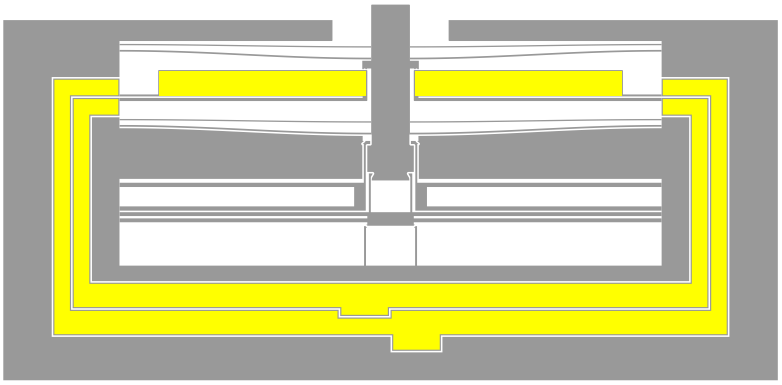

FIGURE *5.6: Layout of an accurate bistable module (system 1).*

U-shaped actuators tests

Prototypes for testing the U-shaped actuators were made, with different dimensions, with and without loads, and with and without gold layers on the cold arms. Figure 5.7 shows a layout of

the actuator prototypes with and without loads. The load is simply an elastic beam in front of the actuator. The gold layer above the elastic beam serves for measuring its electrical potential after contact. A scale is added on the top of each actuator in order to measure its displacement during the experiments.

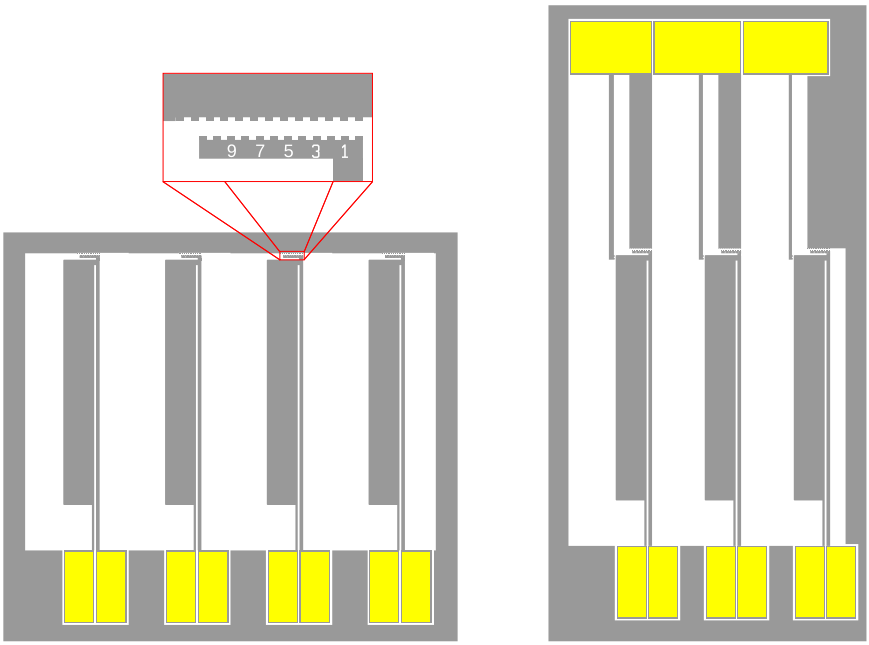

FIGURE 5.7: *Layout of the actuator prototypes with and without loads.*

Curved beams

In addition, prototypes for measuring the snapping forces of hinged and uniform preshaped curved beams were made in the first run of fabrication. As shown in Figure 5.8, the test consists of two curved beams connected by a shuttle in the middle in order to constraint the asymmetrical modes of buckling. In order to solidify the structure, the prototype is connected at the handle layer between two sides of the structure. Prototypes in the wafer consist of three structures as the one in the layout with different curved beams dimensions.

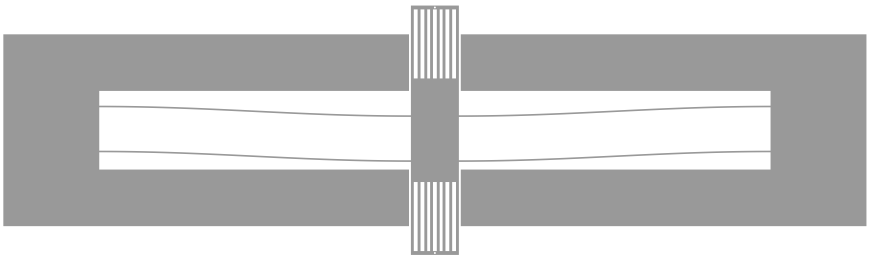

FIGURE 5.8: *Layout of preshaped curved beams test.*

Stiffness tests

Further, Figure 5.9 shows the layout of a prototype for measuring the stiffness of rectilinear beams with various dimensions. This test allows verifying the stiffness of the components in the device layer of the wafers, the fabrication quality and geometric parameters. The experiments on this test and the previous one are made using a force sensor.

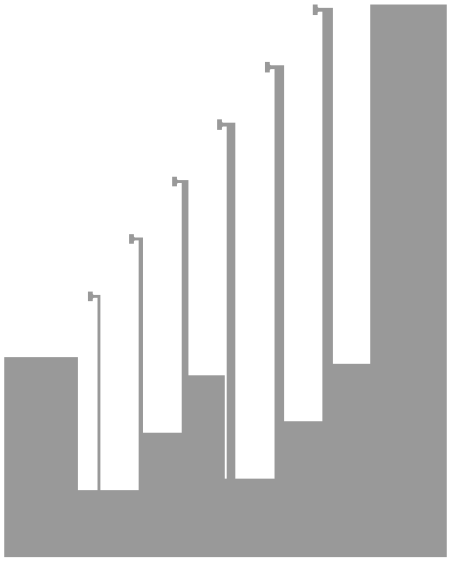

FIGURE *5.9: Layout of a prototype for measuring the stiffness of rectilinear beams.*

All of these prototypes are distributed on the total surface of the wafer. Various other tests are placed in different places on the wafer in order to follow and control evolution of the different steps in the fabrication process, such as etching, lithography etc.. Noting that these prototypes were not fabricated in the same run. Two runs of fabrication were made in the thesis with different layouts. Several difficulties were encountered in each run as will be clarified in the next section.

5.3 Technological aspects in the fabrication process

The general fabrication steps are almost the same between the two runs of fabrication. However, the changes are in the details of each step. These changes were made consecutively with respect to the results and remarks noticed during the fabrication. The different fabrication steps were realized using the facilities in the clean room MIMENTO. The technological aspects and details of each step are clarified in the following.

5.3.1 Hard mask (Photomask A)

The hard mask stands for the silicon dioxide layer in the backside that is patterned and used as a mask for etching the silicon handle layer. The different steps for patterning the backside oxide

layer in the SOI wafer are clarified in Figure 5.10. This layer is used later as a hard mask to etch the handle layer.

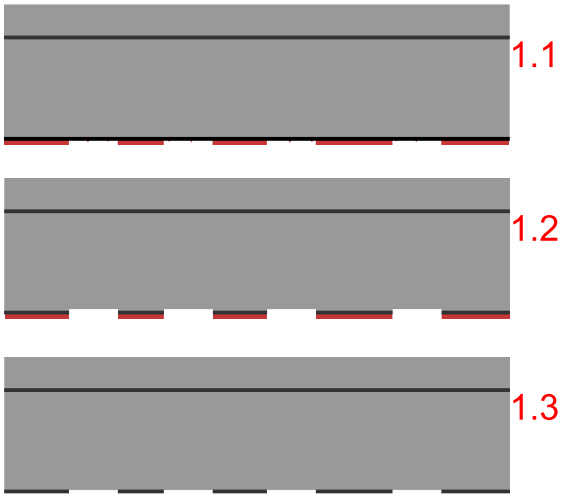

FIGURE *5.10: Process steps for patterning the hard mask in the backside.*

The first step is to deposit a photoresist layer on the bottom of the wafer and lithographically pattern it (step 1.1). After cleaning the wafer with acetone or Piranha, a photoresist layer is deposited by spin coating using RC8 spinner. After that, the photoresist is insolated (exposed to UVs) through the photomask A using an aligner (EV620). The photoresist parts exposed to UVs are then developed using a specific developer solution (positive photoresist). Noting that resting time and heating between each step in the lithography is needed with respect to the photoresist. These steps are repeated at each photoresist patterning process.

The second step is the descumming after lithography (step 1.2). This step is made by exposing the photoresist pattern to plasma in order ensure there is no residual photoresists in the openings. The descuming is made in MIMENTO using the Nanoplas machine or scouring using Plassys 500. This step is recommended since the next step is the wet etching where a very thin layer of residual photoresist may interfere with the etching and may lead to various etching speeds.

The third step is to make the etching by introducing the wafer in a BHF solution. The etching speed is related to the concentration of the BHF solution. For example, the etching speed in the first run was slower than in the second run after several months. Therefore, the etching speed must be measured each time before realizing the etching. Otherwise, dry etching is another solution to realize the etching properly.

5.3.2 Gold patterns (Photomask B)

The second main step in the fabrication process is the deposition of the gold patterns on the top of the device layer. This is the most difficult step in our fabrication process due to the difficulties encountered in the very last step of fabrication where the wafer is inserted in a HF solution to release the different structures.

The necessary time to release the structures in the HF solution was around 30 minutes as remarked in the tests. During this time, the metal patterns peel-off due to the effect of HF acid. This was the main difficulty encountered in the first run of fabrication. For this reason, the different prototypes obtained in the first run are without any gold layer on the top of them. However, we used these prototypes for making some mechanical tests before proceeding to a second run of fabrication.

The gold is used because it is an inert material in HF solutions while a chromium layer is used to enhance the adhesion of the gold with the silicon. However, during the HF releasing, the HF leaks and attacks the metals and oxides under the gold layer. Many tests were made to enhance the resistivity of the metal layer in front of the HF solution either by changing the width or number of layers, or by covering the metals with photoresist, or using lift off etc.. We have been blocked for several months on this issue trying to improve the adhesion of the metal layers in the HF solution. Finally, no important advancements were made in these tests.

Thereafter, we have decided to proceed to the second run of fabrication with trying to reduce the necessary time to release the structures in the HF solution to less than 10 minutes. This can be reached by reducing the releasing distance. This distance was reduced from $30\mu m$ in the first fabrication run to $10\mu m$ in the second run. Fortunately, this solution worked in the second run and operational prototypes were obtained.

Figure 5.11 shows the different steps for sputtering and patterning the gold patterns. Firstly, the metal layers are sputtered on the top of the wafer using Plassys 500 (step 2.1). The metal layers in the final process consist of 4 layers Cr/Au/Cr/AU. The different layers are deposited respectively after scouring the wafer in a vacuum. The metal deposition is made while the wafers are in continuous motion under the electrode which ensures obtaining an homogeneous metal layer throughout the wafer.

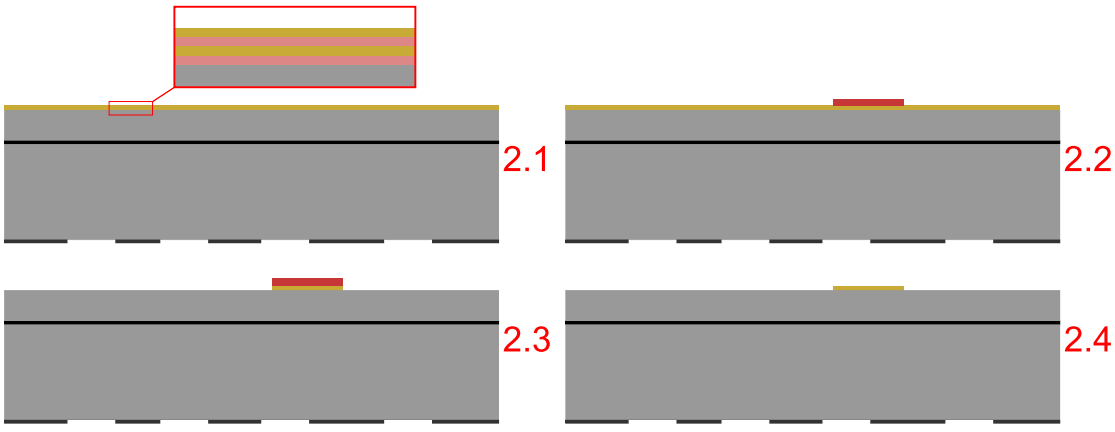

FIGURE *5.11: Process steps for sputtering and patterning the gold patterns.*

After the metal deposition, a photoresist layer is deposited on the metals and patterned lithographically using the photomask B (step 2.2). The photomask is aligned with the patterns in the backside hard mask using the aligner EV620. In step 2.3, the metal layers where the photoresist is clear are etched using specific solutions for each material respectively. This is

made by inserting the wafer in the Au and Cr etching solutions successively. The end of etching in each solution is followed by the color change.

It is recommended to make a descumming phase before the metal etching, but no oxygen must be used because the oxygen attacks the metal layers. The last step is to release the photoresist using acetone in an ultrasonic bath and then rinse it with ethanol (step 2.4).

Figure 5.12 shows a photo of the gold patterns deposited and patterned on a wafer at the end of this step. Reducing the releasing distance in the layout helped us in the second run to release the structures without loosing the gold. So far, we can not consider this process as reproducible since limited number of wafers were tested. Otherwise, if this doesn't work, the other plan is to deposit the metals after the HF releasing through a patterned wafer (Shadow mask).

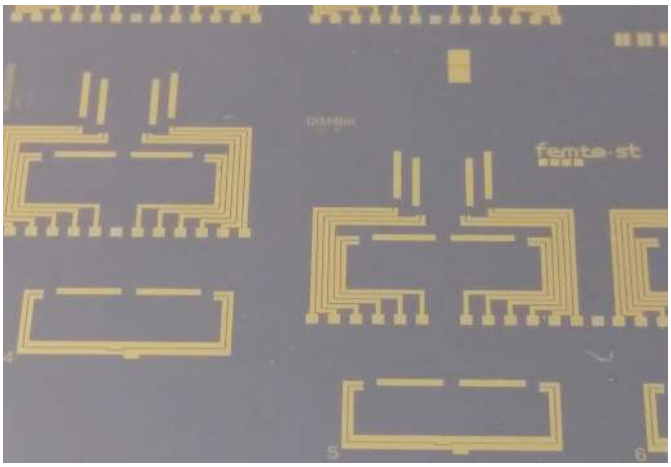

FIGURE *5.12: Gold patterns after sputtering and patterning.*

5.3.3 Device layer etching (Photomask C)

After the deposition of the gold patterns, the next step is the etching of the device layer. This step is usually simple, but it is the most important since the dimensions and sidewalls quality of all the active elements in the wafer are defined in this step. The process must ensure accurate patterns and reduce the fabrication tolerances as possible. In order to ensure that, several tests are made before in order to define the lithography and etching parameters while each process step is verified and controlled in the microscope.

Figure 5.13 shows the different steps for patterning the device layer. Firstly, a photoresist layer is deposited on the top of the device layer and lithographically patterned using the photomask C (step 3.1). The photomask is aligned with the gold patterns in the front. The gold patterns remain covered with photoresist after patterning since there is no openings under the gold patterns.

After lithography, the device layer is etched using DRIE process. The wafer is inserted in a conditioned chamber in the etching machine (SPTS) and exposed to subsequent loops of etching (SF_6) and passivation (C_4F_8). The etching rate and quality is controlled with several parameters including cycle time, gas flow rate, pressure, temperature, etc.. However, these parameters

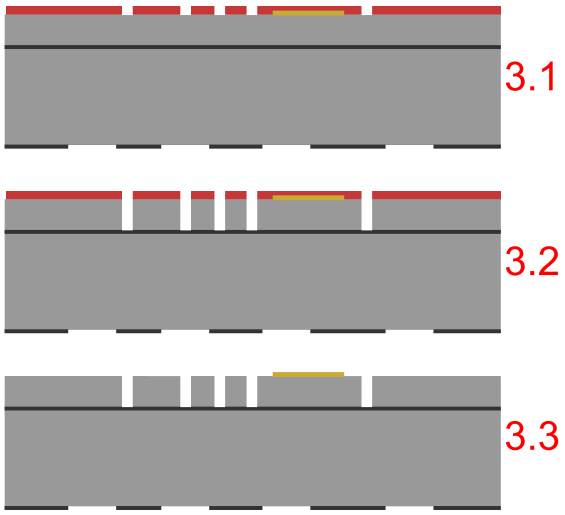

FIGURE *5.13: Process steps for etching the device layer.*

are fixed with respect to the application while the etching depth is controlled in function of the number of loops. Figure 5.14 shows SEM photos of the device layer after etching. The undulating structure at the sidewalls is a result of the subsequent etching loops.

Once the etching is done, the next step is to release the photoresist layer (step 3.3). This step is a bit tricky since the ultrasonic bath cannot be used due to the fragile structure of the device layer after etching. We have lost several prototypes in the first run at this stage where the weak components in the wafer were damaged. Several tests were made to find a solution to remove the photoresist without ultrasonic. After testing, the acetone without ultrasonic and removers with heating were able to remove the majority of the photoresist ($\sim 70-80$ %). However, finalizing with piranha was found to be a solution to remove almost the totality of the photoresist (>98 %). After that, the wafer is dried carefully with low air flow nozzles.

Noting that before etching the device layer in the SOI wafers, we have remarked in some etching tests that the fabrication tolerances lead to an excess of etching of $\sim 1\mu m$ at each sidewall. This distance variates slightly with each etching, but it remains close since the fabrication conditions are not changed. Figure 5.15 shows microscopic photos of the device layer after etching with some dimensions that are changed after fabrication. The first photo is for a multistable module and the other is for a loaded actuator prototype. As shown in the figure, these tolerances were considered in the layout of the main components. For example, thickness of the curved beam and of the actuator arms was raised $2\mu m$ in the layout to compensate the fabrication tolerances.

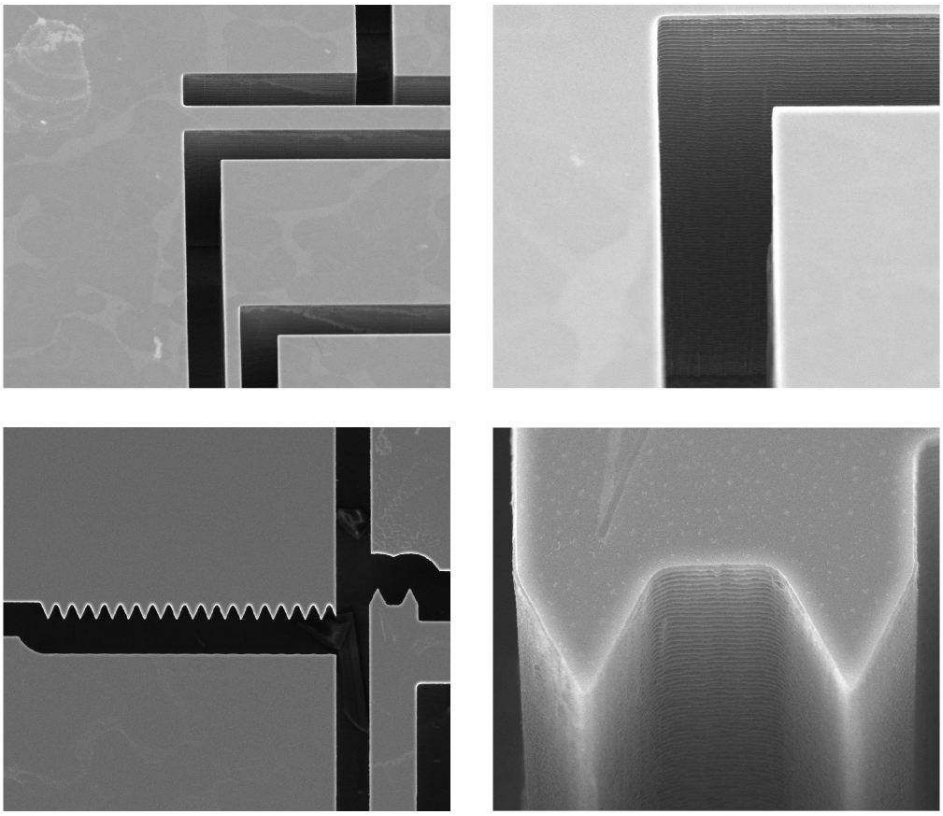

FIGURE *5.14: SEM photos of the device layer in different places.*

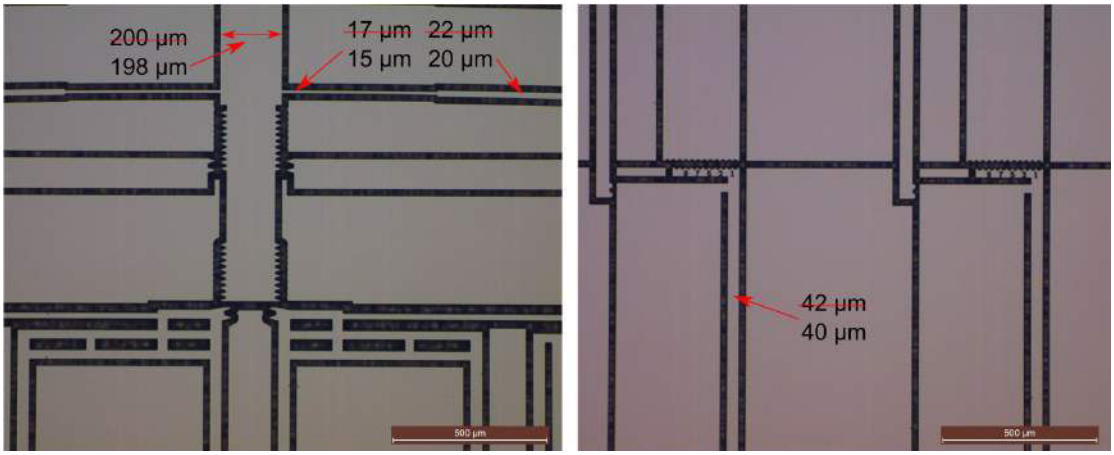

FIGURE *5.15: Microscopic photos of the device layer after etching. Barred dimensions are the layout dimensions, while the others are the real dimensions after fabrication*

5.3.4 Substrate etching

After the device layer, the handle layer is etched. The etching process is also the DRIE process. The removal of the photoresist in the previous step is mandatory where no photoresist is allowed in the backside to hold the wafer during etching in the SPTS.

The backside oxide layer is used as a hard mask which avoided the necessity of a thick photoresist layer to make the deep etching. The accuracy is less important in this step and no specific difficulties were expected.

This was the situation in the first run. However, in the second run after several months, the etching quality was worst, this was the main difficulty in the second run. Excess loops were made to finish the etching throughout the wafer where the etching was not homogeneous throughout the wafer. This problem was worst due to an excess of wet etching in the hard mask in the backside due to the unexpected high speed of etching of the BHF solution. In result, the excess of silicon etching make the weak components more fragile which led to loose several prototypes, most of them are the DiMiBot that are failed mostly at the flexible hinges.

Normally, this problem is not persistent if other fabrication runs are developed. However, we are satisfied in the thesis by the operational prototypes of the multistable modules that showed a proper functioning in the experiments which validate the principle and design of the module. One of the future prospects of the thesis is to launch new runs of fabrication that take into account the remarks and problems encountered in the first two runs of fabrication.

5.3.5 HF release

The last step in the fabrication process is to release the structure using the HF solution In this step, the wafer is inserted in a HF solution, the HF is very selective, it starts to attack the silicon oxide all around the wafer without etching the silicon. The first parts of SiO_2 that disappear are the oxide in the backside layer and in the openings of the middle layer. After that, the HF attacks transversally the oxides in between the up and down silicon patterns.

The distance that must be etched transversally in order to release the structure is the releasing distance as mentioned before and shown in Figure 5.16.a. We have used a specific wafer holder (Figure 5.16.b) to make the releasing. This holder is made by Teflon which is a HF compatible material. The wafer is inserted in the holder on the top of the rings inside, and then the holder is inserted in the HF solution. In this way, the released structures fall into the bottom of the holder due to their weight.

The end of the releasing is recognized by the fall of all the useless parts. At the end of releasing, the wafer is inserted in three baths of ethanol successively for cleaning it and then it is dried by the ambient air. Afterwards, the different prototypes are released manually using an external probe. Some prototypes were released in the HF solution. These prototypes are collected from the holder without problems.

As mentioned before, we have encountered a difficulty with the gold adhesion in the HF solution in the first run of fabrication. Figure 5.17 shows a wafer from the first run of fabrication where the gold patterns started to peel off from the wafer.

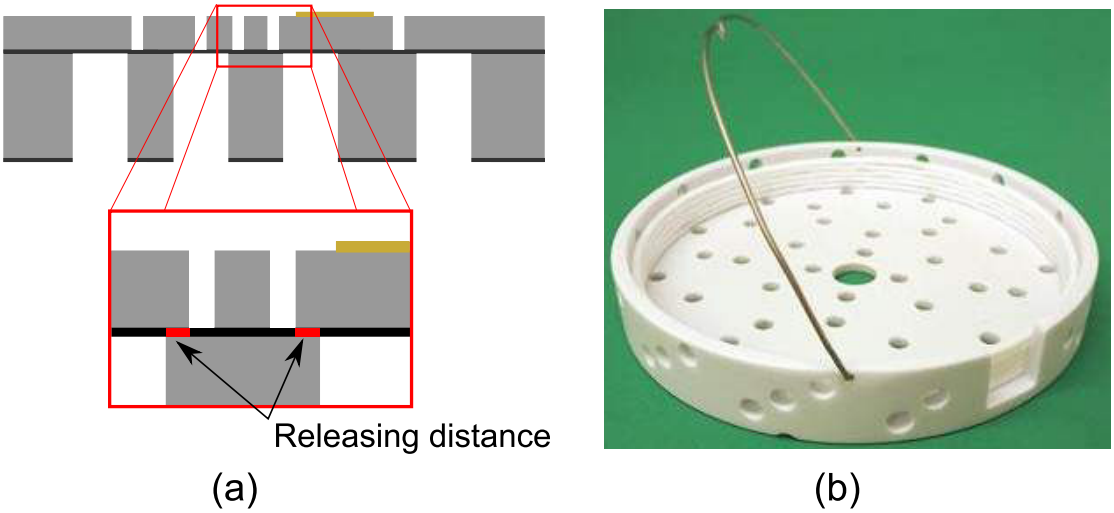

FIGURE *5.16: Zoom on the releasing distance in the wafer before HF releasing (a), HF compatible wafer holder (b).*

FIGURE *5.17: The gold patterns started to peel off from the wafer after inserting it in the HF solution.*

In the other side, this problem was resolved in the second run of fabrication. Figure 5.18 shows a wafer from the second run with operational prototypes where the gold patterns remain attached and all the structures are released.

However, due to some errors in the layout and some accidents, no functional prototypes of the DiMiBot were obtained. A photo of the DiMiBot which have some defects is shown in Figure 5.19. Normally, there is high success possibility for realizing operational prototype of the DiMiBot in future runs of fabrication. However, we have decided to end the fabrication at this level, due to the lack of time and since the multistable modules showed a good functioning

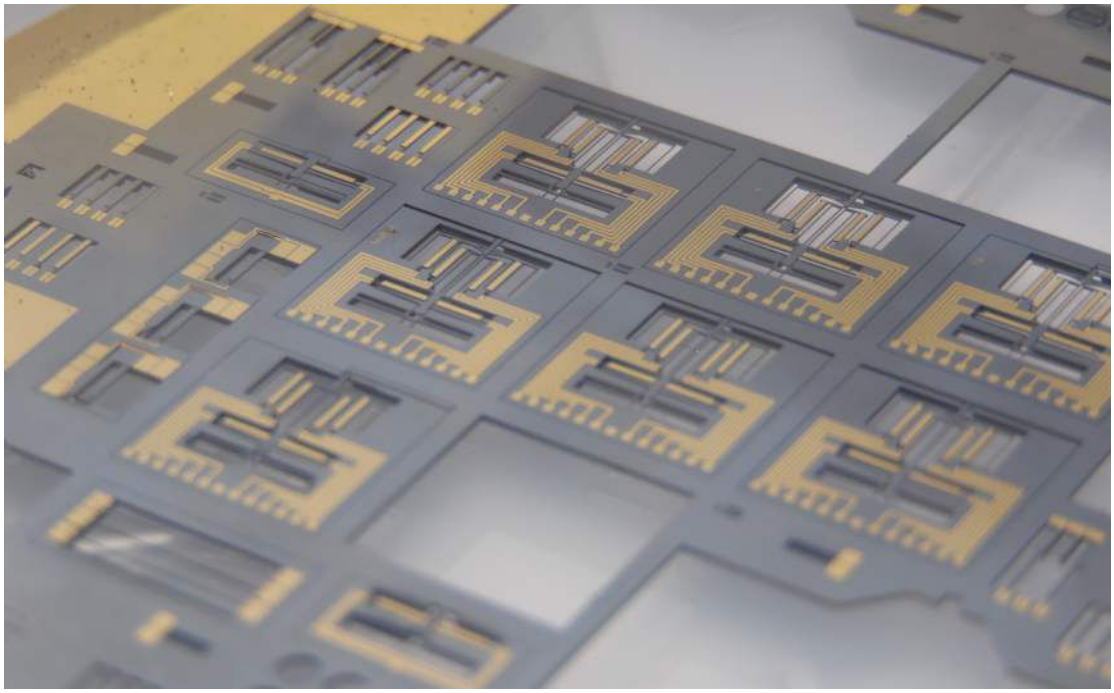

FIGURE *5.18: Wafer from the second run of fabrication where all the structures are released without peeling off the gold patterns.*

as will be shown in the experiments, which validate their principle and design. In the following sections, the experiments on the different prototypes obtained in the fabrication are presented.

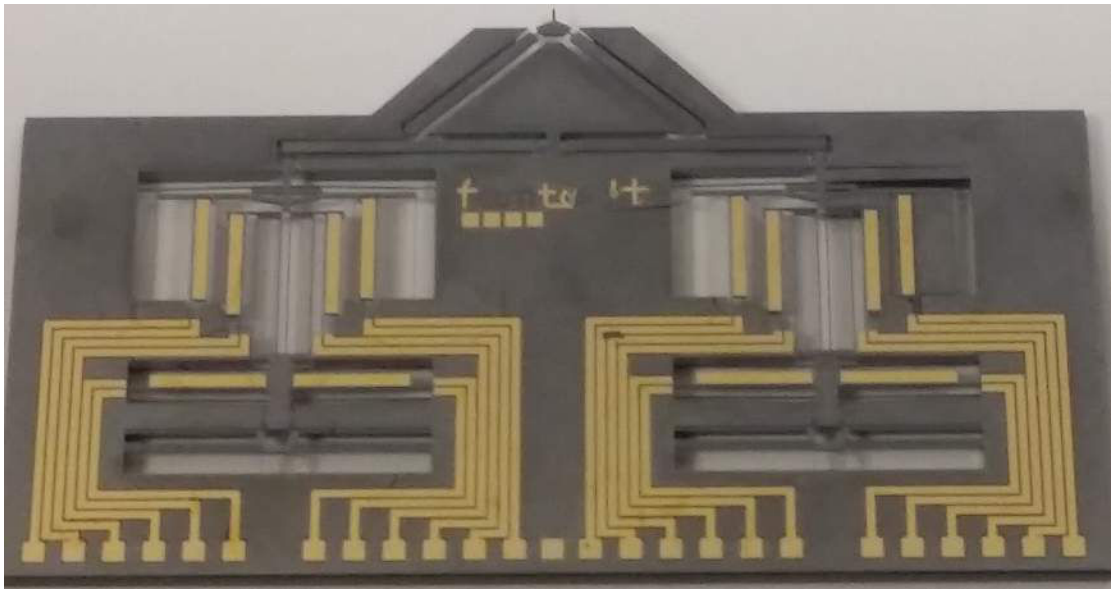

FIGURE *5.19: Prototype of the DiMiBot obtained in the second run of fabrication.*

5.4 Force measurement experiments

Several structures were fabricated in the first run in order to measure evolution of the elastic forces with deformation. These structures include the rectilinear beams (Figure 5.9) and pre-shaped curved beams (Figure 5.8). The prototypes were designed to make the experiments with a Femtotools force sensor which consists of microforce sensing probe capable of measuring forces from millinewtons (10^{-3} N) down to several nanonewtons (10^{-9} N) along the probe axis.

The force sensor in the experiments is mounted on a robotic stage with embedded displacement sensors. The force sensor probe acts mechanically on the prototype after moving it through the robotic stage. Figure 5.20 shows a schematic diagram of the elements used in the force measurement experiments.

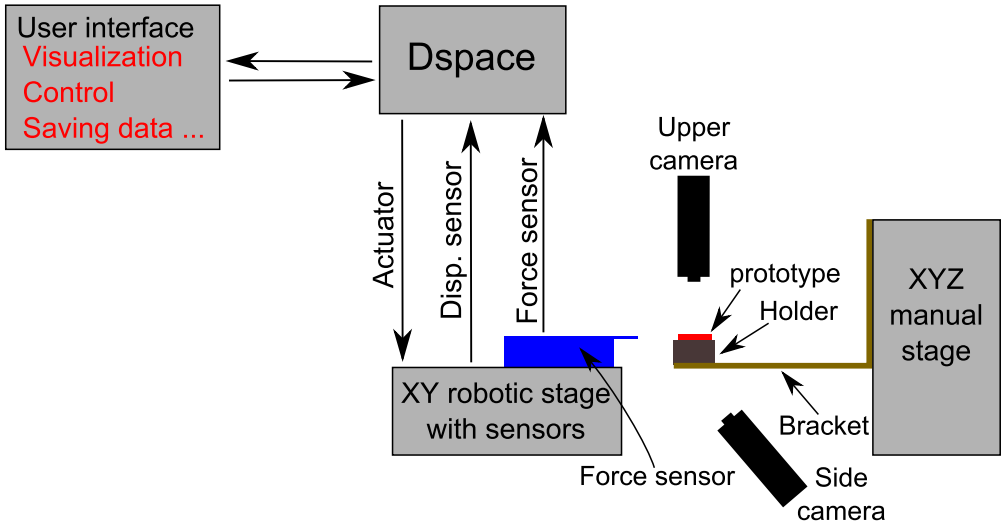

FIGURE *5.20: Schematic diagram of the elements used in the force measurement experiments.*

After releasing from the wafer, the prototype is bonded to a bottom holder, which is fixed on a bracket with a screw. The bracket is connected in the other side to a XYZ manual stage. In this way, the prototype is placed in front of the force sensor probe using the XYZ manual stage. Side and upper cameras, which provide a magnified direct image on two large screens besides, serve for placing and orienting the different components and following up the experiment.

The robotic stage which carries the force sensor is able to generate and measure displacement in two axes in the plane. However, the displacement in our experiments is made only in one direction parallel to the force sensor probe axis. Both the robotic and manual stages are fixed on an anti-vibration table.

A dSPACE real time system is used to collect the data from the sensors (force and displacement) and sending control signals for the displacement of the robotic stage in real time. The input and output signals are visualized and controlled using a PC software.

Before the experiments, the actuator and sensor of the robotic stage (in the axis of motion) are calibrated using an interferometer. The calibration is made by sending a displacement order to the robotic stage and measuring the displacement from two sources: the embedded sensor and

an external interferometer. The interferometer is placed in front of the robotic stage in parallel to its motion axis as shown in Figure 5.21. This allows determining the gain between the robotic stage signals and displacement.

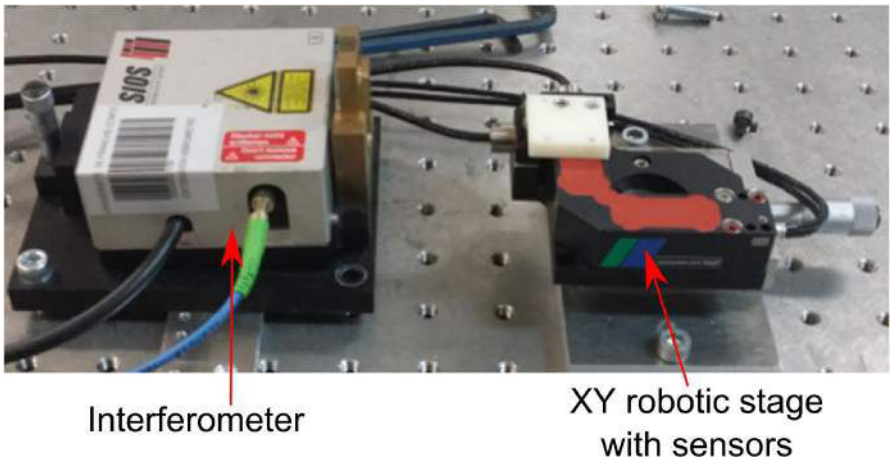

FIGURE *5.21: Calibration of the robotic stage signals (actuator and sensor) using an interferometer.*

After that, the experiment is prepared as explained in the schematic diagram in Figure 5.20. A photo of the experiment is shown in Figure 5.22 with the different components around the prototype and force sensor.

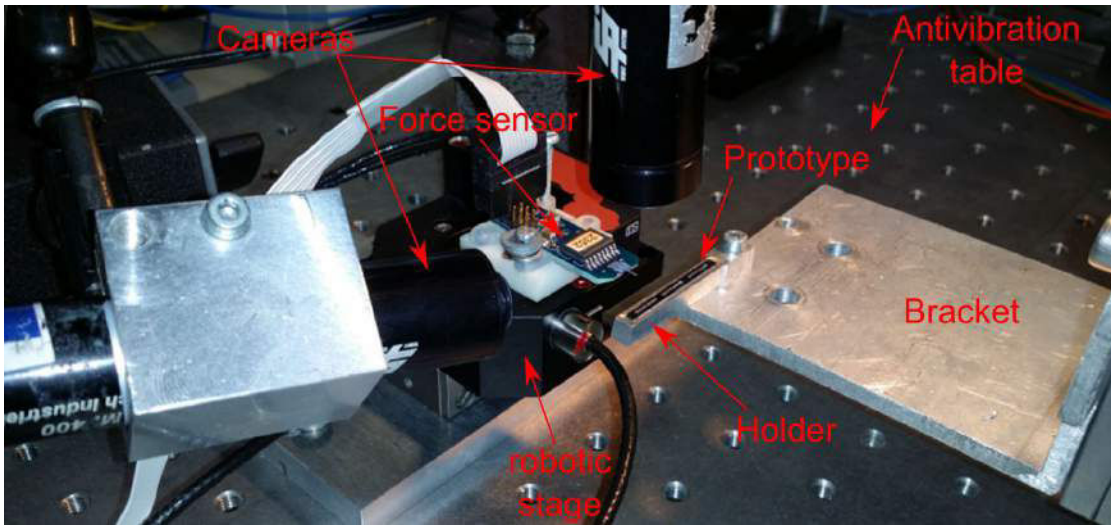

FIGURE *5.22: Photo of the experience using force sensor.*

Curved and rectilinear beam structures, which are bonded to a holder, are used as prototypes for this experiment. Curved and rectilinear beam prototypes are shown in Figure 5.23.a. The direct image from the cameras is displayed on two screens as shown in Figure 5.23.b.

FIGURE *5.23: Curved and rectilinear beam prototypes (a), screens showing a direct image from the side and top of the prototypes and force sensor probe (b).*

5.4.1 Rectilinear beams

The test with rectilinear beams is useful to verify the beam stiffness in the U-shaped actuator tests and in the multistable modules. The stiffness is related to the Young's modulus and the geometric dimensions. Thus, this test allows verifying the Young's modulus, geometric parameters and fabriquation quality.

The rectilinear beams prototype are bonded on the end of a holder as shown in Figure 5.23.a. Otherwise, the probe may be not long enough to reach all the beams in the prototype where the displacement becomes limited due to the contact between the structure of the holder and that of the force sensor.

The experiment on this prototype is made by placing it manually close as possible to the sensor probe and at the same level. The angle of contact is adjusted manually by turning the holder around the screw before tightening. After that, the robotic stage moves the force sensor to make the contact, and then, it continues until the measured force reach a limit defined in the control. Afterwards, the robotic stage comes backs to the initial position.

Figure 5.24 shows evolution of the measured forces with displacement and a comparison with theoretical calculation. These results are for a beam with the following dimensions (as in the layout): thickness $t = 30\mu m$, length $l = 2040\mu m$ and depth $b = 100\mu m$.

The comparison with the theoretical curve shows to be in very good agreement where the force is calculated with the silicon Young's modulus $E = 169GPa$. This indicates a good quality of etching in the fabrication process and validates the value of the Young's modulus. Noting that an excess of etching of $1\mu m$ was taken into account in the layouts. This consideration was made after several etching tests.

5.4.2 Curved beams

As for the curved beams prototype, the experiment is made in two stages, one at each side of buckling. After placing the sensor probe in front of the shuttle of the curved beams, the sensor

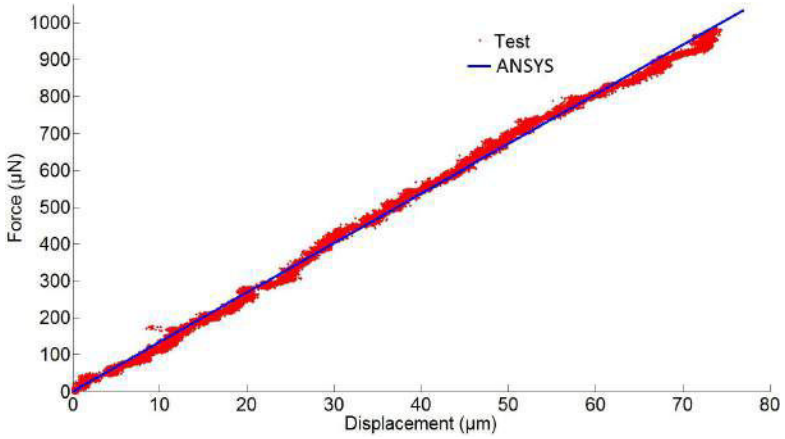

FIGURE *5.24: force curves of a rectilinear beam obtained in the experiment and FEM simulations. The beam dimensions are as follows:* $t = 30\mu m$, $l = 2040\mu m$, *and* $b = 100\mu m$.

probe pushes the shuttle towards the other side of buckling. The snapping force increases after displacement to a maximum (f_{top} in Figure 2.22), and then it decreases to reach the zero force unstable position. After that, the bistable curved beam is switched due to the negative snapping force.

In the second stage, the holder is turned 180°around the screw, the shuttle of the prototype is replaced in front of the force sensor probe, and the same experiment is repeated from the other side of buckling. The results of the experiments in the two stages are then put together to form the snapping force curve of the curved beam prototype.

Figure 5.25 shows the measured snapping curve of a couple of two hinged preshaped curved beams prototype with the following dimensions: $t = 20\mu m$, $l = 6.8mm$, $b = 100\mu m$, $t_{hinges} = 15\mu m$, $l_{hinges} = 500\mu m$.

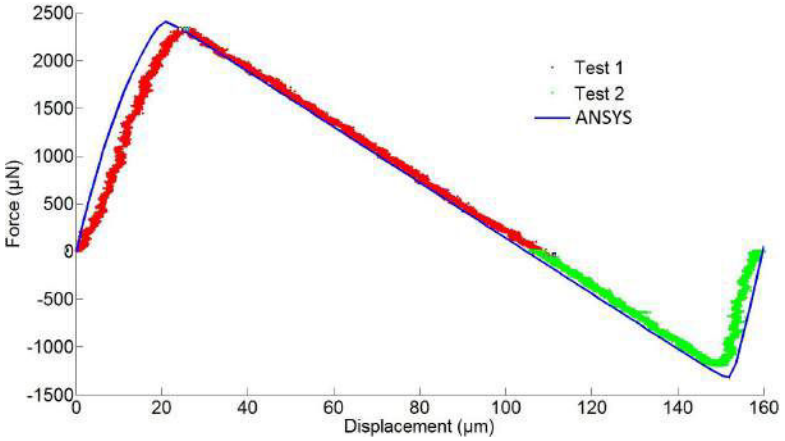

FIGURE *5.25: Snapping force curves of a hinged preshaped curved beams prototype obtained in the experiment and FEM simulations. The beam dimensions are as follows:* $t = 20\mu m$, $l = 6.8mm$, $b = 100\mu m$, $t_{hinges} = 15\mu m$, $l_{hinges} = 500\mu m$.

In comparison with a FEM simulation, the measured force curve show to be in good agreement with the simulations which validate the FEM simulations. Noting that the prototypes of uniform preshaped curved beams were damaged before making the experiments due to some defects and an accident. However, the modeling without high modes of buckling was validated previously by experiments in [106]. The modeling with high modes of buckling, which is presented in Chapter 2 and is more precise, is validated by FEM simulations. In turn, the FEM simulations are validated by the experiments presented in this section.

5.5 Experiments on the actuators

Several prototypes were designed in the two runs of fabrication to make experiments on the actuators. These prototypes are actuated directly on the wafer (in situ) in a micromanipulation station using electrical conductive probes. The main purpose of these tests is to characterize experimentally the actuators before realizing the experiments on the multistable modules or the DiMiBot. The experimental dynamic behavior and characteristics were presented and analyzed in details in Chapter 3. However, the experimental setup and some remarks noticed in the experiments are presented hereinafter.

5.5.1 Experimental setup

The experimental setup in these experiments is shown in Figure 5.26. The prototypes are placed under a microscope (Olympus) on a micromanipulation station (PM5 Manual Analytical Probe).

A high speed camera (Phantom V710) is connected on the top of the microscope. It allows recording the motion of the prototype throughout the microscope. A PC is connected to the camera to record videos and take snapshots. Probeheads (PH100) are placed at the borders of the micromanipulation station. Each probehead allows moving its probe in the space manually with micrometric resolution.

The electrical signal is supplied by an arbitrary generator (Tabor 1074) and a power amplifier (Tabor 9400). The electrical connection with each actuator in the prototypes is provided by 2 conductive probes that are connected to the actuator pads. An accurate current measuring device (KEITHLEY DMM 7510) is connected in series with the actuator for measuring the electric current in real time. The different voltages are visualized using an oscilloscope (Tektronix TDS 3014).

The use of a high speed camera allowed detecting the behavior of the actuator in response to an electrical step activation with a frame rate of up to several ten thousands of frames per second. The displacement of the actuator is measured on the recorded videos point-by-point using a specific software. Figure 5.27.a shows an actuator in the initial position where a reference position is defined in the video frame. Figure 5.27.b shows the actuator after supplying where the displacement is measured with respect to the reference position.

After applying a voltage step on the actuator, an overshoot of displacement is observed followed by a slow stabilization phase until the steady state. This dynamic behavior was presented and analyzed in details in Chapter 3.

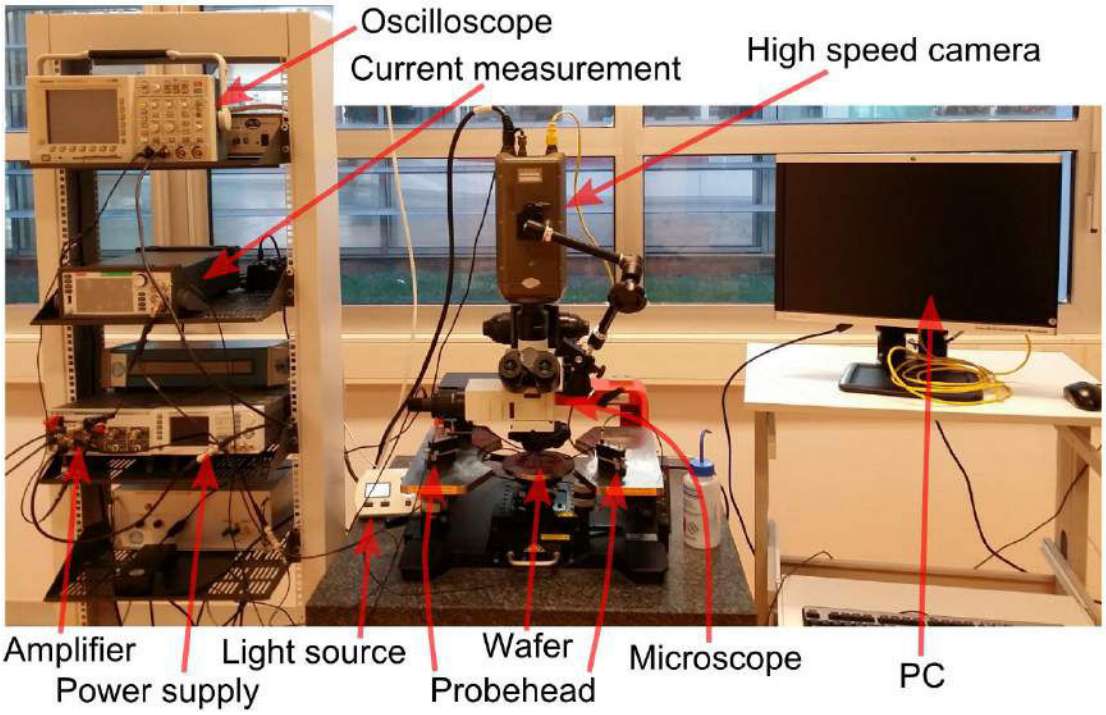

FIGURE *5.26: Micromanipulation station used in the experiments.*

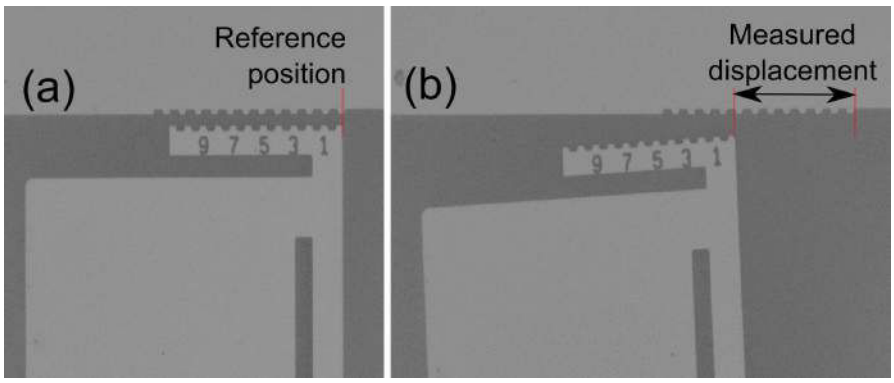

FIGURE *5.27: An actuator in the initial position (a) and after supplying (b).*

The actuator dynamic behavior was not expected firstly in the experiments where very few works in the literature have cited this behavior. The use of a high speed camera was an advantage that allowed detecting the actuator dynamic. After that, we have started analyzing the experimental results using FEM simulations and we have developed the dynamic models presented in Chapter 3.

5.5.2 Remarks noticed in the experiments

In the other side, many remarks are noticed in the experiments on the actuators. These remarks are presented point-by-point in the following.

The experiments on the actuator were made for several dimensions, with and without loads and with and without gold layer on the top of the cold arm. The dynamic behavior is remarked to be similar in all the experiments. Taking the example of the tests made with loads, Figure 5.28 shows the displacement curves of two actuators with the same dimensions at the same voltage, no loads are applied on the first one, while the second actuator acts on an elastic beam (Figure 5.7). The beam dimensions are as follows: thickness= $30\mu m$, length= $2040\mu m$, width= $100m$.

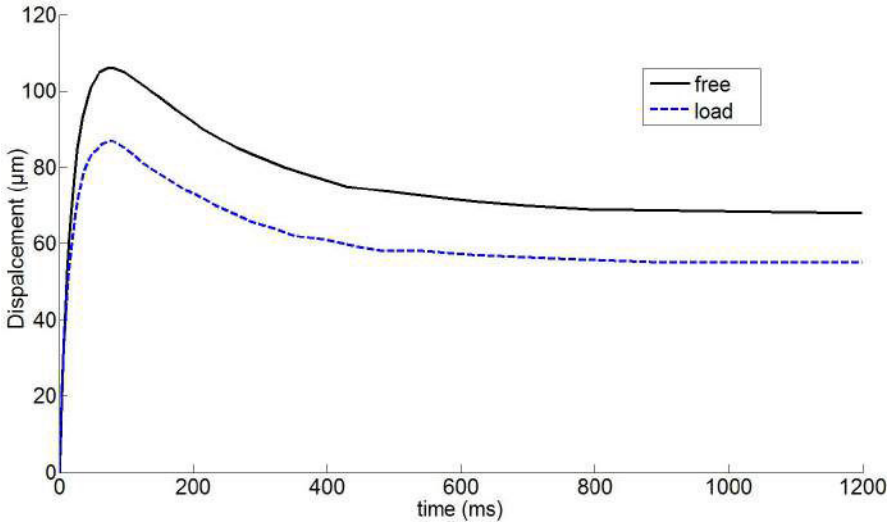

FIGURE *5.28: Example of the displacement curves of two actuators with the same characteristics, one is free and the other acts on an elastic beam as a load.*

Figure 5.28 shows the same dynamic behavior between the free and loaded actuators. However, the displacement amplitude decreases with respect to the load. Dimensions of the elastic beams (loads) in these tests are chosen to have the same stiffness of the loads on the actuators in the multistable module. In this way, the experiments with loads serve for determining the voltage level and supplying time required for the actuators in the multistable module.

The resistivity of the silicon in the device layer is naturally high. A doping of the device layer in the wafers is made during fabrication of the wafer in order to reduce the silicon resistivity. The resistivity depends on the level of the doping. However, we have noticed that the resistivity was not the same between the different wafers. This changed the voltage range that can be applied on the actuators with respect to the wafers.

In the other side, the resistivity of the doped silicon depends also on the temperature. As the temperature in the actuator evolves after applying the electricity, the resistivity of the actuator decreases and thereby the input electrical power increases. Consequently, greater displacement is remarked with respect to the electrical input. This phenomenon was observed in our experiments where after applying a constant voltage step on the actuator, the measured current increases with time and even with successive trials with small delay between each step.

Figure 5.29 shows a current measurement in the actuators of the second run of fabrication after applying a constant voltage of $10V$. Two trials are presented, in the first one, the actuator is supplied in one long voltage step (200s), in the second one, the actuator is supplied in 5 successive voltage steps with small delay between each step.

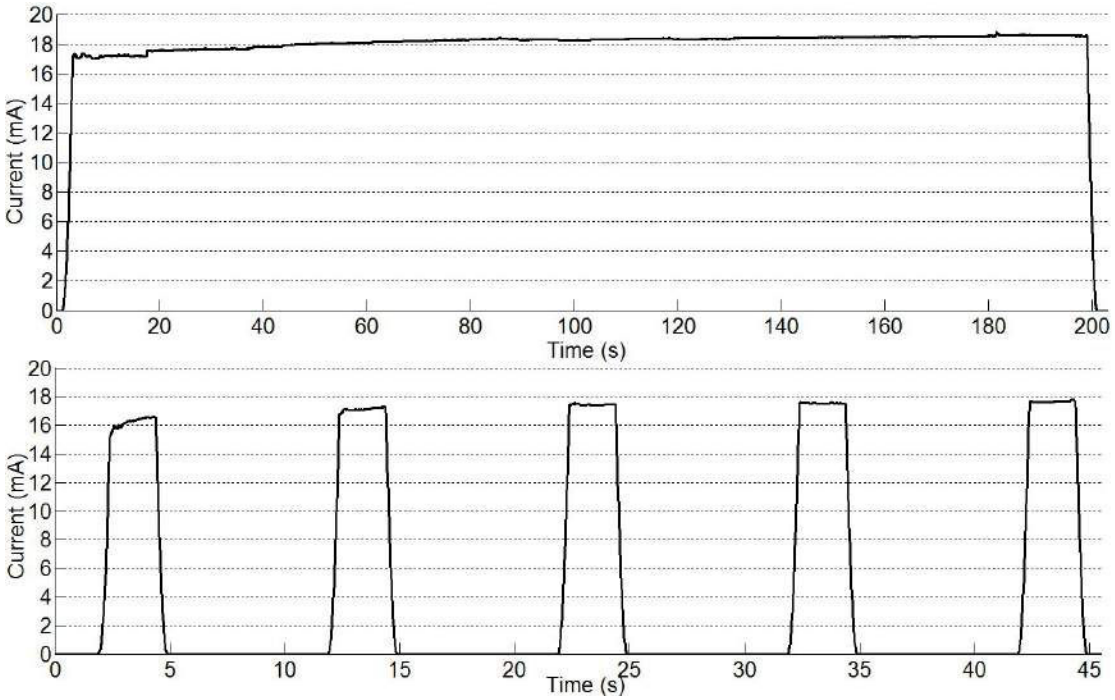

FIGURE *5.29: Evolution of the electrical current after applying a voltage step of* $10V$ *in one long step (upper curve) and in successive steps with small delay between each step (lower curve).*

In the first trial, we notice that the current continues to rise even with long supply time. This behavior confirms the temperature dependency of the silicon actuators. In the second trial, we notice that the current increases at each new trial when the delay in between is small. If another step is applied after a while, the current level return to the level of the first step. This means that the resistivity takes some time to recover its initial value after cooling. However, in the analytical modeling and FEM simulations presented in Chapter 3, a constant resistivity is considered which is the average of the measured resistivity.

Another remark concerns the direction of the current, we have noticed that the displacement is more important when the potential is applied on the hot arm pad while the flexure pad is on the ground. Giving an example, for the same applied voltage, the peak of displacement is equivalent to $132\mu m$ when the current direction is from the hot arm to the flexure, while it is equivalent to $119\mu m$ in the other direction. We don't have a clear explication for this phenomenon. However, the current in the actuator has a direction in the hot arm and a reverse direction in the cold arm and flexure in the other side. The inverse current direction in two juxtaposed lines induces an electromagnetic force. The electromagnetic effect in the actuator is compatible with the experimental results in terms of the direction, but this effect is generally neglected in front of

the electrothermal effect. The actuators in the multistable modules are supplied from the hot arms while the flexure is on the ground, in order to improve their performance.

Further, it is remarked that the actuator transmits the electricity after contact with the load. This means that, in the multistable module structure, the electricity is almost everywhere when the actuators are supplied. In the second run of fabrication, this remark was considered in the design where the different components were electrically separated at the borders to avoid applying a potential difference.

Furthermore, another remark is that when an excess of heating occurs in the actuator, the final position after cooling does not return to the initial position but mostly to a position in the negative side. This probably occurs after exceeding the temperature limits of plastic reshaping. A rapid change in the crystal phase of the silicon occurs during the cooling phase where the actuator is in the negative positions.

The last remark is related to the failure of the actuator, a failure occurs due to an excess of stress at the weak points after a very high displacement. The failure of the loaded actuators occurs more rapidly than the free load actuators. Many actuators were failed in the tests after the first run of fabrication at the link between hot and cold arms. In the second run, the width of this link was increased. The new weak point in the actuators of the second run is the flexure. However, the failure of these actuators is not reached before exceeding the temperature limits. The failure of these actuators in the two case is shown in Figure 5.30.

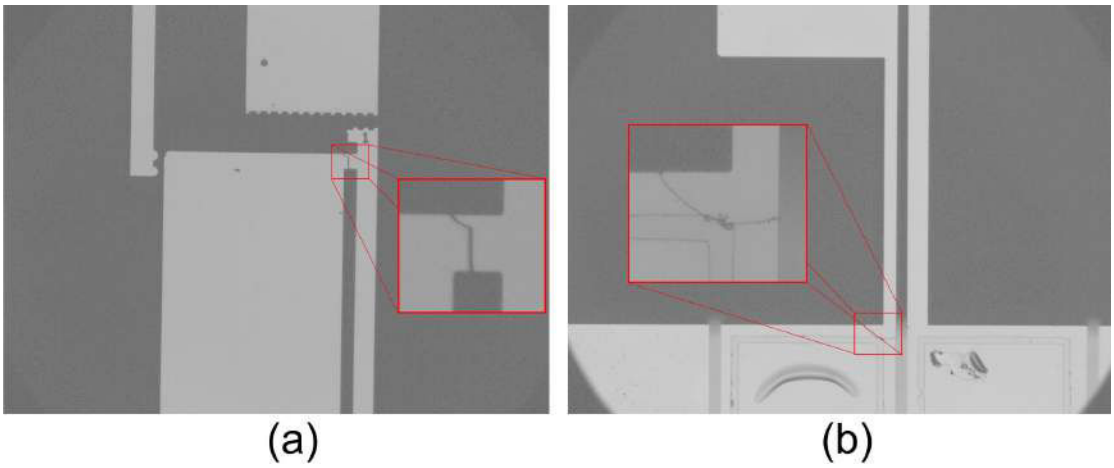

FIGURE *5.30: Failure of the actuators during the experiments at the link between the hot and cold arms for the actuators of the first run (a), and at the flexure for those of the second run of fabrication.*

5.6 Multistable module experiment

Experiments on the multistable modules are presented in this section. These experiments are made in several steps. Firstly, after fabrication and releasing from the wafer, the multistable module is activated to become functional. Secondly, the activated module is wire bonded to a printed circuit board (PCB). Thirdly, the PCB is connected to an electronic circuit, which

consists of microcontroller and switches, for supplying the actuators in the multistable module. Fourthly, each system in the module is tested separately before making a complete sequence in the fifth step. The experiments are recorded using the high speed camera shown in Figure 5.26. The multistable modules showed a proper functioning in the experiments while a defect in the design were deduced. All of these steps are presented one by one in the following. The sequence order, defined in the microcontroller to switch up and down, are presented before the experiments.

5.6.1 Activation of the multistable modules

The first step after fabrication and releasing of the multistable module is to activate it. As explained in Chapter 4, the activation phase consists in arming the different components in the accurate positioning mechanism in system 1 and arming the teeth between S_2 latch and the moving part.

During activation, the multistable module is placed under the microscope in the micromanipulation station and the different components are armed using the needles of three probeheads. Figure 5.31 shows the different steps in the activation phase. Firstly, the upper movable parts are suspended to the upper locks ((a) & (d)), the bottom movable part is then suspended to the bottom lock ((b) & (e)), and then the shuttle of system 1 is pushed to its first position ((c) & (f)). Before pushing the shuttle of system 1 (connected to S_2 latch) upwards, S_2 latch is opened using two needles as shown in (g) to avoid crushing the structure. Thereby, after pushing up and releasing S_2 latch, it becomes engaged to the teeth of the moving part as shown in ((h) & (f)).

5.6.2 Wire bonding

After activation, a PCB is prepared to make the electrical connectivity between the multistable module and an external circuit. The wire bonding is made in the clean room using an ultrasonic wire bonding machine. Figure 5.32 shows a multistable module prototype glued on the PCB where the gold lines in the prototype are wire bonded to the copper lines in the PCB. The prototype is glued at the top edge of the PCB as shown in the figure, while a plastic board is glued under the PCB to protect the multistable module.

5.6.3 Electronic circuit

An electronic circuit was prepared to supply the multistable module. It consists of a microcontroller to control the supply time and sequence order for supplying the different actuators, a relay circuit to switch on or off the current at each actuator, control buttons to choose between upward and downward steps and different connectors. The electronic circuit is supplied by two external electrical sources of 5 and 20V, where 5V is the voltage needed for the microcontroller and the relays and 20V is the voltage to be applied on the actuators. The output of the relays are connected to a ZIF (an electrical connector with zero insertion force), so the PCB with the multistable module can be connected directly to the electronic circuit by inserting it in the ZIF. The electronic circuit with a connected multistable module prototype is shown in Figure 5.33.

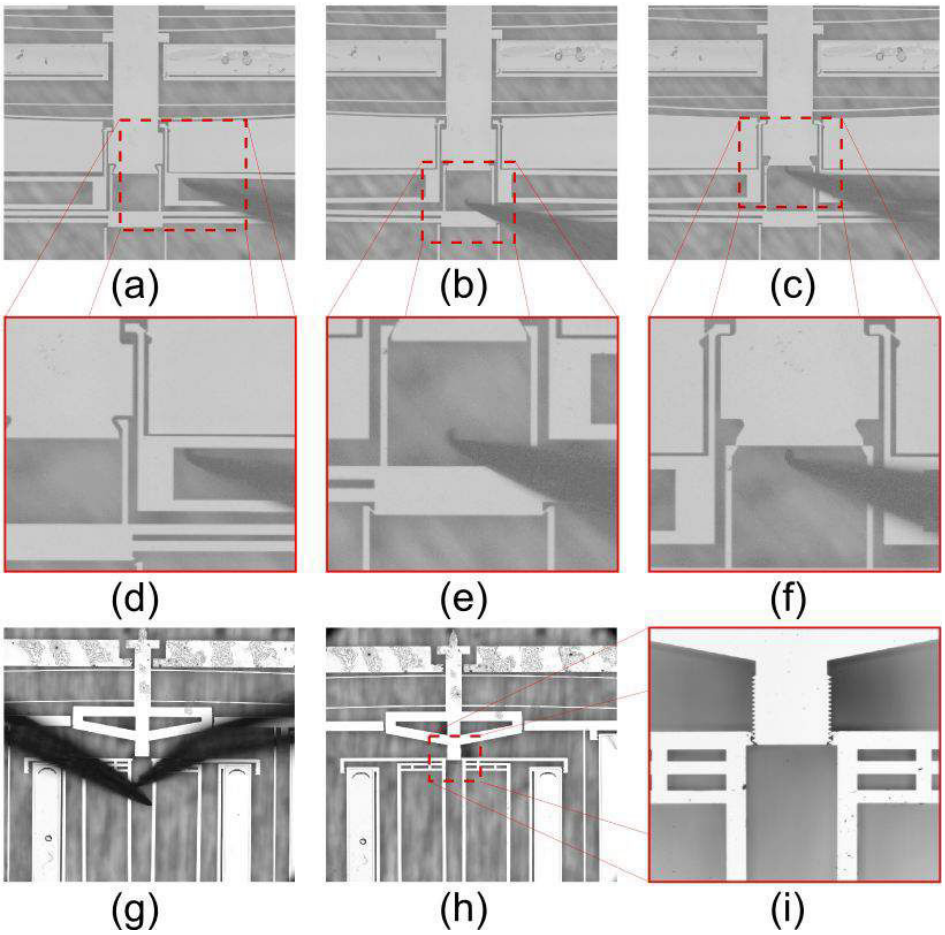

FIGURE *5.31: Activation steps of the multistable module under a microscope using three probe needles.*

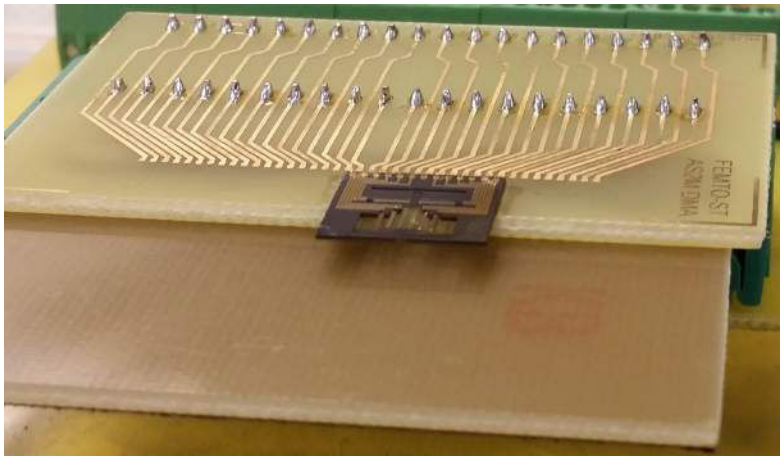

FIGURE *5.32: A multistable module prototype glued and wire bonded on a PCB*

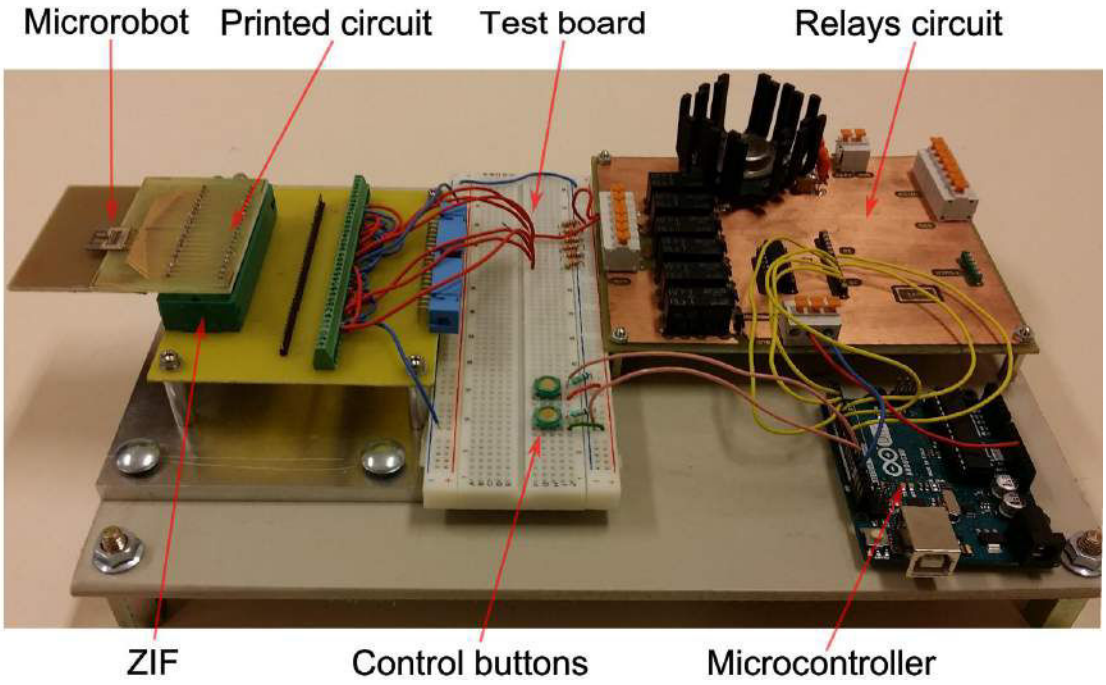

FIGURE *5.33: The electronic circuit for supplying the multistable module prototype.*

The relay circuit is explained in Figure 5.34. A NPN transistor is used as an electrical switch controlled by the microcontroller and a freewheeling diode is connected in parallel with the input of the electromagnetic relay to avoid overvoltage during switching.

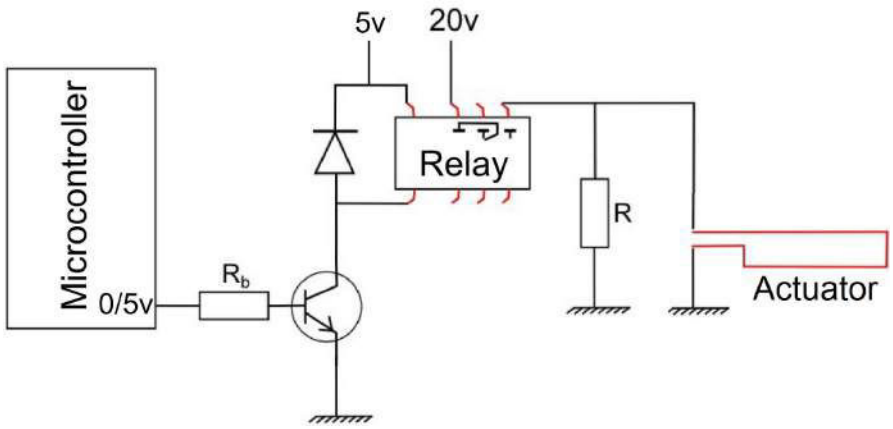

FIGURE *5.34: Schematic of the relay circuit.*

When the microcontroller output is at 5V, the relay becomes activated and the actuator is supplied. A high impedance resistance is connected in parallel with the actuator to ensure a zero voltage at rest.

The two actuators of each system in the multistable module are supplied by the same relay output. Thereby, the multistable module is controlled with 3 relays while 6 relays are required for a complete DiMiBot. A difference of less than $1ms$ is measured between the response time of the different electromagnetic relays which is acceptable for our application.

5.6.4 Tests on the different systems of the multistable module

After preparing the prototypes and the circuit, the different systems are tested separately. These tests are necessary, before testing the functioning of the whole multistable module, to verify the connectivity, the programs in the microcontroller, and to determine the supply time for each system.

Figure 5.35 shows examples of tests made on each of the three systems separately. Three photos are presented for each system, one in the off state, one in the on state and the third one is a zoom on the part that moves. No specific problems were encountered and the actuators in the three systems work properly.

Noting that, on the prototypes obtained in the first run of fabrication, this kind of tests (on systems 1, 2 and 3) were made using the probeheads. These tests served for verifying the functioning of the different systems and detecting some defects in their design and layout. Thereby, the easy success to operate the different systems (after second run of fabrication) without problems, is related to the remarks extracted from the tests made on the prototypes of the first run.

5.6.5 Sequence orders to make steps

The time needed to make a step and to do the different tasks of each system is limited by the response time of the U-shaped actuator. The supply times required for the actuators of the different systems was determined experimentally by trial and error as mentioned in the previous section. Thereafter, the sequence orders to make upward and downward steps are defined in the program of the microcontroller. The sequence orders to make upward and downward steps are shown in Figure 5.36.

A supply time of $20ms$ is chosen for supplying each actuator in order to switch it to the activated state. In the other side, a time of $10ms$ is chosen when releasing each system to return to its initial state elastically. The time to make a step, upward or downward, is equivalent to $80ms$. If faster steps are required, higher voltages can be applied for lower time.

5.6.6 Experimental functioning

The experimental functioning of the multistable module is presented in this section. The functioning is recorded using the high speed camera mounted on a microscope. Applying the sequence orders presented in the last section on the multistable modules allowed making proper steps in the experiments. Figure 5.37 shows the functioning of a multistable module during the different internal steps to make a downward step of displacement.

The moving part is initially in a position (a), S_3 latch is firstly closed (b), S_2 latch is then opened (c), and then moved up ((d) & (e)), after that, S_2 latch closes (f), S_3 latch opens (g) and

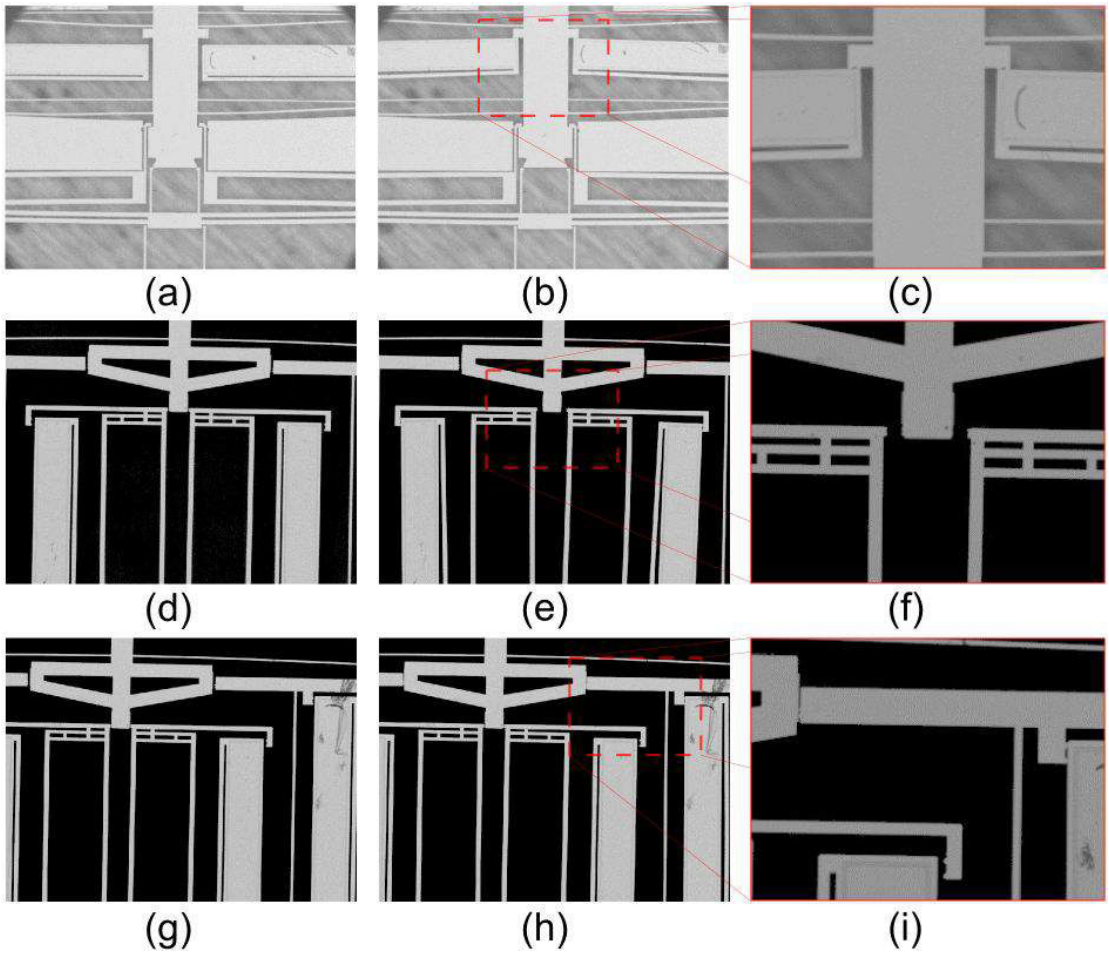

FIGURE *5.35: Tests on systems 1, 2 and 3 respectively. Three photos are presented for each system, one in the off state, one in the on state and the third one is a zoom on the part that moves. System 1 ((a), (b) & (c)), system 2 ((d), (e) & (f)), system 3 ((g), (h) & (i)).*

finally, S_2 latch moves down with the moving part (h), in result, the moving part is now in a lower position as shown in (i).

In result, the proper functioning of the multistable module in the experiments validates its principle and design. These modules are then operational and useful for digital MEMS applications. However, despite the proper functioning, we found some defects concerning the size and type of teeth.

As explained previously in Section 4.4, two configurations of the teeth are used in the multistable modules between the latches and the moving part. In the experiments, we have remarked two defects, one for each teeth configuration. As for the wide teeth configuration, the problem is in the teeth of S_3 latch. After activating and dis-activating system 3, the teeth of S_3 latch remain attached with those of the moving part. In result, the latch remains closed which impedes

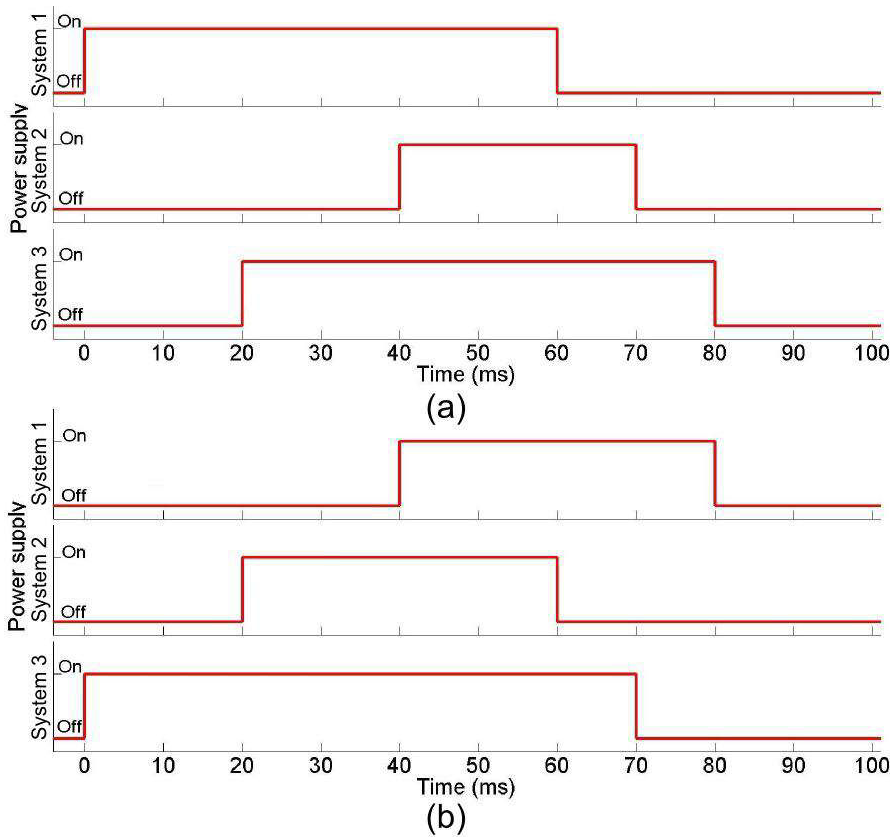

FIGURE *5.36: Sequence order for supplying the actuators of each system in the multistable module in order to make upward and downward steps ((a) and (b) respectively).*

the functioning of the multistable module. This problem is presented in Figure 5.38.a where S_3 latch remains closed after dis-activating system 3.

In contrast, this problem was not encountered in system 2 since the force of the actuators is sufficient to release the teeth, while the stiffness of the gantries of S_3 latch is not sufficient to release the teeth in system 3. This problem was not encountered also with the small teeth configuration. Several hypotheses may explain this phenomenon, the teeth in the small teeth configuration are engaged between the heads and the holes, while in the wide teeth configuration, the teeth are engaged in the sides which may create a kind of permanent sticking. Another hypothesis is that the only two points of contacts in the wide teeth configuration may induce a rotation during closing and opening which lead to be fastened. Another hypothesis is that the etching of the small teeth is not complete at the bottom which make it easy to release the teeth.

In the other side, for the small teeth configuration, the problem is in the teeth of S_2 latch, the teeth start to be broken after several steps back and forth around them. This may return to the weak structure of the teeth. In addition, if the teeth are not totally engaged due to their etching quality, this means that the teeth are engaged at their top which is weaker in result. Figure 5.38.b shows several teeth broken during an experiment.

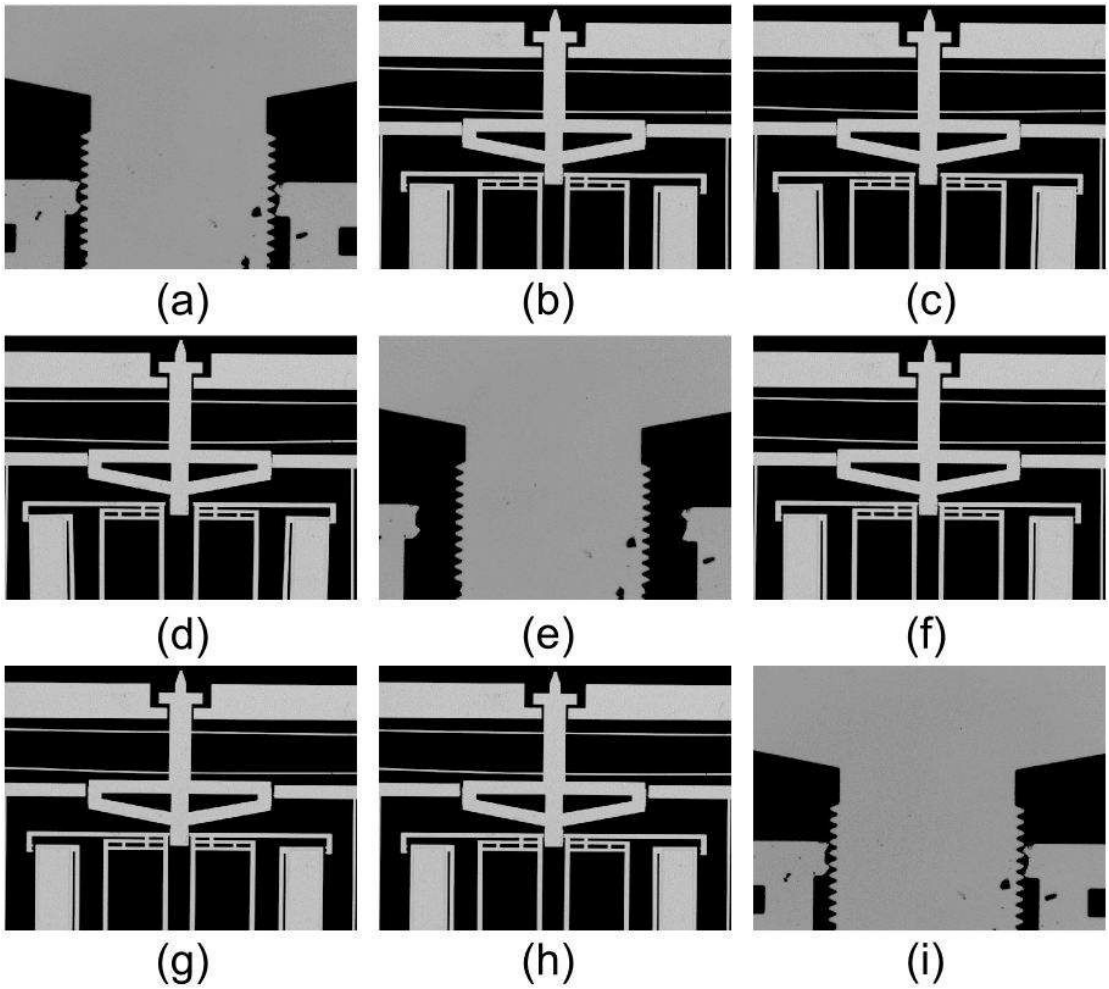

FIGURE *5.37: Functioning of a multistable module during a downward step. The moving part is initially in an upper position (a), S_3 latch is firstly closed (b), S_2 latch is then opened (c), and then moved up ((d) & (e)), after that, S_2 latch closes (f), S_3 latch opens (g) and finally, S_2 latch moves down with the moving part (h), lower position of the moving part is shown in (i).*

This problem does not exist in system 3. A possible explanation is that S_3 latch does not pull or push the moving part vertically during holding, which create additional transversal loads on the teeth. This problem was not encountered also with the wide teeth configuration, the teeth in this configuration are wide and stiffer, and probably their etching quality is better.

A possible solution for the future DiMiBot and multistable modules is simply to use the wide teeth configuration for S_2 latch and the small teeth configuration for S_3 latch. Otherwise, if the step is wider (more than $20\mu m$ for example), the small teeth configuration can be useful for the two latches since the teeth are stiff enough.

In result, experiments show that the multistable module and the different systems inside work properly and are able to make upward and downward steps repeatedly. Optimizing and

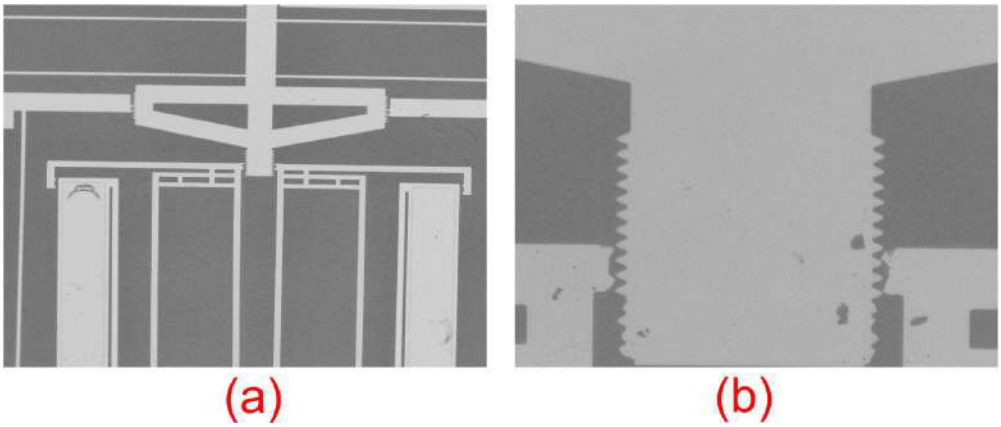

FIGURE *5.38: S_3 latch remains closed after dis-activating system 3 in the modules with wide teeth configuration (a), the teeth with the small configuration of S_2 latch are broken during the experiments (b).*

reducing the sequence time for each step and for the supply time of each actuator remains a matter of concern. Faster steps can be achieved either by making the U-shaped actuator faster (higher voltages with lower time) or by using other actuation technologies with instant response. The electronic circuit was prepared for the experience, it can be miniaturized and incorporated in a single printed circuit. The multistable module itself is a digital positioning system, and it is able to be integrated in more complex systems such as the DiMiBot. However, fabricating a functional DiMiBot prototype remains a task for short term future works.

5.7 Conclusion

Fabrication and experiments was presented in this chapter. After presenting the process flow and layouts, all the difficulties encountered and solutions provided in the fabrication were presented. The advantages of the fabrication process were clarified with respect to that followed in the previous thesis. The experiments are then presented, firstly, force measurement experiments were presented including tests for verifying the stiffness and tests on curved beams. Experiments on the U-shaped actuators were then presented including the experimental setup and some remarks noticed in the experiments. Afterwards, experiments on operational prototypes of the multistable module were presented. These experiments showed a proper functioning of the multistable module and validated its principle and design. Some difficulties were encountered in the fabrication of the DiMiBot, this task remains one of the short term prospects.

Conclusion and perspectives

Conclusion

A new version of a digital microrobot DiMiBot with multistable modules is proposed and developed in this thesis. The DiMiBot has many advantages for MEMS applications, it can perform high accurate and repeatable positioning without the need of a feedback or measurement systems. Digital microrobotics is a topic of concern in our laboratory where a previous version of the DiMiBot with bistable modules was proposed in a previous thesis.

Based on the past achievements, the thesis objectives at the beginning focused on improving the functioning of the DiMiBot, optimizing its design and improving its fabrication process, in order to make it more accurate, more controllable and smaller. Two working axes were followed in order to achieve these goals: the first axis focus on optimizing the design of the main components analytically, the second axis focus on proposing new architectures in order to improve the functioning and the accuracy and going further in the miniaturization.

In the first axis, the main components in the DiMiBot (old and new versions) are the preshaped curved beams and U-shaped electrothermal actuators. Analytical models for these components were developed. As for the preshaped curved beam, in a first stage, the snapping force solution is developed including high modes of buckling which are neglected in literature. In a second stage, evolution of internal stresses during deflection between the two sides of buckling were calculated. Comparison of the analytical results with FEM simulations have shown to be in excellent agreement and showed the importance of considering high modes of buckling in the modeling.

As for the U-shaped actuator, the modeling problem is treated by a sequence of two analytical models: electro-thermal and thermo-mechanical. The electrothermal model provides an exact solution of the hybrid PDEs that describe the electrothermal behavior in the three arms of the actuator. The relation between the displacement and the thermal distribution is then provided in the thermo-mechanical model. Comparison with FEM simulations and experiments showed a good agreement for the two models.

Based on the analytical expressions obtained in the modeling, the influence of the material properties and the different dimensions on the behavior of the curved beam and the U-shaped actuator were investigated. In light of that, design methods were proposed in order to choose the optimal dimensions that ensure the desired outputs and characteristics. These components

are commonly used in MEMS and few works cover their modeling and design in literature, so the models and design methods were developed in a general context and then applied on our specific application.

A new generation of the DiMiBot was proposed in the thesis with several advantages that meet our goals. The new mechanism of the DiMiBot consists of a single multistable module instead of several bistable modules in each side as in the previous structure. This new configuration of the DiMiBot keeps most of the advantages of the old structure and help to overcome several disadvantages that were presented in the old configuration, such as limiting the size from increasing significantly with the number of modules and the ability to realize complex trajectories in the workspace which was not possible previously.

The principle of the new multistable module combines the advantages of stepping actuation in the sense of generating an infinite number of positions simply by extending the range of motion but with stability and accuracy in the positioning as in the bistable modules. The moving part of one multistable module has several stable positions that are distributed vertically on a rectilinear axis. Upward and downward steps are made by a specific sequence of moving and opening normally closed latch arms in a part and closing other normally open latch arms in the other part. Each latch holds the moving part in its closed state either during transition or at rest.

In the other side, an accurate positioning mechanism, which compensate the fabrication tolerances, was developed and used in the multistable module in order to ensure accurate steps and maintained positions.

Figure 1 shows the old and the new generations of the DiMiBot in comparison. The old DiMiBot was fabricated with four bistable modules, its size is equivalent to $36mm \times 24.5mm$ and its workspace consists of $2^4 = 16$ discrete positions. However, size of the new DiMiBot is equivalent to $25mm \times 15mm$ and its workspace consists of $13^2 = 169$ discrete positions. The number of metal lines for supplying the actuators is 24 in the two cases.

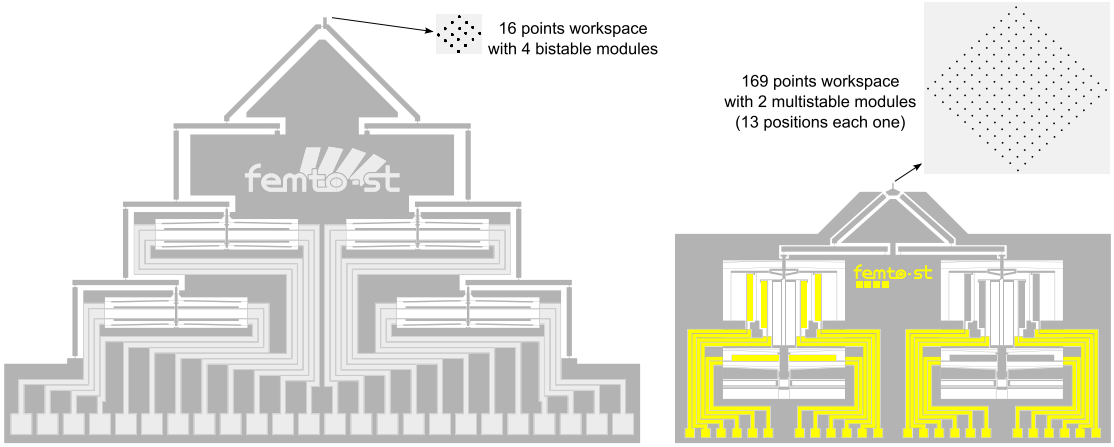

FIGURE *1: Comparison of the size and workspace between the old and the new generation of the DiMiBot. The two workspaces are at the same scale.*

The use of only two elementary modules in the new DiMiBot has many advantages: it makes the DiMiBot more compact and allows generating more positions in the workspace. In contrast,

adding more bistable modules in the old DiMiBot to obtain more positions in the workspace has many drawbacks. For example, if we choose a workspace with 256 discrete positions, 8 bistable modules are required in the old DiMiBot with a total size of $50.5mm \times 33.5mm$ and 48 metal lines. However, the only change to be made in the new DiMiBot is that the range of motion of the moving part of each module must be extended to include 3 more positions.

The DiMiBot with 8 bistable modules has a big size with high number of tiny components distributed on a large surface. This makes the structure more fragile, increases possibilities of failure in the fabrication process and high number of metal lines are required. In addition, the transition in the DiMiBot with multistable module is made between the adjacent positions, not by binary jumps as with the bistable modules. This allows realizing any complex trajectory with an open loop control.

After making the design and plotting the different layouts, two runs of fabrication were made in the clean room MIMENTO in order to realize operational prototypes. Some differences were made in the fabrication process in order to avoid the problems encountered in the previous theses. All the difficulties encountered and solutions provided in the fabrication are detailed in the thesis.

The final phase treated in the thesis is the experiments, including force measurement experiments, experiments on the U-shaped actuators and experiments on some operational prototypes of the multistable module. The experiments show that the multistable module and the different systems inside work properly and are able to make upward and downward steps repeatedly. Fabricating a functional DiMiBot prototype remains a task for short term future works.

Perspectives

The presented work opens up important perspectives for most of the subjects treated in the thesis. The works presented on the modeling and design of the preshaped curved beam are satisfactory for our needs. As for the U-shaped actuator, the consideration of some neglected effects in the modeling, the calculation of the internal stresses and the design to have the capacity to output a required performance at a transient instant are topics that can be addressed. The multistable module development outlooks include the improvement of its performance, making it faster and even more compact. The principle of the DiMiBot must be developed towards more accurate steps with maintained positions in the planar workspace. In a long term, developing a 3D digital microrobot is also one of the perspectives.

Actuators

The analytical models for the U-shaped actuator showed an agreement with FEM simulations and experiments, but with slight differences. Improving the accuracy of the modeling is possible by considering some phenomena neglected in the present approach (convection or radiation, different boundary conditions, temperature dependency of the material properties, 1D simplification, etc.). However, the consideration of some of these simplifications complicates the solution and to date, the problem can be solved only by numerical methods. This results in losing the benefits of the analytical solution for the design.

Further, the calculation method used in the electrothermal model has an original contribution mathematically. It can be developed to solve analytically other physical problems where the problem is described by hybrid PDEs and the variables evolve between multiple connected mediums such as the wave propagation in various environments.

In addition, providing analytical models to describe evolution of the internal stresses is important to avoid the fracture of the weak points in the actuator at high displacement. Until now, the stresses are calculated numerically.

As for the design, in view to the complexity of the analytical expressions, the influence of the various variables on the transient behavior is not totally investigated. Therefore, the proposed design method is made based on the outputs at the steady state. More works must be made to investigate the variables influence on the transient behavior and to provide a design method which ensures to have the capacity to output a required performance at a transient instant.

Multistable module

The multistable module showed to be operational in the experiments. It can be used for accurate positioning applications in MEMS, integrated in more complex systems for more advanced tasks and used in compact environments.

However, the stepping speed remains a matter of concern for the module. Faster motion can be achieved by improving the response time of the actuator. In the case of the U-shaped actuator, this can be achieved by increasing the input voltage with lower supply time while ensuring that the temperature remains in the acceptable margin. Otherwise, other actuation technologies with very low response time can be used.

In the other side, the design of the module can be changed for other number of stable positions and other step dimensions with respect to the design requirements and specific application. However, reducing the step size and increasing the stroke as possible with faster steps pave the way to reach a continuous micropositioning performance with all the advantages of the digital concept previously cited.

New runs of fabrication are expected in the near future with considering the remarks noticed in the first two runs and the experiments. The experimental electronic circuit can be miniaturized and incorporated in a single and compact PCB.

Towards a planar multistable microrobot with holding forces

The top head flexible structure is the solution used in the DiMiBot (old and new generation) to combine the one-axis displacement at the two sides in one planar workspace. However, positions of the end effector in the workspace are stable but not maintained due to the use of the top head flexible structure. The robustness and holding forces in the stable positions of the modules are loosen in the DiMiBot due to the top head flexible structure relating the modules to the end effector. In addition, the different positions in the workspace are not perfectly equidistant due to the small displacement hypothesis and the imperfection of the flexible hinges.

A solution is proposed in Figure 2 for a new planar multistable microrobot architecture, with holding forces and equidistant positions in the workspace. The end effector in this structure is the square bloc in the middle. The displacement in the X axis is made using one multistable

system that place the square bloc in the X direction. The displacement in the Y axis is made using a similar system where the moving part is the totality of the system of the X axis. In this way, no elastic deformation is allowed in the components that hold the end effector

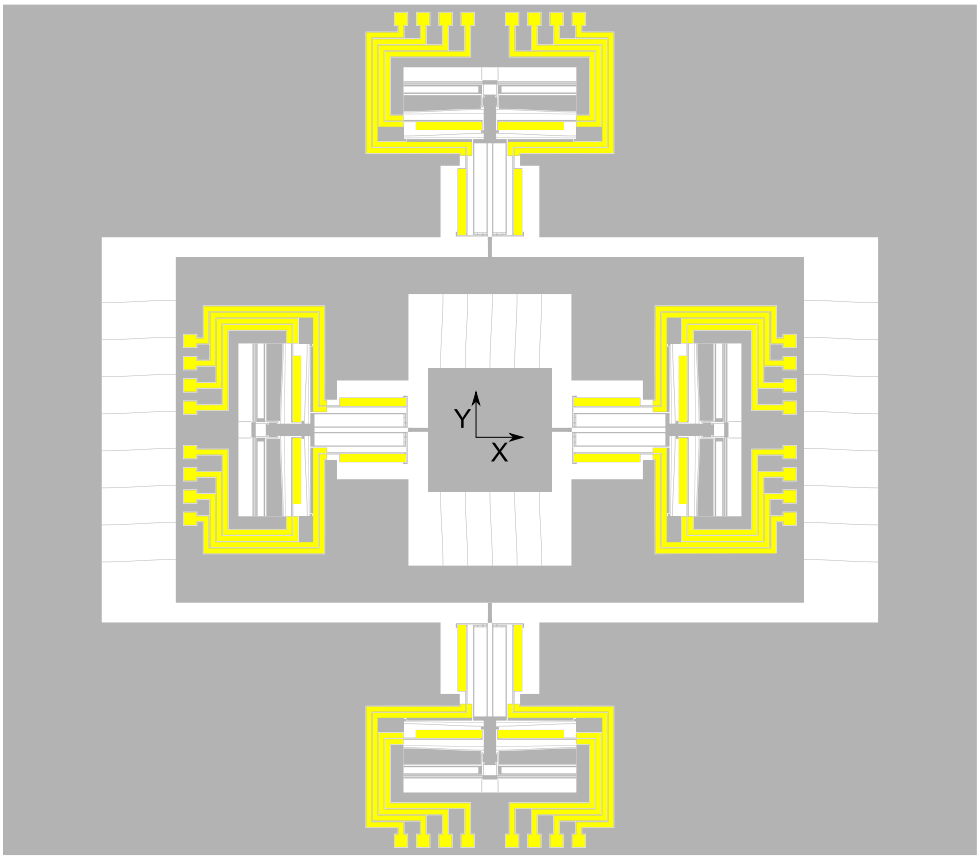

FIGURE 2: *A proposition of a planar multistable microrobot.*

The stepping principle of this microrobot in each axis is very close to the principle of the multistable module presented in the thesis. The stepping in each axis is made by two similar latches normally closed that are placed in opposition in each side of the moving part. Each latch is opened and moved forward similarly to system 1 and 2 in the multistable module. The difference here is that the temporary holding of the moving part ensured by system 3 in the multistable module is made in the new system by the other latch in the other side. This structure allows new sequence orders with faster steps. The stable positions in the workspace are equidistant with holding forces in the two directions at each position. The power supply of the internal system can be insured for example using the curved beams at the borders between it and the substrate or through wire bonding.

Towards a 3D multistable microrobot in three dimensions

Making a 3D digital microrobot is also one of the perspectives in long term. The realization of such a microrobot with micromachining fabrication techniques is quite difficult. Orthogonal assembly of several digital actuators can be a solution to realize 3D digital actuators. Otherwise, elastic mechanisms that converts in plane motion to out of plane motion can be also a solution to fabricate these actuators.

In the other side, new fabrication techniques for microstructures are booming and under development, including the 3D micro-printing and Smart Composite Microstructures (SCM). In the 3D printing, successive layers of material are laid down to build a 3D structure. However, the difficulty in this technique is in adding active materials for the actuation. In the SCM technique, flexible polymer layer is sandwiched between two patterned face sheets of rigid composite materials in one monolithic flat structure. The advantage of this technology is that planar fabrication is employed to yield 3D structure by folding. These microfabrication techniques are promising and could lead soon to perform advanced 3D multistable mechanisms for digital microrobotics.

Bibliography

[1] ABADIE, J., CHAILLET, N., AND LEXCELLENT, C. Modeling of a new sma microactuator for active endoscopy applications. *Mechatronics 19*, 4 (2009), 437–442.

[2] ARTHUR, C., ELLERINGTON, N., HUBBARD, T., AND KUJATH, M. Mems earthworm: a thermally actuated peristaltic linear micromotor. *Journal of Micromechanics and Microengineering 21*, 3 (2011), 035022.

[3] ASHEGHI, M., KURABAYASHI, K., KASNAVI, R., AND GOODSON, K. Thermal conduction in doped single-crystal silicon films. *Journal of Applied Physics 91*, 8 (2002), 5079–5088.

[4] ATRE, A. Effect of shape factors and material property variations on modeling the response of thermal microactuators. *Sensors and Actuators A: Physical 134*, 1 (2006), 69–76.

[5] BARTH, J., AND KOHL, M. A bistable magnetically enhanced shape memory microactuator with high blocking forces. *Physics Procedia 10* (2010), 189–196.

[6] BINTORO, J. S., AND HESKETH, P. J. An electromagnetic actuated on/off microvalve fabricated on top of a single wafer. *Journal of Micromechanics and Microengineering 15*, 6 (2005), 1157.

[7] BÖHM, S., BURGER, G., KORTHORST, M., AND ROSEBOOM, F. A micromachined silicon valve driven by a miniature bi-stable electro-magnetic actuator. *Sensors and Actuators A: Physical 80*, 1 (2000), 77–83.

[8] BRENNER, M. P., LANG, J. H., LI, J., QIU, J., AND SLOCUM, A. H. Optimal design of a bistable switch. *Proceedings of the National Academy of Sciences 100*, 17 (2003), 9663–9667.

[9] CAMESCASSE, B. *Actionnements statique et dynamique dun mecanisme bistable : aspects modlisation, conception et exprimental*. PhD thesis, Universit Pierre et Marie Curie, 2013.

[10] CAZOTTES, P. *Actionnement des systemes bistables: modlisation et tudes exprimentales*. Thse de doctorat, Universit Pierre et Marie Curie, Paris, France, 2009.

[11] CAZOTTES, P., FERNANDES, A., POUGET, J., AND HAFEZ, M. Actuation of bistable buckled beams with macro-fiber composites. In *Intelligent Robots and Systems, 2008. IROS 2008. IEEE/RSJ International Conference on* (2008), IEEE, pp. 564–569.

[12] CHALVET, V. *Conception, réalisation et commande d'un microrobot numérique, planaire, non-redondant et en technologie MEMS.* PhD thesis, Université de Franche-Comté, 2013.

[13] CHALVET, V., HADDAB, Y., AND LUTZ, P. A microfabricated planar digital microrobot for precise positioning based on bistable modules.

[14] CHAPUIS, Y.-A., FUKUTA, Y., MITA, Y., AND FUJITA, H. Autonomous decentralized systems based on distributed controlled mems actuator for micro conveyance application. *56*, 1 (2004), 109–115.

[15] CHARLOT, B., SUN, W., YAMASHITA, K., FUJITA, H., AND TOSHIYOSHI, H. In-plane bistable nanowire for memory devices. In *Design, Test, Integration and Packaging of MEMS/MOEMS, 2008. MEMS/MOEMS 2008. Symposium on* (2008), IEEE, pp. 254–258.

[16] CHEN, G., ATEN, Q. T., ZIRBEL, S., JENSEN, B. D., AND HOWELL, L. L. A tristable mechanism configuration employing orthogonal compliant mechanisms. *Journal of Mechanisms and Robotics 2*, 1 (2010), 014501.

[17] CHEN, G., GOU, Y., AND ZHANG, A. Synthesis of compliant multistable mechanisms through use of a single bistable mechanism. *Journal of Mechanical Design 133*, 8 (2011), 081007.

[18] CHEN, G., WILCOX, D. L., AND HOWELL, L. L. Fully compliant double tensural tristable micromechanisms (dttm). *Journal of Micromechanics and Microengineering 19*, 2 (2009), 025011.

[19] CHEN, J.-S., AND TSAO, H.-W. Static snapping load of a hinged extensible elastica. *Applied Mathematical Modelling* (2013).

[20] CHEN, Q. *Microrobotique numérique fondée sur l'utilisation de modules bistables : conception, fabrication et commande de modules monolithiques.* phdthesis, Université de Franche-Comté, 2010.

[21] CHEN, Q., HADDAB, Y., AND LUTZ, P. Digital microrobotics based on bistable modules: Design of compliant bistable structures. In *IEEE/ASME International Conference on Mechtronic and Embedded Systems and Applications, 2008. MESA 2008* (2008), p. 3641.

[22] CHEN, Q., HADDAB, Y., AND LUTZ, P. Microfabricated bistable module for digital microrobotics. *Journal of Micro-Nano Mechatronics 6*, 1-2 (2011), 1–12.

[23] CHEN, R., NGUYEN, H., AND WU, M. A high-speed low-voltage stress-induced micromachined 2 x 2 optical switch. *IEEE Photonics Technology Letters 11*, 11 (1999), 1396–1398.

[24] CHEN, S.-C., AND CULPEPPER, M. L. Design of a six-axis micro-scale nanopositionerμhexflex. *Precision engineering 30*, 3 (2006), 314–324.

[25] CHIAO, M., AND LIN, L. Self-buckling of micromachined beams under resistive heating. *Microelectromechanical Systems, Journal of 9*, 1 (2000), 146–151.

[26] COCHRAN, K. R., FAN, L., AND DEVOE, D. L. High-power optical microswitch based on direct fiber actuation. *Sensors and Actuators A: Physical 119*, 2 (2005), 512–519.

[27] COMTOIS, J. H., AND BRIGHT, V. M. Applications for surface-micromachined polysilicon thermal actuators and arrays. *Sensors and Actuators A: Physical 58*, 1 (Jan. 1997), 19–25.

[28] DAS, A. N., SIN, J., POPA, D. O., AND STEPHANOU, H. E. On the precision alignment and hybrid assembly aspects in manufacturing of a microspectrometer. In *Automation Science and Engineering, 2008. CASE 2008. IEEE International Conference on* (2008), IEEE, pp. 959–966.

[29] DE DOBBELAERE, P., FALTA, K., GLOECKNER, S., AND PATRA, S. Digital mems for optical switching. *Communications Magazine, IEEE 40*, 3 (2002), 88–95.

[30] DEVOS, S., VAN DE VIJVER, W., DECOSTER, K., REYNAERTS, D., AND VAN BRUSSEL, H. A planar piezoelectric drive with a stepping and a resonant operation mode. In *Proc. of 4th International Conference of the European Society for Precision Engineering and Nanotechnology, Glasgow, May 30th–June 3rd* (2004).

[31] DIEPPEDALE, C., DESLOGES, B., ROSTAING, H., DELAMARE, J., CUGAT, O., AND MEUNIER-CARUS, J. Magnetic bistable micro-actuator with integrated permanent magnets. In *IEEE Sensors conference* (2004).

[32] DRIESEN, M., CEYSSENS, F., DECOSTER, J., AND PUERS, R. Nickel-plated thermal switch with electrostatic latch. *Sensors and Actuators A: Physical 164*, 1 (2010), 148–153.

[33] EMAM, S. A., AND NAYFEH, A. H. On the nonlinear dynamics of a buckled beam subjected to a primary-resonance excitation. 117.

[34] ENIKOV, E. T., KEDAR, S. S., AND LAZAROV, K. V. Analytical model for analysis and design of v-shaped thermal microactuators. *Microelectromechanical Systems, Journal of 14*, 4 (2005), 788–798.

[35] ERISMIS, M. A., NEVES, H. P., DE MOOR, P., VAN HOOF, C., AND PUERS, R. Low voltage electrostatic inchworm actuators in aqueous environments. *Procedia Chemistry 1*, 1 (2009), 686–689.

[36] FREUDENREICH, M., MESCHEDER, U., AND SOMOGYI, G. Simulation and realization of a novel micromechanical bi-stable switch. *Sensors and Actuators A: Physical 114*, 2 (2004), 451–459.

[37] FUKUTA, Y., CHAPUIS, Y.-A., MITA, Y., AND FUJITA, H. Design, fabrication, and control of mems-based actuator arrays for air-flow distributed micromanipulation. *Microelectromechanical Systems, Journal of 15*, 4 (2006), 912–926.

[38] GALAMBOS, P., LANTZ, J., BAKER, M. S., MCCLAIN, J., BOGART, G. R., AND SIMONSON, R. J. Active mems valves for flow control in a high-pressure micro-gas-analyzer. *Microelectromechanical Systems, Journal of 20*, 5 (2011), 1150–1162.

[39] GAO, Y., YOU, Z., AND ZHAO, J. Electrostatic comb-drive actuator for mems relays/switches with double-tilt comb fingers and tilted parallelogram beams. *Journal of Micromechanics and Microengineering 25*, 4 (2015), 045003.

[40] GEISBERGER, A. A., SARKAR, N., ELLIS, M., AND SKIDMORE, G. D. Electrothermal properties and modeling of polysilicon microthermal actuators. *Microelectromechanical Systems, Journal of 12*, 4 (2003), 513–523.

[41] GERDES, H., DINULOVIC, D., AND GATZEN, H. Electromagnetic dual-position actuator for measurement applications. In *Proceedings of Actuator* (2006), pp. 824–827.

[42] GERSON, Y., KRYLOV, S., ILIC, B., AND SCHREIBER, D. Design considerations of a large-displacement multistable micro actuator with serially connected bistable elements. *Finite Elements in Analysis and Design 49*, 1 (2012), 58–69.

[43] GIANNOPOULOS, G., MONREAL, J., AND VANTOMME, J. Snap-through buckling behavior of piezoelectric bimorph beams: I. analytical and numerical modeling. *Smart materials and structures 16*, 4 (2007), 1148.

[44] GIDDINGS, P. F., KIM, H. A., SALO, A. I., AND BOWEN, C. R. Modelling of piezoelectrically actuated bistable composites. *Materials Letters 65*, 9 (2011), 1261–1263.

[45] GLASSBRENNER, C., AND SLACK, G. A. Thermal conductivity of silicon and germanium from 3 k to the melting point. *Physical Review 134*, 4A (1964), A1058.

[46] GOMEZ, S., BELEN, R. J., KIEHLBAUCH, M., AND AYDIL, E. S. Etching of high aspect ratio structures in si using sf 6/o 2 plasma. *Journal of Vacuum Science & Technology A: Vacuum, Surfaces, and Films 22*, 3 (2004), 606–615.

[47] GUCKEL, H., KLEIN, J., CHRISTENSON, T., SKROBIS, K., LAUDON, M., AND LOVELL, E. Thermo-magnetic metal flexure actuators. In *Solid-State Sensor and Actuator Workshop, 1992. 5th Technical Digest., IEEE* (1992), IEEE, pp. 73–75.

[48] HAGA, Y., MAKISHI, W., IWAMI, K., TOTSU, K., NAKAMURA, K., AND ESASHI, M. Dynamic braille display using sma coil actuator and magnetic latch. *Sensors and Actuators A: Physical 119*, 2 (2005), 316–322.

[49] HÄLG, B. On a micro-electro-mechanical nonvolatile memory cell. *Electron Devices, IEEE Transactions on 37*, 10 (1990), 2230–2236.

[50] HAN, J. S., MÃŽLLER, C., WALLRABE, U., AND KORVINK, J. G. Design, simulation, and fabrication of a quadstable monolithic mechanism with x-and y-directional bistable curved beams. *Journal of Mechanical Design 129*, 11 (2007), 1198–1203.

[51] HEDLUND, C., BLOM, H.-O., AND BERG, S. Microloading effect in reactive ion etching. *Journal of Vacuum Science & Technology A 12*, 4 (1994), 1962–1965.

[52] HENNEKEN, V. A., TICHEM, M., AND SARRO, P. M. Improved thermal u-beam actuators for micro-assembly. *Sensors and Actuators A: Physical 142*, 1 (2008), 298–305.

[53] HERDING, M., JOBST, G., URBAN, G., AND WOIAS, P. A polymer-based optical 1×2 fiber switch. In *Int. Conference on New Actuators* (2004), pp. 246–249.

[54] HICKEY, R., KUJATH, M., AND HUBBARD, T. Heat transfer analysis and optimization of two-beam microelectromechanical thermal actuators. *Journal of Vacuum Science & Technology A 20*, 3 (2002), 971–974.

[55] HICKEY, R., SAMEOTO, D., HUBBARD, T., AND KUJATH, M. Time and frequency response of two-arm micromachined thermal actuators. *Journal of Micromechanics and Microengineering 13*, 1 (2002), 40.

[56] HUANG, H.-W., AND YANG, Y.-J. A MEMS bistable device with push-On_Push-Off capability. 79.

[57] HUANG, Q.-A., AND LEE, N. K. S. Analysis and design of polysilicon thermal flexure actuator. *J. Micromech. Microeng. 9*, 1 (Mar. 1999), 64.

[58] HUANG, Q.-A., AND LEE, N. K. S. Analytical modeling and optimization for a laterally-driven polysilicon thermal actuator. *Microsystem Technologies 5*, 3 (Feb. 1999), 133–137.

[59] HUSSEIN, H., CHALVET, V., LE MOAL, P., BOURBON, G., HADDAB, Y., AND LUTZ, P. Design optimization of bistable modules electrothermally actuated for digital microrobotics. In *Advanced Intelligent Mechatronics (AIM), 2014 IEEE/ASME International Conference on* (2014), IEEE, pp. 1273–1278.

[60] HWANG, G. S., AND GIAPIS, K. P. On the origin of the notching effect during etching in uniform high density plasmas. *Journal of Vacuum Science & Technology B 15*, 1 (1997), 70–87.

[61] JENSEN, B., HOWELL, L., AND SALMON, L. Design of two-link, in-plane, bistable compliant micro-mechanisms. *Journal of Mechanical Design 121*, 3 (1999), 416–423.

[62] JENSEN, B. D., PARKINSON, M. B., KURABAYASHI, K., HOWELL, L. L., AND BAKER, M. S. Design optimization of a fully-compliant bistable micro-mechanism. 2125.

[63] JIA, C., ZHOU, J., DONG, W., AND CHEN, W. Design and fabrication of silicon-based 8× 8 mems optical switch array. *Microelectronics Journal 40*, 1 (2009), 83–86.

[64] JUNGEN, A., PFENNINGER, M., TONTELING, M., STAMPFER, C., AND HIEROLD, C. Electrothermal effects at the microscale and their consequences on system design. *Journal of Micromechanics and Microengineering 16*, 8 (2006), 1633.

[65] KHAN, M. U. *Contribution to the design and fabrication of an integrated micro-positioning system*. PhD thesis, Université de Technologie de Compiègne, 2014.

[66] KO, J. S., LEE, M. G., HAN, J. S., GO, J. S., SHIN, B., AND LEE, D.-S. A laterally-driven bistable electromagnetic microrelay. *ETRI journal 28*, 3 (2006), 389–392.

[67] KOHL, M., KREVET, B., AND JUST, E. Sma microgripper system. *Sensors and Actuators A: Physical 97* (2002), 646–652.

[68] KOLESAR, E. S., ALLEN, P. B., HOWARD, J. T., WILKEN, J. M., AND BOYDSTON, N. Thermally-actuated cantilever beam for achieving large in-plane mechanical deflections. *Thin Solid Films 355* (1999), 295–302.

[69] KRYLOV, S., AND DICK, N. Dynamic stability of electrostatically actuated initially curved shallow micro beams. *Continuum Mechanics and Thermodynamics 22*, 6-8 (2010), 445–468.

[70] KRYLOV, S., ILIC, B. R., SCHREIBER, D., SERETENSKY, S., AND CRAIGHEAD, H. The pull-in behavior of electrostatically actuated bistable microstructures. *Journal of Micromechanics and Microengineering 18*, 5 (2008), 055026.

[71] KUANG, Y., HUANG, Q.-A., AND LEE, N. K. S. Numerical simulation of a polysilicon thermal flexure actuator. *Microsystem Technologies 8*, 1 (Mar. 2002), 17–21.

[72] KWON, H. N., HWANG, I.-H., AND LEE, J.-H. A pulse-operating electrostatic microactuator for bi-stable latching. *Journal of Micromechanics and Microengineering 15*, 8 (2005), 1511.

[73] KWON, H. N., JEONG, S. H., LEE, S. K., AND LEE, J. H. Design and characterization of a micromachined inchworm motor with thermoelastic linkage actuators. *Sensors and Actuators A: Physical 103*, 1 (2003), 143–149.

[74] LEESTER-SCHÄDEL, M., HOXHOLD, B., LESCHE, C., DEMMING, S., AND BÜTTGENBACH, S. Micro actuators on the basis of thin sma foils. *Microsystem Technologies 14*, 4-5 (2008), 697–704.

[75] LERCH, P., SLIMANE, C. K., ROMANOWICZ, B., AND RENAUD, P. Modelization and characterization of asymmetrical thermal micro-actuators. *Journal of Micromechanics and Microengineering 6*, 1 (1996), 134.

[76] LI, J., LIU, A., AND ZHANG, Q. Tolerance analysis for comb-drive actuator using drie fabrication. *Sensors and Actuators A: Physical 125*, 2 (2006), 494–503.

[77] LI, J., ZHAO, H., QU, H., CUI, T., FU, L., HUANG, H., REN, L., AND FAN, Z. A piezoelectric-driven rotary actuator by means of inchworm motion. *Sensors and Actuators A: Physical 194* (2013), 269–276.

[78] LI, S. S. The dopant density and temperature dependence of hole mobility and resistivity in boron doped silicon. *Solid-State Electronics 21*, 9 (1978), 1109–1117.

[79] LIAO, B.-T., SHEN, H.-H., LIAO, H.-H., AND YANG, Y.-J. A bi-stable 2x2 optical switch monolithically integrated with variable optical attenuators. *Optics express 17*, 22 (2009), 19919–19925.

[80] LIN, L., AND CHIAO, M. Electrothermal responses of lineshape microstructures. *Sensors and Actuators A: Physical 55*, 1 (1996), 35–41.

[81] LUCHETTI, T., ZANELLA, A., BIASIOTTO, M., AND SACCAGNO, A. Electrically actuated antiglare rear-view mirror based on a shape memory alloy actuator. *Journal of materials engineering and performance 18*, 5-6 (2009), 717–724.

[82] LUHARUKA, R., AND HESKETH, P. J. A bistable electromagnetically actuated rotary gate microvalve. *Journal of Micromechanics and Microengineering 18*, 3 (2008), 035015.

[83] MAEKOBA, H., HELIN, P., REYNE, G., BOUROUINA, T., AND FUJITA, H. Self-aligned vertical mirror and v-grooves applied to an optical-switch: modeling and optimization of bi-stable operation by electromagnetic actuation. *Sensors and Actuators A: Physical 87*, 3 (2001), 172–178.

[84] MAHMOUDI, P., AND MAHMOUDI, A. An electrothermally-driven low voltage micro switch for high frequency applications. *Journal of Electrical Engineering 14*, 21 (2014).

[85] MASTERS, N. D., AND HOWELL, L. L. A self-retracting fully compliant bistable micromechanism. *Microelectromechanical Systems, Journal of 12*, 3 (2003), 273–280.

[86] MATSUNAGA, T., TOTSU, K., ESASHI, M., AND HAGA, Y. Tactile display using shape memory alloy micro-coil actuator and magnetic latch mechanism. *Displays 34*, 2 (2013), 89–94.

[87] MATSUURA, T., FUKAMI, T., CHABLOZ, M., SAKAI, Y., IZUO, S.-I., UEMURA, A., KANEKO, S.-I., TSUTSUMI, K., AND HAMANAKA, K. Silicon micro optical switching device with an electromagnetically operated cantilever. *Sensors and Actuators A: Physical 83*, 1 (2000), 220–224.

[88] MAURINI, C., POUGET, J., AND VIDOLI, S. Distributed piezoelectric actuation of a bistable buckled beam. *European Journal of Mechanics-A/Solids 26*, 5 (2007), 837–853.

[89] MAYYAS, M., SHIAKOLAS, P. S., LEE, W. H., AND STEPHANOU, H. Thermal cycle modeling of electrothermal microactuators. *Sensors and Actuators A: Physical 152*, 2 (2009), 192–202.

[90] MOULTON, T., AND ANANTHASURESH, G. Micromechanical devices with embedded electro-thermal-compliant actuation. *Sensors and Actuators A: Physical 90*, 1 (2000), 38–48.

[91] MURATET, S. *Conception, caractérisation et modélisation: Fiabilité prédictive de MEMS à actionnement électrothermique*. PhD thesis, INSA de Toulouse, 2005.

[92] NAYFEH, A. H., AND EMAM, S. A. Exact solution and stability of postbuckling configurations of beams. 395408.

[93] NIU, X., BROCHU, P., STOYANOV, H., YUN, S. R., AND PEI, Q. Bistable electroactive polymer for refreshable braille display with improved actuation stability. In *Proc. of SPIE Vol* (2012), vol. 8340, p. 83400R1.

[94] NOMURA, Y., AND AOYAMA, H. Development of inertia driven micro robot with nano tilting stage for sem operation. *Microsystem technologies 13*, 8-10 (2007), 1347–1352.

[95] OBERHAMMER, J., TANG, M., LIU, A.-Q., AND STEMME, G. Mechanically tri-stable, true single-pole-double-throw (SPDT) switches. 2251.

[96] OH, Y. *Synthesis of multistable equilibrium compliant mechanisms*. Ph.d theisis, University of Michigan, 2008.

[97] OH, Y. S., AND KOTA, S. Synthesis of multistable equilibrium compliant mechanisms using combinations of bistable mechanisms. *Journal of Mechanical Design 131*, 2 (2009), 021002.

[98] OKADA, Y., AND TOKUMARU, Y. Precise determination of lattice parameter and thermal expansion coefficient of silicon between 300 and 1500 k. *Journal of applied physics 56*, 2 (1984), 314–320.

[99] OKHOTIN, A. S., PUSHKARSKIJ, A. S., AND GORBACHEV, V. V. Thermophysical properties of semiconductors.

[100] OZSUN, O., ALACA, B. E., YALCINKAYA, A. D., YILMAZ, M., ZERVAS, M., AND LEBLEBICI, Y. On heat transfer at microscale with implications for microactuator design. *Journal of Micromechanics and Microengineering 19*, 4 (2009), 045020.

[101] PANE, I. Z., AND ASANO, T. Investigation on bistability and fabrication of bistable prestressed curved beam. 5291.

[102] PARK, S., AND HAH, D. Pre-shaped buckled-beam actuators: theory and experiments. *Sensors and Actuators A: Physical 148*, 1 (2008), 186–192.

[103] PENGFEI, H. *Electromagnetic digital actuators array: Characterization of a planar conveyance application and optimized design*. PhD thesis, Université de technologie de Compiégne, 2015.

[104] PETIT, L. *Contribution aux techniques d'actionnement numérique : cas d'un système électromagntique 2D*. 2009.

[105] PHAM, H.-T., AND WANG, D.-A. A quadristable compliant mechanism with a bistable structure embedded in a surrounding beam structure. *Sensors and Actuators A: Physical 167*, 2 (2011), 438–448.

[106] QIU, J., LANG, J., AND SLOCUM, A. A curved-beam bistable mechanism. 137146.

[107] QIU, J., LANG, J. H., SLOCUM, A. H., AND WEBER, A. C. A bulk-micromachined bistable relay with u-shaped thermal actuators. *Microelectromechanical Systems, Journal of 14*, 5 (2005), 1099–1109.

[108] RAKOTONDRABE, M., HADDAB, Y., AND LUTZ, P. Development, modeling, and control of a micro-/nanopositioning 2-dof stick–slip device. *Mechatronics, IEEE/ASME Transactions on 14*, 6 (2009), 733–745.

[109] REBEIZ, G. M., AND MULDAVIN, J. B. Rf mems switches and switch circuits. *Microwave Magazine, IEEE 2*, 4 (2001), 59–71.

[110] RECEVEUR, R. A., MARXER, C. R., WOERING, R., LARIK, V. C., AND DE ROOIJ, N.-F. Laterally moving bistable mems dc switch for biomedical applications. *Microelectromechanical Systems, Journal of 14*, 5 (2005), 1089–1098.

[111] REMMERT, R. Modes of convergence in function theory. In *Theory of Complex Functions*. Springer, 1991, pp. 91–107.

[112] REN, H., AND GERHARD, E. Design and fabrication of a current-pulse-excited bistable magnetic microactuator. 259264.

[113] ROBERT, P., SAIAS, D., BILLARD, C., BORET, S., SILLON, N., MAEDER-PACHURKA, C., CHARVET, P., BOUCHE, G., ANCEY, P., AND BERRUYER, P. Integrated rf-mems switch based on a combination of thermal and electrostatic actuation. In *TRANSDUCERS, Solid-State Sensors, Actuators and Microsystems, 12th International Conference on, 2003* (2003), vol. 2, IEEE, pp. 1714–1717.

[114] ROODENBURG, B., AND EVENBLIJ, B. H. Design of a fast linear drive for (hybrid) circuit breakers–development and validation of a multi domain simulation environment. *Mechatronics 18*, 3 (2008), 159–171.

[115] SAHU, B., TAYLOR, C. R., AND LEANG, K. K. Emerging challenges of microactuators for nanoscale positioning, assembly, and manipulation. *Journal of manufacturing science and engineering 132*, 3 (2010), 030917.

[116] SARAJLIC, E., BERENSCHOT, E., TAS, N., FUJITA, E., KRIJNEN, G., AND ELWENSPOEK, M. High performance bidirectional electrostatic inchworm motor fabricated by trench isolation technology. In *Solid-State Sensors, Actuators and Microsystems, 2005. Digest of Technical Papers. TRANSDUCERS'05. The 13th International Conference on* (2005), vol. 1, IEEE, pp. 53–56.

[117] SHIGEMATSU, R., HIGO, A., TOSHIYOSHI, H., AND FUJITA, H. An electrostatically latched and magnetically erased mems re-writable bitmap image display. *IEICE Electronics Express 3*, 5 (2006), 87–91.

[118] STOIMENOV, B. L., ROSSITER, J. M., AND MUKAI, T. Manufacturing of ionic polymer-metal composites (IPMCs) that can actuate into complex curves. In *The 14th International Symposium on: Smart Structures and Materials & Nondestructive Evaluation and Health Monitoring* (2007), International Society for Optics and Photonics, pp. 65240T65240T–11.

[119] SUJAN, V., LICHTER, M. D., DUBOWSKY, S., ET AL. Lightweight hyper-redundant binary elements for planetary exploration robots. In *Advanced Intelligent Mechatronics, 2001. Proceedings. 2001 IEEE/ASME International Conference on* (2001), vol. 2, IEEE, pp. 1273–1278.

[120] SUTHAKORN, J., AND CHIRIKJIAN, G. S. A new inverse kinematics algorithm for binary manipulators with many actuators. *Advanced Robotics 15*, 2 (2001), 225–244.

[121] SYMS, R. Long-travel electrothermally driven resonant cantilever microactuators. *Journal of Micromechanics and Microengineering 12*, 3 (2002), 211.

[122] TAJADDODIANFAR, F., YAZDI, M. H., AND PISHKENARI, H. N. Dynamics of bistable initially curved shallow microbeams: Effects of the electrostatic fringing fields. In *IEEE/ASME International Conference on Advanced Intelligent Mechatronics AIM* (2014), p. 12791283.

[123] TAN, Y., ZHOU, R., ZHANG, H., LU, G., AND LI, Z. Modeling and simulation of the lag effect in a deep reactive ion etching process. *Journal of Micromechanics and Microengineering 16*, 12 (2006), 2570.

[124] TIMOSHENKO, S. *Theory of elastic stability*. McGraw-Hill, 1961.

[125] TSUCHIYA, Y., TAKAI, K., MOMO, N., NAGAMI, T., MIZUTA, H., ODA, S., YAMAGUCHI, S., AND SHIMADA, T. Nanoelectromechanical nonvolatile memory device incorporating nanocrystalline si dots. *Journal of applied physics 100*, 9 (2006), 094306.

[126] VANGBO, M. An analytical analysis of a compressed bistable buckled beam. 212216.

[127] VITUSHINSKY, R., SCHMITZ, S., AND LUDWIG, A. Bistable thin-film shape memory actuators for applications in tactile displays. *Microelectromechanical Systems, Journal of 18*, 1 (2009), 186–194.

[128] WANG, D.-A., CHEN, J.-H., AND PHAM, H.-T. A tristable compliant micromechanism with two serially connected bistable mechanisms. *Mechanism and Machine Theory 71* (2014), 27–39.

[129] WANG, D.-A., PHAM, H.-T., AND HSIEH, Y.-H. Dynamical switching of an electromagnetically driven compliant bistable mechanism. *Sensors and Actuators A: Physical 149*, 1 (2009), 143–151.

[130] WANG, J., GAO, F., AND ZHANG, Y. Study on binary driven pneumatic unit for hyper-redundant robots. In *Automation, Robotics and Applications (ICARA), 2011 5th International Conference on* (2011), IEEE, pp. 329–333.

[131] WANG, Z., SHEN, X., AND CHEN, X. Design, modeling, and characterization of a mems electrothermal microgripper. *Microsystem Technologies* (2015), 1–8.

[132] WILCOX, D. L., AND HOWELL, L. L. Fully compliant tensural bistable micromechanisms (ftbm). *Microelectromechanical Systems, Journal of 14*, 6 (2005), 1223–1235.

[133] WU, Y., DING, G., ZHANG, C., WANG, J., MAO, S., AND WANG, H. Design and implementation of a bistable microcantilever actuator for magnetostatic latching relay. 325330.

[134] YEOM, J., WU, Y., AND SHANNON, M. A. Critical aspect ratio dependence in deep reactive ion etching of silicon. In *TRANSDUCERS, Solid-State Sensors, Actuators and Microsystems, 12th International Conference on, 2003* (2003), vol. 2, IEEE, pp. 1631–1634.

[135] YU, Z., NIU, X., BROCHU, P., YUAN, W., LI, H., CHEN, B., AND PEI, Q. Bistable electroactive polymers (BSEP): large-strain actuation of rigid polymers. In *SPIE Smart Structures and Materials+ Nondestructive Evaluation and Health Monitoring* (2010), International Society for Optics and Photonics, pp. 76420C76420C–9.

[136] ZAIDI, S. S. H., CHERFI-BOULANGER, Z., AND LAMARQUE, F. *Contactless Energy Transfer and Control Strategy for Bistable Micro-Actuator*. Ph.d theisis, Université de Technologie de Compiègne, 2011.

[137] ZHANG, Y.-H., DING, G., SHUN, X., GU, D., CAI, B., AND LAI, Z. Preparing of a high speed bistable electromagnetic RF MEMS switch. 532537.

[138] ZHANG, Y.-H., DING, G.-F., FU, S., AND CAI, B.-C. A fast switching bistable electromagnetic microactuator fabricated by uv-liga technology. *Mechatronics 17*, 2 (2007), 165–171.

[139] ZHAO, J., GAO, R., CHEN, G., LIU, S., CAO, Q., AND QIU, T. Nonlinear coupling mechanical model for large stroke magnetic-based multistable mechanisms. *Mechanism and Machine Theory 83* (2015), 56–68.

[140] ZHAO, J., ZHANG, Y., HUANG, Y., LIU, S., CHEN, G., GAO, R., AND YANG, Y. Mechanical-magnetic coupling analysis of a novel large stroke penta-stable mechanism possessing multistability transforming capability. *Journal of Mechanisms and Robotics 6*, 3 (2014), 031004.

Résumé :

Un nombre de sujets concernant la microrobotique numériques ont été abordés dans le cadre de cette thèse. Une nouvelle génération du microrobot numérique ”DiMiBot” a été proposé, ce qui rend le DiMiBot plus précis, plus controllable et plus petit. La nouvelle structure est formée de deux modules multistables seulement, ce qui ajoute des fonctionnalités importantes comme l'augmentation du nombre de positions avec une taille plus réduite et la capacité de réaliser des trajectoires complexes dans l'espace de travail. Le principe du nouveau module multistable combine les avantages des microactionneurs pas à pas en termes du principe et du concept numérique en termes de la répétabilité et la robustesse en boucle ouverte. Un mécanisme de positionnement précis, capable de compenser les incertitudes de fabrication a été développé et utilisé pour assurer un positionnement précis. En parallèle, des modèles analytiques ont été développés pour les principaux composants dans le DiMiBot: poutres flambées préformées et actionneurs électrothermiques en U. Des méthodes de conception ont été développées par la suite qui permettent de choisir les dimensions optimales garantissant les performances requises en respectant les spécifications et limites de design. Des prototypes de modules multistables, fabriqués dans la salle blanche MIMENTO, ont montré un bon fonctionnement dans les expériences.

Mots-clés : Microrobotique numérique, DiMiBot, basculement, maintien, mécanismes multistables, optimisation, miniaturisation, poutre flambée préformée, actionneur électrothermique en U, module multistable, microfabrication, micro-usinage de volume

Abstract:

A number of topics concerning digital microrobotics were addressed in this thesis. A new generation of the digital microrobot ”DiMiBot” was proposed with several advantages making the DiMiBot more accurate, more controllable and smaller. The new structure consists of only two multistable modules which adds some important features such as increasing the number of positions with smaller size and the ability to realize complex trajectories in the workspace. The principle of the new multistable module combines the advantages of the stepping microactuators in terms of the principle and of the digital concept in terms of the repeatability and robustness without feedback. The accuracy is ensured with an accurate positioning mechanism that compensate the fabrication tolerances. In parallel, analytical models was developed for the main components in the DiMiBot: preshaped curved beams and U-shaped electrothermal actuators. Subsequently, design methods were developed that allow choosing the optimal dimensions that ensure the desired outputs and respecting the design specifications and limitations. Multistable module prototypes, fabricated in the clean room MIMENTO, showed a proper functioning in the experiments.

Keywords: Digital Microrobotics, DiMiBot, switching function, holding function, multistable mechanisms, optimization, miniaturization, preshaped curved beam, U-shaped electrothermal actuator, multistable module, microfabrication, bulk micromachining

SPIM

■ École doctorale SPIM 16 route de Gray F - 25030 Besançon cedex

■ tél. +33 (0)3 81 66 66 02 ■ ed-spim@univ-fcomte.fr ■ www.ed-spim.univ-fcomte.fr

UFC UNIVERSITÉ DE FRANCHE-COMTÉ